APPLIED COMPUTATIONAL ELECTROMAGNETICS SOCIETY JOURNAL

June 2017
Vol. 32 No. 6
ISSN 1054-4887

The ACES Journal is abstracted in INSPEC, in Engineering Index, DTIC, Science Citation Index Expanded, the Research Alert, and to Current Contents/Engineering, Computing & Technology.

The illustrations on the front cover have been obtained from the research groups at the Department of Electrical Engineering, The University of Mississippi.

EMERITUS EDITORIAL ASSISTANTS

JUNE 2017 REVIEWERS

THE APPLIED COMPUTATIONAL ELECTROMAGNETICS SOCIETY

JOURNAL

Vol. 32 No. 6 June 2017

TABLE OF CONTENTS

Analysis of Truncated Gratings and a Novel Technique for Extrapolating their Characteristics to those of Infinite Gratings

Nikolaos L. Tsitsas [1] and Raj Mittra [2,3]

[1] Department of Informatics
Aristotle University of Thessaloniki, Greece
ntsitsas@csd.auth.gr

[2] Electromagnetic Communication Laboratory
University of Central Florida, USA
rajmittra@ieee.org

[3] King Abdulaziz University, Saudi Arabia

Abstract ― Periodic gratings, such as Frequency Selective Surfaces (FSSs) and EBG (electromagnetic band gap) structures, are used in a wide variety of electromagnetic applications and are typically analyzed under the assumption that they are infinite periodic. Since the real-word structures are necessarily finite, and are derived by truncating the corresponding infinite structures, it is of interest to determine how large the finite structure needs to be so that it mimics its infinite counterpart. A related question is how to extrapolate the simulation results of a finite structure to predict the performance of the corresponding infinite structure in a computationally efficient manner. The objectives of this work are to address both of these questions and to present a novel computational technique which hybridizes analytical and numerical techniques to provide the answers. We illustrate the application of the proposed technique by considering the test case of plane wave scattering by a strip grating and investigate the asymptotic behavior of the solution for the current on a truncated periodic grating as we increase its size. The proportionality constant, relating the current distribution on the unit cell of the infinite grating to the corresponding distribution in the truncated grating, is computed, and its asymptotic value is accurately predicted by using an extrapolation algorithm presented in the paper. The required number of strips is estimated such that the current on the finite structure is sufficiently close to that on the infinite one. The results obtained for the current are found to be in excellent agreement with those derived from full-wave simulations.

Index Terms ― Current density, electromagnetic scattering, extrapolation algorithms, frequency selective surfaces, periodic strip gratings.

I. INTRODUCTION

Frequency selective surfaces (FSSs) composed of periodic arrays of perfectly conducting elements have been extensively used in several applications, *e.g.*, controlling reflection and transmission of electromagnetic waves, electromagnetic band gap (EBG) materials, and metamaterials [1-3]. A review of techniques for the electromagnetic analysis of FSSs is presented in [4]. Established methodologies for the numerical solution of the pertinent boundary value problems entail the application of periodic boundary conditions [1]; the subdomain basis discretization and conjugate gradient techniques [5]; the finite difference time domain (FDTD) method [6]; the finite element method (FEM) [7]; as well as equivalent circuit modeling techniques [8]. Typically, the periodic Green's function (PGF) is used to generate the interaction fields between the elements of the FSS; however, the expression of the PGF is a slowly-convergent infinite series [9].

A representative class of FSSs used to model several applications of the type mentioned above is that of periodic perfectly conducting strip gratings. Electromagnetic scattering by infinite periodic perfectly conducting strip gratings located in free space has been investigated by a number of researchers [10-21], who have implemented both analytical as well as purely numerical methodologies. On the other hand, reported publications dealing with the problem of scattering by truncated periodic gratings, which provide more realistic models for real-world problems, have been relatively sparse and primarily based on the implementation of numerical techniques [22-26].

In this work, we consider a grating composed of periodic perfectly conducting strips as a test example to illustrate the application of a novel solution approach

Submitted On: February 6, 2017
Accepted On: April 23, 2017

of the problem at hand. The approach begins with a truncated ("finite") periodic structure, with a moderate number of cells, and investigates the asymptotic behavior of its solution to develop a novel technique for predicting the performance of the corresponding "infinite" periodic structure. The current induced in the inner region of this truncated grating is computed numerically, and is next utilized as an initial estimate for the computation of the induced current on the corresponding "infinite" grating. We exploit the fact that the current distribution in the inner region of the *truncated* grating with only a moderate number of cells is found to be *proportional* in scale to that of the corresponding induced distribution on the unit cell of the infinite periodic grating, while its shape is essentially the same as that of the periodic one. The proportionality constant is calculated analytically as a sum of a doubly-infinite series, by exploiting the integral representation of the electric field, expanding the unknown current as a Fourier series and then using suitable expressions of the involved functions in the spatial and spectral domains.

By following the above approach, we analyze how the solution of the finite problem converges to that of the infinite one and, also, address the important issue of the minimum number of strips we need in the finite structure in order for it to mimic its infinite counterpart. Examining particular features of the solution of the finite problem is always useful because, realistically, a physical FSS is always finite. The developed approach offers an alternative route for achieving possible speedup in obtaining the solution of the infinite problem by first treating the respective finite problem. Moreover, it circumvents the need to derive the PGF, as well as issues related to convergence of slowly varying infinite series associated with the PGF.

The validity of the derived formulas is tested by examining two limiting cases for which the current is known a *priori*. Numerical results are presented for the computation of the proportionality constant relating the current on the unit cell of the infinite grating to that of the distribution in the inner region of the corresponding finite truncated grating; the latter is computed numerically by an electromagnetic field simulation software. The numerical convergence of this constant with respect to the number of terms retained in the involved series representation is analyzed. It is shown that the limiting value of the constant can be quickly and accurately obtained by using a numerical extrapolation algorithm, which first smoothens the initial oscillations and then predicts the exponentially-decaying behavior of the resulting functions. The current computed by the proposed approach is found to be in excellent agreement with that computed from a full-wave numerical simulation of the infinite periodic structure.

II. ANALYTICAL CONSIDERATIONS

Figure 1 depicts the scattering geometry comprising a grating with period D composed of perfect electric conducting (PEC) strips of width w and illuminated by a normally incident plane wave with electric field given by (under the assumption of $\exp(+j\omega t)$ time dependence):

$$\mathbf{E}^{inc}(z)=E^{inc}(z)\hat{\mathbf{y}}=-\exp(jk_0 z)\hat{\mathbf{y}}\,, \tag{1}$$

where k_0 is the free-space wavenumber. The developed approach can be generalized to the oblique incidence case with only minor modifications.

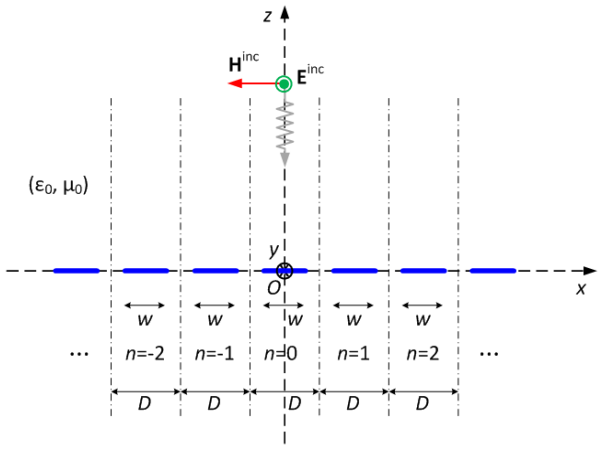

Fig. 1. Geometry of the periodic strip-grating scattering configuration.

First, we consider the *truncated finite* grating comprising of a *moderate* number of cells and solve the problem for the current distribution $\tilde{\mathbf{J}}_0(x)=\tilde{J}_0(x)\hat{\mathbf{y}}$, induced in the center region (*i.e.*, on the unit cell which is indexed as n=0). This distribution is expanded in a Fourier series:

$$\tilde{J}_0(x)=\frac{1}{Z_0 k_0 \frac{w}{2}\sqrt{1-\left(\frac{x}{\frac{w}{2}}\right)^2}}\sum_{\nu=0}^{\infty}(-j)^{\nu}A_{\nu}\cos\left(\tfrac{\nu\pi}{w}\left(x+\tfrac{w}{2}\right)\right), \tag{2}$$

where Z_0 denotes the free-space impedance. The Fourier coefficients A_ν are calculated in the standard way and found to be:

$$A_0=\frac{Z_0 k_0}{2}\int_{-\frac{w}{2}}^{\frac{w}{2}}\sqrt{1-\left(\frac{x}{\frac{w}{2}}\right)^2}\,\tilde{J}_0(x)\,\mathrm{d}x$$

.

$$A_{\nu}=j^{\nu}Z_0 k_0\int_{-\frac{w}{2}}^{\frac{w}{2}}\sqrt{1-\left(\frac{x}{\frac{w}{2}}\right)^2}\,\tilde{J}_0(x)\cos\left(\tfrac{\nu\pi}{w}\left(x+\tfrac{w}{2}\right)\right)\mathrm{d}x,\ \nu=1,2,... \tag{3}$$

In case that $\tilde{J}_0$ is a constant, then the latter expressions are simplified to:

$$A_0 = \frac{Z_0\pi}{8} k_0 w \tilde{J}_0$$
$$A_{2\nu-1} = 0, \quad A_{2\nu} = Z_0 k_0 w \tilde{J}_0 \frac{J_1(\nu\pi)}{2\nu}, \ \nu = 1,2,... \qquad (4)$$

where J_1 denotes the first-order cylindrical Bessel function.

On the basis of past experience with similar grating problems (see, *e.g.*, [19-20]), we postulate that the true current induced on the unit cell of the *infinite* grating structure would simply be $c\tilde{J}_0(x)$, *i.e.*, proportional to the current in the center cell of the finite grating, where c is a complex constant, as yet undetermined. The physical justification of the latter postulate is as follows. In a truncated periodic structure there are reflections from the edges, which decline gradually as we move inwards from the edges. As the size of the grating becomes sufficiently large, the edge effect is substantially reduced in the center region, where only the dominant mode survives. This, in turn, just changes the scale of the field distribution on the unit cell but not its shape, which has presumably stabilized. The scale factor is calculated next, by applying the boundary condition on the unit cell, to eliminate the contributions from the edge reflections.

Next, we show how to determine the scale factor c in a systematic way. The current $c\tilde{J}_0(x)$ is induced on every grating's cell indexed by n (under a shift of the spatial variable x so that it is centered at the center on the n-th cell). Hence, we begin by computing the contributions of the currents:

$$J_n(x) = c\tilde{J}_0(x-nD), \quad nD-\tfrac{w}{2} < x < nD+\tfrac{w}{2}, \qquad (5)$$

induced on the cells $n\neq 0$ to the unit cell $n=0$. The electric fields generated by these currents are given by:

$$E_n(x,z) = (-j\omega\mu_0) \int_{nD-\frac{w}{2}}^{nD+\frac{w}{2}} J_n(x') G(x,z;x',0)\,\mathrm{d}x', \qquad (6)$$

where G is the free-space Green's function,

$$G(x,z;x',z') = -\frac{j}{4} H_0^{(2)}\left(k_0\sqrt{(x-x')^2+(z-z')^2}\right), \qquad (7)$$

with $H_0^{(2)}$ denoting the zero-order cylindrical Hankel function of the second kind.

By combining (2)-(7), we get:

$$E_n(x,0) = -\frac{c}{2w}\sum_{\nu=0}^{\infty}(-j)^\nu A_\nu \times$$
$$\int_{nD-\frac{w}{2}}^{nD+\frac{w}{2}} \frac{\cos\left(\frac{\nu\pi}{w}(x'-nD+\frac{w}{2})\right)}{\sqrt{1-\left(\frac{x'-nD}{\frac{w}{2}}\right)^2}} H_0^{(2)}\left(k_0 \mid x-x' \mid\right)\mathrm{d}x' \qquad (8)$$

Then, by performing the change of variables $x' = nD+\xi$ and summing up all the infinite contributions, we can write the *total* electric field induced on the unit cell as:

$$E(x,0) = \sum_{n=-\infty}^{+\infty} E_n(x,0) = -\frac{c}{2w}\sum_{n=-\infty}^{+\infty}\sum_{\nu=0}^{\infty}(-j)^\nu A_\nu \times$$
$$\int_{-\frac{w}{2}}^{+\frac{w}{2}} \frac{\cos\left(\frac{\nu\pi}{w}(\xi+\frac{w}{2})\right)}{\sqrt{1-\left(\frac{\xi}{\frac{w}{2}}\right)^2}} H_0^{(2)}\left(k_0 \mid x-nD-\xi \mid\right)\mathrm{d}\xi \qquad (9)$$

The involved series and integrals in (9) can be handled analytically as follows. First, we recall the well-known Fourier integral expression of the Hankel function:

$$H_0^{(2)}\left(k_0 \mid x-x' \mid\right) = \tfrac{1}{\pi}\int_{-\infty}^{+\infty} \frac{e^{-jk_x(x-x')}}{\sqrt{k_0^2-k_x^2}}\mathrm{d}k_x \ . \qquad (10)$$

Now, by substituting (10) in (9), changing the orders of integration and taking into account that (see, *e.g.*, [14]):

$$\int_{-\frac{w}{2}}^{+\frac{w}{2}} \frac{\cos\left(\frac{\nu\pi}{w}(\xi+\frac{w}{2})\right)}{\sqrt{1-\left(\frac{\xi}{\frac{w}{2}}\right)^2}} e^{jk_x\xi}\mathrm{d}\xi =$$
$$\frac{1}{4}(-j)^\nu \pi w\left[J_0(\tfrac{1}{2}(\pi\nu-k_x w)) + (-1)^\nu J_0(\tfrac{1}{2}(\pi\nu+k_x w))\right] \qquad (11)$$

where J_0 denotes the zero-order cylindrical Bessel function, we get that,

$$E(x,0) = -\frac{c}{8}\sum_{n=-\infty}^{+\infty}\sum_{\nu=0}^{\infty} A_\nu \int_{-\infty}^{+\infty} \frac{e^{-jk_x(x-nD)}}{\sqrt{k_0^2-k_x^2}}\left[J_0(\tfrac{1}{2}(\pi\nu+k_x w))\right.$$
$$\left. +(-1)^\nu J_0(\tfrac{1}{2}(\pi\nu-k_x w))\right]\mathrm{d}k_x \qquad (12)$$

Moreover, we use the following relation (resulting by the Fourier series expression of the Dirac comb):

$$\sum_{n=-\infty}^{+\infty} e^{jk_x nD} = \frac{2\pi}{D}\sum_{n=-\infty}^{+\infty}\delta\left(k_x - n\tfrac{2\pi}{D}\right), \qquad \textbf{(13)}$$

to obtain that the total electric field induced on the unit cell takes the form,

$$E(x,0) = -\frac{c}{4}\frac{\pi}{D}\sum_{n=-\infty}^{+\infty}\sum_{\nu=0}^{\infty} A_\nu \frac{e^{-jn\frac{2\pi}{D}x}}{\sqrt{k_0^2-(n\frac{2\pi}{D})^2}} \times$$
$$\left[J_0(\tfrac{1}{2}(\pi\nu+\tfrac{2\pi w}{D}n)) + (-1)^\nu J_0(\tfrac{1}{2}(\pi\nu-\tfrac{2\pi w}{D}n))\right] \qquad (14)$$

Finally, we impose the boundary condition on the PEC strip of the unit cell as follows:

$$E(x,0) = \sum_{n=-\infty}^{+\infty} E_n(x,0) = -E^{inc}(0)=1, \qquad (15)$$

to determine the unknown constant c as,

$$c = -\frac{4D}{\pi}\left\{\sum_{n=-\infty}^{+\infty}\sum_{\nu=0}^{\infty} A_\nu \frac{e^{-jn\frac{2\pi}{D}x}}{\sqrt{k_0^2-(n\frac{2\pi}{D})^2}} \times\right.$$
$$\left.\left[J_0(\tfrac{1}{2}(\pi\nu+\tfrac{2\pi w}{D}n)) + (-1)^\nu J_0(\tfrac{1}{2}(\pi\nu-\tfrac{2\pi w}{D}n))\right]\right\}^{-1} \qquad (16)$$

The current distribution on the strip in the unit cell of the

infinite grating can now be obtained, once c has been computed and all the subsequent field quantities of interest can be readily determined.

III. LIMITING CASES

The developed approach is validated by examining two limiting cases. The first is a "test" case and corresponds to normal incidence plane wave scattering by an *infinite* PEC plane, which is decomposed into periodic cells as shown in Fig. 2.

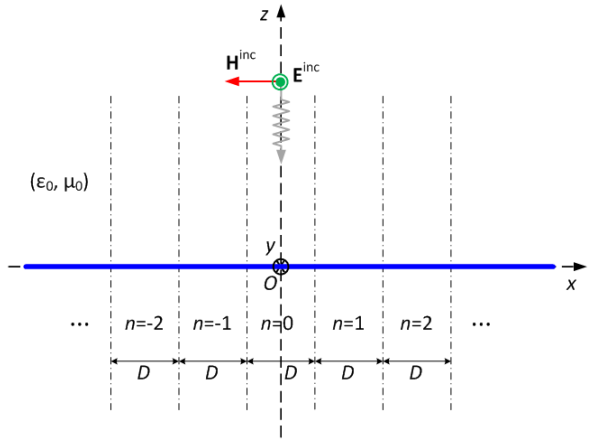

Fig. 2. Geometry of the "test" case corresponding to normal incidence plane wave scattering by an infinite PEC plane.

The *approximate* initial electric current distribution induced on the unit cell n=0 is assumed to be:

$$\tilde{\mathbf{J}}_0 = 2\hat{\mathbf{z}}\times\mathbf{H}^{inc}(0)=2H_x^{inc}(0)\hat{\mathbf{y}}=-2\tfrac{1}{Z_0}\hat{\mathbf{y}}, \qquad (17)$$

where

$$\mathbf{H}^{inc}(z)=H_x^{inc}(z)\hat{\mathbf{x}}=-\tfrac{1}{Z_0}\exp(jk_0 z)\hat{\mathbf{x}},$$

is the magnetic field of the incident plane wave (see (1)). Equation (17) is actually the correct "physical optics" current induced on the infinite PEC plane.

Now, we follow the methodology described in Section II above. The current induced on the unit cell of the infinite structure is taken to be $c\tilde{J}_0 = -2c/Z_0$, with c is yet to be determined. The currents induced on the cells $n\neq 0$ are given by:

$$J_n(x)=c\tilde{J}_0(x-nD)=-2c/Z_0,\ (2n-1)\tfrac{D}{2}<x<(2n+1)\tfrac{D}{2},$$

while the total electric field induced on the unit cell is calculated by (6), (7), and (17) as:

$$E(x,0)=\sum_{n=-\infty}^{+\infty}E_n(x,0)=\frac{k_0 c}{2}\sum_{n=-\infty}^{+\infty}\int_{-\frac{D}{2}}^{\frac{D}{2}}H_0^{(2)}\left(k_0\,|\,x-nD-\xi\,|\right)\mathrm{d}\xi\,. \qquad (18)$$

By combining (10) and (18), we find:

$$E(x,0)=c\,\frac{k_0 D}{2\pi}\sum_{n=-\infty}^{+\infty}\int_{-\infty}^{+\infty}\frac{\mathrm{sinc}(k_x\frac{D}{2})}{\sqrt{k_0^2-k_x^2}}e^{-jk_x(x-nD)}\,\mathrm{d}k_x\,, \qquad (19)$$

where sinc(z)=sin(z)/z. Then, we apply the boundary condition (15) on the unit cell and determine c as:

$$c=\frac{2\pi}{k_0 D\sum_{n=-\infty}^{+\infty}\left(\int_{-\infty}^{+\infty}\frac{\mathrm{sinc}(k_x\frac{D}{2})}{\sqrt{k_0^2-k_x^2}}e^{-jk_x(x-nD)}\,\mathrm{d}k_x\right)}.$$

The latter is written by means of (13) as:

$$c=\frac{1}{k_0\sum_{n=-\infty}^{+\infty}\frac{\mathrm{sinc}(n\pi)}{\sqrt{k_0^2-(n\frac{2\pi}{D})^2}}e^{-jn\frac{2\pi}{D}x}},$$

which by taking into account that sinc($n\pi$)=0, $n\neq 0$, gives the expected result that c=1 (since we have considered in (17) as the initial current on the unit cell the correct current induced on the infinite PEC plane.)

The second limiting case is for $w\to D$, when the infinite periodic grating is reduced to an infinite PEC plane. The approximate initial current distribution induced on the unit cell is taken again to be given by (17). The Fourier coefficients are calculated by (4) as:

$$\begin{aligned}&A_0=-\tfrac{\pi}{4}k_0 w\\ &A_{2\nu-1}=0,\quad A_{2\nu}=-k_0 w J_1(\nu\pi)/\nu,\ \nu=1,2,...\end{aligned}. \qquad (20)$$

By following the methodology of Section II, we find that c is given by (16) where A_ν are given by (20). By letting $w\to D$ in (16), and using (20), we obtain:

$$c=\frac{4}{\pi}\left\{\sum_{n=-\infty}^{+\infty}\frac{e^{-jn\frac{2\pi}{D}x}}{\sqrt{1-(\frac{2\pi}{k_0 D}n)^2}}\times\right.$$

$$\left.\left\{\frac{\pi}{2}J_0(\pi n)+\sum_{\nu=1}^{\infty}\frac{J_1(\nu\pi)}{\nu}\left[J_0(\pi(\nu+n))+J_0(\pi(\nu-n))\right]\right\}\right\}^{-1} \qquad (21)$$

The series appearing in (21) are computed numerically. Figures 3 and 4 depict the real and imaginary parts of c as computed by (21) vs N_2 for constant N_1=10 and vs N_1 for constant N_2=30, where N_1 and N_2 denote the truncation orders of the series in (21) with respect to the variables n and ν, respectively. In the numerical computations, we take x=0 and tested that other values of x give similar results. It is evident that c converges to 1 as expected because as $w\to D$ the problem is reduced to scattering by an infinite PEC plane for which it is known that (17) gives the correct "physical optics" current induced on the plane. A technique for the fast extrapolation of oscillatory curves, such as the one in Fig. 4 (b), is analyzed in the next section by retaining a smaller number of terms in the series.

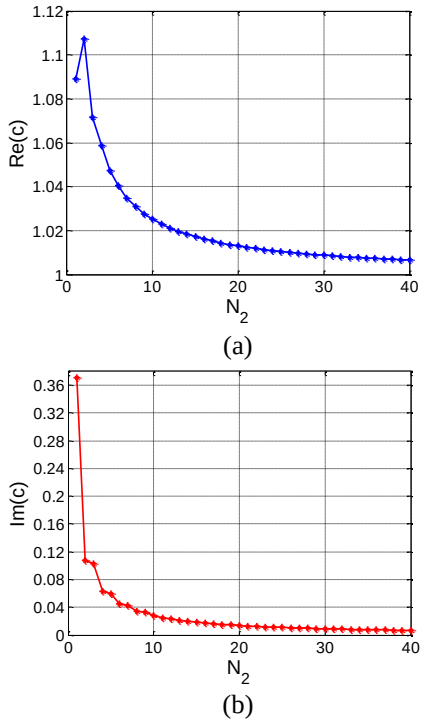

Fig. 3. Real and imaginary parts of c as computed by (21) vs the truncation order N_2 of the series with respect to v for N_1=10 retained terms of the series with respect to n.

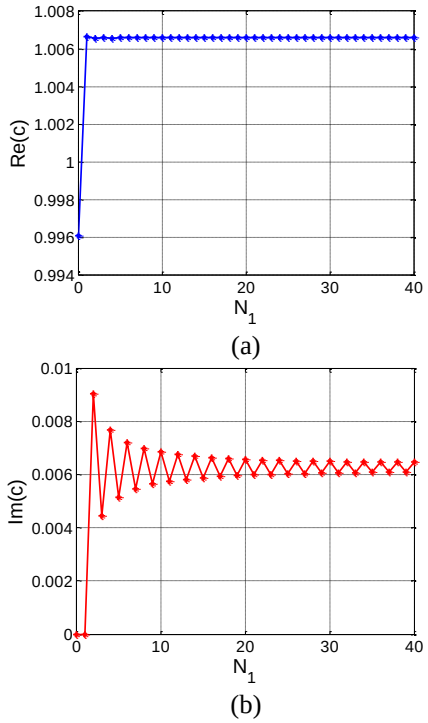

Fig. 4. Real and imaginary parts of c as computed by (21) vs the truncation order N_1 of the series with respect to n for N_2=30 retained terms of the series with respect to v.

IV. NUMERICAL RESULTS AND DISCUSSION

First, we consider a periodic grating with parameters D=λ/2 and w=D/3 and frequency of the incident field at f=1 GHz. Figure 5 depicts the real and imaginary parts of the current induced on the unit cells, as computed by the commercial code Ansoft HFSS [27], for a finite grating with 5, 7, and 21 strips. Magnifications in the region of the center of the unit cells are depicted in Fig. 6. In addition to these results, we have carried out extensive numerical experiments by increasing the number of strips from 5 to 21 in steps of 2. We have concluded that convergence in the second decimal digit of the induced current is attained for 7 to 9 strips, while we can realize convergence in the third decimal place by using 15 strips. The current induced on the center strip of a truncated grating with 7 strips, shown in Fig. 5, will be considered as the initial approximate current $\tilde{J}_0(x)$ in the numerical algorithm implementing the developed methodology. Figure 7 depicts the real and imaginary parts of c, as computed by means of (16), versus the number N_1 of retained terms in the series of (16) with respect to n for constant number N_2=10 of terms in the series with respect to v.

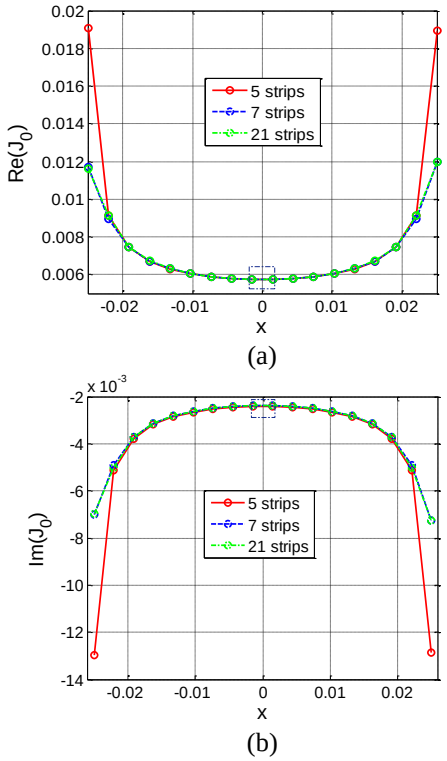

Fig. 5. Real and imaginary parts of the considered approximate initial current $\tilde{J}_0(x)$ induced on the unit cell of a finite grating with 5, 7, and 21 strips, as computed by the HFSS.

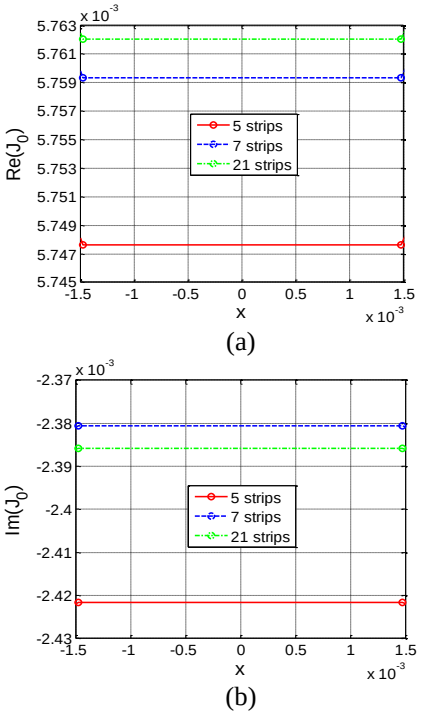

Fig. 6. Magnifications of Fig. 5 in the region of the center of the unit cell.

The limiting values of the oscillatory curves of Fig. 7 can be extrapolated by following the numerical procedure described below. The first two periods of the oscillations are excluded from the extrapolation procedure we follow. Then, from the third period on, we take the averages between successive maximum and minimum values. In this way, we obtain a new set of curves where the initial oscillations are smoothened. The outcomes of this procedure on the oscillating curves of Figs. 7 (a) and 7 (b) are shown in Figs. 8 (a) and (b). By repeating the procedure a second time on the curves of Figs. 8 (a) and 8 (b), we finally obtain the curves of Figs. 8 (c) and 8 (d), where the oscillations are significantly suppressed.

Now, the monotonic behavior of the curves of Re(c) and Im(c) of Figs. 8 (c) and 8 (d) can be predicted in the following way. A two-term exponential model of the form:

$$y(x) = a^* \exp(b^* x) + c^* \exp(d^* x), \qquad (22)$$

is fitted to the data yielding the results of Fig. 9, where it is observed that the fitted curves provide very good approximations of the initial data. The obtained limiting value of the complex constant c is very close to the value c=1.007–0.004j, which is obtained by dividing the current induced on the unit cell of the infinite grating over the corresponding current on the truncated grating with 7 strips (the latter quantities were both computed by using HFSS simulations). As shown in Fig. 10, the current computed by the proposed approach is in excellent agreement with that computed from the HFSS simulation of the infinite periodic grating.

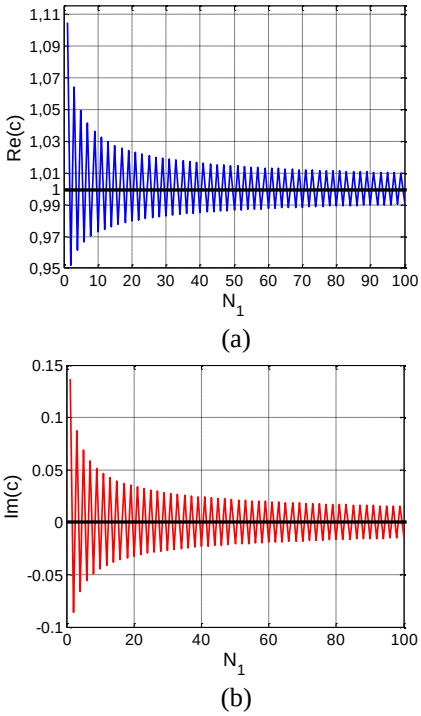

Fig. 7. Real and imaginary parts of c vs the truncation order N_1 for N_2=10, D=λ/2, w=D/3, and f=1 GHz. The black lines show the mean values of the oscillatory curves.

Furthermore, we are interested in predicting/ extrapolating the behaviors of Re(c) and Im(c) by reducing the total number of terms considered (that is without retaining up to N_1=100, for instance, as in Fig. 9). The variations of Re(c) and Im(c) when only N_1=20 and 30 terms are retained in the series (16) are depicted in Figs. 11 (a), (b) and (c), (d), respectively. The respective fitted curves by means of the two-term exponential model (22) are also depicted. We observe that truncating these exponentially-decaying curves at N_1=20 or 30 and applying the above described extrapolation algorithm can provide quite accurate results for the limiting value of c.

Finally, we consider as a second example, an infinite periodic grating with parameters D=λ and w=D/2 at the same frequency of f=1 GHz. Figure 12 depicts the real and imaginary parts of c, as computed by means of (16), versus N_1 for N_2=10. Also in this case, the obtained result converges to the expected one for the current induced on the unit cell of the infinite grating structure. As in the previously examined example, the obtained curves can be extrapolated by using the algorithm described above to predict their monotonic behavior by considering a relatively small number of N_1 terms.

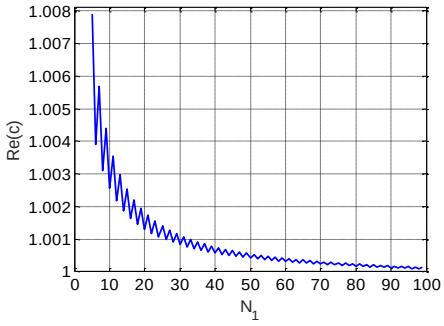

(a)

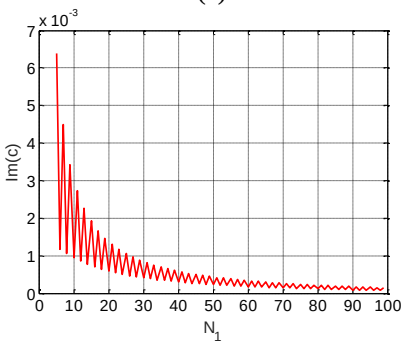

(b)

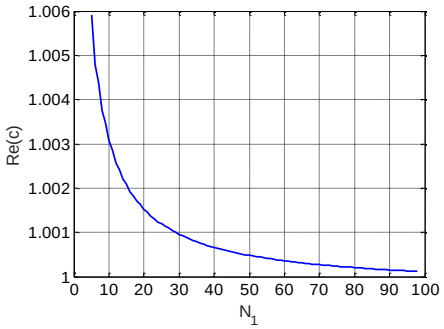

(c)

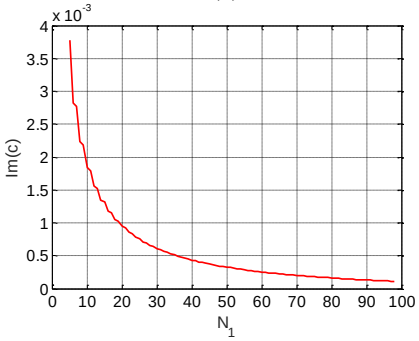

(d)

Fig. 8. (a) and (b) Real and imaginary parts of c vs N_1 after implementing the numerical algorithm of smoothening the oscillations on the curves of Figs. 7 (a) and 7 (b). (c) and (d) Corresponding results after implementing a second time the oscillations smoothening algorithm on the previously derived curves of Figs. 8 (a) and 8 (b).

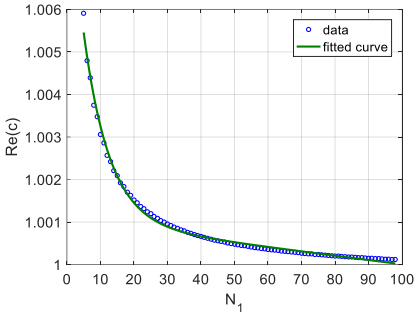

(a)

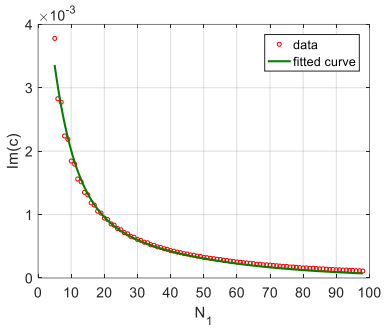

(b)

Fig. 9. Real and imaginary parts of c (bullets denoted as "data") for the parameters values of Figs. 8 (c) and 8 (d) together with the respective fitted curves by means of the model (22).

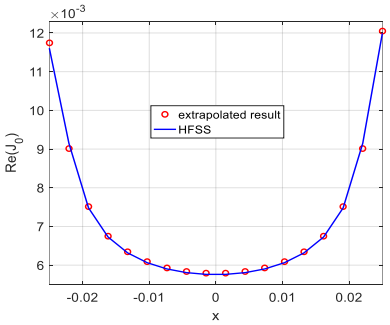

(a)

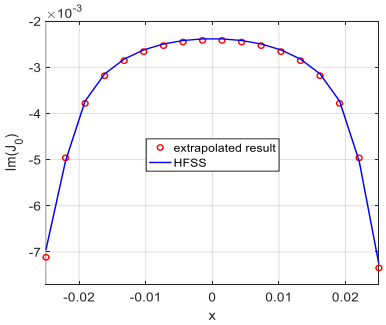

(b)

Fig. 10. Current induced on the unit cell of the infinite grating for the parameters of Fig. 5, as computed by the proposed method [*c.f.* model (22)] and by the HFSS.

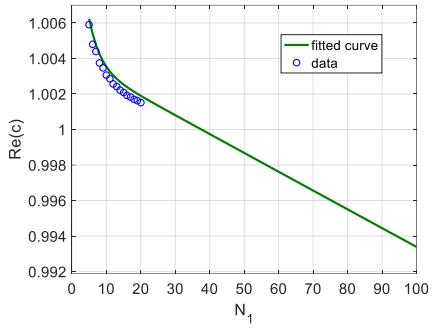

(a)

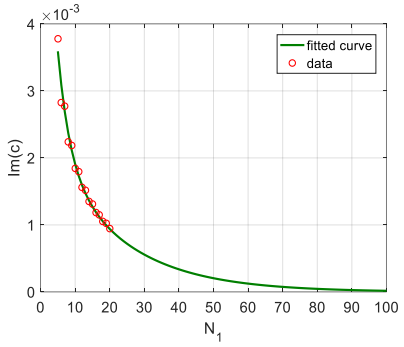

(b)

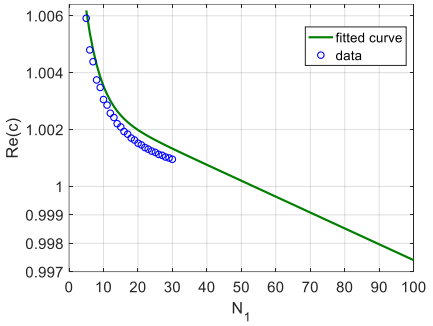

(c)

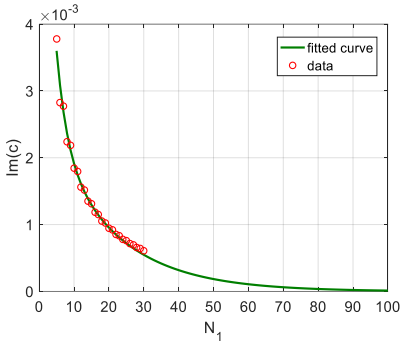

(d)

Fig. 11. Real and imaginary parts of *c* (bullets denoted as "data") for the parameters values of Figs. 8 (c) and 8(d) when only N_1=20 in (a) and (b) and N_1=30 in (c) and (d) terms are retained in the series (16). In every figure, the respective fitted curves by means of the two-term exponential model (22) are also depicted.

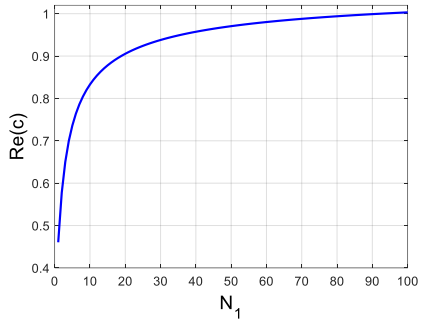

(a)

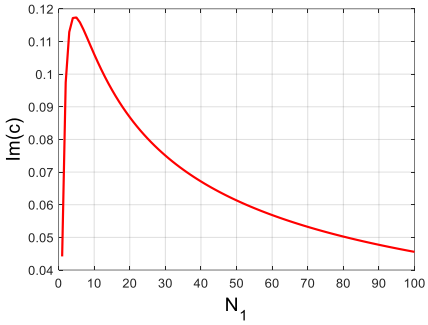

(b)

Fig. 12. Real and imaginary parts of *c* vs the truncation order N_1 for N_2=10, D=λ, w=D/2, and f=1 GHz.

V. CONCLUSIONS

The problem of electromagnetic scattering by a periodic perfectly conducting strip grating was considered. An analytical methodology was developed for extracting the solution for the current induced on the infinite grating from that induced on the respective finite grating with a moderate number of cells. The validity was tested by examining two limiting cases for which the current is known *a priori*. Numerical results were presented for the proportionality constant relating the current on the unit cell of the infinite grating to that of the distribution in the inner region of the corresponding truncated grating. The convergence of this constant with respect to the number of retained terms in the involved series representation was investigated. It was shown that the limiting value of the constant can be quickly and accurately obtained by using a numerical extrapolation algorithm which first smoothens the initial oscillations and then predicts the monotonic behavior of the resulting functions.

The procedure presented in the paper is general. It was applied here to one-dimensional (1-D) gratings with infinite perfectly conducting strips of arbitrary width and can be easily generalized to the oblique incidence case as well as to other similar grating structures, including gratings lying on dielectric substrates (infinite gratings of the latter type have been analyzed by different methodologies; see *e.g.* [28]). The suitable initial number

of cells of the truncated finite grating is chosen by examining the field's distribution in the region of the center cell. When this distribution is stabilized, then the current on the center strip of the infinite grating will be the current on the center strip of the corresponding finite grating times a scale factor which has to be determined. By following this approach, we also gain an understanding of the convergence behavior of the current distribution of the finite grating, and how it relates to that of the infinite grating, to determine when the scattering characteristics of the truncated grating are close to those of the infinite one. Additionally, by implementing the proposed approach and examining the aforementioned convergence, we do not need to rely upon commercial codes to validate the results for the current on an infinite grating.

The basic principles of the developed methodology were demonstrated for 1-D FSSs. The methodology can be generalized to two-dimensional (2-D) FSSs, for example phased antenna arrays. The field in the center region of a truncated 2-D antenna array stabilizes to a shape distribution, as one increases the dimensions of the array along the *x*- and *y*-axis, which is the same as the corresponding distribution in the center cell of the infinite 2-D antenna array. This fundamental property was shown in [29]. In this way, we can extend the numerical procedure presented in the paper and compute the scale factor of the current on the center cell of the infinite 2-D antenna array over the respective current of the corresponding truncated 2-D array (composed of that number of elements for which the field's distribution was already found to have stabilized).

REFERENCES

[1] B. Munk, *Frequency Selective Surfaces: Theory and Design*. John Wiley, 2000.

[2] Y. Rahmat-Samii, "The marvels of electromagnetic band gap (EBG) structures," *ACES Journal*, vol. 18, pp. 1-10, 2003.

[3] A. Mackay, B. Sanz-Izquierdo, and E. A. Parker, "Evolution of frequency selective surfaces," *Forum for Electromagnetic Research Methods and Application Technologies (FERMAT)*, vol. 2, 2014.

[4] R. Mittra, C. H. Chan, and T. Cwik, "Techniques for analyzing frequency selective surfaces-A review," *Proceedings of the IEEE*, vol. 76, pp. 1593-1615, 1988.

[5] C. H. Chan and R. Mittra, "On the analysis of frequency-selective surfaces using subdomain basis functions," *IEEE Transactions on Antennas and Propagation*, vol. 38, pp. 40-50, 1990.

[6] Y. Hao and R. Mittra, *FDTD Modeling of Metamaterials: Theory and Applications*. Artech House, 2009.

[7] I. Bardi, R. Remski, D. Perry, and Z. Cendes, "Plane wave scattering from frequency-selective surfaces by the finite-element method," *IEEE Transactions on Magnetics*, vol. 38, pp. 641-644, 2002.

[8] F. Costa, A. Monorchio, and G. Manara, "An overview of equivalent circuit modeling techniques of frequency selective surfaces and metasurfaces," *ACES Journal*, vol. 29, pp. 960-976, 2014.

[9] J. Blackburn and L. R. Arnaut, "Numerical convergence in periodic method of moments analysis of frequency-selective surfaces based on wire elements," *IEEE Transactions on Antennas and Propagation*, vol. 53, pp. 3308-3315, 2005.

[10] G. L. Baldwin and A. E. Heins, "On the diffraction of a plane wave by an infinite plane grating," *Mathematica Scandinavica*, vol. 2, pp. 103-118, 1954.

[11] E. Luneburg and K. Westpfahl, "Diffraction of plane waves by an infinite strip grating," *Annalen der Physik*, vol. 7, pp. 257-288, 1971.

[12] J. H. Richmond, "On the edge mode in the theory of TM scattering by a strip or strip grating," *IEEE Transactions on Antennas and Propagation*, vol. AP-28, pp. 883-887, 1980.

[13] W. A. Walker and C. M. Butler, "A method for computing scattering by large arrays of narrow strips," *IEEE Transactions on Antennas and Propagation*, vol. AP-32, pp. 1327-1334, 1984.

[14] K. Uchida, T. Noda, and T. Matsunaga, "Spectral domain analysis of electromagnetic wave scattering by an infinite plane metallic grating," *IEEE Transactions on Antennas and Propagation*, vol. AP-35, pp. 46-52, 1987.

[15] M. Ando and K. Takei, "Reflection and transmission coefficients of a thin strip grating for antenna application," *IEEE Transactions on Antennas and Propagation*, vol. AP-35, pp. 367-371, 1987.

[16] A. Matsushima and T. Itakura, "Singular integral equation approach to plane wave diffraction by an infinite strip grating at oblique incidence," *Journal of Electromagnetic Waves and Applications*, vol. 4, pp. 505-519, 1990.

[17] F. B. Gross and W. J. Brown, "New frequency-dependent edge mode current density approx.-imations for TM scattering from a conducting strip grating," *IEEE Transactions on Antennas and Propagation*, vol. 41, pp. 1302-1307, 1993.

[18] E. Danicki, B. Langli, and K. Blotekjaer, "Spectral theory of EM wave scattering by periodic strips," *IEEE Transactions on Antennas and Propagation*, vol. 43, pp. 97-104, 1995.

[19] R. Mittra, C. Pelletti, N. L. Tsitsas, and G. Bianconi, "A new technique for efficient and accurate analysis of FSSs, EBGs and meta-materials," *Microwave and Optical Technology Letters*, vol. 54, pp. 1108-1116, 2012.

[20] C. Pelletti, R. K. Arya, A. Rashidi, H. Mosallaei, and R. Mittra, "Numerical techniques for efficient analysis of FSSs, EBGs and metamaterials," Chapter 11, *Computational Electromagnetics: Recent Advances and Engineering Applications*, R. Mittra (Ed.), Springer, 2014.

[21] N. L. Tsitsas, C. Pelletti, and R. Mittra, "Efficient analysis of scattering by strip gratings," *Proceedings of the 2016 USNC-URSI Radio Science Meeting*, pp. 61-62, 2016.

[22] T. Cwik and R. Mittra, "The effects of the truncation and curvature of periodic surfaces: A strip grating," *IEEE Transactions on Antennas and Propagation*, vol. 36, pp. 612-622, 1988.

[23] L. Gurel and W. Chew, "Recursive algorithms for calculating the scattering from *N* strips or patches," *IEEE Transactions on Antennas and Propagation*, vol. 38, pp. 507-515, 1990.

[24] E. G. Johnson and C. G. Christodoulou, "Electromagnetic scattering from aperiodic strip gratings," *Journal of Electromagnetic Waves and Applications*, vol. 6, pp. 219-234, 1992.

[25] H. Shigesawa and M. Tsuji, "A new equivalent network approach to electromagnetic wave problems," *Progress in Electromagnetics Research*, vol. PIER 13, pp. 243-291, 1996.

[26] Y. Shifman, Z. Baharav, and Y. Leviatan, "Analysis of truncated periodic array using two-stage wavelet-packet transformations for impedance matrix compression," *IEEE Transactions on Antennas and Propagation*, vol. 47, pp. 630-636, 1999.

[27] HFSS, ANSYS: www.ansys.com/Products/Electronics/ANSYS-HFSS

[28] K. Chen, J. Song, and T. Kamgaing, "Metal strip grating on grounded dielectric slab and PEC/PMC shielded interconnect: Modal relationships," *ACES Journal*, vol. 29, pp. 828-836, 2014.

[29] N. Farahat, R. Mittra, and N.-T. Huang, "Modeling large phased array antennas using the finite difference time domain method and the characteristic basis function approach," *ACES Journal*, vol. 21, pp. 218-225, 2006.

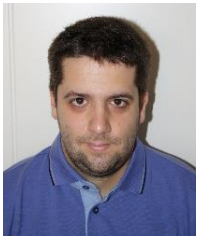

Nikolaos L. Tsitsas was born in Athens, Greece, in 1979. He received the Diploma and Ph.D. degree in Electrical Engineering from the National Technical University of Athens (NTUA) in 2002 and 2006 respectively, and the M.Sc. degree in Applied Mathematics from the National and Kapodistrian University of Athens in 2005.

From 2008 to 2011, he was an Adjunct Lecturer at the School of Applied Mathematical and Physical Sciences of the NTUA. From 2009 to 2011, he was an Adjunct Lecturer at the Hellenic Army Academy. Since 2012, he has been an Assistant Professor at the Department of Informatics of the Aristotle University of Thessaloniki. He is the author or co-author of 47 papers in scientific journals and over 50 papers in conference proceedings. His research interests include analytical and numerical methods in wave scattering and propagation theory and applied mathematics. He is a Senior Member of the Optical Society of America, and a Member of the IEEE, the American Mathematical Society, and the Technical Chamber of Greece.

Raj Mittra is a Professor in the Department of Electrical Engineering & Computer Science of the University of Central Florida in Orlando, FL., where he is the Director of the Electromagnetic Communication Laboratory. Prior to joining the University of Central Florida, he worked at Penn State as a Professor in the Electrical and Computer Engineering from 1996 through June, 2015. He was a Professor in the Electrical and Computer Engineering at the University of Illinois in Urbana Champaign from 1957 through 1996, when he moved to the Penn State University. Currently, he also holds the position of Hi-Ci Professor at King Abdulaziz University in Saudi Arabia.

He is a Life Fellow of the IEEE, a Past-President of AP-S, and he has served as the Editor of the Transactions of the Antennas and Propagation Society. He won the Guggenheim Fellowship Award in 1965, the IEEE Centennial Medal in 1984, and the IEEE Millennium Medal in 2000. Other honors include the IEEE/AP-S Distinguished Achievement Award in 2002, the Chen-To Tai Education Award in 2004, the IEEE Electromagnetics Award in 2006, and the IEEE James H. Mulligan Award in 2011.

Recently he founded the e-Journal FERMAT (www.e-fermat.org) and is serving as the Co-Editor-in-Chief of the same. Mittra is a Principal Scientist and President of RM Associates, a consulting company founded in 1980, providing services to industrial and governmental organizations in the U.S. and abroad.

Comparisons Among EIT Data Collection Techniques and Reconstruction Algorithms

Stefano Pisa, Erika Pittella, and Emanuele Piuzzi

Dept. of Information Engineering, Electronics and Telecommunications (DIET)
Sapienza University of Rome, via Eudossiana, 18, 00184, Rome, Italy
stefano.pisa@uniroma1.it, erika.pittella@uniroma1.it, emanuele.piuzzi@uniroma1.it

Abstract ─ Electrical Impedance Tomography (EIT) is an imaging technique that aims to reconstruct the spatial electrical conductivity distribution in sections of the human body. In this paper, in order to solve the EIT forward and inverse problems, a finite difference approach to the solution of Maxwell's equations and the Newton-Raphson algorithm have been employed, respectively. In particular, the inverse problem has been solved using the Tikhonov regularization with various choices of the regularization matrix. Moreover, different data collection methods have been tested on simulated measurements. The obtained results have been compared based on the average deviation of the estimated conductivity distribution with respect to the reference one. The reconstruction procedure has been validated through a comparison with the EIDORS open source software. The best image reconstruction has been obtained by using the neighboring data collection method with null regularization matrix, and using the truncated singular value decomposition to perform the matrix inversion. Moreover, the cross and opposite data collection methods showed better performance than the neighboring one in the presence of a random noise added to the measured signal, while the opposite method evidenced the best results with respect to electrode positioning uncertainties.

Index Terms ─ Electrical impedance tomography, finite difference method, Newton-Raphson algorithm.

I. INTRODUCTION

Electrical impedance tomography (EIT) is an imaging technique, which leads to an estimation of the spatial electrical conductivity distribution in a section of the human body, by injecting currents and measuring voltages between pairs of electrodes distributed upon the body surface [1-3]. Compared with standard biomedical imaging techniques (e.g., Magnetic Resonance Imaging or Computed Tomography), the EIT has lower spatial resolution [4] but many advantages, mainly a simpler and cheaper experimental set-up, and the total absence of health risks for the patient. In particular, the typical frequencies and amplitudes of the driving currents, from 10 kHz to 100 kHz, and lower than 10 mA, respectively, cannot interfere with the normal electrophysiological activities of excitable biological tissues. Typical EIT applications are the dynamic monitoring of respiratory and cardiac activities, the study of cerebral hemodynamics, stomach emptying, and fracture healing [1-3].

To reconstruct the spatial electrical conductivity distribution in the investigated section, EIT uses reconstruction algorithms requiring two data sets. One data set is represented by the measured voltages collected on the surface of the real body, and the other is constituted by the computed voltages on the surface of a body model with the same boundary of the real one and with an a priori established conductivity distribution.

In order to compute the voltages on the body surface, the forward problem, namely Poisson's equation with known boundary conditions, needs to be solved. For the solution of the EIT forward problem, various numerical techniques have been proposed. The finite element method (FEM) is the mostly used technique [1, 5], but finite difference (FD) methods have been also suggested [6-8].

With reference to reconstruction algorithms, the first to be developed were the back projection and the sensitivity methods [9-11], but today the most used is the modified Newton-Raphson method [12]. This method follows the nonlinear least square approach applied to the minimization of an error function. The minimization process leads to an updating equation, for the discrete conductivity distribution, involving the computation of the Jacobian matrix of the forward operator. Moreover, the solution of the conductivity updating linear system needs the inversion of a quadratic form of the Jacobian, which is an ill-conditioned matrix. In order to improve the conditioning of this matrix, Tikhonov regularization method [13] can be applied with different choices of the regularization matrix [8, 13-17].

For the measurement collection, a given number (E) of equally spaced electrodes are placed upon the surface of the object under investigation. In some techniques, like the neighboring [1], the opposite (polar) [2], or the cross [2], a current is injected through a pair of electrodes

Submitted On: June 20, 2016
Accepted On: April 8, 2017

and voltages are measured between the remaining pairs. Other techniques apply a current through all the electrodes and measure the resulting voltages at the same electrodes using one of them as reference [1]. In the latter approach, more data are collected with respect to the former methods, with the disadvantage that voltage measurements are dependent on the unknown contact impedance existing between skin and electrode.

Due to the availability of multiple reconstruction algorithms and data collection techniques, the question arises about the best choice for the implementation of an experimental set-up. In [12] many reconstruction algorithms have been compared, evidencing the superior capability of the modified Newton-Raphson method with regularization. Various data collection techniques have been compared with respect to their performance and resolution, by using a modified back projection technique, and the superiority of the neighboring method has been evidenced [18]. However, in [12] and [18] only very simplified models of the investigated region have been considered, not allowing a realistic study of the performance of the various techniques. Moreover, in order to thoroughly test a technique it is also important to check its robustness with respect to sources of error like the random noise affecting the measured data and the misalignment between measurement electrodes on the subject and on the numerical phantom.

For these reasons, in this work an anatomical model will be considered. The neighboring, cross and opposite methods of data collection will be compared by using a regularized version of the Newton-Raphson method with various choices of the regularization matrix. A FD solution of Maxwell's equations in quasi-static conditions, namely the admittance method, will be used for the solution of the direct problem involved in EIT. The effect of noise sources and electrode misalignment on the reconstruction algorithms will be investigated. Preliminarily, the proposed reconstruction procedure will be validated by studying a canonical body model constituted by a square geometry with a square anomaly and comparing the results with those achieved by using the EIDORS open source software [19].

II. METHODS AND MODELS

A. Considered models

Two thorax models have been considered in this study. The first is a simple square geometry with a conductivity of 0.12 S/m filled with a square central anomaly with conductivity equal to 0.24 S/m (see Fig. 1 (a)).These two values roughly correspond to the average conductivity of the thorax and of the deflated lung, respectively.

The second is an anatomical thorax model (45 × 45 pixels, 1 cm side) obtained by under-sampling a section, at the thorax level, of the Visible Human (VH) data set [20], and it comprises skin/fat, muscle, bone, lung, and heart tissues. The conductivity values of the various tissues at the frequency of 50 kHz have been taken from literature data [21]. For skin/fat, heart, muscle, and bone, these values are 0.03, 0.45, 0.35, and 0.02, S/m, respectively. Finally, for the lungs a conductivity value of 0.25 S/m has been assumed corresponding to the deflated lung condition. Figure 1 (b) shows a conductivity map of the considered section.

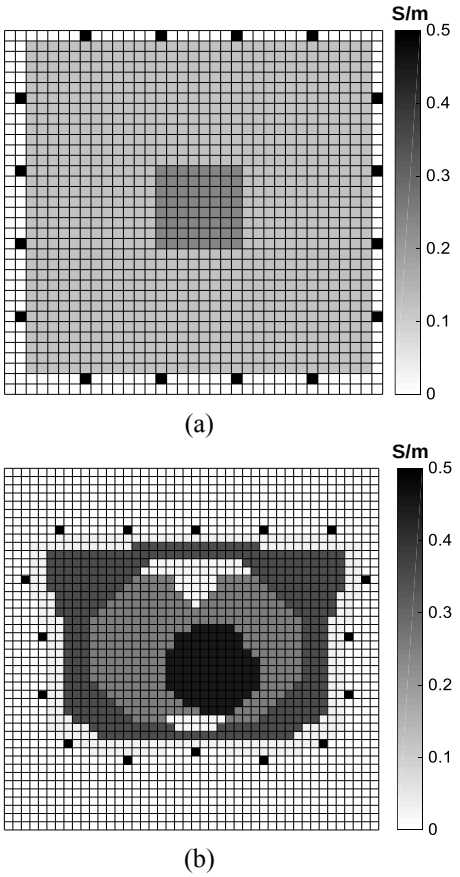

Fig. 1. Conductivity map of the square geometry (a) and of the under-sampled visible human section at thorax level (b). Black squares represent the electrodes.

B. Data collection methods

Three data collection techniques have been considered, namely the neighboring, the cross, and the opposite methods. In all cases, 16 equally-spaced electrodes are placed upon the surface of the body, as shown in Fig. 2. Concerning the neighboring method, the current is injected through a pair of adjacent electrodes (1 and 2 in Fig. 2 (a)) and voltages are measured between the remaining different pairs of adjacent electrodes [1]. Then, the driving pair is changed and the measuring process is repeated, until each pair has been used as driving. In this way, $16 \times 13 = 208$ potential differences are collected, but only 104 of these are linearly independent due to the reciprocity theorem.

In the cross method, the current is injected through a couple of odd electrodes (1 and 3 in Fig. 2 (b)) and voltages are measured between the other electrodes, except the current ones, with electrode 2 chosen as voltage-reference [2]. Then, the current is applied to the remaining odd electrodes (1-5, 1-7 etc.) and voltages are measured using the electrode 2 as voltage reference. In this manner $7 \times 13 = 91$ potential differences are collected. The measurement sequence is then repeated applying currents through even electrodes and measuring with the electrode 1 as voltage reference. A total number of 182 measurements is finally collected, with only 104 independent.

In the opposite method, current is injected through a pair of diametrically opposed electrodes (1-9 in Fig. 2 (c)) and voltages are measured on each electrode, with respect to a reference node adjacent to the current-injecting electrode [2]. Then, the driving pair is switched to the next pair of opposite electrodes in the clockwise direction, changing the voltage reference node accordingly. Here again 208 potential differences are collected, but only 104 of these are linearly independent for reciprocity.

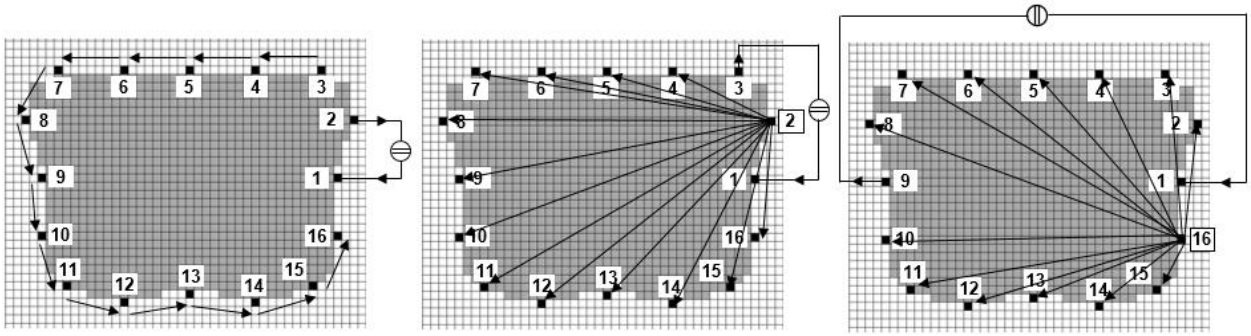

Fig. 2. Data collection techniques: neighboring (a), cross (b), and opposite (c).

C. The admittance method

In the EIT forward problem the section is discretized in a bi-dimensional grid of N square (homogeneous) cells and the continuous conductivity distribution is discretized in a real matrix $\underline{C}$ whose generic element c(x,y) is the discretized conductivity value at the grid nodes (cell center). The admittance method is a finite difference approach to the solution of Maxwell's equations in quasi-static conditions [22]. In this method, the discretized domain is modeled as a network of admittances (see Fig. 3) and the application of Kirchhoff's current law gives rise, for each cell, to the following linear equation:

$$V(x,y) = \frac{1}{Y_{x^+} + Y_{x^-} + Y_{y^+} + Y_{y^-}} \cdot \begin{pmatrix} Y_{x^+} V(x+\Delta x, y) + Y_{x^-} V(x-\Delta x, y) + \\ Y_{y^+} V(x, y+\Delta y) + Y_{y^-} V(x, y-\Delta y) - I_{ie} \end{pmatrix}, \quad (1)$$

where $V(x,y)$ represents the discretized potential at the (x,y) node, I_{ie} is the known forcing term (source) of the equation, and the admittance terms are computed, looking for example, at Y_{x^+}, as follows:

$$Y_{x^+} = c_{x^+} \frac{\Delta y \Delta z}{\Delta x} = \frac{2\, c(x,y) * c(x+\Delta x, y)}{c(x,y) + c(x+\Delta x, y)} \frac{\Delta y \Delta z}{\Delta x}. \quad (2)$$

The resulting linear system of N equations in N unknowns can be solved by using either an iterative or a direct approach.

In the iterative technique, an estimation of the potential $V^{n+1}(x,y)$ of the (x,y) cell at the $(n+1)^{th}$ step can be obtained by adding to the previous estimation, $V^n(x,y)$, a correction term as follows:

$$V^{n+1}(x,y) = V^n(x,y) + \alpha[V(x,y) - V^n(x,y)], \quad (3)$$

where $1 < \alpha < 2$ is called the over-relaxation parameter and $V(x,y)$ is given by (1). The iterative procedure stops when, for every cell, the following condition is met:

$$|V^{n+1}(x,y) - V^n(x,y)| < \varepsilon, \quad (4)$$

with ε an arbitrarily small positive quantity.

In the direct approach, in order to obtain linearly independent equations, the (N×N) system matrix described by (1), which associates a unique integer number to each cell, is reduced to a (N-1×N-1) matrix by choosing a reference cell with respect to which every voltage is computed. This system can be written in a matrix form as:

$$\underline{Y} \cdot \underline{V} = \underline{I}, \quad (5)$$

where $\underline{V}$ is the (N-1×1) vector of the unknown discrete voltage distribution, $\underline{I}$ is the (N-1×1) vector of the known discrete current distribution, and $\underline{Y}$ is the (N-1×N-1) admittance matrix, each row of which has all zero elements, except usually for five of them. By inverting $\underline{Y}$, the solution vector $\underline{V}$ to the linear system (5) can be obtained.

To collect the computed voltages a number P (with P equal to 16 or 14, see Section II.B) of current injection patterns are applied through the electrodes placed upon the body surface. All the implemented reconstruction algorithms need to compute, for each injection pattern, a

number G (typically 13) of voltage differences between well-defined electrode pairs. The computed voltages are stored into an (M×1) vector $\underline{g}^{comp}$ (M = P·G).

In order to collect the measured voltages, the same current injection patterns used in the simulations are applied through electrodes placed upon the surface of the real body whose conductivity has to be estimated. In this work, the measured voltages have been obtained through simulations performed on the considered conductivity distributions (see Fig. 1) by using the admittance method, and stored into the (Mx1) vector $\underline{g}^{meas}$.

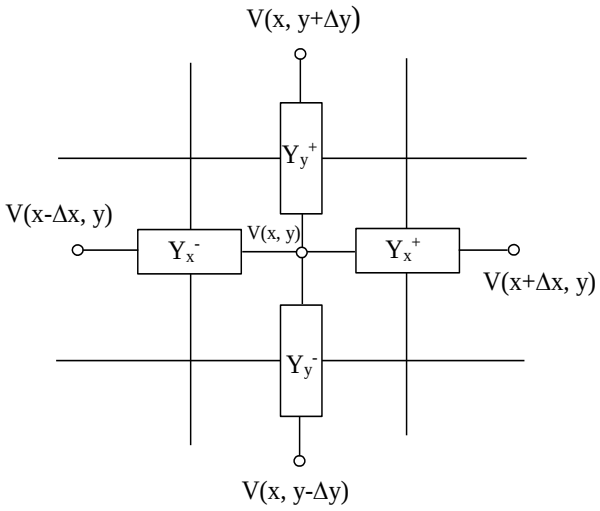

Fig. 3. Network of admittances modeling the discretized domain.

D. The Newton-Raphson reconstruction algorithm

The Newton-Raphson (N&R) method has been specifically developed for problems whose mathematical models are non-linear and it has been extensively described by Yorkey [12]. The aim of this technique is to minimize an error function $\Phi(\underline{e})$, where $\underline{e}$ is the difference vector between the voltages measured on the real conductivity distribution and those calculated on a known, discretized conductivity distribution. $\Phi(\underline{e})$ is defined as:

$$\Phi(\underline{e}) = \frac{1}{2} \left\| \underline{g}^{comp}(\underline{c}) - \underline{g}^{meas} \right\|^2, \quad (6)$$

where $\| \ \|^2$ represents the standard 2-norm of a vector. Starting from (6), it can be shown that the conductivity update distribution at k^{th} step is approximately given by:

$$\underline{\Delta c}^k = -\left[\underline{J}_k^T \underline{J}_k\right]^{-1} \cdot \underline{J}_k^T \cdot \left[\underline{g}^{comp}(\underline{c}^k) - \underline{g}^{meas}\right], \quad (7)$$

where $\underline{J}_k = \underline{J}(\underline{c}^k)$ is the (M×N) Jacobian matrix of the forward transformation $\underline{g}^{comp}(\underline{c}^k)$ defined as [1]:

$$\underline{J}(\underline{c}) = \frac{\partial \underline{g}^{comp}(\underline{c})}{\partial \underline{c}}. \quad (8)$$

Finally, the conductivity at the $(k+1)^{th}$ step is given by:

$$\underline{c}^{k+1} = \underline{c}^k + \underline{\Delta c}^k. \quad (9)$$

This procedure is repeated until $\Phi(\underline{e})$ is less than an a priori chosen value.

The updating Equation (7) of the N&R algorithm needs the inversion of the matrix $\underline{J}_k^T \underline{J}_k$, which is a very ill conditioned matrix. The best way to solve this problem is to use regularization techniques, like the one proposed by Tikhonov [13].

The basic idea is to modify the functional $\Phi(\underline{e})$ in (6) as follows:

$$T(\underline{c}) = \frac{1}{2} \left\| \underline{g}^{comp}(\underline{c}) - \underline{g}^{meas} \right\|^2 + \alpha \left\| \underline{L} \cdot \underline{c} \right\|^2, \quad (10)$$

where α is called the regularization parameter and $\underline{L}$ is a real banded regularization matrix.

For the iterative linearized problem, the conductivity updating term becomes [3]:

$$\underline{\Delta c}^k = -\left[\underline{J}_k^T \underline{J}_k + \alpha \underline{L}^T \underline{L}\right]^{-1} \cdot \underline{J}_k^T \left[\left(\underline{g}^{comp}(\underline{c}^k) - \underline{g}^{meas}\right) - \alpha \underline{L}^T \underline{L}\, \underline{c}^k\right]. \quad (11)$$

In this work, various choices for $\underline{L}$ have been implemented. First of all the $\underline{L} = \underline{0}$ null matrix has been considered (L0 condition). In this case, to perform the matrix inversion, a suitable technique is the singular value decomposition (SVD) [23]. Let $\underline{A}$ be the matrix to be inverted, $\underline{U}$ the matrix of the eigenvectors of $\underline{A}\,\underline{A}^T$, $\underline{V}$ the matrix of the eigenvectors of $\underline{A}^T\underline{A}$, and $\underline{\Sigma}$ the matrix whose main diagonal contains the square root of the eigenvalues of $\underline{A}^T\underline{A}$ in descending order; the following result is obtained:

$$\underline{A}^{-1} = \underline{V}\ \underline{\Sigma}^{-1}\ \underline{U}^T. \quad (12)$$

In EIT problems, the truncated SVD (TSVD) is generally employed. In the TSVD, only the largest singular values (beyond a certain established tolerance) are considered, setting to zero the smaller ones (with the corresponding singular vectors). This choice avoids to introduce "noise" in the solution produced by the small singular values.

Another considered choice is $\underline{L} = \underline{I}$ where the regularization matrix is equal to the identity matrix (LI condition). Finally, the matrix $\underline{L}$ has been taken as a discretization of the second order differential operator ∇^2 (LD2 condition). In the latter cases, the matrices to be inverted are all full rank and standard LU factorization can be applied for their inversion.

III. RESULTS

The Newton-Raphson algorithm has been implemented in Fortran 90 language and the IMSL libraries have been used for the classical and generalized inversion of the involved matrices.

In order to quantitatively compare the reconstructed voltages, a weighed version of the functional defined in

(6) for the k^{th} step of iteration has been used, given by:

$$e_g^k = \frac{\left[\underline{g}^{comp}(\underline{c}^k) - \underline{g}^{meas}\right]^T \cdot \left[\underline{g}^{comp}(\underline{c}^k) - \underline{g}^{meas}\right]}{\left(\underline{g}^{meas}\right)^T \cdot \underline{g}^{meas}} \times 100 \quad (13)$$

Moreover, in order to better quantify the accuracy of the reconstructed images, a second error, namely the percentage average deviation of the estimated conductivity distribution $\underline{c}^k$ with respect to the real one $\underline{c}$, has been defined as:

$$e_c^k = \frac{[\underline{c} - \underline{c}^k]^T \cdot [\underline{c} - \underline{c}^k]}{\underline{c}_{av}^T \cdot \underline{c}_{av}} \times 100, \quad (14)$$

where $\underline{c}_{av}$ is a vector with elements equal to the arithmetic average of $\underline{c}$.

A. Numerical codes validation

The square model with a square central anomaly shown in Fig. 1 (a) has been studied by using the neighboring data collection method and LI reconstruction algorithm with $\alpha = 10^{-3}$ and background conductivity equal to 0.12 S/m. The same problem has been solved with the EIDORS absolute solver with hyperparameter equal to 10^{-3} and background conductivity equal to 0.12 S/m [19].

Figure 4 shows the simulated electrode voltages, for the first injection couple, obtained by using as direct solver the FD method proposed in this work, compared with those achieved by using the FEM method implemented in EIDORS. A very good agreement between the two techniques can be observed.

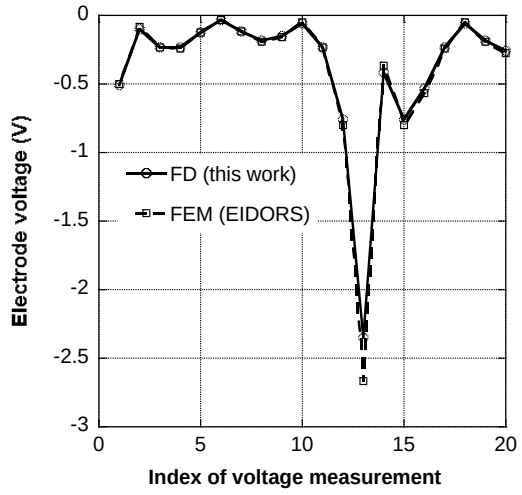

Fig. 4. Electrode voltages for the square geometry with square anomaly computed by using the FD method and the FEM method implemented in EIDORS.

The reconstructed conductivity distribution obtained with EIDORS is reported in Fig. 5 (a) and the one obtained by using the approach proposed in this paper in Fig. 5 (b). The two reconstructions look very similar. In fact, the application of (14) gives a reconstruction error of 0.9697% and 0.9696% for the EIDORS and the proposed method, respectively.

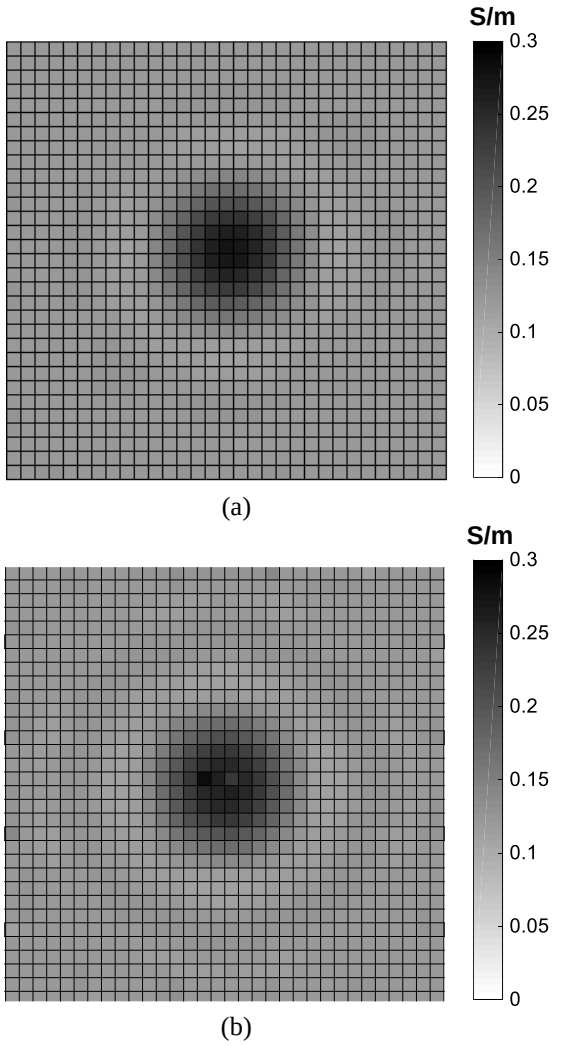

Fig. 5. Reconstructed conductivity maps for the square geometry by using EIDORS (a), and the technique proposed in this paper (b).

With reference to the best case for the voltage driven approach (opposite with L0), Fig. 6 shows the reconstructed images and voltages. In particular, Fig. 6 (a) shows the reconstructed image after seven iterations (ε_c = 22.59%), while Fig. 6 (b) reports a comparison between the simulated voltage measurements and the reconstructed voltages after seven steps (ε_g = 0.0001%). Figure 7 (b) shows that after seven iterations of the opposite L0 method, the reconstructed voltage

measurements almost perfectly match the measurement on the phantom, but a considerable error on the reconstructed image is present. Concerning the voltage driven approach, the best-reconstructed image is obtained by using the cross method with LI (ε_c = 18.07%), in this case the error on the voltage is very small (ε_g = 0.0098%) but higher than the previous case.

By using the image driven approach, the best image reconstruction is achieved by the neighboring method with L0 (see Fig. 7 (a)). The superiority of this image reconstruction with respect to the previous ones is evident. By comparing this figure with Fig. 1 (b), the good contour identification of all the thorax tissues is well evidenced.

B. Comparisons among different data collection and reconstruction algorithms

In the following, the anatomical thorax model has been considered and two sets of simulations have been performed. Each set contains simulation performed by using L0, LI and LD2 reconstruction methods and the neighboring, cross, and opposite data collection techniques.

In the first set (called voltage driven) the background conductivity, and the tolerance or the regularization parameter have been optimized in order to achieve the lowest error as defined in (13), while in the second set (called image driven) the parameters have been optimized in order to achieve the lowest error as defined in (14). The first approach is representative of the situation encountered in realistic experiments, where the goal of the reconstruction procedure is to achieve a distribution of the simulated voltages between the electrodes placed on the body surface as close as possible to the measured one. The second approach, instead, gives a better evaluation of the ability of the various techniques in reconstructing the internal geometry of the body.

The results obtained with the voltage driven approach are reported in Table 1. The table shows that the lowest reconstruction error is obtained by using the opposite method with L0 (0.00001%), while the highest error is obtained with the neighboring method with LI (0.1745%). In these simulations, the image reconstruction errors (as defined in (14)) are always higher than 18%. It is worth noting that the method with the lowest voltage reconstruction error gives rise to a very high image reconstruction error (22.59%). The table also shows that in all the situations the best background conductivity is equal to 0.12 S/m.

The results obtained with the image driven approach are reported in Table 2. In this case, the lowest reconstruction error is obtained by using the neighboring method with L0 (13.44%), while the highest error is obtained with the opposite method with LD2 (23.55%). Moreover, in all cases the best results are obtained by using a background conductivity equal to 0.06 S/m.

Table 1: Parameters that give rise to the best e_g^k for the L0, LI and LD2 reconstruction methods and the neighboring, cross, and opposite data collection techniques for the voltage driven approach. In the table the e_c^k obtained at the last step are also reported

		L0	LI	LD2
Neighboring Method	σ_{BG}	0.12	0.12	0.12
	Tol	$1.0e^{-2}$	/	/
	α	/	$2.0e^{-1}$	$1.0e^{-2}$
	e_g^N	0.0279%	0.1745%	0.0204%
	e_c^N	24.32%	18.97%	18.16%
Cross Method	σ_{BG}	0.12	0.12	0.12
	Tol	$1.0e^{-2}$	/	
	α	/	$2.0e^{-1}$	$5.0e^{-1}$
	e_g^N	0.0004%	0.0098%	0.0107%
	e_c^N	21.31%	18.07%	19.31%
Opposite Method	σ_{BG}	0.12	0.12	0.12
	Tol	$1.0e^{-2}$	/	/
	α	/	$5.0e^{-2}$	$5.0e^{-2}$
	e_g^N	0.0001%	0.0167%	0.0035%
	e_c^N	22.59%	18.90%	19.84%

Table 2: Parameters that give rise to the best e_c^k for the L0, LI and LD2 reconstruction methods and the neighboring, cross, and opposite data collection techniques for the image driven approach. In the Ttble the e_g^k obtained at the last step are also reported

		L0	LI	LD2
Neighboring Method	σ_{BG}	0.06	0.06	0.06
	Tol	1.0e-4	/	/
	α	/	1.0e-3	5.0e-4
	e_c^N	13.44%	15.98%	23.37%
	e_g^N	1.00%	2.98%	1.91%
Cross Method	σ_{BG}	0.06	0.06	0.06
	Tol	1.0e-4	/	
	α	/	1.0e-3	5.0e-4
	e_c^N	15.52%	17.19%	22.61%
	e_g^N	0.09%	3.21%	3.34%
Opposite Method	σ_{BG}	0.06	0.06	0.06
	Tol	1.0e-4	/	/
	α	/	1.0e-3	5.0e-4
	e_c^N	16.92%	15.50%	23.55%
	e_g^N	0.08%	0.38%	2.72%

C. Effects of noise and electrode misalignment

The above reported image reconstructions have been performed by neglecting the presence of noise on the measured data and supposing that measured and simulated data are collected by means of electrodes placed in the same positions. In an experimental set up the measuring apparatus introduces a random noise. Moreover, measurements are performed by placing the electrodes on a belt in approximately equally spaced positions, while the simulations are performed on a phantom that roughly mimics the real electrode positioning.

In order to investigate the relevance of the random noise on the reconstructions, the simulated measurements have been modified by adding to the voltage data ($\underline{g}^{meas}$) a Gaussian voltage noise with zero mean and with various levels of standard deviation. Figure 8 shows the obtained image reconstruction error as a function of the noise standard deviation, by considering three data collection methods and the L0 reconstruction algorithm. The figure evidences that for low noise levels the neighboring method allows the best image reconstruction while, increasing the noise standard deviation, the cross and opposite methods give better results. This is probably because, as evidenced in Fig. 6 (b), the opposite technique gives rise to higher electrode voltages that are less influenced by noise. On the same figure, the image reconstruction error achieved with the opposite method with LI is also reported. This curve shows a strong increase, with the noise standard deviation, of the error at low noise levels. This result suggests that the L0 technique is more efficient in reducing the effect of noise.

In order to study the effect of the electrode misalignment, a set of reconstructions has been performed by using simulated measurement data obtained by shifting of one cell (about 1 cm) a single electrode and evaluating the image reconstruction error with simulations performed with the electrode in its initial position. In all the simulations, the L0 reconstruction method with a background conductivity of 0.06 S/m has been used

These simulations have been repeated for all the sixteen electrodes, by considering the neighboring, cross, and opposite data collection techniques.

The variations of the image reconstruction error with respect to the aligned case are reported in Fig. 9. The figure shows that the variations are generally lower than 2%. However, by evaluating the average over the sixteen positions, values of 1.425%, 1.474% and 1.097% are obtained for the neighboring, cross and opposite methods, respectively. In conclusion, this analysis seems to indicate that the opposite method is the most robust data collection technique with respect to the electrode misalignment.

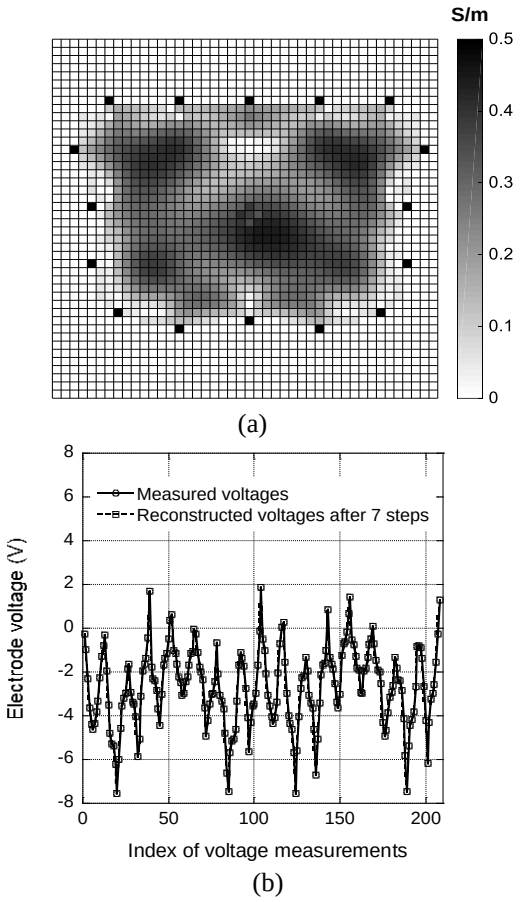

Fig. 6. Opposite method with L0: (a) conductivity distribution, and (b) comparison between measured and simulated electrode voltages after seven iterations.

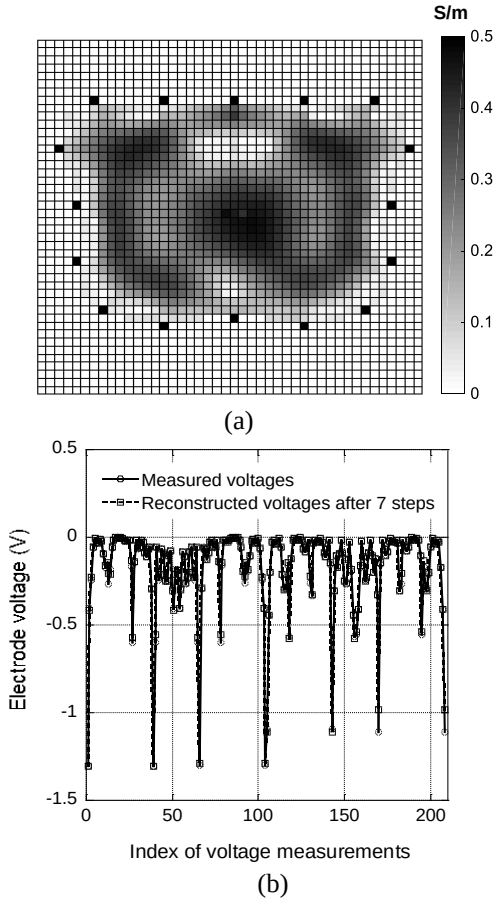

Fig. 7. Neighboring method with L0: (a) conductivity distribution, and (b) comparison between measured and simulated electrode voltages after seven iterations.

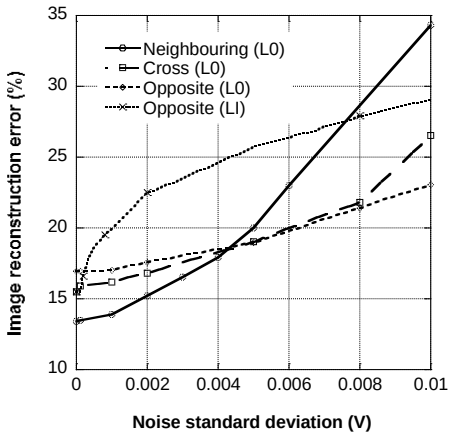

Fig. 8. Image reconstruction error as a function of the noise standard deviation.

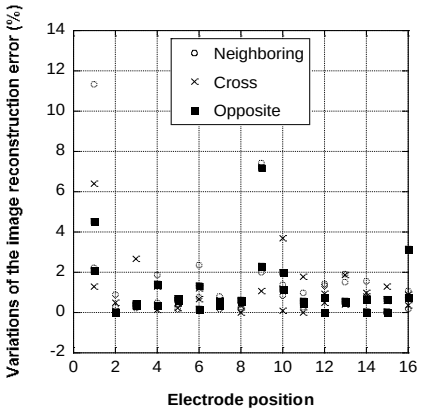

Fig. 9. Variations of the image reconstruction error due to electrode misalignment as a function of the electrode position.

IV. CONCLUSION

In this paper, the mathematical background and the implementation details of the admittance and Newton-Raphson methods, applied to the EIT problem, have been described.

The reconstruction procedure has been validated

through a comparison with the EIDORS open source software. The obtained results show that the FD method gives electrode voltage distributions in very good agreement with the FEM method implemented in EIDORS. Moreover, the errors on the image reconstruction are comparable. It is worth to be noted that FEM is a very accurate technique but needs complex mesh generators. On the contrary, the use of FD methods with square cells in a Cartesian reference system makes the modeling and computation of voltage distributions easy and accurate. Moreover, the memory occupation of FEM technique grows as the square of the number of cells while the memory occupation of the FD technique grows linearly with the cell number. This makes the FD a preferred choice for 3D problems with a high number of cells [24].

It is worth noting that for the considered EIT problem the FD method has been solved by considering only the real part of the tissue conductivity. However, the same method can also be applied by considering both the real and the imaginary part (related to the permittivity) of the conductivity of the tissues. This last approach could be useful in applications where it is necessary to increase the operating frequency. Moreover, by adding to the circuit in Fig. 3 current generators related to the vector potential distribution [22] the same method can be used to study the magnetic detection electrical impedance tomography [25, 26].

Various reconstruction algorithms and data collection techniques have been compared by using a realistic model instead of the simplified square or cylindrical models previously considered in papers where different EIT techniques were compared [12, 18, 27]. In fact, as evidenced by Grychtol et al. [28], for testing inversion algorithms and data collection techniques it is important to use anatomical, morphologically accurate, models. This is another advantage of the FD method that allows to study realistic, pixel based, anatomical human models easily imported in the FD grid. Recently, realistic human models, generated from the visible human data set [20] to be used with FEM mesh, have been proposed [29, 30]. However, these models take into account only the external body surface and a few organs. The FD method, on the contrary, by using the full pixel based models, can consider the high variability of the human anatomy.

The reconstruction problem has been solved using Tikhonov regularization with various choices of the regularization matrix and of the data collection method. The obtained results have been compared by using the percentage deviation of the simulated electrode voltages with respect to the measured one and the percentage deviation of the evaluated conductivity distribution with respect to the real one. By using the first metric to stop the simulations, very low voltage reconstruction errors are achieved but this does not give rise to good image reconstructions, as compared with those obtained by using the image driven approach. In particular, in the performed study the best image reconstruction has been obtained by using the neighboring method with null regularization matrix and using the truncate singular value decomposition to perform the matrix inversion. In conclusion, the better reconstruction properties of the neighboring technique with respect to the other approaches, previously evidenced by using simplified body models and a back projection algorithm [18, 31], have been confirmed, in the present paper, by using a more realistic anatomical model and various forms of the Newton-Raphson algorithm.

Various inversion and data collection techniques have been compared in terms of robustness to random noise and electrode misalignments. To this end, the cross and opposite methods show better performance with respect to the neighboring method in the presence of a random noise over imposed to the measured signals. This is probably because the cross and opposite techniques give rise to higher electrode voltages, that are less influenced by the noise. This result is in agreement with literature data [18] achieved on simplified circular geometries. The opposite method showed the best performance with respect to electrode positioning uncertainties. A possible explanation is the uniform field distribution produced by the electrodes excitation used in the opposite technique that is less influenced by an electrode misalignment.

Finally, it is important to note that the EIT reconstructed images lack a good resolution and give only a rough representation of the body section. However, their acquisition is very fast thus allowing, for example, the monitoring of lung movement and conductivity variations during the breathing cycle [32].

REFERENCES

[1] J. G. Webster, *Electrical Impedance Tomography*. Adam Hilger, Bristol, New York, 1990.

[2] J. Malmivuo and R. Plonsey, *Bioelectromagnetism: Principles and Application of Bioelectric and Biomagnetic Fields*. Oxford University Press, New York, 1995.

[3] D. S. Holder, *Electrical Impedance Tomography: Methods, History and Applications*. Institute of Physics, Great Britain, CRC Press, 2005.

[4] A. D. Seagar, D. C. Barber, and B. H. Brown, "Theoretical limits to sensitivity and resolution in impedance imaging," *Clin. Phys. Physiol. Meas*., vol. 8(A), pp. 13-31, 1987.

[5] T. M. Murai and Y. Kagawa, "Electrical impedance computed tomography based on a finite element model," *IEEE Transactions on Biomedical Engin-eering*, vol. 32, no. 3, pp. 177-184, 1985.

[6] R. P. Patterson and J. Zhang, "Evaluation of an EIT reconstruction algorithm using finite difference human thorax models as phantoms," *Physiol. Meas*.,

vol. 24, pp. 467-475, 2003.

[7] P. Kauppinen, J. Hyttinen, P. Laarne, and J. Malmivuo, "A software implementation for detailed volume conductor modelling in electrophysiology using finite difference method," *Computer Methods and Programs in Biomedicine*, vol. 58, pp. 191-203, 1999.

[8] D. Romano, S. Pisa, and E. Piuzzi, "Implementation of the Newton-Raphson and admittance methods for EIT," *International Journal of Bioelectromagnetism*, vol. 1, pp. 12-20, 2010.

[9] C. C. Barber and B. H. Brown "Imaging spatial distributions of resistivity using applied potential tomography," *Electronics Letters*, vol. 19, no. 22, pp. 933-935, 1983.

[10] L. Hao, L. Xu, B. Yang, and G. Li, "Image reconstruction based on the anatomical information for magnetic resonance electrical impedance tomography," *Applied Computational Electromagnetics Society Journal*, vol. 31, no. 6, pp. 700-705, 2016.

[11] D. Romano, S. Pisa, E. Piuzzi, and L. Podestà, "A comparison between back projection and sensitivity methods in EIT reconstruction problems," *In Proceedings of 19th International Zurich Symposium on Electromagnetic Compatibility*, Singapore, pp. 930-933, 2008.

[12] T. J. Yorkey, J. G. Webster, and W. J. Tompkins, "Comparing reconstruction algorithms for electrical impedance tomography," *IEEE Transactions on Biomedical Engineering*, vol. 34, no. 11, pp. 843-852, 1987.

[13] A. N. Tikhonov, "Solution of incorrectly formulated problems and the regularization method," *Soviet Math Dokl*, vol. 4, pp. 1035-1038, English translation of Dokl Akad Nauk SSSR, vol. 151, pp. 501-504, 1963.

[14] P. Hua, J. G. Webster, and W. J. Tompkins, "A regularised electrical impedance tomography recon-struction algorithm," *Clin. Phys. Physiol. Meas*., vol. 9(A), pp. 137-141, 1988.

[15] P. Hua, E. J. Woo, J. W. Webster, and W. J. Tompkins, "Iterative reconstruction methods using regularization and optimal current patterns in electrical impedance tomography," *IEEE Trans. Med. Imag.*, vol. 10, pp. 621-628, 1991.

[16] D. C. Dobson and F. Santosa, "An image enhancement technique for electrical impedance tomography," *Inverse Prob*., 10, pp. 317-334, 1994.

[17] A. Borsic, R. B. Lionheart, and N. McLeod, "Generation of anisotropic-smoothness regular-izeation filters for EIT," *IEEE Transactions on Medical Imaging*, vol. 21, no. 6, pp. 579-587, 2002.

[18] N. J. Avis and D. C. Barber, "Image reconstruction using non-adjacent drive configurations," *Physiol. Meas.*, vol. 15, pp. 153-160, 1994.

[19] A. Adler and W. R. B. Lionheart, "Uses and abuses of EIDORS: an extensible software base for EIT," *Physiol. Meas*., vol. 27, pp. 25-42, 2006.

[20] M. J. Ackerman, "The visible human project," *Proc. IEEE*, vol. 86, no. 3, pp. 504-511, 1998.

[21] D. Andreuccetti, R. Fossi, and C. Petrucci, *An internet resource for the calculation of the dielectric properties of body tissues in the frequency range 10 Hz - 100 GHz*, Internet document; URL: http:// niremf.ifac.cnr.it/ tissprop/

[22] G. d'Inzeo, C. Giacomozzi, and S. Pisa, "Analysis of the stimulation of a nerve fiber surrounded by an inhomogeneus, anisotropic, and dispersive tissue," *Applied Computational Electromagnetics Society Journal*, vol. 7, no. 2, pp. 179-190, 1992.

[23] G. H. Golub and C. F. Van Loan, *Matrix Computation*. 4rd ed., The Johns Hopkins University Press, Baltimore, 2013.

[24] J. Goble, M. Cheney, and D. Isaacson, "Electrical impedance tomography in three dimensions," *Applied Computational Electromagnetics Society Journal*, vol. 7, no. 2, pp. 128-147, 1992.

[25] J. C. Tozer, R. H. Ireland, D. C. Barber, and A. T. Barker, "Magnetic impedance tomography," *Ann. N. Y. Acad. Sci*., vol. 873, pp. 353-359, Apr. 1999.

[26] L. Hao and L. Xu, "Joint L1 and total variation regularization for magnetic detection electrical impedance tomography," *Applied Computational Electromagnetics Society Journal*, vol. 31, no. 6, pp. 677-683, June 2016.

[27] V. Sarode, S. Patkar, and A. N. Cheeran, "Comparison of 2-D algorithms in EIT based image reconstruction," *Int. Journal of Computer Applications*, vol. 8, pp. 6-11, 2013.

[28] B. Grychtol, G. Elke, P. Meybohm, N. Weiler, I. Frerichs, and A. Adler, "Functional validation and comparison framework for EIT lung imaging," *PLoS ONE*, vol. 9, pp. 1-13, 2014.

[29] A. Adler, J. H. Arnold, R. Bayford, A. Borsic, B. Brown, P. Dixon, T. J. C. Faes, I. Frerichs, H. Gagnon, Y. Garber, B. Grychtol, G. Hahn, W. R. B. Lionheart, A. Malik, R. P. Patterson, J. Stocks, A. Tizzard, N. Weiler, and G. K. Wolf, "GREIT: A unified approach to 2D linear EIT reconstruction of lung images," *Physiol. Meas*., vol. 30, pp. 169-191, 2009.

[30] A. Tizzard, L. Horesh, R. J. Yerworth, D. S. Holder, and R. H. Bayford, "Generating accurate finite element meshes for the forward model of the human head in EIT," *Physiol. Meas.*, vol. 26, pp. 251-261, 2005.

[31] W. R. Breckon and M. K. Pidcock, "Some mathematical aspects of electrical impedance tomogramphy," *Mathematics and Compute Science in Medical*

Imaging, ed. M. A. Viergever and A. E. Todd-Pokropek (Berlin: Springer), pp. 204-215, 1988.

[32] F. Grunberg "Respiratory cycle in 90 images," *Drager Review*, vol. 99, no. 1, Feb. 2010.

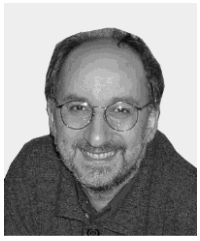

Stefano Pisa received the Electronic Engineering and Ph.D. degrees from the University of Rome "La Sapienza," Rome, Italy, in 1985 and 1988, respectively. In 1989, he joined the Department of Electronic Engineering, University of Rome "La Sapienza," as a Researcher. Since 2001, he has been an Associate Professor with the same university. His research interests are the interaction between electromagnetic fields and biological systems, therapeutic and diagnostic applications of electromagnetic fields, and the modeling and design of MW circuits. He has authored over 150 scientific papers and numerous invited presentations at international workshops and conferences. Pisa is a Member of the IEEE Microwave Theory and Techniques Society. He serves as a Reviewer for different international journals.

Erika Pittella received the M.S. (cum laude) and Ph.D. degrees in Electronic Engineering from the Sapienza University of Rome, Rome, Italy, in 2006 and 2011, respectively. She is currently a Research Associate with the Department of Information Engineering, Electronics and Tele-communications, Sapienza University of Rome. Pittella's research interests are electromagnetism applied to medicine, main research activities are related to the modeling of ultra wideband radars for the remote monitoring of cardiorespiratory activity, to the design of sources, antennas, and receivers of such systems, and the measurement of dielectric characteristics of materials. She is also interested in dosimetric aspects of the interaction between electromagnetic fields radiated by ultra wideband radar systems and exposed subjects. Pittella is a Member of the IEEE Instrumentation and Measurement Society, and of the Italian Group of Electrical and Electronic Measurements (GMEE). She serves as a Reviewer for different international journals.

Emanuele Piuzzi received the M.S. (cum laude) and Ph.D. degrees in Electronic Engineering from Sapienza University of Rome, Rome, Italy, in 1997 and 2001, respectively. He is currently an Assistant Professor of Electrical and Electronic Measure-ments with the Department of Infor-mation Engineering, Electronics and Telecommunications, Sapienza University of Rome. He is the co-author of over 100 publications. His current research interests include the measurement of complex permittivity of materials, time domain reflectometry applications, biomedical instrumentation design, and evaluation of human exposure to electromagnetic fields. Piuzzi is a Member of the IEEE Instrumentation and Measurement Society, of the Italian Group of Electrical and Electronic Measurements (GMEE), and of the Italian Electrotechnical Committee (CEI). He serves as a Reviewer for different international journals.

Optimal Design of Electromagnetic Devices Using the League Championship Algorithm

Houssem R. E. H. Bouchekara [1], Mouaaz Nahas [2], and Hamza M. Kaouach [3,4]

[1] Laboratory of Electrical Engineering of Constantine, LGEC, Department of Electrical Engineering
University of Freres Mentouri Constantine, 25000 Constantine, Algeria
bouchekara.houssem@gmail.com

[2] Department of Electrical Engineering, College of Engineering and Islamic Architecture
Umm Al-Qura University, P.O. Box: 5555, Makkah, 21955 Saudi Arabia
mmnahas@uqu.edu.sa

[3] ECE Department, Umm Al-Qura University, 21493 Al-Lith, Saudi Arabia
hkaouach@uqu.edu.sa

[4] HF APW Communications, University Campus, 29238 Brest, France
hamza.kaouach@gmail.com

Abstract ─ Nowadays, there is an increasing attention on novel metaheuristics and their applications in different problems of science and engineering. A new efficient optimization method, called the League Championship Algorithm (LCA) is applied in this paper for the optimal design of electromagnetic devices. This method is inspired by the competition of sport teams in an artificial sport league for several weeks and over a number of seasons. The performance of the proposed algorithm is tested against two benchmark problems: the magnetizer and the outrunner-type brushless DC motor. The obtained results show that the LCA is an efficient and competitive algorithm for constructing optimal design of electromagnetic devices.

Index Terms ─ Electromagnetic devices, league championship algorithm, metaheuristics, optimal design, optimization.

I. INTRODUCTION

Optimal design of devices is one of the major problems in electrical engineering. It involves choosing – from many possible variants – the best or the optimum variant based on one or several criteria [1].

The optimal design of Electromagnetic Devices (EMD) using metaheuristics has been successfully implemented and applied since the development of such algorithms in the early 1980s. Some relatively recent examples of the application of metaheuristics for the optimal design of EMD include, among others, Genetic Algorithms [2], Evolution Strategies [3], Tabu Search [4], Artificial Immune Systems [5], Particle Swarm Optimization [6], Electromagnetism-Like Mechanism [7], Imperialist Competitive Algorithm [8], Bacterial Chemotaxis [9], Black-Hole-Based Optimization [10] and Teaching Learning Based Optimization [11].

Furthermore, recently, great deals of efforts have been devoted to the development and application of new optimization metaheuristics inspired from real life phenomena. In this context, a new developed metaheuristic which has not yet received adequate attention in the electromagnetic optimization community is the League Championship Algorithm (LCA). The LCA is a novel algorithm inspired from the concept of sport league championships. In LCA, the league (population) is composed of teams (individuals) that compete in an artificial league over several weeks for a number of seasons [12], [13].

The main objective of this paper is, first, to review the basic algorithmic features of the LCA optimizer and, second, to apply LCA for achieving optimal design of EMD. The LCA algorithm proposed is then tested on a magnetizer benchmark problem and an Outrunner-type Brushless DC (OBLDC) motor benchmark problem.

The remainder of this paper is organized as follows. Section 2 provides a detailed description of the LCA. In Section 3, the proposed algorithm is applied to the two benchmark problems mentioned above. Finally, summary and conclusions are drawn in Section 4.

II. LEAGUE CHAMPIONSHIP ALGORITHM (LCA)

A. Overview

The LCA introduced by Husseinzadeh [12] is a new

Submitted On: June 25, 2016
Accepted On: April 29, 2017

metaheuristic algorithm developed to solve continuous optimization problems [14]. Like some other known optimization algorithms, LCA uses a population of solutions to obtain the optimal one. Each team (i.e., individual) in the league (i.e., population) represents a feasible solution to the problem that is being solved. These teams compete in an artificial league for several weeks (iterations). Based on the league schedule for each week, teams play in pairs (say, for example, team i plays against team j) and the outcome is determined in terms of win or loss based on the playing strength of the teams. The team strength (which is basically corresponding to the fitness value) results from a particular team formation (solution). Keeping track of the previous week events, each team can make the required changes in the recovery period in order to set up a new formation for the next week competition (this simply means that a new solution is generated). In the same way, the championship continues for a number of seasons (stopping criterion) [14].

B. The algorithm

Algorithm 1 provides the basic steps of the LCA in a greater detail. As in the other optimization algorithms, the LCA works with a population of individuals. Therefore, in the initialization process, a league of L teams is generated and the teams' playing strengths are evaluated. Here, the league, teams, and playing strengths represent the population, solutions and fitness values (respectively). Also, L is an even number which represents the league size. Considering a function of n variables, each team comprises n players, where each one corresponds to a different variable. In the first step, the teams' best formations take the initialization values. In the second step – which is the competition phase – the teams compete in pairs based on the league scheduler for $S\times(L-1)$ weeks; where S is the number of seasons and a week (iteration) is represented by t. After each competition (or game) between team i and team j (for example), the outcome is produced in terms of win or loss based on the playing strength of each team; here, we assume no tie games can occur. In the recovery step (which is the third step), each team devises a new formation based on the team's current best formation and the previous week events, too. Selection in LCA is greedy in the sense that the current best formation is replaced by a more productive team formation that has a better playing strength. In other words, If the new formation is the fittest one (i.e., the new solution is considered the best solution obtained so far for the ith member of the population), then the new formation is considered as the team's current best formation. The algorithm stops after a certain number of seasons [12], [13].

In our description of the LCA algorithm, we have used some concepts like: generating the league schedule, determining the winning or losing team and finally setting up a new team formation. More details on the mechanism of these concepts are given in [12] and [13].

Algorithm 1: The League championship algorithm [12]

1. Initialize the league size (L) and the number of seasons (S); t=1;
2. Generate a league schedule;
3. Initialize team formations (generate a population of L solutions) and determine the playing strengths (function or fitness value) along with them. Let the initialization be also the teams' current best formation;
4. While $t \leq S.(L-1)$:
5. Based on the league schedule at week t, determine the winner/loser among every pair of teams using a playing strength based criterion;
6. t=t+1;
7. For i=1 to L:
8. Devise a new formation for team i for the forthcoming match, while taking into account the team's current best formation and previous week events. Evaluate the playing strength of the resulting arrangement;
9. If the new formation is the fittest one (that is, the new solution is the best solution achieved so far for the ith member of the population), hereafter consider the new formation as the team's current best formation;
10. End for
11. If mod(t,L-1)=0
12. Generate a league schedule;
13. End if
14. End while.

C. Implementation of the LCA for the optimal design of EMD

The implementation of the LCA for the optimal design of EMD is illustrated in Fig. 1. It can be seen that the process begins by selecting the device to be optimized. This step is followed by: defining the objective function, providing the design variables with their mapping ranges, and imposing some constraints if needed. Then, the Decision Maker (DM) has to choose the more appropriate model for the selected EMD; i.e., it can be based on an analytical model or numerical models such as the Finite Element Method (FEM), the Finite Difference Method (FDM), or any others. Once the model is selected, the DM has to select the software among many (commercial or open source) software which are available for the designers. After that, and in order to apply the LCA, parameters like the league size, the number of seasons, the type of formation and the

probability of success have to be defined. The LCA is then run for the optimization. Once the results are obtained, the DM has to decide – using his/her experience – whether the design is satisfactory or not. If it is so, the process must be stopped, otherwise the LCA parameters should be modified and the LCA run until the designer is satisfied with the obtained results.

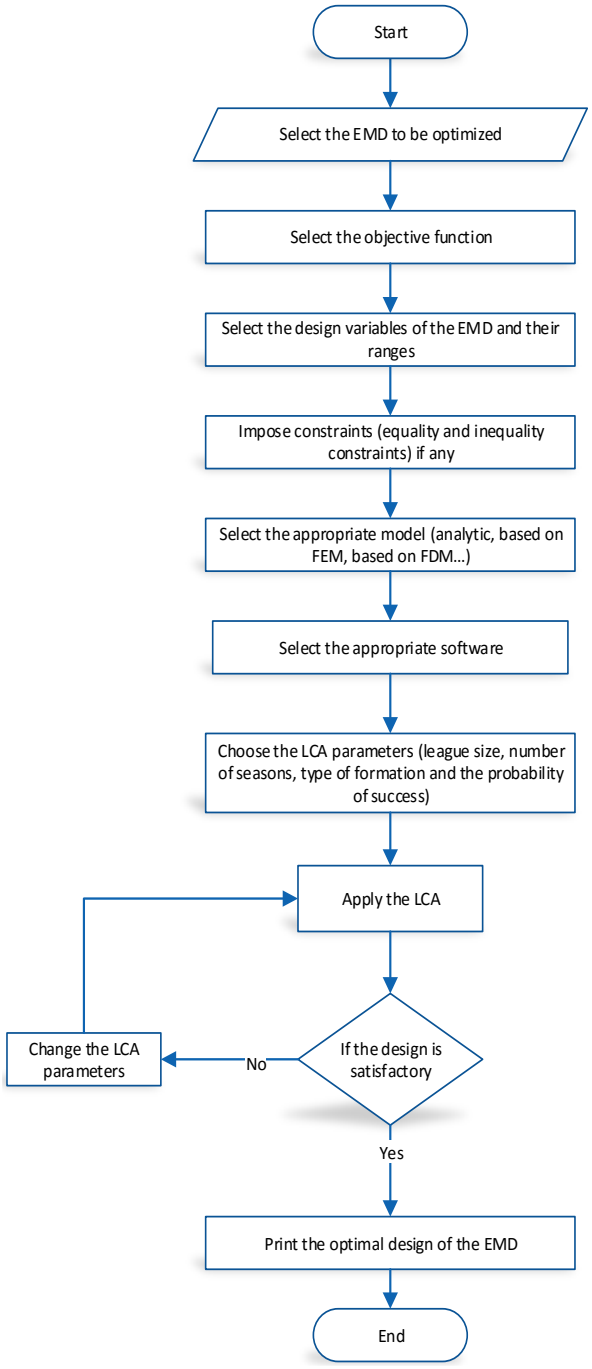

Fig. 1. Flowchart of the implementation of LCA for the optimal design of EMD.

III. APPLICATIONS

As mentioned earlier, the LCA has been applied to the following two benchmarks: the magnetizer benchmark problem and the OBLDC motor benchmark problem. Here is the detailed description of the two benchmarks.

A. The magnetizer problem

1) Description

The magnetizer problem is modeled as a linear 2D magnetostatic field analysis using the Finite Element Method (FEM). The geometry of the modeled part of the magnetizer is shown in Fig. 2. The key objective here is to optimize the pole shape of the magnetizer in order to get a predefined profile of the magnetic flux density along chord AB positioned halfway through the width of the magnetized piece [10].

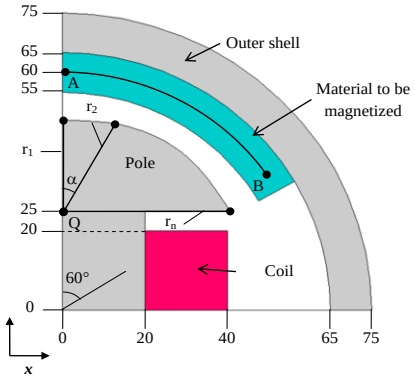

Fig. 2. Geometry of the magnetizer [15], [16].

The pole shape is modeled using Uniform Nonrational Cubic B-Splines (UNBS) with n control points P_1, P_2…P_n corresponding to the radial distances r_1, r_2… r_n and separated by α as shown in Fig. 2. UNBS interpolation provides local control of the curve, i.e., when a control point is moved, this affects only a small part of the curve. A B-spline curve is confined to the convex hull formed by the control points, and unless a control point is repeated at least three times, it does not touch the control points [15], [16].

In the FEM model, a low permeability (close to that of the air) is assigned to the object that is to be magnetized (nonmagnetic material), a permeability of 1000 is assigned to the pole face and the outer shell and a high current is applied to the coil region (5 A/mm^2).

2) Design variables

As mentioned above, the pole shape is modeled using n control points. In this work, we have chosen two values for n: n=4 and n=6. The n control points can move radially from the fixed point Q. Therefore, there are n design variables which are the radial distances from Q,

i.e., r_1 through r_n with mapping ranges given in Table 1. Once the locations of the control points are found, the curve that shapes the pole face is constructed with B-splines. This curve touches the control points P_1 and P_n, each of which is represented with three coinciding B-spline control points.

Table 1: Design variables and their ranges used in the magnetizer problem for n=4 and n=6

	n=4		n=6	
Design Variable	Lower Bound [mm]	Upper Bound [mm]	Lower Bound [mm]	Upper Bound [mm]
r_1	22.0	29.5	22.0	29.5
r_2	22.0	31.3	22.0	30.2
r_3	22.0	38.7	22.0	32.3
r_4	22.0	48.5	22.0	36.0
r_5	-	-	22.0	41.4
r_6	-	-	22.0	48.5

3) Objective function

The distribution of the magnetic flux density is evaluated at N sample points along the chord AB. Based on the desired profile of the magnetic flux density distribution in the chord AB, two cases are proposed and investigated in this paper:

CASE 1: the objective is to get a sinusoidal increasing distribution of B.

CASE 2: the objective is to get a uniform distribution of B.

In both cases the objective is to minimize the summed square of the difference between the desired and calculated magnetic flux densities (along the chord AB) which is identified as the error. Thus, the objective function can be written as follows:

$$f_{obj} = \sum_1^N \left(B_{desired_i} - B_{calculated_i}\right)^2, \qquad (1)$$

where: $B_{desiredi}$ and $B_{calculatedi}$ represent the desired and calculated magnetic flux densities at i, respectively. The desired flux density distribution $B_{desired}$ is calculated using the following formula:

$$B_{desired} = \begin{cases} B_0 \sin(\theta_i) & \text{CASE 1} \\ B_0 & \text{CASE 2'} \end{cases} \qquad (2)$$

where: $35° \leq \theta_i \leq 89°$, $i = 1, \ldots, N$, B_0 is chosen to be equal to 0.27 T and N = 50.

4) Results

The proposed algorithm has been applied to the magnetizer problem for CASE 1 and CASE 2. The optimal solutions found are tabulated in Table 2. Moreover, Fig. 3 shows a set of results for both cases; i.e., evolutions of the objective function over iterations, isopotential lines, comparison between the desired and optimal magnetic flux densities, and comparison between optimal profiles.

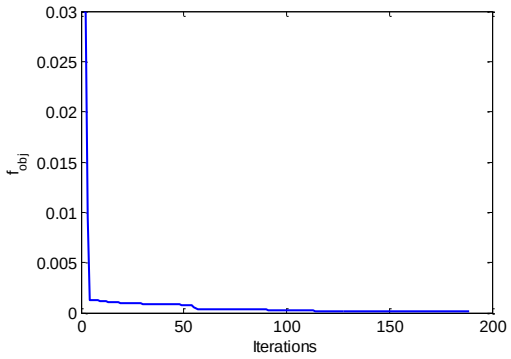

(a) Evolution of the objective function over iterations for CASE 1 (n=4)

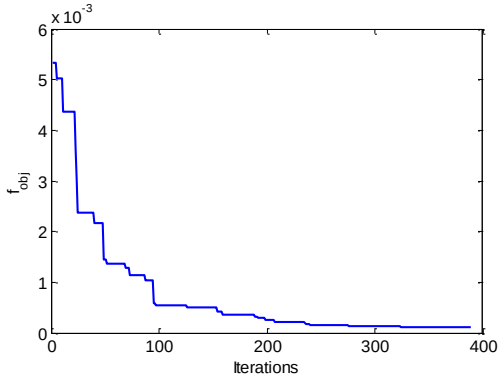

(b) Evolution of the objective function over iterations for CASE 1 (n=6)

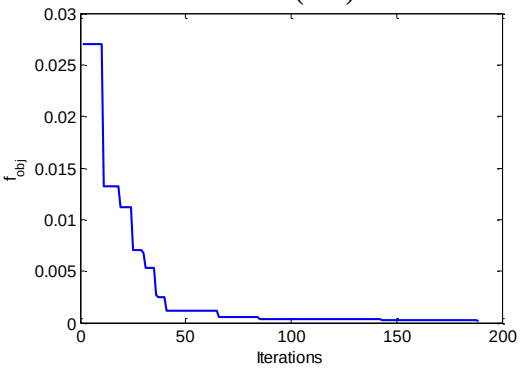

(c) Evolution of the objective function over iterations for CASE 2 (n=4)

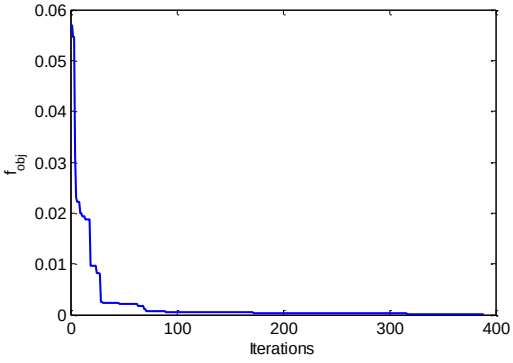

(d) Evolution of the objective function over iterations for CASE 2 (n=6)

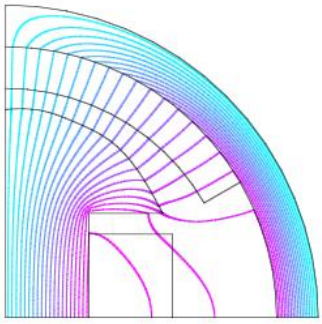

(e) Optimized magnetizer pole face and isopotential lines for CASE 1 (n=6)

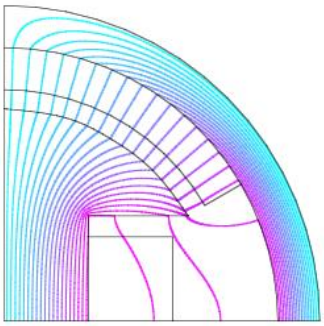

(f) Optimized magnetizer pole face and isopotential lines for CASE 2 (n=6)

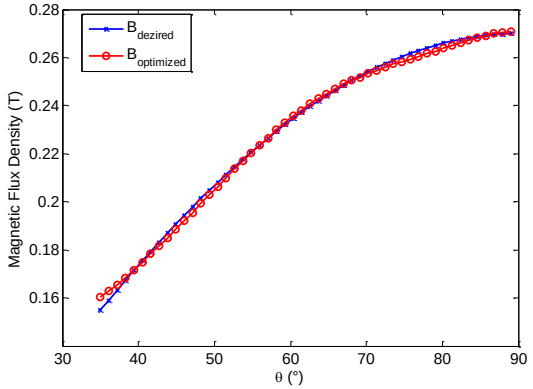

(g) Comparison between the desired and optimal magnetic flux densities for CASE 1 (n=4)

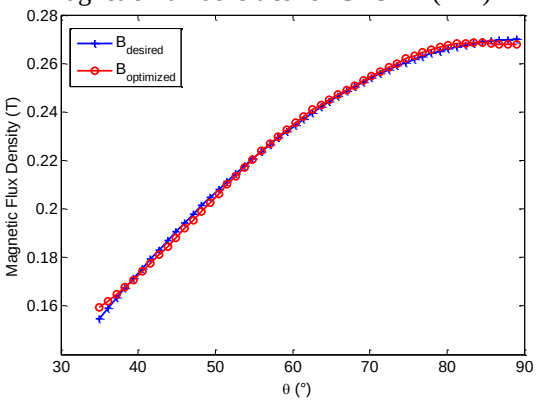

(h) Comparison between the desired and optimal magnetic flux densities for CASE 1 (n=6)

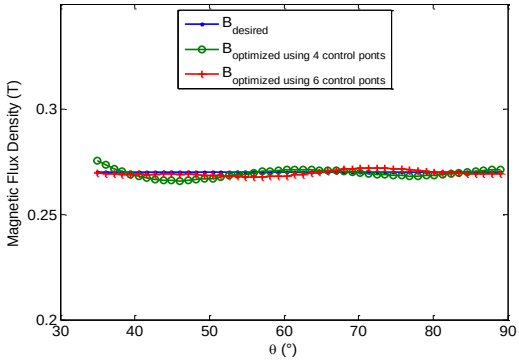

(i) Comparison between the desired and optimal magnetic flux densities for CASE 2

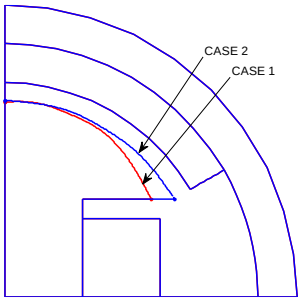

(g) Comparison between the optimal profiles found in CASE 1 and in CASE 2

Fig. 3. Obtained results for the magnetizer problem.

It can be clearly noticed that there is an improvement in the results when a higher number of control points is used. Furthermore, it is worth highlighting that the difference in the profiles depends on the objective function, i.e., whether the desired magnetic flux density is constant or sinusoidal. The optimized pole face has a constant air gap in CASE 1, however, this air gap gradually increases in CASE 2.

The proposed LCA is compared with some well-known optimization methods which are: Genetic Algorithm (GA), Particle Swarm Optimization (PSO), Black Hall Based Optimization (BHBO) and Electromagnetics Like-Mechanism (EM). The results of such a comparison are summarized in Table 3.

Table 2: Optimal solutions found for the magnetizer problem

	Optimal Values [mm]			
	n=4		n=6	
Design Variable	CASE 1	CASE 2	CASE 1	CASE 2
r_1	25.64	25.60	24.96	25.44
r_2	27.51	27.78	26.66	26.03
r_3	33.25	34.68	27.39	28.55
r_4	37.79	44.26	31.07	31.38
r_5	-	-	33.82	37.50
r_6	-	-	37.67	43.68

Table 3: Coordinates of the optimized control points for the magnetizer problem for CASE 1 compared with those obtained using some well-known optimization methods

	Optimal Values [mm]				
Design Variable	LCA	GA	PSO	EM [7]	BHBO [10]
r_1	24.96	25.882	25.639	25.239	25.444
r_2	26.66	25.537	25.779	26.338	25.941
r_3	27.39	28.140	28.149	27.583	28.232
r_4	31.07	30.565	30.161	30.544	29.715
r_5	33.82	34.401	35.058	34.318	35.691
r_6	37.67	37.380	36.764	37.405	36.351

B. OBLDC motor problem

1) Description

In this second example, we aim to optimize a 12 stator tooth 14-magnet outrunner-type (a motor with exterior rotor) brushless DC motor of the type commonly used to propel small Unmanned Aerial Vehicles (UAVs) (Fig. 4). The objective here is to minimize the size of the motor, given a specified bulk current density in the windings and a desired torque that should be produced at the specified current density [17].

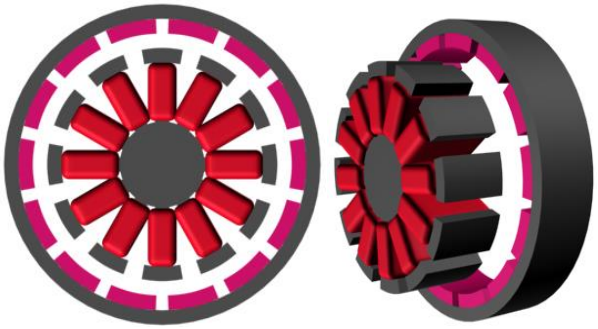

Fig. 4. Geometry of the OBLDC motor.

2) Design variables

In this example, we have 10 design variables that represent the geometry of the motor. These variables with their mapping ranges are detailed in Table 4.

3) Objective function

As mentioned before, the objective for this example is to minimize the size of the motor. In this work the desired torque is selected as 1 N.m. Therefore, the objective function can be expressed as follows [17]:

$$f_{obj} = \frac{1}{1000}\left(\pi \times \frac{\mathrm{hh} + \mathrm{rso}}{2} \times (\mathrm{rro}^2 - \mathrm{rsi}^2)\right), \quad (3)$$

where: rro is the rotor outer radius and the factor $\frac{1}{1000}$ is to scale the objective function to units of cm^3.

Table 4: Design variables and their ranges used in the OBLDC motor problem

Design Variable	Lower Bound [mm]	Lower Bound [mm]	Upper Bound [mm]
rso	Stator outer radius	8.0	20.0
rsi	Stator inner radius	2.0	5.0
dm	Magnet thickness	0.1	2.0
ds	Depth of slot opening	0.1	2.0
dc	Can thickness	0.1	2.0
fm	Pole fraction spanned by the magnet	0.2	1.0
fp	Pole fraction spanned by the iron	0.2	1.0
ft	Width of tooth as a fraction of pole pitch at stator ID	0.2	1.0
fb	Back iron thickness as a fraction of tooth thickness	0.2	1.0
hh	Length	15.0	50.0

4) Results

The proposed algorithm has been applied to the OBLDC motor problem. The optimal results found are tabulated in Table 5. Moreover, Fig. 5 shows the isopotential lines of the optimal motor obtained. The objective function using LCA gives the value of 43.0644 cm^3 which is better than the one obtained using Random Optimization (RO) that is 45.002 cm^3 [17].

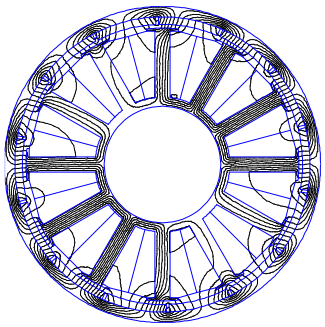

Fig. 5. Optimized 14 magnet OBLDC motor and isopotential lines.

Table 5: Optimal design of the OBLDC motor problem

Design Variable	Optimal Values [mm]
rso	18.736
rsi	8.000
dm	1.033
ds	1.446
dc	0.322
fm	0.959
fp	0.450
ft	0.507
fb	0.588
hh	24.267

IV. CONCLUSION

In this paper, the recently-developed LCA optimization algorithm has been used to find the optimal design of EMD. In order to assess its effectiveness in the selected problem domain, the proposed LCA algorithm has specifically been applied to the magnetizer problem and to the OBLDC motor problem. In the first problem, two cases with different number of control points were studied. In both cases, it was found that the LCA converged rapidly to optimum. In the second problem, the size of the motor was minimized as a result of applying the LCA algorithm. Also, a comparison with other optimization algorithms for this particular benchmark was performed and our results show that LCA is a competitive optimization algorithm.

The results obtained in this paper clearly show that the LCA constitutes a potential (as well as efficient) tool to be used for the optimal design of EMD. Detailed comparison with alternative optimization algorithms for the two benchmark problems (and many others in the same domain) can be a good base for future research work.

REFERENCES

[1] V. L. Chechurin, N. V. Korovkin, and M. Hayakawa, *Inverse Problems in Electric Circuits and Electromagnetics*. Springer, ISBN 0-387-33524-2, 2007.

[2] F. Zaoui and C. Marchand, "Using genetic algorithm for the optimization of electromagnetic devices," *COMPEL: The Int. J. for Comp. and Math. in Electr. and Electron. Eng.*, vol. 17, no. 1-3, pp. 181-185, 2007.

[3] L. S. Coelho and P. Alotto, "Electromagnetic device optimization by hybrid evolution strategy approaches," *COMPEL: The Int. J. for Comp. and Math. in Electr. and Electron. Eng.*, vol. 26, no. 2, pp. 269-279, 2007.

[4] E. Cogotti, A. Fanni, and F. Pilo, "A comparison of optimization techniques for Loney's solenoids design: An alternative tabu search algorithm," *IEEE Trans. Magn.*, vol. 36, no. 4, pp. 1153-1157, Apr. 2000.

[5] F. Campelo, F. G. Guimarães, H. Igarashi, J. A. Ramírez, and S. Noguchi, "A modified immune network algorithm for multimodal electromagnetic problems," *IEEE Trans. Magn*., vol. 42, no. 4, pp. 1111-1114, Apr. 2006.

[6] G. Ciuprina, D. Ioan, and I. Munteanu, "Use of intelligent-particle swarm optimization in electromagnetics," *IEEE Trans. Magn*., vol. 38, no. 2, pp. 1037-1040, Feb. 2002.

[7] H. R. E. H. Bouchekara, "Electromagnetic device optimization based on electromagnetism-like mechanism," *Appl. Comput. Electromagn Soc. J*., vol. 28, no. 3, pp. 241-248, 2013.

[8] L. D. S. Coelho, L. D. Afonso, and P. Alotto, "A modified imperialist competitive algorithm for optimization in electromagnetics," *IEEE Trans. Magn*., vol. 48, no. 2, pp. 579-582, Feb. 2012.

[9] S. Cocoa, A. Laudanib, F. R. Fulgineib, and A. Salvinib, "Bacterial chemotaxis shape optimization of electromagnetic devices," *Inverse Problems in Science and Engineering*, vol. 22, iss. 6, pp. 910-923, 2014.

[10] H. R. E. H. Bouchekara, "Optimal design of electromagnetic devices using a black-hole-based optimization technique," *IEEE Trans. Magn*., vol. 49, iss. 12, pp. 5709-5714, Dec. 2013.

[11] H. R. E. H Bouchekara and M. Nahas, "Optimization of electromagnetics problems using an improved teaching-learning-based-optimization technique," *Appl. Comput. Electromagn Soc. J*., vol. 30, no. 12, pp. 1341-1347, 2015.

[12] A. H. Kashan, "League championship algorithm: A new algorithm for numerical function optimization," In: *Proceedings of the International Conference of Soft Computing and Pattern Recognition. SoCPaR 2009, IEEE Computer Society*, pp. 43-8, 2009.

[13] A. H. Kashan, "An efficient algorithm for constrained global optimization and application to mechanical engineering design: League championship algorithm (LCA)," *Computer-Aided Design*, vol. 43, iss. 12, pp. 1769-1792, Dec. 2011.

[14] Z. Pourali and M. Aminnayeri, *A Novel Discrete League Championship Algorithm for Minimizing Earliness/Tardiness Penalties with Distinct Due Dates and Batch Delivery Consideration*. In: Advanced Intelligent Computing, Springer, pp. 139-146, 2012.

[15] G. F. Uler, O. A. Mohammed, and K. Chang-Seop, "Design optimization of electrical machines using genetic algorithms," *IEEE Trans. Magn*., vol. 31, no. 3, pp. 2008-2011, May 1995.

[16] O. A. Mohammed and G. F. Uler, "A hybrid technique for the optimal design of electromagnetic devices using direct search and genetic algorithms," *IEEE Trans. Magn*., vol. 33, no. 2, pp. 1931-1934, Mar. 1997.

[17] http://www.femm.info/wiki/RandomOptimization

Effective Medium Model for Multilayered Anisotropic Media with Different Orientations

Yang Bao and Jiming Song

Department of Electrical and Computer Engineering
Iowa State University, Ames, 50011, Iowa
brianbao@iastate.edu, jisong@iastate.edu

Abstract ─ An efficient model is developed to simulate multilayered biaxial anisotropic material with different orientations by using effective medium theory. Equivalent model is used to extract effective permittivity, permeability and orientation angle for multilayered biaxial anisotropic medium. Analytical expressions for effective parameters and orientation angle are derived for low frequency (LF) limit. The model also gives a non-magnetic effective anisotropic layer if each layer is non-magnetic anisotropic dielectric. Good agreement is achieved by comparing the effective parameters extracted with and without low frequency approximation. We show that the frequency-independent equivalent model is valid for frequency up to 10 GHz.

Index Terms ─ Effective medium theory, multilayered anisotropic media, parameter extraction.

I. INTRODUCTION

Anisotropic property is very popular among modern engineering materials such as composites, fibers, crystals, wood and so on. These kinds of materials have a lot of usages as housings and casings in aerospace, transportation, civil infrastructure, electronics, appliance and marine due to its characteristics such as: low weight, less tooling costs, high stiffness, low corrosion and easy to fabricate [1-5]. In aerospace industry, composites can be replacements for metals due to its good features that they are not as electrically conductive as traditional ones [2]. Thus, it becomes more and more important to understand the electromagnetic interactions (i.e., reflection, transmission) of composites [3, 5]. Multilayered anisotropic material with different orientations is very common in composites. However, electromagnetic modelling of multilayered anisotropic material needs huge CPU time and memory requirements. Using effective medium theory, by combining multilayered anisotropic medium with a single equivalent layer for the permittivity, permeability and orientation, CPU time and memory requirements can be significantly reduced [6].

In this paper, effective medium theory is applied to model multilayered biaxial anisotropic material with different orientations for a plane wave incidence at the normal direction. Basing on the same reflection and transmission coefficients, effective permittivity, permeability and orientation angle are extracted, similar to the approach used to extract effective parameters from measurements and numerical modeling of periodic structures as isotropic materials. With the low frequency (LF) limit, analytical expressions for effective parameters and orientation angle are derived and result in a frequency-independent equivalent model. Finally, effective parameters using low frequency approximation are compared with the ones from parameter extraction method. Good agreements in effective parameters and angle are observed between with and without the approximations for the frequency up to 10 GHz.

II. FORMULATION

In Fig. 1, the equivalent model is presented for multilayered biaxial anisotropic media with different orientations between two half spaces. A plane wave travels at the normal direction (z direction) to x-y plane. A global Cartesian coordinate x-y-z is used in the two half spaces and local coordinate x'-y'-z for each layer between two half spaces with x_n' rotating θ_n from x. The relative permeability and permittivity of the biaxial anisotropic layer can be expressed in tensor form as $\bar{\boldsymbol{\mu}}_n = \mathrm{diag}(\mu_{xn}, \mu_{yn}, \mu_{zn})$, $\bar{\boldsymbol{\varepsilon}}_n = \mathrm{diag}(\varepsilon_{xn}, \varepsilon_{yn}, \varepsilon_{zn})$.

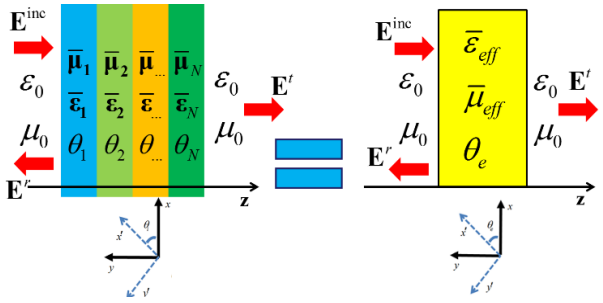

Fig. 1. Multilayered biaxial anisotropic media and its equivalent single layer model.

Submitted On: November 17, 2016
Accepted On: February 14, 2017

A. Reflection and transmission coefficient for equivalent layer

For the equivalent layer model, suppose electromagnetic field propagates in *z* direction with electric field polarized in *x* and *y* directions. We can get reflection and transmission coefficient matrices by expressing the electromagnetic field in all three regions and matching boundary conditions. The reflection coefficient **R** and transmission coefficient **T** are 2 by 2 matrices and are defined similar to S parameters [7]:

$$\begin{aligned} R_{pp} &= A_p \cos^2\theta_e + A_{\tilde{p}} \sin^2\theta_e, \\ R_{yx} &= R_{xy} = \left(A_x - A_y\right)\sin\theta_e \cos\theta_e, \\ T_{pp} &= B_p \cos^2\theta_e + B_{\tilde{p}} \sin^2\theta_e, \\ T_{yx} &= T_{xy} = \left(B_x - B_y\right)\sin\theta_e \cos\theta_e, \end{aligned} \tag{1}$$

where

$$A_p = \frac{\Gamma_{0p}\left(1-e^{-2j\beta_p d_t}\right)}{1-\Gamma_{0p}^2 e^{-2j\beta_p d_t}}, \quad B_p = \frac{\left(1-\Gamma_{0p}^2\right)e^{-jd_t\beta_p}}{1-\Gamma_{0p}^2 e^{-2j\beta_p d_t}}, \quad \Gamma_{0p} = \frac{\tilde{\eta}_p - 1}{\tilde{\eta}_p + 1},$$

$$\beta_p = \beta_0\sqrt{\varepsilon_{pe}\mu_{\tilde{p}e}}, \quad \tilde{\eta}_p = \sqrt{\frac{\mu_{\tilde{p}e}}{\varepsilon_{pe}}}, \quad p = x, y, \quad \tilde{p} = \begin{cases} x, & p = y \\ y, & p = x \end{cases}.$$

A_p and B_p are the same as the reflection and transmission coefficients derived using isotropic layer with $\mu_{\tilde{p}}$ and ε_p. d_t is the total thickness and $\beta_0 = \omega\sqrt{\varepsilon_0\mu_0}$.

B. Reflection and transmission coefficients for multilayers

The first method to derive the reflection and transmission matrices is similar to the transmission line theory. For region *n* (1 to *N*), $z_n < z < z_{n+1}$, *z* there are two types of propagation modes in local coordinate:

$$\mathbf{E}_n = \begin{bmatrix} E_{nx'} \\ E_{ny'} \end{bmatrix} = \left[e^{-j\bar{\boldsymbol{\beta}}_n\left(z-z_{n+1}\right)} + e^{j\bar{\boldsymbol{\beta}}_n\left(z-z_{n+1}\right)}\bar{\mathbf{R}}_{n,n+1}^{-}\right]\begin{bmatrix} A_n \\ B_n \end{bmatrix}, \tag{2}$$

$$\begin{aligned} \eta_0\bar{\mathbf{Z}}_{n0}\bullet\mathbf{H}_n &= \eta_0\begin{bmatrix} \eta_{nx} & 0 \\ 0 & \eta_{ny} \end{bmatrix}\begin{bmatrix} H_{ny'} \\ -H_{nx'} \end{bmatrix} \\ &= \left[e^{-j\bar{\boldsymbol{\beta}}_n\left(z-z_{n+1}\right)} - e^{j\bar{\boldsymbol{\beta}}_n\left(z-z_{n+1}\right)}\bar{\mathbf{R}}_{n,n+1}^{-}\right]\begin{bmatrix} A_n \\ B_n \end{bmatrix}, \end{aligned} \tag{3}$$

where $\bar{\mathbf{Z}}_{n0} = \mathrm{diag}\left(\eta_{nx}, \eta_{ny}\right)$, $\bar{\boldsymbol{\beta}}_n = \mathrm{diag}\left(\beta_{nx}, \beta_{ny}\right)$, $\bar{\mathbf{R}}_{n,n+1}^{-}$ is the 2 by 2 reflection matrix in region *n* at z_{n+1}.

The fields also can be written in the global coordinate

$$\begin{bmatrix} E_{nx'} \\ E_{ny'} \end{bmatrix} = \bar{\mathbf{O}}_n\begin{bmatrix} E_{nx} \\ E_{ny} \end{bmatrix}, \quad \begin{bmatrix} H_{ny'} \\ -H_{nx'} \end{bmatrix} = \bar{\mathbf{O}}_n\begin{bmatrix} H_{ny} \\ -H_{nx} \end{bmatrix}, \tag{4}$$

where the rotation matrix $\bar{\mathbf{O}}_n$ is given as:

$$\bar{\mathbf{O}}_n = \begin{bmatrix} \cos\theta_n & \sin\theta_n \\ -\sin\theta_n & \cos\theta_n \end{bmatrix}, \quad \bar{\mathbf{O}}_n^{-1} = \bar{\mathbf{O}}_n^{T}. \tag{5}$$

The relation between the electric and magnetic fields at $z = z_{n+1}$ is:

$$\mathbf{E}_n(z_{n+1}) = \eta_0\bar{\mathbf{Z}}_{n,n+1}^{-}\bullet\mathbf{H}_n(z_{n+1}), \tag{6}$$

$\bar{\mathbf{Z}}_{n,n+1}^{-}$ is the input impedance at $z = z_{n+1}$. Submitting (2) and (3) into (6) yields:

$$\bar{\mathbf{R}}_{n,n+1}^{-} = \left[\bar{\mathbf{Z}}_{n,n+1}^{-}\bar{\mathbf{Z}}_{n0}^{-1} + \bar{\mathbf{I}}\right]^{-1}\left[\bar{\mathbf{Z}}_{n,n+1}^{-}\bar{\mathbf{Z}}_{n0}^{-1} - \bar{\mathbf{I}}\right], \tag{7}$$

where $\bar{\mathbf{I}} = \mathrm{diag}\left(1,1\right)$ and matrix multiplications are involved. At $z = z_n$, similarly, we have:

$$\mathbf{E}_n(z_n) = \eta_0\bar{\mathbf{Z}}_{n-1,n}^{+}\bullet\mathbf{H}_n(z_n). \tag{8}$$

It is found that,

$$\begin{aligned} \bar{\mathbf{Z}}_{n-1,n}^{+} = &\left[\bar{\mathbf{I}} + e^{-j\bar{\boldsymbol{\beta}}_n d_n}\bar{\mathbf{R}}_{n,n+1}^{-}e^{-j\bar{\boldsymbol{\beta}}_n d_n}\right] \\ &\cdot\left[\bar{\mathbf{I}} - e^{-j\bar{\boldsymbol{\beta}}_n d_n}\bar{\mathbf{R}}_{n,n+1}^{-}e^{-j\bar{\boldsymbol{\beta}}_n d_n}\right]^{-1}\bar{\mathbf{Z}}_{n0}, \end{aligned} \tag{9}$$

where $d_n = z_{n+1} - z_n$. At the interface, the tangential components of both electric and magnetic fields should be continuous. Using the equations above, we find the impedance matrices at two sides and field components as:

$$\bar{\mathbf{Z}}_{n-1,n}^{-} = \bar{\mathbf{O}}_{n-1}\bar{\mathbf{O}}_n^{T}\bar{\mathbf{Z}}_{n-1,n}^{+}\bar{\mathbf{O}}_n\bar{\mathbf{O}}_{n-1}^{T}, \tag{10}$$

$$\begin{aligned} \begin{bmatrix} A_n \\ B_n \end{bmatrix} = &e^{-j\bar{\boldsymbol{\beta}}_n d_n}\left[\bar{\mathbf{I}} + e^{-j\bar{\boldsymbol{\beta}}_n d_n}\bar{\mathbf{R}}_{n,n+1}^{-}e^{-j\bar{\boldsymbol{\beta}}_n d_n}\right]^{-1} \\ &\cdot\bar{\mathbf{O}}_n\bar{\mathbf{O}}_{n-1}^{T}\left[\bar{\mathbf{I}} + \bar{\mathbf{R}}_{n-1,n}^{-}\right]\begin{bmatrix} A_{n-1} \\ B_{n-1} \end{bmatrix}. \end{aligned} \tag{11}$$

In Region 0, which is the half-space for the incident wave, the electric field is written as:

$$\mathbf{E}_0 = \begin{bmatrix} E_{0x} \\ E_{0y} \end{bmatrix} = \left[e^{-j\bar{\boldsymbol{\beta}}_0\left(z-z_1\right)} + e^{-j\bar{\boldsymbol{\beta}}_0\left(z-z_1\right)}\bar{\mathbf{R}}\right]\begin{bmatrix} A_0 \\ B_0 \end{bmatrix}, \tag{12}$$

where $\bar{\mathbf{R}} = \bar{\mathbf{R}}_{0,1}^{-}$ is the reflection matrix defined at $z = z_1$ and can be calculated recursively using (10), (7) and (9) with $\bar{\mathbf{Z}}_{N,N+1}^{+} = \bar{\mathbf{Z}}_{(N+1)0} = \bar{\mathbf{I}}$.

In the half-space Region $N+1$, the electric field is written as:

$$\mathbf{E}_{N+1} = \begin{bmatrix} E_{N+1\,x} \\ E_{N+1\,y} \end{bmatrix} = e^{-j\bar{\boldsymbol{\beta}}_0\left(z-z_{N+1}\right)}\bar{\mathbf{T}}\begin{bmatrix} A_0 \\ B_0 \end{bmatrix}. \tag{13}$$

Using (11) recursively, the total transmission matrix defined at $z = z_{N+1}$ is represented as:

$$\begin{aligned} \bar{\mathbf{T}} = &\bar{\mathbf{O}}_N^{T}\left[\bar{\mathbf{I}} + \bar{\mathbf{R}}_{N,N+1}^{-}\right] \\ &\cdot\prod_{n=1}^{N} e^{-j\bar{\boldsymbol{\beta}}_n d_n}\left[\bar{\mathbf{I}} + e^{-j\bar{\boldsymbol{\beta}}_n d_n}\bar{\mathbf{R}}_{n,n+1}^{-}e^{-j\bar{\boldsymbol{\beta}}_n d_n}\right]^{-1}\bar{\mathbf{O}}_n\bar{\mathbf{O}}_{n-1}^{T}\left[\bar{\mathbf{I}} + \bar{\mathbf{R}}_{n-1,n}^{-}\right], \end{aligned} \tag{14}$$

where $d_{N+1} = 0$, $\bar{\mathbf{O}}_0 = \bar{\mathbf{O}}_{N+1} = \bar{\mathbf{I}}$.

Another method to get total reflection and transmission coefficients for multilayers can be followed an approach in [8]. The basic idea is to calculate reflection and transmission coefficients from an

interface between two half spaces and then get total reflection and transmission coefficients recursively.

When Regions n and $n+1$ are half-space, the electric and magnetic fields at the interface are written in local coordinates as:

$$\begin{aligned}\mathbf{E}_n &= \begin{bmatrix} E_{nx'} \\ E_{ny'} \end{bmatrix} = \left[\bar{\mathbf{I}} + \bar{\mathbf{R}}_{n,n+1}\right] e^{-j\bar{\boldsymbol{\beta}}_n d_n} \begin{bmatrix} A_n \\ B_n \end{bmatrix}, \\ \eta_0 \bar{\mathbf{Z}}_{n0} \bullet \mathbf{H}_n &= \left[\bar{\mathbf{I}} - \bar{\mathbf{R}}_{n,n+1}\right] e^{-j\bar{\boldsymbol{\beta}}_n d_n} \begin{bmatrix} A_n \\ B_n \end{bmatrix},\end{aligned} \tag{15}$$

$$\begin{aligned}\mathbf{E}_{n+1} &= \begin{bmatrix} E_{(n+1)x'} \\ E_{(n+1)y'} \end{bmatrix} = \bar{\mathbf{T}}_{n,n+1} e^{-j\bar{\boldsymbol{\beta}}_n d_n} \begin{bmatrix} A_n \\ B_n \end{bmatrix}, \\ \eta_0 \bar{\mathbf{Z}}_{(n+1)0} \bullet \mathbf{H}_{(n+1)} &= \bar{\mathbf{T}}_{n,n+1} e^{-j\bar{\boldsymbol{\beta}}_n d_n} \begin{bmatrix} A_n \\ B_n \end{bmatrix}.\end{aligned} \tag{16}$$

Matching the boundary conditions at the interface using the global coordinate yields:

$$\bar{\mathbf{O}}_n^T \left[\bar{\mathbf{I}} + \bar{\mathbf{R}}_{n,n+1}\right] = \bar{\mathbf{O}}_{n+1}^T \bar{\mathbf{T}}_{n,n+1}, \tag{17}$$

$$\bar{\mathbf{O}}_n^T \bar{\mathbf{Z}}_{n0}^{-1} \left[\bar{\mathbf{I}} - \bar{\mathbf{R}}_{n,n+1}\right] = \bar{\mathbf{O}}_{n+1}^T \bar{\mathbf{Z}}_{(n+1)0}^{-1} \bar{\mathbf{T}}_{n,n+1}. \tag{18}$$

The half-space reflection and transmission coefficients are found as:

$$\begin{aligned}\bar{\mathbf{R}}_{n,n+1} &= \left[\bar{\mathbf{Z}}_{n0}^{-1} + \bar{\mathbf{O}}_n \bar{\mathbf{O}}_{n+1}^T \bar{\mathbf{Z}}_{(n+1)0}^{-1} \bar{\mathbf{O}}_{n+1} \bar{\mathbf{O}}_n^T\right]^{-1} \\ &\quad \cdot \left[\bar{\mathbf{Z}}_{n0}^{-1} - \bar{\mathbf{O}}_n \bar{\mathbf{O}}_{n+1}^T \bar{\mathbf{Z}}_{(n+1)0}^{-1} \bar{\mathbf{O}}_{n+1} \bar{\mathbf{O}}_n^T\right],\end{aligned} \tag{19}$$

$$\begin{aligned}\bar{\mathbf{T}}_{n,n+1} &= \bar{\mathbf{O}}_{n+1} \bar{\mathbf{O}}_n^T \left[\bar{\mathbf{I}} + \bar{\mathbf{R}}_{n,n+1}\right] \\ &= 2\bar{\mathbf{O}}_{n+1} \bar{\mathbf{O}}_n^T \left[\bar{\mathbf{Z}}_{n0}^{-1} + \bar{\mathbf{O}}_n \bar{\mathbf{O}}_{n+1}^T \bar{\mathbf{Z}}_{(n+1)0}^{-1} \bar{\mathbf{O}}_{n+1} \bar{\mathbf{O}}_n^T\right]^{-1} \bar{\mathbf{Z}}_{n0}^{-1}.\end{aligned} \tag{20}$$

It can be verified that the reflection matrix is symmetrical, but the transmission matrix is not in general, and,

$$\bar{\mathbf{R}}_{n+1,n} = -\bar{\mathbf{O}}_{n+1} \bar{\mathbf{O}}_n^T \bar{\mathbf{R}}_{n,n+1} \bar{\mathbf{O}}_n \bar{\mathbf{O}}_{n+1}^T, \tag{21}$$

$$\bar{\mathbf{T}}_{n+1,n} = \bar{\mathbf{O}}_n \bar{\mathbf{O}}_{n+1}^T \left[\bar{\mathbf{I}} + \bar{\mathbf{R}}_{n+1,n}\right] = \left[\bar{\mathbf{I}} - \bar{\mathbf{R}}_{n,n+1}\right] \bar{\mathbf{O}}_n \bar{\mathbf{O}}_{n+1}^T. \tag{22}$$

The total reflection and transmission coefficients in [8] can be written as:

$$\begin{aligned}\bar{\mathbf{R}}_{n,n+1}^- &= \bar{\mathbf{R}}_{n,n+1} + \bar{\mathbf{T}}_{n+1,n} e^{-j\bar{\boldsymbol{\beta}}_{n+1} d_{n+1}} \bar{\mathbf{R}}_{n+1,n+2}^- \\ &\cdot \left[\bar{\mathbf{I}} - e^{-j\bar{\boldsymbol{\beta}}_{n+1} d_{n+1}} \bar{\mathbf{R}}_{n+1,n} e^{-j\bar{\boldsymbol{\beta}}_{n+1} d_{n+1}} \bar{\mathbf{R}}_{n+1,n+2}^-\right]^{-1} e^{-j\bar{\boldsymbol{\beta}}_{n+1} d_{n+1}} \bar{\mathbf{T}}_{n,n+1},\end{aligned} \tag{23}$$

$$\bar{\mathbf{T}} = \bar{\mathbf{T}}_{N,N+1} \prod_{n=1}^{N} \left[\bar{\mathbf{I}} - e^{-j\bar{\boldsymbol{\beta}}_n d_n} \bar{\mathbf{R}}_{n,n-1} e^{-j\bar{\boldsymbol{\beta}}_n d_n} \bar{\mathbf{R}}_{n,n+1}^-\right]^{-1} e^{-j\bar{\boldsymbol{\beta}}_n d_n} \bar{\mathbf{T}}_{n-1,n}. \tag{24}$$

C. Equivalent model and low frequency approximation

Basing on same reflection and transmission coefficients for the single equivalent layer and multilayer, we express θ_e, A_p and B_p as functions of the reflection and transmission coefficients of multilayer structures:

$$\begin{aligned}\tan 2\theta_{er} &= \frac{2R_{xy}}{R_{xx} - R_{yy}}, \\ \tan 2\theta_{et} &= \frac{2\bar{T}_{xy}}{T_{xx} - T_{yy}},\end{aligned} \tag{25}$$

$$\begin{aligned}A_{x,y} &= \frac{1}{2}\left(R_{xx} + R_{yy}\right) \pm \frac{R_{xy}}{\sin 2\theta_{er}}, \\ B_{x,y} &= \frac{1}{2}\left(T_{xx} + T_{yy}\right) \pm \frac{\bar{T}_{xy}}{\sin 2\theta_{et}},\end{aligned} \tag{26}$$

where $R_{xy} = R_{yx}, T_{xy} \neq T_{yx}, \bar{T}_{xy} = \frac{1}{2}\left(T_{xy} + T_{yx}\right)$, the " ± " is for x- and y-component, respectively.

Then the effective parameters of the effective medium can be calculated from A_p and B_p using the approach for the isotropic layer [9-13]. The flowchart summarizing this procedure is shown in Fig. 2.

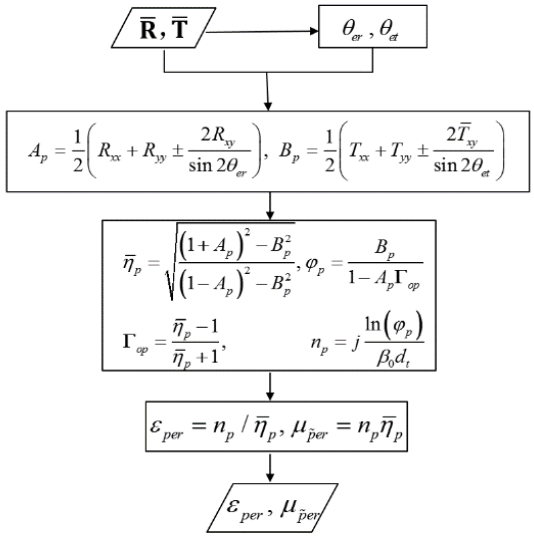

Fig. 2. Flowchart for effective parameters extraction.

For the low frequency limit, we follow the similar procedure to the isotropic case in [6]. The condition for low frequency approximation is satisfied when the wavelength is much bigger than the thickness of the structures. When $\beta_{np} d_n \ll 1$, applying Taylor series expansion to (9) and (14) and taking the first-order approximation yields:

$$e^{-j\bar{\boldsymbol{\beta}}_n d_n} \approx \bar{\mathbf{I}} - j d_n \bar{\boldsymbol{\beta}}_n. \tag{27}$$

Using $\bar{\mathbf{Z}}_{N,N+1}^+ = \bar{\mathbf{Z}}_{(N+1)0} = \bar{\mathbf{I}}$, we have:

$$\bar{\mathbf{Z}}_{N,N+1}^- = \bar{\mathbf{O}}_N \bar{\mathbf{O}}_{N+1}^T \bar{\mathbf{Z}}_{N,N+1}^+ \bar{\mathbf{O}}_{N+1} \bar{\mathbf{O}}_N^T = \bar{\mathbf{I}}, \tag{28}$$

$$\bar{\mathbf{R}}_{N,N+1}^- = \left[\bar{\mathbf{Z}}_{N,N+1}^- \bar{\mathbf{Z}}_{N0}^{-1} + \bar{\mathbf{I}}\right]^{-1} \left[\bar{\mathbf{Z}}_{N,N+1}^- \bar{\mathbf{Z}}_{N0}^{-1} - \bar{\mathbf{I}}\right] = \bar{\Gamma}_N, \tag{29}$$

where $\bar{\Gamma}_n = \mathrm{diag}\left(\Gamma_{nx}, \Gamma_{ny}\right)$. Since $\bar{\Gamma}_n$ is a diagonal matrix, submitting it into (9) and using (27) yields:

$$\bar{\mathbf{Z}}^{+}_{N-1,N} = \bar{\mathbf{I}} + \bar{\mathbf{z}}^{+}_{N-1,N}, \quad \bar{\mathbf{z}}^{+}_{N-1,N} = j\beta_0 d_N \bar{\Delta}_N, \tag{30}$$

where $\bar{\Delta}_n = \mathrm{diag}\left(\mu_{ny} - \varepsilon_{nx}, \mu_{nx} - \varepsilon_{ny}\right)$. In deriving (30) we use the relations $\bar{\mathbf{D}}_1\bar{\mathbf{D}}_2 = \bar{\mathbf{D}}_2\bar{\mathbf{D}}_1$, if both $\bar{\mathbf{D}}_1$ and $\bar{\mathbf{D}}_2$ are diagonal, and $\left[\bar{\mathbf{A}}+\bar{\mathbf{B}}\right]^{-1} \approx \bar{\mathbf{A}}^{-1} - \bar{\mathbf{A}}^{-1}\bar{\mathbf{B}}\bar{\mathbf{A}}^{-1}$, if $\left\|\bar{\mathbf{A}}\right\| \gg \left\|\bar{\mathbf{B}}\right\|$. Using (10) and (28), we have,

$$\bar{\mathbf{Z}}^{-}_{N-1,N} = \bar{\mathbf{I}} + \bar{\mathbf{z}}^{-}_{N-1,N}, \tag{31}$$

where $\bar{\mathbf{z}}^{-}_{N-1,N} = j\beta_0 d_N \bar{\mathbf{O}}_{N-1}\bar{\mathbf{O}}^T_N \bar{\Delta}_N \bar{\mathbf{O}}_N \bar{\mathbf{O}}^T_{N-1}$.

Submitting (31) into (7) yields:

$$\bar{\mathbf{R}}^{-}_{N-1,N} \approx \bar{\Gamma}_{N-1} + \left[\bar{\mathbf{Z}}^{-1}_{(N-1)0} + \bar{\mathbf{I}}\right]^{-1} \bar{\mathbf{z}}^{-}_{N-1,N} \bar{\mathbf{Z}}^{-1}_{(N-1)0} \left[\bar{\mathbf{I}} - \bar{\Gamma}_{N-1}\right]. \tag{32}$$

Following the steps from (30) to (32) recursively with the form:

$$\bar{\mathbf{Z}}^{-}_{n,n+1} = \bar{\mathbf{I}} + \bar{\mathbf{z}}^{-}_{n,n+1}, \tag{33}$$

$$\bar{\mathbf{z}}^{-}_{n,n+1} = j\beta_0 \bar{\mathbf{O}}_n \left[\sum_{m=n+1}^{N} d_m \bar{\mathbf{O}}^T_m \bar{\Delta}_m \bar{\mathbf{O}}_m\right] \bar{\mathbf{O}}^T_n. \tag{34}$$

Similar to the approximation to get (32), we have:

$$\bar{\mathbf{R}}^{-}_{n,n+1} \approx \bar{\Gamma}_n + \left[\bar{\mathbf{Z}}^{-1}_{n0} + \bar{\mathbf{I}}\right]^{-1} \bar{\mathbf{z}}^{-}_{n,n+1} \bar{\mathbf{Z}}^{-1}_{n0} \left[\bar{\mathbf{I}} - \bar{\Gamma}_n\right], \tag{35}$$

$$\bar{\mathbf{Z}}^{+}_{n-1,n} \approx \bar{\mathbf{I}} + j\beta_0 d_n \bar{\Delta}_n + \bar{\mathbf{z}}^{-}_{n,n+1} = \bar{\mathbf{I}} + \bar{\mathbf{z}}^{+}_{n-1,n}, \tag{36}$$

where

$$\bar{\mathbf{z}}^{+}_{n-1,n} = j\beta_0 \bar{\mathbf{O}}_n \left[\sum_{m=n}^{N} d_m \bar{\mathbf{O}}^T_m \bar{\Delta}_m \bar{\mathbf{O}}_m\right] \bar{\mathbf{O}}^T_n. \tag{37}$$

Submitting it to (10), we approximate $\bar{\mathbf{Z}}^{-}_{n-1,n}$ to the form similar to (34). Finally, we have:

$$\bar{\mathbf{Z}}^{-}_{0,1} \approx \bar{\mathbf{I}} + j\beta_0 \sum_{n=1}^{N} d_n \bar{\mathbf{O}}^T_n \bar{\Delta}_n \bar{\mathbf{O}}_n, \tag{38}$$

and the total reflection coefficient,

$$\bar{\mathbf{R}} = \bar{\mathbf{R}}^{-}_{0,1} \approx \frac{j\beta_0}{2} \sum_{n=1}^{N} d_n \bar{\mathbf{O}}^T_n \bar{\Delta}_n \bar{\mathbf{O}}_n. \tag{39}$$

The low frequency limit of the total transmission coefficient is found in a similar way as:

$$\bar{\mathbf{T}} \approx \bar{\mathbf{I}} - \frac{j\beta_0}{2} \sum_{n=1}^{N} d_n \bar{\mathbf{O}}^T_n \bar{\mathbf{s}}_n \bar{\mathbf{O}}_n, \tag{40}$$

where $\bar{\mathbf{s}}_n = \mathrm{diag}\left(\mu_{ny} + \varepsilon_{nx}, \mu_{nx} + \varepsilon_{ny}\right)$.

Applying the low frequency limit of the reflection and transmission matrices for equivalent layer and multiple layers to (25) and (26), we have effective parameters as:

$$\theta_{et} = \frac{1}{2}\tan^{-1}\frac{\sum_{n=1}^{N} d_n\left(\varepsilon_{nx} - \varepsilon_{ny} + \mu_{nx} - \mu_{ny}\right)\sin 2\theta_n}{\sum_{n=1}^{N} d_n\left(\varepsilon_{nx} - \varepsilon_{ny} + \mu_{nx} - \mu_{ny}\right)\cos 2\theta_n},$$
$$\theta_{er} = \frac{1}{2}\tan^{-1}\frac{\sum_{n=1}^{N} d_n\left(\varepsilon_{nx} - \varepsilon_{ny} - \mu_{nx} + \mu_{ny}\right)\sin 2\theta_n}{\sum_{n=1}^{N} d_n\left(\varepsilon_{nx} - \varepsilon_{ny} - \mu_{nx} + \mu_{ny}\right)\cos 2\theta_n}, \tag{41}$$

$$\Delta_{xe,ye} = \frac{1}{2d_t}\sum_{n=1}^{N} d_n\left[\Delta_{nx} + \Delta_{ny} \pm \left(\Delta_{nx} - \Delta_{ny}\right)\frac{\sin 2\theta_n}{\sin 2\theta_{er}}\right],$$
$$s_{xe,ye} = \frac{1}{2d_t}\sum_{n=1}^{N} d_n\left[s_{nx} + s_{ny} \pm \left(s_{nx} - s_{ny}\right)\frac{\sin 2\theta_n}{\sin 2\theta_{et}}\right], \tag{42}$$

where $d_t = \sum_{n=1}^{N} d_n$ and $\boldsymbol{\mu}, \boldsymbol{\varepsilon}$ can be achieved by:

$$\mu_{\tilde{p}e} = \frac{s_{pe} + \Delta_{pe}}{2}, \quad \varepsilon_{pe} = \frac{s_{pe} - \Delta_{pe}}{2}. \tag{43}$$

Here, although there are two kinds of expressions for the effective angle, the relative difference between them is small and is about 1% in difference at frequency up to 10 GHz.

If we consider about non-magnetic materials or $\boldsymbol{\mu}$ is scaler, (41)-(43) can be simplified as:

$$\theta_e = \theta_{er} = \theta_{et} = \frac{1}{2}\tan^{-1}\frac{\sum_{n=1}^{N} d_n\left(\varepsilon_{nx} - \varepsilon_{ny}\right)\sin 2\theta_n}{\sum_{n=1}^{N} d_n\left(\varepsilon_{nx} - \varepsilon_{ny}\right)\cos 2\theta_n}, \tag{44}$$

$$\varepsilon_{xe,ye} = \frac{1}{2d_t}\sum_{n=1}^{N} d_n\left[\varepsilon_{nx} + \varepsilon_{ny} \pm \left(\varepsilon_{nx} - \varepsilon_{ny}\right)\frac{\sin 2\theta_n}{\sin 2\theta_e}\right]. \tag{45}$$

If all layers are same but with different orientations, (41)-(43) can be further simplified as:

$$\theta_e = \theta_{er} = \theta_{et} = \frac{1}{2}\tan^{-1}\frac{\sum_{n=1}^{N} d_n \sin 2\theta_n}{\sum_{n=1}^{N} d_n \cos 2\theta_n}, \tag{46}$$

$$\varepsilon_{xe,ye} = \frac{1}{2}\left[\varepsilon_x + \varepsilon_y \pm \left(\varepsilon_x - \varepsilon_y\right)\frac{\sum_{n=1}^{N} d_n \sin 2\theta_n}{d_t \sin 2\theta_e}\right],$$
$$\mu_{xe,ye} = \frac{1}{2}\left[\mu_x + \mu_y \pm \left(\mu_x - \mu_y\right)\frac{\sum_{n=1}^{N} d_n \sin 2\theta_n}{d_t \sin 2\theta_e}\right], \tag{47}$$

which is the same as the result reported earlier in [7].

The *z*-component of the effective permittivity and permeability of the multilayered biaxial media can be found [6]:

$$\frac{1}{\varepsilon_{ze}} = \sum_{n=1}^{N} \frac{1}{\varepsilon_{nz}}\frac{d_n}{d_t}, \qquad \frac{1}{\mu_{ze}} = \sum_{n=1}^{N} \frac{1}{\mu_{nz}}\frac{d_n}{d_t}. \tag{48}$$

III. NUMERICAL RESULTS

In this section, we present numerical results showing the effective medium theory works well for multilayered anisotropic material with different orientations up to 10 GHz by comparing the parameters extracted without low frequency approximation with the ones with low frequency approximation.

The composite structure investigated is the four-layer non-magnetic medium. Figure 3 plots the real and imaginary parts of relative permittivity and permeability extracted from reflection and transmission coefficients with same thickness, same rotation angles and different relative permittivity (with same loss tangent in four layers) and permeability in *x* and *y* directions. Results

with and without the low frequency approximation are given. The frequency ranges from 10 MHz to 20 GHz. The real part of relative effective permeability is close to one (the relative permeability with low frequency limit is one in both x and y directions) and has nearly 1% difference at frequency up to 10 GHz. The effective permittivity also works up to 10 GHz. At low frequency range, the imaginary part of relative permeability is zero and imaginary part of relative permittivity is negative due to loss. When the frequency goes up, the relative permittivity and permeability would have imaginary parts with opposite signs, but the attenuation constant is still positive [11].

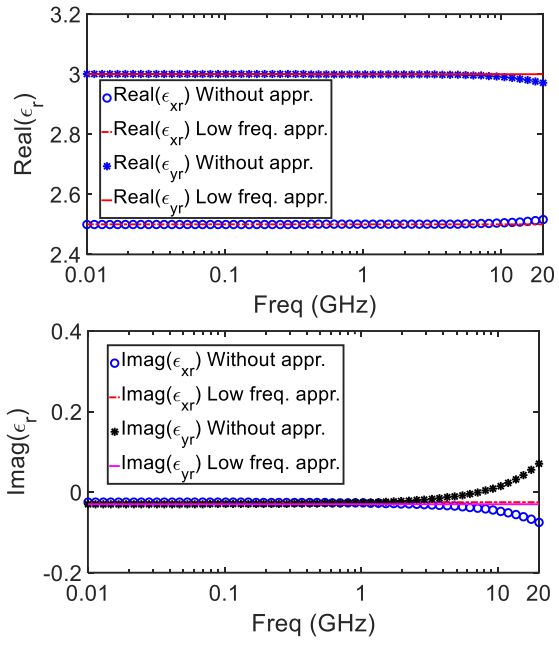

(a) Relative permittivity in x and y directions

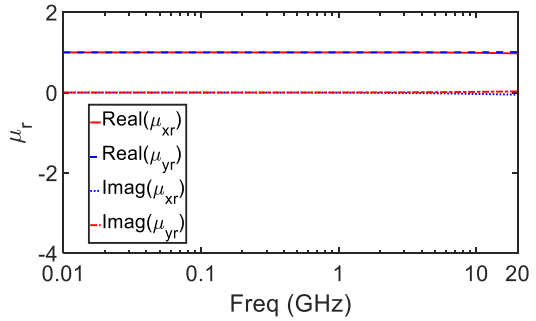

(b) Relative permeability in *x* and *y* directions

Fig. 3. Real and imaginary parts of relative permittivity and permeability of equivalent model with and without low frequency approximation for 4-layer biaxial non-magnetic media. $d_{1,2,3,4}=0.375$ mm, $\varepsilon_{x2,x4}=3(1-0.01j)$, $\varepsilon_{y1,y3}=4(1-0.01j)$, $\varepsilon_{x1,x3,y2,y4}=2(1-0.01j)$, $\theta_{1,2,3,4}=30°$, $\theta_e=30°$.

Figure 4 plots the real part of relative permittivity and permeability extracted from reflection and transmission coefficients with same thickness, different rotation angles and different relative permittivity and permeability in *x* and *y* directions. Again, there is a very good agreement for relative dielectric constants and effective angle between low frequency approximation and without it. The real part of relative effective permeability is almost one for frequency up to several GHz. Comparing without low frequency approximation the frequency independent model has a good agreement for frequency up to 10 GHz.

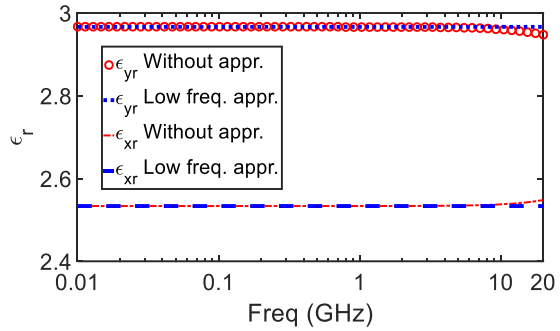

(a) Relative permittivity in x and y directions

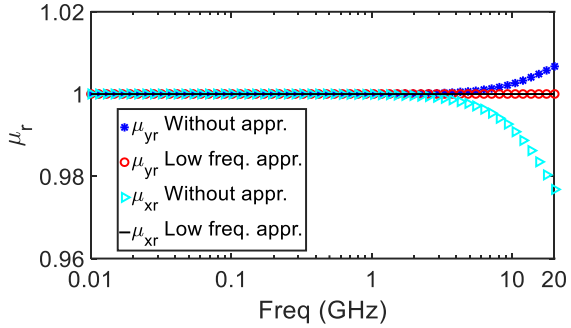

(b) Relative permeability in x and y directions

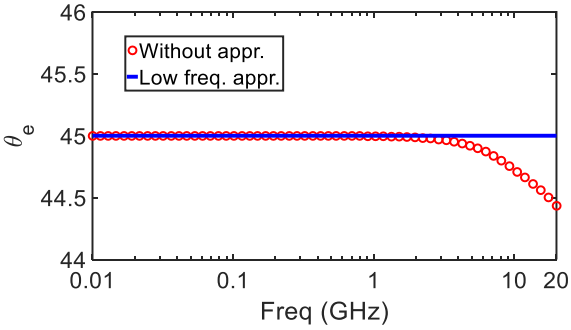

(c) Effective angle

Fig. 4. Real part of relative permittivity and permeability of equivalent model with and without low frequency approximation for different 4-layer biaxial non-magnetic media. $d_{1,2,3,4}=0.375$ mm, $\theta_{1,4}=30°$, $\theta_{2,3}=60°$, $\varepsilon_{x2,x4}=3$, $\varepsilon_{y1,y3}=4$, $\varepsilon_{x1,x3,y2,y4}=2$.

IV. CONCLUSION

We have presented the method to model the multilayered biaxial anisotropic material with different orientation using effective medium theory. By using this method, multilayered biaxial anisotropic media with different orientations can be numerically regarded as an effective medium. A frequency independent model is derived using the low frequency approximation. Numerical examples show the good agreements for effective parameters between with and without low frequency approximation for the frequency up to 10 GHz.

ACKNOWLEDGMENT

This work is supported in part by the NSF IUCRC Program of the Center for Nondestructive Evaluation at Iowa State University and by the China Scholarship Council.

REFERENCES

[1] L. A. Pilato and M. J. Michno, *Advanced Composite Materials*. Springer-Verlag, 1994.

[2] H. M. Flower, *High Performance Materials in Aerospace*. Chapman & Hall, 1995.

[3] H.-C. Chu, S.-K. Jeng, and C.-H. Chen, "Reflection and transmission characteristics of lossy periodic composite structures," *IEEE Trans. Antennas Propag*., vol. 44, no. 3, pp. 580-587, Mar. 1996.

[4] C. L. Holloway, M. S. Sarto, and M. Johansson, "Analyzing carbon-fiber composite materials with equivalent-layer models," *IEEE Trans. Electromagn. Compat*., vol. 47, no. 4, pp. 368-381, Aug. 2001.

[5] M. S. Sarto, S. Di Michele, and P. Leerkamp, "Electromagnetic performance of innovative light-weight shields to reduce radiated emissions from PCBs," *IEEE Trans. Electromagn. Compat*., vol. 44, no. 2, pp. 353-363, May 2002.

[6] F. G. Hu, J. M. Song, and T. Kamgaing, "Modeling of multilayered media using effective medium theory," *IEEE Electrical Performance of Electronic Packaging and Systems*, pp. 225-228, Oct. 2010.

[7] Y. Bao and J. M. Song, "Modeling of multilayered anisotropic media using effective medium theory," *IEEE Antennas and Propagation International Symposium*, Paper WEP-A4. 2P. 2, pp. 2097-2098, Fajardo, PR, June 2016.

[8] W. C. Chew, *Waves and Fields in Inhomogeneous Media*. IEEE Press, pp. 133-140, 1995.

[9] D. R. Smith, S. Schultz, P. Marko, and C. M. Soukoulis, "Determination of effective permittivity and permeability of metamaterials from reflection and transmission coefficients," *Phys. Rev. B*, vol. 65, 195104, Apr. 2002.

[10] X. D. Chen, T. M. Grzegorczyk, B. I. Wu, J. Pacheco, and J. A. Kong, "Robust method to retrieve the constitutive effective parameters of metamaterials," *Phys. Rev. E*, vol. 70, 016608, 2004.

[11] J. Wang, T. Zhao, J. Song, and K. Telesphor, "Modeling of multilayered media for oblique incidence using effective medium theory," *Annual Review of Progress in Applied Computational Electromagnetics*, Columbus, OH, pp. 812-817, Apr. 2012.

[12] S. Arslanagic, T. V. Hansen, N. A. Mortensen, A. H. Gregersen, O. Sigmund, R. W. Ziolkowski, and O. Breinbjerg, "A review of the scattering-parameter extraction method with clarification of ambiguity issues in relation to metamaterial homogenization," *IEEE Antennas Propag. Mag*., vol. 55, no. 2, pp. 91-106, Apr. 2013.

[13] T. Zhao, J. Song, and T. Kamgaing, "IE based approach to determine the effective constitutive parameters of periodic structure using microstrip measurement," *2016 IEEE International Workshop on Electromagnetics: Applications and Student Innovation Competition (iWEM)*, Nanjing, China, pp. 1-3, May 2016.

Yang Bao was born in Nanjing, Jiangsu, China. He received the B.S. and M.S. degrees in Nanjing University of Posts and Telecommunications in 2011 and 2014, respectively. He is currently working toward his Ph.D. in Department of Electrical and Computer Engineering in Iowa State University. His research interests focus on modeling and simulations of composite material, electromagnetic wave scattering using fast algorithms and eddy current nondestructive evaluation.

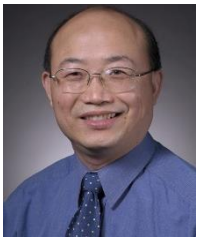

Jiming Song received the B.S. and M.S. degrees in Physics from Nanjing University, China, in 1983 and 1988, respectively, and the Ph.D. degree in Electrical Engineering from Michigan State University, East Lansing, in 1993.

From 1993 to 2000, he worked as a Postdoctoral Research Associate, a Research Scientist and Visiting Assistant Professor at the University of Illinois at Urbana-Champaign. From 1996 to 2000, he worked part-time as a Research Scientist at SAIC-DEMACO. Song was the principal author of the Fast Illinois Solver Code (FISC). He was a Principal Staff Engineer/Scientist at Semiconductor Products Sector of Motorola in Tempe, Arizona before he joined Department

of Electrical and Computer Engineering at Iowa State University as an Assistant Professor in 2002.

Song currently is a Professor at Iowa State University's Department of Electrical and Computer Engineering. His research has dealt with modeling and simulations of interconnects on lossy silicon and RF components, electromagnetic wave scattering using fast algorithms, the wave propagation in metamaterials, acoustic and elastic wave propagation and non-destructive evaluation, and transient electromagnetic field. He was selected as a National Research Council/ Air Force Summer Faculty Fellow in 2004 and 2005 and received the NSF Career Award in 2006. Song is an IEEE Fellow, an Associate Editor for *IEEE Antennas and Wireless Propagation Letters* (AWPL) and *ACES Express*.

Effects of Room Dimensions on the Frequency Response of Indoor Wave Propagation

Hany M. El-Maghrabi [1], Ahmed M. Attiya [2], and Essam A. Hashish [3]

[1] Department of Electromechanical
Housing and National Research Center, Cairo, Egypt
helmaghrabi@hbrc.edu.eg

[2] Department of Microwave Engineering
Electronic Research Institute, Cairo, Egypt
attiya@eri.sci.eg

[3] Department of Electronics and Electrical Communication
Cairo University, Cairo, Egypt
essamhh@ieee.org

Abstract ─ In analogy with room acoustics, various aspects of microwave propagation in a room are treated. This paper presents the effect of the room dimensions on the frequency response of a propagating wave inside rooms. It is found by simulation and measurements that room dimensions affect the propagating waves in the rooms and degenerated bands can appear. In critical environments this may cause unwanted coloration effects, which decrease the signal quality. Appropriate choice of room dimensions may reduce the coloration effects of modes. A numerical optimization technique implemented in FEKO software package is used for finding the optimum room dimensions as to achieve the flattest possible frequency response. The effect of the room dimensions on wave propagating in corridors is presented. It is found that the room length has more effects on the frequency response of the signal than the room width for signals excited and transmitted in corridors.

Index Terms ─ Indoor wave propagation, numerical optimization, optimum room dimensions.

I. INTRODUCTION

With reference to room acoustics, a lot of attention has been drawn to modes in rooms which often lead to extended sound decays and uneven frequency responses [1-3]. In critical listening spaces, this causes unwanted coloration effects that can decrease the sound quality. The problem arises at low frequencies because of the relatively low modal density. Many designers try to overcome the problems of modes coloration by choosing an appropriate room dimensions and by the use of bass absorbers [1], [4-5]. As per literature, it is shown that there is a close resemblance between room acoustics and room electromagnetics [6-8], since the wavelengths are nearly of the same order for acoustic audio frequencies and part of microwave frequencies, namely in the centimeter range. As room dimensions are much larger than the wavelength, ray-tracing techniques can be used to predict with sufficient precision the radio coverage for large buildings containing a large number of walls between the transmitter and receiver [9-12]. Most indoor studies focus on the coverage and delay spread problems not on the frequency response of the signal. A stochastic approach for indoor diffuse scattering is described in [13] based on path loss distributions. Extracting diffuse scattering from measurements is discussed in [14], and ultra-wideband diffuse scattering is measured in several rooms [15]. The power delay profile was calculated based on averaging plane wave reflection coefficients of smooth surfaces [16]. It is found that the previous work didn't take into consideration the frequency response of the propagating microwave signal inside rooms and the effect of the room dimensions on the signal frequency response which is one of the main objectives of the presented paper. A similar approach as in the present paper was used in [1], while in the former paper the analysis is done is in the acoustics band and in the presented paper the analysis is done in the electromagnetic band. Normally, with room limited connectivity it is not expected to find signal resonance in the electromagnetic band while the paper introduced that this can happen with different room dimensions.

The simulation is done using computational electromagnetic software FEKO [24] based on Ray Launching Geometrical Optics (RL-GO) method. The concept of RL-GO modeling is based on the fact that at

Submitted On: June 29, 2016
Accepted On: March 28, 2017

high frequencies electromagnetic waves are like rays which travel in straight lines provided that the permittivity of the medium is homogeneous [17]. Geometrical Optics (GO) [18] approximates the field strength at any point as the sum of the field associated with the direct ray from the transmitter to the receiver, plus the field of rays reflected from surfaces. Discontinuities occur when reflection points move off the edges of reflecting surfaces. Geometrical Theory of Diffraction (GTD) and its uniform extension, Uniform Theory of Diffraction (UTD) include rays diffracted from edges, which smooth such discontinuities [19-22].

FEKO's RL-GO [24] method is a ray-based technique that models objects based on optical propagation, reflection and refraction theory [21-23], [25]. Ray-interactions with metallic and dielectric structures are modelled using Huygens sources, placed at each ray, contact point on material boundaries. The ray-launching process is easily controlled, based on the angular spacing (for localized sources) or transverse spacing (for plane wave sources) of the rays and the number of multiple interactions allowed. The simulation is done for 3D analysis for all presented examples.

In order to gain the most benefit from the computational hardware, in FEKO all the solution phases for RL-GO technique have been parallelized, the near- and far-field calculations and also seemingly simple things such as power loss computations. The efficiency of the parallel implementation in FEKO is in the order of 80% to 95%, depending on the problem and the solution phase etc. This means that for a system with 32 cores the run-time would be approximately 26 times (0.8*32) faster than on a sequential run. FEKO also allow the specification of planes of symmetry that may be used to accelerate the simulation and reduce the memory requirements for the solution of a problem.

The purpose of this paper is to demonstrate the applicability of methods applied in room acoustics to microwave propagation in a room and corridors. The paper focuses on the choice of room dimensions to minimize the coloration effects of modes in different bands. It discusses the effect of the room dimensions on signal excited and transmitted in rooms as to avoid any signal resonance which can decrease the signal quality. On the other hand, the authors studied the room dimension effects on signal excited and transmitted in corridors as most of the wireless access points are installed in corridors especially in buildings designed with big corridors as commercial buildings, hospitals and hotels. A Simplex numerical optimization technique implemented in FEKO is used to achieve the flattest possible frequency response. The room dimensions effects on the signal transmitted in indoor corridors are discussed in Sec. 3. Finally, experimental results are conducted in order to verify the presented theory.

II. SIGNAL FREQUNCY RESPONSE INSIDE ROOMS

In acoustics, the room relative dimensions of length, width, and height are acoustical sensitive [1-2]. If plans are being made for constructing such a room, there are usually ideas on floor-space requirements. The literature is full of early quasi-scientific guesses [2-4], and later statistical analyses of room proportions give good mode distribution in the acoustics band. The same problem is studied in the proposed paper while for the microwave band and it is found by simulation and measurements that the dimensions of the room including the length, width, and height are also electromagnetic sensitive and the frequency response of the signal excited inside rooms is sensitive to these dimensions. Consequently, the method for choosing these dimensions is based on a better prediction model based on the proposed ray launching technique.

The modal response of the signal inside room is defined as the frequency spectrum received by an omni-directional antenna in a corner of the room, when the room is excited by a short dipole with a flat power spectrum placed in the opposite corner as shown in Fig. 1. Using FEKO simulation RL-GO method for 3D analysis, the simulation frequency response of the signal in the presented room layout is shown in Fig. 2, where the room with width, length and height of 5 m, 4.5 m and 3 m, respectively. The room walls permittivity and conductivity are 3 and 0.01 s/m [26], respectively which is corresponding to brick walls. The simulation is done for frequency range of 0.9-2 GHz. The transmitter and receiver is located at 1.5 m from the ground. It can be noted from figure 2 that the modes inside the room at 1.2 GHz are highly degenerated and dark zone can appear in this band which can affect any application running in such band.

Fig. 1. Room layout (top view).

A numerical optimization technique is used to find the best room dimensions as discussed in [1]. The technique is Simplex (Nealer-Med) method which is implemented in FEKO [24]. The Simplex (Nelder-Mead) algorithm can be categorized as a local or hill-climbing search method, where the final optimum relies strongly on the specified starting point. The maximum and minimum values for the length, width and height are

defined and the dimensions are optimized according to these limits. The analysis is based on calculating the signal modal response for different dimensions within defined limits. Then by comparing the obtained responses it would be possible to determine the ideal response which is judged as the flattest signal response. While it may take time for to complete the optimization process due to big dimensions and high operating frequency, using the parallelization of FEKO can dramatically accelerate the performance.

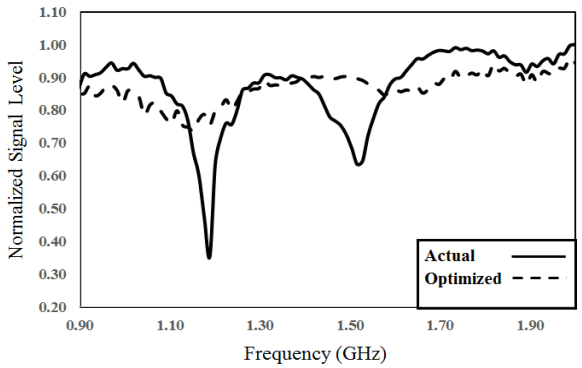

Fig. 2. Modal response of the signal inside room.

The optimization method is applied using FEKO's Simplex (Nealer-Med) method for the above example as shown in Fig. 2. The obtained optimized frequency response is found at a room of width is 4.8 m and length is 4.2 m while the height is 3 m. It can be noted from this result that the frequency response of the signal inside the room with optimized dimensions is better and flatter than the case of original dimensions.

The door effect is simulated for the above room with optimized dimensions. Figure 3 shows the optimized room frequency response with door and without door cases. It can be noted that the door has small effect on the frequency response with optimized dimensions where the door is located on the room side wall with width is 0.9 m and height is 2.1 m as shown in Fig. 4.

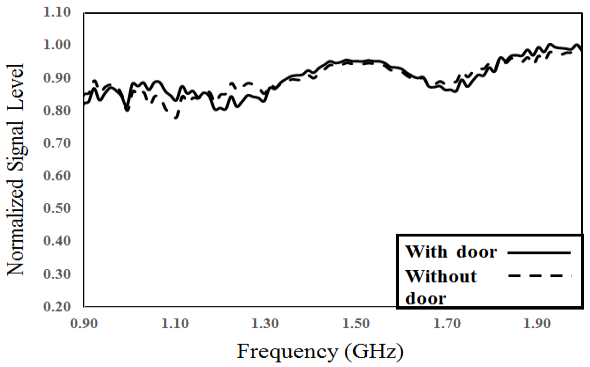

Fig. 3. Door effects on the modal response of the room with optimized dimensions.

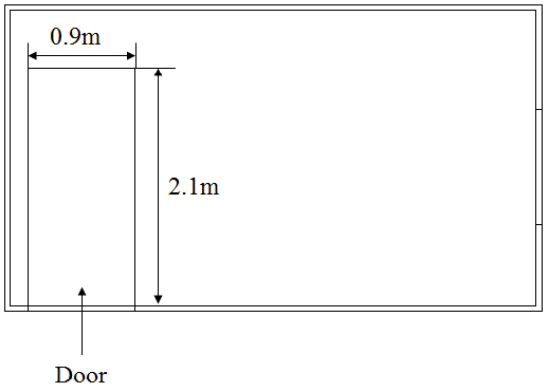

Fig. 4. Room layout with door location (side view).

On the other hand, the modal response is calculated for the same setup but with two different walls materials, Brick with permittivity 3.73 and conductivity 0.462 and Wallboard with permittivity 2.4 and conductivity 0.09 as shown in Fig. 5. It can be noted there is only slight difference in the frequency response for the two materials in the case of the optimized room dimensions.

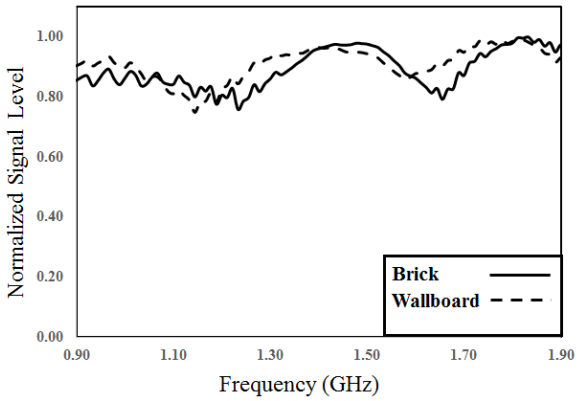

Fig. 5. Walls different materials effects on the modal response of the room with optimized dimensions.

III. ROOM DIMENSIONS EFFECTS ON SIGNAL IN CORRIDOR

The room dimensions can also affect the frequency response and lead to high order modes generation of excited and transmitted signals in indoor corridor with sided rooms like hotels and business buildings. Figure 6 shows the layout structure of two sided rooms in a long corridor section. The room and corridor walls permittivity and conductivity are 3 and 0.01 s/m, respectively [26]. The electric filed is calculated along the corridor due to transmitter in the front of the corridor section. The room length and width are changed for two cases and the fields are calculated for each case. The first case the room length is changed while the width is kept constant, where the length is changed from 2.5 m to 10 m and the width

is 4.5 m. The height for both the room and the corridor is 3.9 m and the operating frequency is 0.9 GHz. The source is a vertically polarized dipole at y direction at z=0.5 m, $y_{source} = 1.95\ m$ above the ground and x_{source} at the middle of the corridor, the electric field is calculated at the center line of the corridor at height of 2.25 m.

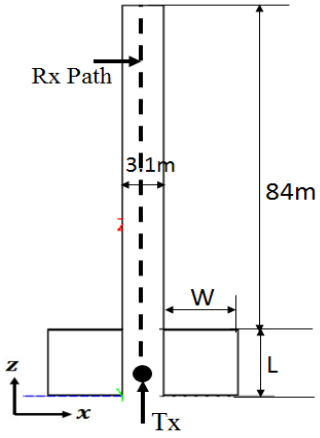

Fig. 6. Long corridor with two sided room layout.

FEKO's RL-GO method is used to calculate the electric field in the corridors using 3D model. The normalized electric field across the center line of the corridor is shown in Fig. 7 for different room lengths, while the frequency response is calculated using Fast Fourier Transform (FFT) as shown in Fig. 8. It can be noted that higher room length, the more high order modes generated and can be detrimental to the signal quality. The choice to calculate the electric field in the center line of the corridor, along x-axis, is to ensure same effect from rooms on both sides by keeping same distance between Rx path and each room side, also in most of indoor wireless designs the transmitter is kept in the corridor center for signal broadcasting equally on both room sides.

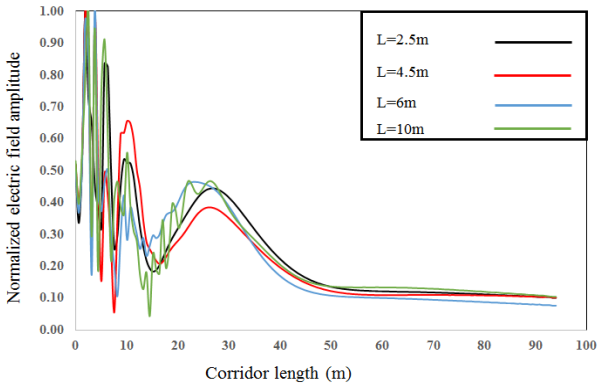

Fig. 7. Normalized electric field distribution at the corridor center with different room lengths.

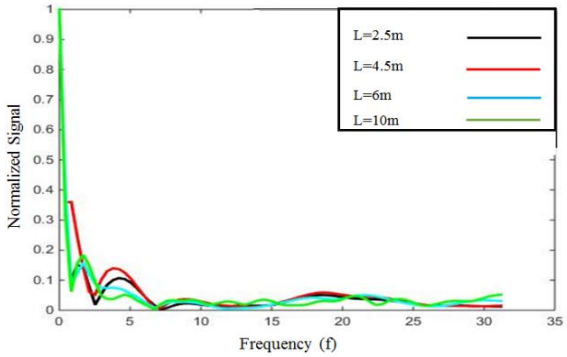

Fig. 8. Frequency response using FFT of electric field distribution at the corridor center with different room lengths.

On the other hand, the same analysis is repeated with changing the width of the room while the length is kept constant. The normalized electric field across the center line of the corridor is shown in Fig. 9 for different room widths, while the FFT for the signal is shown in Fig. 10. It can be noted that changing the room width has lower effect on the signal propagated in corridor.

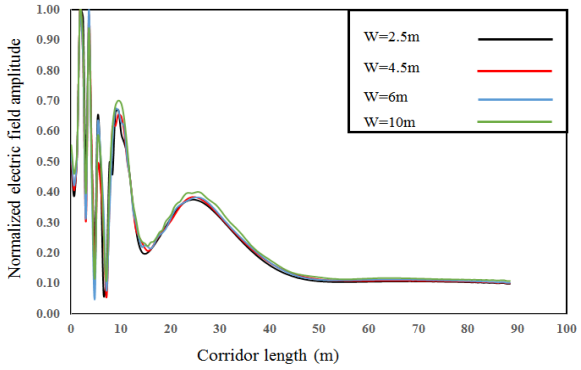

Fig. 9. Normalized electric field distribution at the corridor center for different room widths.

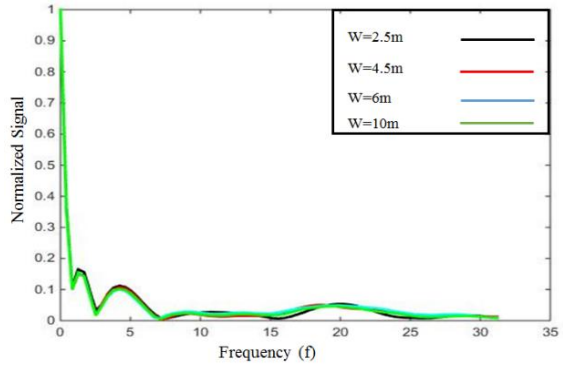

Fig. 10. Frequency response using FFT of electric field distribution at the corridor center for different room widths.

IV. MEASUREMENTS

In this section sample results are presented to verify the accuracy of the present approach for the signal propagated inside room and to verify the accuracy FEKO simulation model. The proposed measurements is used to study the simple wave propagating inside rooms in indoor residential building.

This simple scenario of a room is verified experimentally at frequency range 0.5-1.4 GHz. The scenario was done in room inside residential building with brick walls. The experimental setup consists of two wooden carts. One cart is used to hold the transmitter and the other one is used to hold the receiving antenna and computer for receiving data collection and analysis as shown in Fig. 11. Handheld RF Signal Generator (RFEGEN 1.12) with dipole antenna with gain of 2.2 dBi is used as transmitter while the receiver is RF Viewer wireless USB dongle and data is collected using computer software package RF spectrum analyzer (TOUCHSTONE PRO). The transmitting and receiving antennas are kept vertically polarized. The measurements were taken with the transmitter is located at one corner of the room while the receiver on the other corner of the room as shown in Fig. 12. The room dimensions are highlighted in Fig. 12. The height of the room is 2.7 m. The height of both transmitting and receiving antennas is kept 60 cm above the ground. Figure 13 shows a comparison between the measured received power in dBm and calculated power by FEKO RL-GO method. Good agreement between the measured and calculated power is obtained. The slight differences can be explained due to errors in the manual positioning of the receiving antenna and differences due to the boundary conditions of the actual room. The calculated error between the model and measured results is about 11.3%. It can be noted that the room has degenerated band at 1.2 GHz which can decrease the signal quality in this band and affect any running application in this band. Electromagnetic signal resonance due to room dimensions should be checked by room designers especially for buildings designed with big corridors as commercial buildings, hospitals and hotels to avoid probability of resonance in critical bands as GSM, WIFI which can cause service outage and single degradation

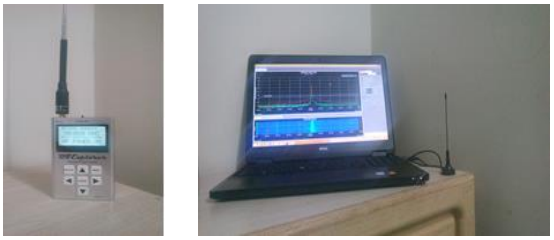

(a) (b)

Fig. 11. Measurement setup: (a) transmitter and (b) receiver.

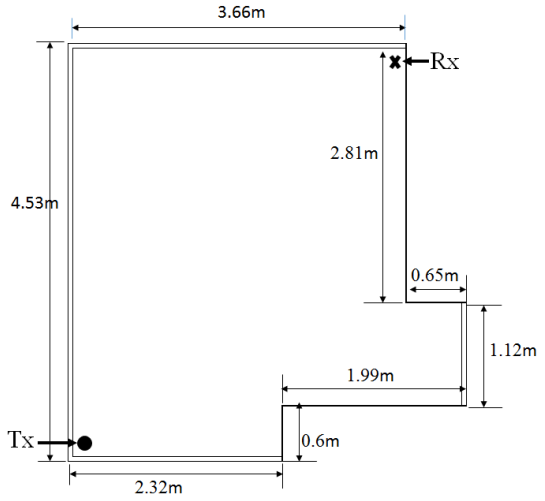

Fig. 12. Room layout.

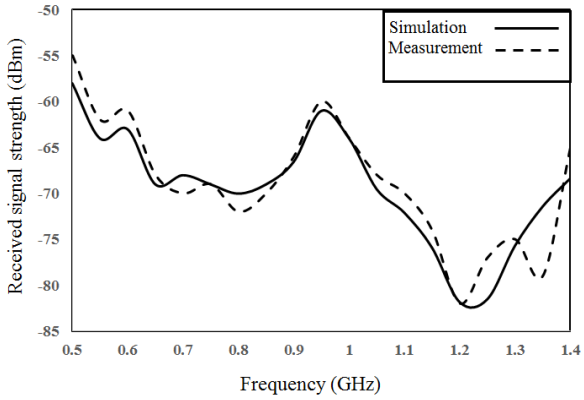

Fig. 13. Received power (dBm) at the room corner.

V. CONCLUSION

The effect of the room dimensions on the frequency response of a propagating wave inside rooms and long corridors is presented. It is shown that the electromagnetic propagation inside rooms is sensitive to the room dimensions. Degenerated modes can appear with variety of room dimensions. An optimization procedure is used for choosing the best room dimensions with maximum flatten modal response. It is found by simulation that the room length has a greater effect on the signal frequency response which is excited and transmitted in corridors than the room width. This can lead to generate of high order modes which can decrease the signal quality. The concept helps the designers to avoid signal resonance due room dimensions. Finally, measurements are introduced to verify the proposed idea for the effect of the room dimension on the signal quality.

REFERENCES

[1] T. Cox and P. D'Antonio, "Determining optimum room dimensions for critical listening environments:

A new methodology," *AES Convention*, paper no. 5353, May 2001.

[2] Y. Tang, M. Cooke, B. Fazenda, and T. Cox, "A glimpse-based approach for predicting binaural intelligibility with single and multiple maskers in anechoic conditions," INTERSPEECH, 2015.

[3] C. L. S. Gilford, "The acoustic design of talk studios and listening rooms," *J. Audio. Eng. Soc.*, no. 27, pp. 17-31, 1979.

[4] M. Louden, "Dimension ratios of rectangular rooms with good distribution of eigentones," *Acustica*, no. 24, pp.101-104, 1971.

[5] R. Walker, "Optimum Dimension Ratios for Small Rooms," Preprint 4191, *Convention of the AES*, 5/1996.

[6] J. Andersen, J. Nielsen, G. Pedersen, G. Bauch, and J. Herdin, "Room electromagnetics," *IEEE Antennas and Propagation Magazine*, pp. 27-33, April 2007.

[7] J. Andersen, K. Chee, M. Jacob, G. Pedersen, and T. Kürner, "Room electromagnetics applied to an aircraft cabin with passengers," *IEEE Transactions on Antennas and Propagation*, pp. 2472-2480, 2012.

[8] G. Steinböck, T. Pedersen, B. H. Fleury, W. Wang, and R. Raulefs, "Experimental validation of the reverberation effect in room electromagnetics," *IEEE Transactions on Antennas and Propagation*, pp. 2041-2053, 2015.

[9] S. Sidhu, A. Khosla, and A. Sharma, "Implementation of 3-D ray tracing propagation model for indoor wireless communication," *International Journal of Electronics Engineering*, vol. 4, no. 1, pp. 43-47, 2012.

[10] T. Sarkar, J. Zhong, K. Kim, A. Medouri, and M. Salazar-Palma, "A survey of various propagation models for mobile communication," *IEEE Antennas and Propagation Magazine*, vol. 45, no. 3, pp. 51-82, June 2003.

[11] C. Trueman, D. Davis, B. Segal, and W. Muneer, "Validation of fast site-specific mean-value models for indoor propagation," *ACES Journal: Applied Computational Electromagnetics Society*, vol. 24, no. 3, pp. 312-323, June 2009.

[12] J. McKown and R. Hamilton, "Ray tracing as a design tool for radio networks," .*IEEE Network*, vol. 6, pp. 27-30, November 1991.

[13] D. Ullmo and H. Baranger, "Wireless propagation in buildings: A statistical scattering approach," *IEEE Trans. on Vehicular Technology*, vol. 48, no. 3, pp. 947-955, May 1999.

[14] A. Richter and R. Thomä, "Joint maximum likelyhood estimation of specular paths and distributed diffuse scattering," *Proc. IEEE Vehicular Technology Conference*, Sweden, vol. 1, pp. 11-15, May 2005.

[15] J. Kunisch and J. Pamp, "Measurement results and modeling aspects for the UWB radio channel," *Proc. IEEE Conference on Ultra Wideband Systems and Technologies*, pp. 19-23, May 2002.

[16] C. L. Holloway, M. C. Cotton, and P. McKenna, "A model for predicting the power delay profile characteristics inside a room," *IEEE Transactions on Vehicular Technology*, vol. 48, no. 4, pp. 1110-1120W, July 1999.

[17] W. K. Tam and V. N. Tran, "Propagation modeling for indoor wireless communication," Electronics & *Communication Engineering Journal*, pp. 221-228, October 1995.

[18] K. Morris, "*Electromagnetic theory and geometrical optics*," New York: Courant Institute of Mathematical Sciences, New York University, 1962.

[19] C. A. Balanis, *Advanced Engineering Electromagnetics*. 2nd edition, Wiley, 2012.

[20] D. Derek A. McNamara, C. W. Carl, W. I. Pistorius, and J. A. G. Malherbe, *Introduction to The Uniform Geometrical Theory of Diffraction*. Artech House, 1990.

[21] J. B. Keller, "Geometrical theory of diffraction," *J. Opt. Soc. Amer*., vol. 52, pp. 116-130, February 1962.

[22] R. Akl, D. Tummala, and X. Li, "Indoor propagation modeling at 2.4 GHz for IEEE 802.11 networks," *The Six IASTED International Muti-Conference on Wireless and Optical Communication*, Banff, AB, Canada, July 3-5, 2006.

[23] R. G. Vaughan and J. Bach Andersen, "*Channels, Propagation and Antennas for Mobile Communications*," The Institution of Engineering and Technology, 2003.

[24] FEKO Suite 7.0, Altair Engineering, 2014.

[25] L. Azpilicueta, M. Rawat, K. Rawat, F. Ghannouchi, and F. Falcone, "Convergence analysis in deterministic 3D Ray launching radio channel estimation in complex environments," ACES Journal, vol. 29, no. 4, April 2014.

[26] J. Leung, "Hybrid Waveguide Theory-Based Modeling of Indoor Wireless Propagation," M.Sc. Dissertation, Department of Electrical and Computer Engineering, University of Toronto, 2009.

Hany M. El-Maghrabi received the B.Sc. degree, with Honor Degree, M.Sc. and Ph.D. degrees in Electrical Engineering from the Cairo University (Egypt). El-Maghrabi has got a position of Research Assistant in Housing and Building National Research Center (HBNRC), Institute of Electromechanical, Department of Communication (Egypt). He became Researcher at HBNRC at 2017. He has co-authored technical journal article and conference papers. El-Maghrabi has an experience in electromagnetics, antennas, microstrip structures, numerical methods, wave propgation and their applications in microwave. El-Maghrabi was awarded The Best Paper in NRSC 2015.

Ahmed M. Attiya M.Sc. and Ph.D. Electronics and Electrical Communications, Faculty of Engineering, Cairo University at 1996 and 2001 respectively. He joined Electronics Research Institute as a Researcher assistant at 1991. In the period from 2002 to 2004 he was a Postdoc in Bradley Department of Electrical and Computer Engineering at Virginia Tech. In the period from 2004 to 2005 he was a Visiting Scholar in Electrical Engineering Dept. in University of Mississippi. In the period from 2008 to 2012 he was a Visiting Teaching Member in King Saud University. He is currently Full Professor and the Head of Microwave Engineering Dept. in Electronics Research Institute. He is also the Director of Nanotechnology Lab. in Electronics Research Institute.

Essam A. Hashish (M'96) received the B.Sc., M.Sc., and Ph.D. degrees from the Electronics and Communications Department, Faculty of Engineering, Cairo University, Giza, Egypt, in 1973, 1977, and 1985, respectively. He is currently a Professor with the Electromagnetics Group at the same department. His main interest is electromagnetic remote sensing, wave propagation, and microwave antennas.

SIW Rotman Lens with Planar Slot Array Antenna at Ku-band

S. A. Hosseini, Z. H. Firouzeh, and M. Maddahali

Dept. of Electrical and Computer Engineering
Isfahan University of Technology, Isfahan, 8415683111, Iran
Alireza.hosseini@ec.iut.ac.ir, Zhfirouzeh@cc.iut.ac.ir, Maddahali@cc.iut.ac.ir

Abstract ─ A multi-beam antenna, which is the combination of a Rotman lens and a planar slot array antenna, is designed in this paper. The lens and the slot array are designed for 15.5 to 16.5 GHz frequency range and implemented in the same substrate using SIW structure. The Rotman lens with 7 input ports and 7 output ports are connected to a planar slotted array antenna with 7 waveguides. This multi-beam antenna consists of seven beams at angles of 0°, ±10°, ±20° and ±30° symmetrically. This antenna is designed for terrestrial and satellite applications, where the low cost, low profile and light multi-beam antennas are needed. Simulated and measured results show that the amplitude and phase distributions and scattering parameters of the antenna are in good agreement. In addition, the SLL, HPBW, main beam direction and cross polarization levels of all the radiation patterns are desirable.

Index Terms ─ Beam steering, Rotman lens, slot array antenna, Substrate Integrated Waveguide (SIW).

I. INTRODUCTION

Multi-beam antennas are used to produce several independent beams at different angles simultaneously or individually. Such antennas are widely used in terrestrial communications, including wireless, MIMO, direction finding, and in satellite communications such as MSS and BSS services [1]. Beamforming that accomplished using an array antenna and a beamforming network (BFN) is one way to realize multiple beams. Beamforming can be implemented by analog [2] and digital methods [3].

In analog BFNs the phase and amplitude distribution of array is controlled by a network of power dividers and phase shifters or transmission lines. There is no need to employ microprocessors and processing algorithms in analog BFNs; therefore these beamformers are simpler, cheaper and lighter than digital types, and are more suitable for some terrestrial and satellite applications. Butler matrix and microwave lenses [2] are some examples of analog BFNs. Rotman lens [4] is the best and most popular lens among microwave lenses, because of its simplicity, compactness, true time delay characteristic and ability of attaching to the linear arrays.

Rotman lens that invented first by Rotman and Turner [4], is a multi-input multi-output network and as can be seen in Fig.1, all of its ports are connected to a parallel plate region. By connecting the output ports of Rotman lens to the array element through transmission lines, a multibeam antenna is realized. In this antenna, by exciting each input port, a particular amplitude and phase distribution is created on array elements which led to the creation of a beam at a specific angle of space. Rotman lens has the superposition property, so each beam can be individually turned on or off.

Substrate Integrated Waveguide (SIW) Rotman lens is a new type of lenses that has been developed in recent years [5, 6], and compared with other types of Rotman lenses, a little works have been devoted to it. This lens has desirable features of microstrip [7] and waveguide lenses [8] simultaneously, and can be integrated with some kind of widely used arrays such as SIW slot array antenna. Thus, the purpose of this paper is to provide a Rotman lens with a slot array antenna based on SIW structure. It should be noted that the design equations vary based on the type of Rotman lens such as microstrip, waveguide, SIW and so on. The design methods and equations of SIW Rotman lens have been reported in [5, 9].

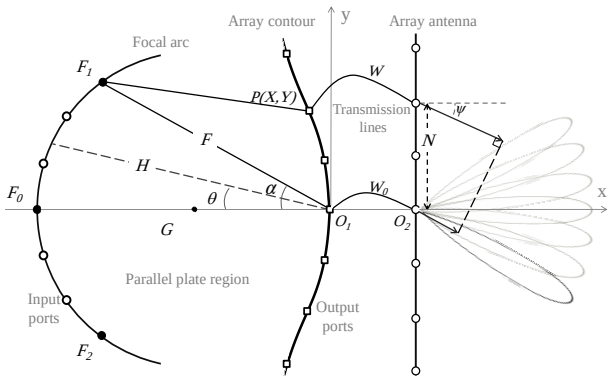

Fig. 1. Schematic of Rotman lens antenna and its parameters.

Submitted On: October 24, 2016
Accepted On: April 8, 2017

This paper is organized as follows. In Section 2, a basic overview of the Rotman lens design considerations is presented, and then it is discussed how to design the SIW Rotman lens, specifically. Also, an approach is explained to improve performance of the proposed SIW lens and the simulation results are represented. Section 3 deals with introducing the slot array antenna on SIW and designing a planar slot array for connecting to the Rotman lens. Simulation and measurement results of the Rotman lens in conjunction with the slot array antenna are shown and compared in Section 4. It is shown that the reflection coefficient of input ports, mutual coupling between them and all of the output patterns are appropriate in the whole frequency range.

II. ROTMAN LENS DESIGN

A. Rotman overview

As shown in Fig. 1, Rotman lens has two arcs that are called "focal arc" and "array contour". The points of array contour are defined by $P(X,Y)$ and connected to the array elements by lines with the length of W. Determining the number of array elements (NE) and the distance between them (d), considering the required scan angle, desired beamwidth and array element type, is the first step in lens designing. In second stage, some of the initial parameters of lens including ε_r of the substrate, focal angle (α), beam angle corresponding to off axis focal point (ψ_α) and off axis to on axis focal length ($G/F=g$) must be determined. The third step is calculation of normalized location of output ports of lens (x,y) and normalized length of transmission lines (w) by using design equations of Rotman and Turner's paper [4]. According to this paper, (x,y) coordinates and (w) length, are calculated from the following equations:

$$x = \frac{-1}{(g-a)}\left((g-1)w + 0.5\eta^2 b_1^2\right), \tag{1}$$

$$y = \frac{b_1}{b_0}\eta(1-w), \tag{2}$$

$$aw^2 + bw + c = 0. \tag{3}$$

Where, $\eta = N/F$ is the normalized coordinate of array elements relating to origin O_2, and a, b and c are determined from [4]. In design equations, all dimensions are normalized to off axis focal length (F), therefore all calculated parameters must be multiplied in F finally. The minimum amount of F is calculated from Equation (4).

$$F_{\min} = \frac{1}{\sqrt{\varepsilon_r}}\frac{N_{\max}}{\eta_{\max}} = \frac{1}{\sqrt{\varepsilon_r}}\frac{(NE-1)d}{2\eta_{\max}}. \tag{4}$$

According to Equation (4), $\eta_{\max}$ must be chosen so that an appropriate value achieved for F, a large amount for F, enlarge the size of lens and increase the spillover and dielectric losses; on the other hand, according to Equation (5), the large amount of $\eta_{\max}$ enhances the aperture phase error. Thus, a trade off must be taken between them:

$$\Delta l = \frac{\Delta L}{F} = \left(h^2 + x^2 + y^2 + 2hx\cos\theta - 2hy\sin\theta\right)^{1/2} - h + w + \eta\sin\psi. \tag{5}$$

h, θ and ψ are shown in Fig. 1.

B. Implementing SIW Rotman lens

Before starting the SIW Rotman lens design, substrate integrated waveguide which is used as input and output ports and transmission lines should be designed at operating frequency. The SIW is in fact the fabrication of a metallic waveguide in the planar form. So, the SIW can be modeled with an equivalent dielectric filled waveguide [10]. The width of SIW (a_s), for particular cutoff frequency is calculated from equation (6), in which the a_d is the width of equivalent waveguide with the same cutoff frequency, d is the diameter of via holes and p is the center to center distance of them:

$$a_d = a_s - 1.08\frac{d^2}{p} + 0.1\frac{d^2}{a_s}. \tag{6}$$

The proposed Rotman lens will operate at center frequency of 16 GHz and has 1 GHz bandwidth. Therefore to achieve appropriate dispersion characteristic in the entire band the width of equivalent waveguide is obtained a_d=8.5 mm. d and p are chosen 0.5 mm and 0.8 mm, therefore the width of SIW can be calculated from Equation (6); i.e., a_s=8.8 mm.

Rotman lens design is started with selecting an appropriate substrate. In this project, Rotman lens is fabricated on Rogers RT/duroid 5880 substrate with ε_r=2.2 and 0.787 mm thickness. Based on the previous section, firstly, the number of array elements and the distance between them should be determined. In this lens we need to 7 beams at 0°, ±10°, ±20° and ±30°, with a beamwidth of approximately 15° for each beam. To achieve these goals, based on linear array theory, NE and d should be chosen 7 and 10.7 mm, respectively. Now the initial value of design should be determined. To have a balanced lens with insignificant aperture phase error, we set α=30°, ψ_α=30° and g=1.137. Since α is equal to the ψ_α, the input ports must located at angles of 0°, ±10°, ±20° and ±30° on focal arc, in order to form the beams at the same angles.

The next step is the calculation of the normalized output ports coordinates and normalized transmission lines length by design Equations (1)-(3) in MATLAB software, and drawing the shape of the lens. In the following, the Δl is calculated and it is seen that the aperture error is acceptable for all elements of the array. Thus the values of $\eta_{\max}$ and F are selected 0.75 and 54.6 mm, respectively. With possessing the focal length, the actual dimensions of Rotman lens are calculated. See Table 1 (because of the symmetry, the dimensions of

ports A5 to A7 are not mentioned). Design of the SIW transmission lines is the next step and is one of the most important steps of the design procedure. In SIW, Instead of creating phase difference by changing the length of transmission lines, the widths of lines must be changed [5]. The last step is to embed the dummy ports at blank spaces between input and output ports for eliminating the unwanted reflection from sides of the lens.

C. Correction the lens shape

As already mentioned, the amplitude distribution of the array elements should be uniform, as far as possible. Incorrect design or improper orientation of input and output ports causes the low level amplitude at all of the array elements. But the low amplitude at one or several array elements is due to the poor design of dummy ports. In fact, the destructive interference of the direct and reflected waves at one or more output ports causes the amplitude of corresponding array elements to degrade. As a result, the orientation of input ports must be toward the central output port. This causes the mutual coupling between the input ports to be reduced; however, the amplitude level of the array elements to be increased. Also, to avoid undesired reflection in the transmission lines and to improve the amplitude and phase distribution of the array elements, the following points should be taken into account. The first, the transmission lines should have no bends as much as possible and the uniformity of them should be sustained. In addition, the dummy ports should be displaced slightly to the back due to decreasing the unwanted reflection from their metallic vias. Regarding to these points, the amplitude distribution of the array elements is achieved more uniform than previous works. The final scheme of Rotman lens is shown in Fig. 2.

D. Results and analysis

All simulations are done by CST Microwave Studio full wave software using time domain solver. The amplitude and phase distributions of the array elements for frequencies of 15.5 GHz, 16 GHz and 16.5 GHz are plotted in Fig. 3 and Fig. 4. As can be observed the levels of amplitudes are appropriate, and the phase distributions are linear.

III. PLANAR SLOT ARRAY ANTENNA

A. Introduction of slot array

Due to the growing demand for the use of low weight and compact antennas, longitudinal shunt resonant slot array implemented on the SIW structure is one of the most widely used antennas in radar and communication applications [11]. The design method of slot array on SIW is quite similar to those at the low height and dielectric filled metallic waveguide slot array one [12].

B. Design of the slot array

To design each kind of slot array, two basic equations are used. These equations for longitudinal shunt resonant slot array on conventional waveguide, and low height and dielectric filled waveguide are presented in [11] and [12] respectively. As previously mentioned, the planar slot array has 7 SIW waveguides. The number of slots of each waveguide depends on the desirable bandwidth. In this work, 4 slots on each waveguide are appropriate. This number of slots is corresponding to 5% bandwidth at center frequency of 16 GHz. The amplitude distribution on all array elements is considered to be uniform, that leading to a pattern with approximately -13 dB SLL. Now the length and offset of all slots can be obtained by employing basic design equations of [12].

Table 1: Coordinates of the output ports and relative length of transmission lines of Rotman lens (in mm)

	A1	A2	A3	A4
X	-6.4	-2.9	-0.7	0
Y	27.6	18.3	9.2	0
W	-0.15	0.24	0.09	0

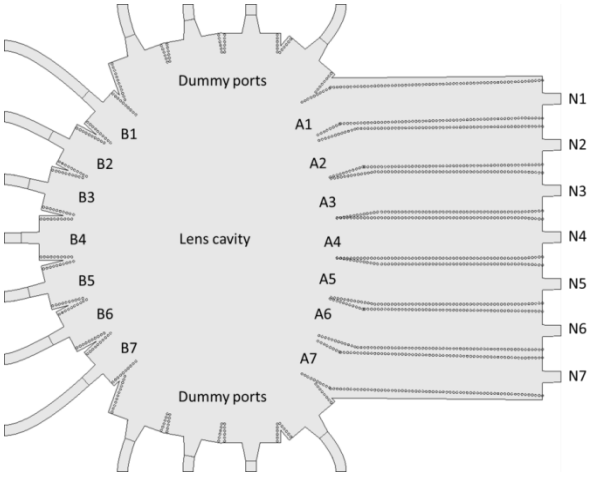

Fig. 2. Final scheme of the SIW Rotman lens. Input ports, output ports and array elements are named with B, A and N respectively.

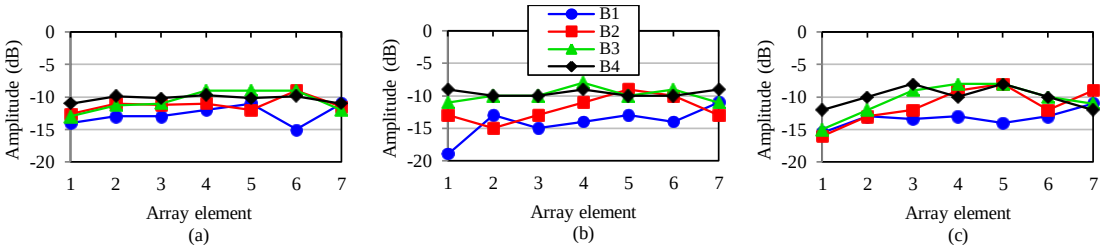

Fig. 3. Amplitude distribution of array elements for three frequencies: (a) 15.5 GHz, (b) 16 GHz, and (c) 16.5 GHz.

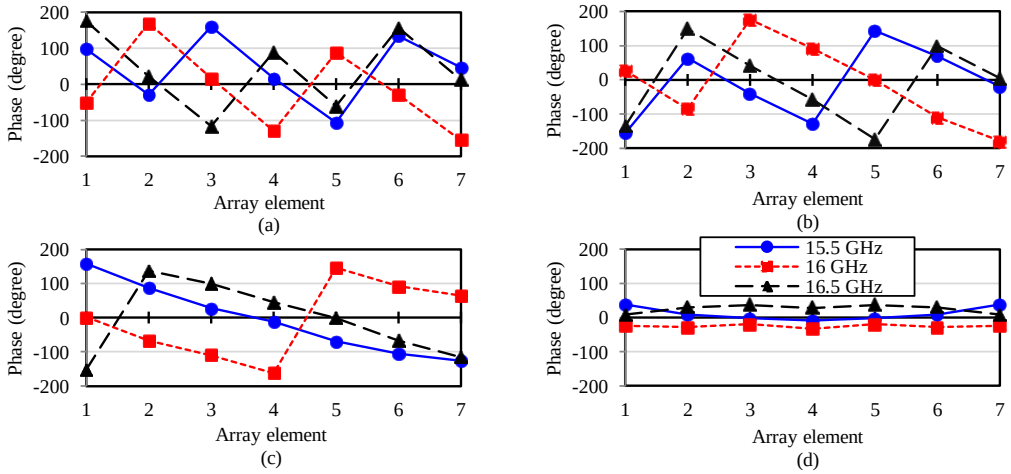

Fig. 4. Relative phase distribution of array elements for three frequencies when the beam ports: (a) B1, (b) B2, (c) B3, and (d) B4 are excited.

IV. INTEGRATING LENS AND SLOT ARRAY ANTENNA

The prototype of Rotman lens antenna that is the combination of Rotman lens and planar slot array is shown in Fig. 5 (a). The width and the length of antenna including connectors are 12.5 cm and 18.5 cm. As shown in Figs. 5 (a), (b), the scattering parameters of antenna are measured by a network analyzer, and during the measurement all ports except the ports under test were terminated with 50 Ω loads.

Figure 6 shows the measured reflection coefficients of all the input ports and also the mutual coupling between some of them. Inspection of Fig. 6 (a) reveals that, only the S44 exceeds the recommended limit -10 dB at high edge of the frequency range, and all the reflection coefficients are less than -10 dB. This occurs due to the smaller bandwidth of the slot array, which is from 15.5 to 16.3 GHz. The mutual coupling between other input ports is similar to those shown in Fig. 6 (b) and all of them are below -10 dB. The radiation patterns of input ports in E-plane (yoz) and radiation pattern of B4 in H-plane (xoz) at center frequency are simulated and measured at a microwave anechoic chamber. The simulated and measured patterns of ports B1 to B4 in E-plane are represented in Figs. 7 (a), (b) respectively. Because of the symmetry, the patterns of input ports B5 to B7 are not plotted. The SLL, HPBW, beam direction and gain of beams B1 to B4 in E-plane at center frequency are presented in Table 2.

Due to the true time delay property of Rotman lens, the characteristics of beams at the other frequencies of the band remain approximately unchanged. Also the simulated and measured co-pol and cross-pol radiation patterns of central port B4 in E-plane and H-plane are shown in Fig. 7 (b) and Fig. 8 respectively. This figure shows the low cross polarization level of the slot array antenna.

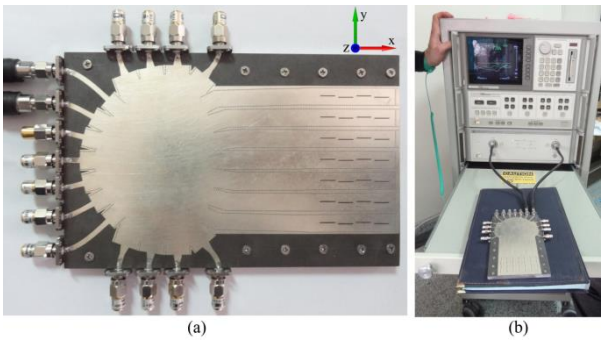

Fig. 5. (a) The prototype of Rotman lens with planar slot array antenna, and (b) scattering parameters measurement.

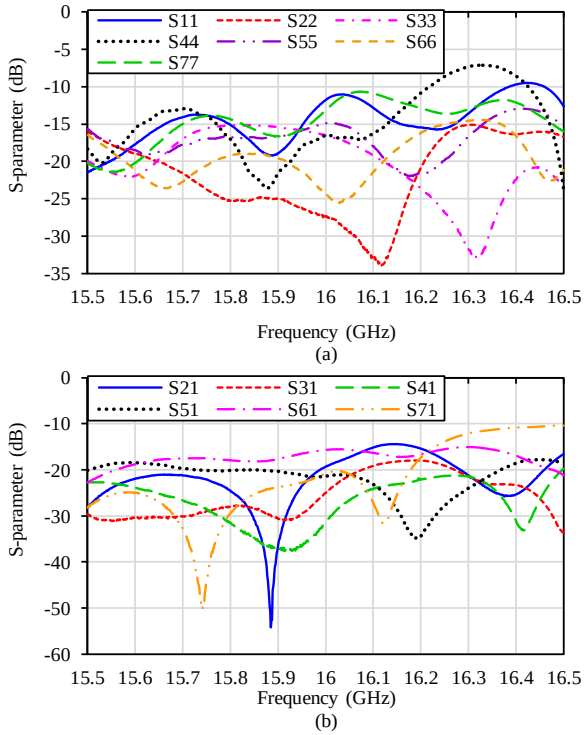

Fig. 6. Measured (a) reflection coefficients of all the input ports, and (b) mutual coupling between some of input ports.

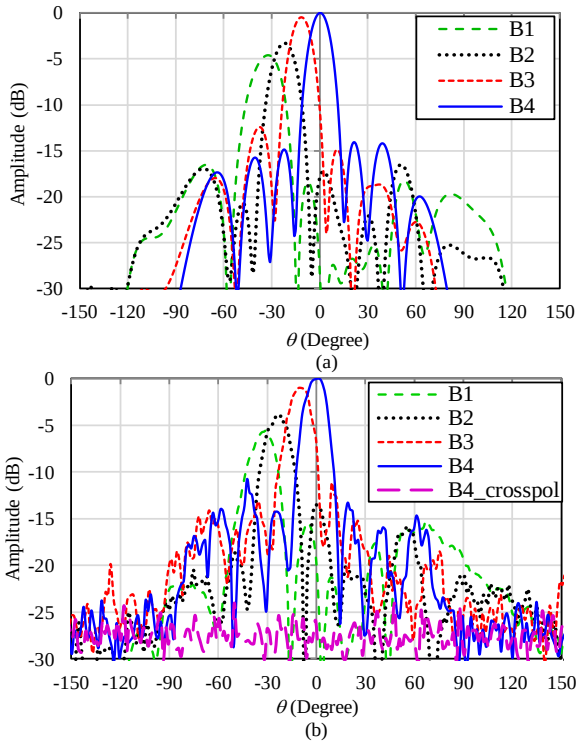

Fig. 7. (a) Simulated and (b) measured patterns of Rotman lens antenna in E-plane at center frequency.

Table 2: SLL, HPBW, beam direction and gain of beams B1 to B4 in E-plane at center frequency

	B1	B2	B3	B4
SLL (dB)	-10.2	-10	-10.3	-11
HPBW (deg)	16	17	15	14
Beam direction (deg)	31.1	21.4	10.7	0.3
Gain (dB)	10.6	12	15.1	16.5

The SLL and HPBW of beam B4 in H-plane at center frequency are -11.1 dB and 25°, respectively. The graph of simulated and measured gain versus frequency for port B4 is shown in Fig. 9. As can be observed, the gain is declined at the end of frequency range. This is also due to the lower bandwidth of the slot array antenna. Because of the errors of fabrication and measurement, the measured gain is usually less than simulated one.

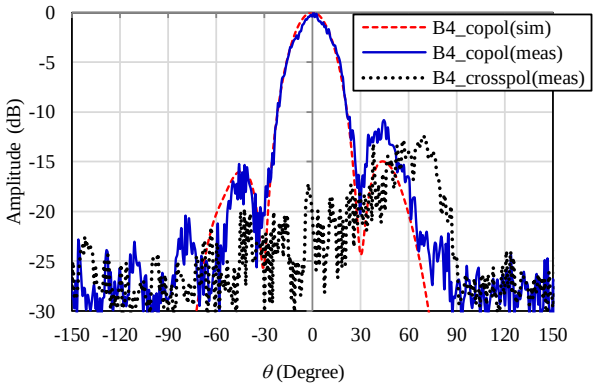

Fig. 8. Simulated and measured co-pol and cross-pol radiation patterns of B4 at center frequency in H-plane.

The SLL and HPBW of beam B4 in H-plane at center frequency are -11.1 dB and 25°, respectively. The graph of simulated and measured gain versus frequency for port B4 is shown in Fig. 9. As can be observed, the gain is declined at the end of frequency range. This is also due to the lower bandwidth of the slot array antenna. Because of the errors of fabrication and measurement, the measured gain is usually less than simulated one.

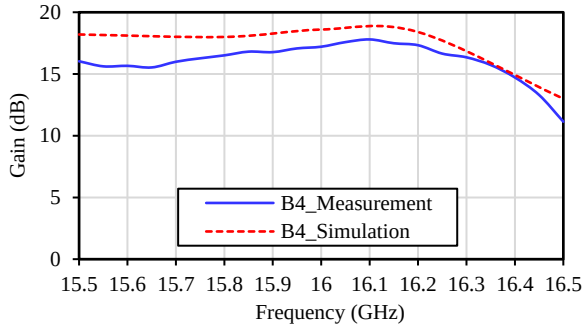

Fig. 9. Simulated and measured gain of input port B4 versus frequency.

V. CONCLUSION

In this paper, a SIW Rotman lens antenna is designed and fabricated to use as a multi-beam antenna. This antenna is made from the integration of a Rotman lens and a planar slotted array antenna. The measured reflection coefficients of input ports and mutual coupling of them are below -10 dB in the range of 15.5 to 16.3 GHz. The simulated and measured patterns are in good agreement; and also the SLL, HPBW, gain and cross polarization are acceptable. This paper revealed that the SIW Rotman lens antenna is a good alternative for heavy and bulky metallic multi-beam antennas in aerial and satellite communication applications.

ACKNOWLEDGMENT

The authors would like to thank Avionics Research Institute, Isfahan University of Technology, Iran to support of this project.

REFERENCES

[1] P.-C. Chiang, W.-J. Liao, Y.-T. Tu, and L. Hsin-Chin, "Implementation of direction-of-arrival estimation using rotman lens array antenna," in *Electromagnetic Theory (EMTS), Proceedings of 2013 URSI International Symposium on*, pp. 855-858, 2013.

[2] R. C Hansen, *Phased Array Antennas*. New Jersey: Wiley & Sons, 2009.

[3] S. Mubeen, A. M. Prasad, and A. J. Rani, "On the beam forming characteristics of linear array using nature inspired computing techniques," *ACES*, vol. 1, no. 6, 2016.

[4] W. Rotman and R. Turner, "Wide-angle microwave lens for line source applications," *IEEE Trans. Antennas Propag.*, vol. 11, no. 6, pp. 623-632, Nov. 1963.

[5] Y. J. Cheng, W. Hong, K. Wu, Z. Q. Kuai, C. Yu, J. X. Chen, J. Y. Zhou, and H. J. Tang, "Substrate integrated waveguide (SIW) Rotman lens and its Ka-band multibeam array antenna applications," *IEEE Trans. Antennas Propag.*, vol. 56, no. 8, pp. 2504-2513, Aug. 2008.

[6] E. Sbarra, L. Marcaccioli, R. V. Gatti, and R. Sorrentino, "A novel Rotman lens in SIW technology," in *2007 European Radar Conference, EURAD*, pp. 236-239, 2007.

[7] Z. X. Wang, D. P. Fan, and L. Z. You, "A design of microstrip Rotman lens," in *2012 International Conference on Microwave and Millimeter Wave Technology (ICMMT)*, pp. 1-4, 2012.

[8] A. F. Peterson and E. O. Rausch, "Scattering matrix integral equation analysis for the design of a waveguide Rotman lens," *IEEE Trans. Antennas Propag.*, vol. 47, no. 5, pp. 870-878, May 1999.

[9] S. A. R. Hosseini, Z. H. Firouzeh, and M. Maddahali, "Design of Rotman lens antenna at Ku-band based on substrate integrated technology," *JCE*, vol. 3, no. 1, pp. 33-44, 2014.

[10] F. Xu and K. Wu, "Guided-wave and leakage characteristics of substrate integrated waveguide," *IEEE Trans. Microw. Theory Tech.*, vol. 53, no. 1, pp. 66-73, Jan. 2005.

[11] R. Elliott and L. Kurtz, "The design of small slot arrays," *IEEE Trans. Antennas Propag.*, vol. 26, no. 2, pp. 214-219, Mar. 1978.

[12] R. Elliott and W. O'Loughlin, "The design of slot arrays including internal mutual coupling," *IEEE Trans. Antennas Propag.*, vol. 34, no. 9, pp. 1149-1154, Sep. 1986.

Seyyed Alireza Hosseini received the B.Sc. degree in Electronics and Telecommunications from Shahed University, Tehran, Iran, in 2011 and the M.Sc. degrees in Electrical Engineering from Isfahan University of Technology (IUT), Isfahan, Iran, in 2014. His research interests include slot array antennas, cavity filters, and phase array antennas.

Zaker Hossein Firouzeh received the B.Sc. degree in Electrical Engineering from Isfahan University of Technology (IUT), Isfahan, in 1999 and the M.Sc. and Ph.D. degrees in Electrical Engineering from Amirkabir University of Technology (AUT), Tehran, Iran, in 2002, and 2011, respectively. He is currently a Faculty Member at the Department of Electrical and Computer Engineering, Isfahan University of Technology. His current research interests include antenna design and measurements, numerical techniques in electromagnetics and EMC/EMI.

Mohsen Maddahali received the B.S. degree in Electronics and Telecommunications from Isfahan University of Technology (IUT), Isfahan, Iran, in 2005 and the M.S. and Ph.D. degrees in Electrical Engineering from Tarbiat Modares University, Tehran, Iran, in 2008 and 2012, respectively. Since 2012, he has been an Assistant Professor with the Department of Electrical and Computer Engineering, IUT. His research interests include computational electromagnetism, waveguide slot antenna design, and phase array antennas.

Improvement of the Broadside Radiation Pattern of a Conformal Antenna Array using Amplitude Tapering

Irfanullah [1], Shahid Khattak [1], and Benjamin D. Braaten [2]

[1] Department of Electrical Engineering
COMSATS Institute of Information Technology Abbottabad, KPK, Pakistan
eengr@ciit.net.pk, skhattak@ciit.net.pk

[2] Department of Electrical and Computer Engineering
North Dakota State University, Fargo, ND, 58102, USA
benjamin.braaten@ndsu.edu

Abstract ─ In this paper, an algorithm for evaluation of near optimal amplitude excitation coefficients for a conformal array on a wedge-shaped surface has been developed in order to maximize the broadside radiation pattern. The radiation pattern for an eight-element conformal antenna has been analyzed and the derived analytical expressions are used to recover the distorted broadside radiation pattern. A heuristic amplitude tapering algorithm is developed to maximize the broadside radiation pattern through the control of individual voltage variable attenuator of each radiating element in the array. It is shown that with appropriate amplitude tapering, the broadside radiation pattern of the array can be improved without phase correction. The pattern recovery information is used to develop a new 1 x 8 microstrip patch antenna array bent at certain angles on a single curved non-conducting structure and the measured results are shown to agree well with the analytical solutions.

Index Terms ─ Adaptive arrays, antenna radiation patterns, conformal antennas, microstrip antenna arrays, phased arrays.

I. INTRODUCTION

Conformal antennas have attracted attention in many wireless applications that require antennas to be placed on non-planar surfaces [1] and well defined techniques are available to use linear and planar array configurations to achieve a desired radiation pattern [2, 3]. However, these techniques assume a fixed position of the antenna elements. In practice though, the position of the antenna elements may be changed (e.g., bending the antenna array), which results in an unwanted change of the original radiation pattern. Several phase- and amplitude- compensation techniques have been investigated and reported to autonomously recover the distorted radiation pattern of a conformal antenna [4-7,12] and more recently genetic algorithms for phase compensation [13,16,19,20]. In [14,15], photo-conductive attenuators have been designed for adaptive nulling antenna array. Traditionally for conformal antenna arrays, the designers use both amplitude and phase correction to correct the broadside radiation pattern and to control the sidelobe characteristics to a desired level, see for example [5-7]. Since additional phase shifters and attenuators are required to implement these compensation techniques, the cost of the system and complexity of the feed network is considerably increased. This work investigates the possibilities of simplifying these techniques and studies the effects of amplitude tapering (instead of altering the phase of each antenna element) on broadside and side lobe level (SLL) radiation patterns. As a result, a low-cost solution can be utilized to improve the broadside pattern recovery and sidelobe level control on a conformal surface. The amplitude tapering for conformal antennas has been investigated in [9] where the amplitude weights have been determined using empirical techniques. No automated algorithm has been proposed to deal with different scenarios.

In this work, an amplitude tapering algorithm is developed using the array factor expression, which nearly gives an optimal amplitude coefficients to improve the radiation pattern in the target (broadside) direction and reduces the energy level in the first side lobes, while keeping the transmit power the same as that of uniform illumination. The amplitude tapering is created by redistributing the power among the antenna elements, so that the total transmit power remains the same, i.e., the sum of the squares of amplitude tapering voltages is the same as the sum of squares of a uniform amplitude excitation voltages of the same number of antenna elements.

This work is organized in the following manner. In Section 2, the radiation pattern correction is presented using analytical expressions and an optimization

Submitted On: November 1, 2016
Accepted On: April 21, 2017

algorithm. Section 3 presents simulation and measurement validation of the pattern correction for a 45 degree conformal wedge. Finally Section 4 concludes the paper.

II. ARRAY FACTOR (AF) AND OPTIMIZATION ALGORITHM

Consider the eight-element array attached to a conformal wedge-shaped surface shown in Fig. 1. The location of the n^{th}element in the array is represented as a function of distance a_n from the origin, and angle ϕ_n from the x-axis, where $n = 1,2,\dots,8$. ϕ_b is the bend angle of the wedge and the broadside main beam direction is in the $+y$-direction.

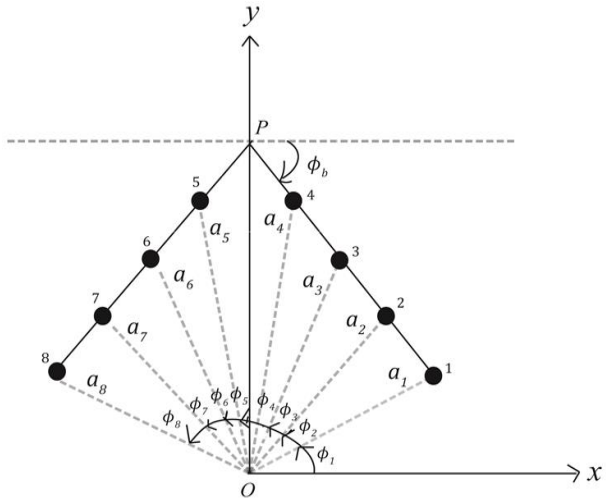

Fig. 1. A drawing of the eight-element amplitude-tapered array antenna on a conformal wedge-shaped surface.

A. Array Factor (*AF*)

The radiation pattern produced by the array configuration in Fig. 1 can be written as (chapter 5 in [1]):

$$AF = \sum_{n=1}^{N} F_n(\theta,\phi)\, w_n e^{jk[x_n \cos\phi + y_n \sin\phi]}, \quad (1)$$

where k is the free space wave number, N is number of antenna elements, (x_n, y_n) is the location of n^{th} antenna element on the conformal surface in Fig. 1, and $F_n(\theta,\phi) = \cos(\phi - \phi_b)$ is the pattern for right four-elements and $F_n(\theta,\phi) = \cos(\phi + \phi_b)$ is the pattern of left four-elements in Fig. 1. $w_n = I_n e^{j\Delta\phi}$ is the complex weighting function required to drive the n^{th} antenna element. For this work, the phase difference $\Delta\phi$ between adjacent antenna elements was made zero, and the amplitude tapering coefficient I_n was computed for various bend angles to correct the main beam direction towards the broadside. Putting $w_n = I_n$ for amplitude tapering, (1) can be written as:

$$AF = \sum_{n=1}^{N} F_n(\theta,\phi)\, I_n e^{jk[x_n \cos\phi + y_n \sin\phi]}. \quad (2)$$

To determine the amplitude tapering coefficients I_n in (2), the following optimization algorithm was developed to correct the broadside main beam target direction.

B. Algorithm development to compute amplitude coefficients

A classical antenna array synthesis problem assigns complex weights to each array element so as to maximize the radiation pattern in the target directions while minimizing the side-lobes below a certain level. This can be easily formulated as a convex optimization problem which minimizes the total radiated power subject to the constraints on the radiation in the target direction while suppressing the side-lobes radiation to a value below γ_{SLL} [8]:

$$\begin{aligned} &\min |w|_2^2, \\ \text{subject to } &|AF_{tar}(w)| = 1, \\ \text{and } &|AF_{SLL}(w)| \le \gamma_{SLL}, \end{aligned} \quad (3)$$

where $w = [w_1, w_2, \dots, w_N]^T$ represents the complex antenna element weights. AF_{tar} is the radiation in the target direction and AF_{SLL} is the radiation pattern of the side lobes. The objective function in (3) ensures that the total radiated power of the antennas is constrained. Its implementation, however, necessitates both attenuators and phase shifters which leads to an expensive solution. A less expensive but suboptimal approach is to use only the amplitude tapering, i.e.,

$$\begin{aligned} &\arg\max_{I} |AF_{tar}(I)|, \\ \text{subject to } &|I|_2^2 \le 1, \\ \text{and } &|AF_{SLL}(I)| \le \gamma_{SLL}, \end{aligned} \quad (4)$$

where the weights $I = [I_1, I_2, \dots, I_N]^T$ represents the amplitude coefficients I_n in (2). Although this problem can be solved through the classical descent algorithms, a simpler approach involves growing I incrementally one antenna element at a time by making a locally optimal choices at each stage. During each incremental increase in I, a multi-criteria objective function is formed using the change in the radiated power in the target direction $\Delta AF_{tar}^2(I)$ and the maximum change encountered in the first sidelobe $\max(\Delta AF_{SLL}^2(I))$. A scalarization parameter β is used to controlthe emphasis to either of these two parameters, i.e., ΔAF_{tar}^2 and ΔAF_{SLL}^2. This multi-criteria objective function is then normalized with respect to the change in the total transmit power given by the increase in the square of Euclidean modulus of the weight vector $\Delta|I|_2^2$. The process of adding weights continues for as long as the weight constraint in (4) is not violated. The objective function over each incremental change is now written as:

$$\arg\max_{I_n'} \frac{\Delta AF_{\mathrm{tar}}{}^2 - \beta \max(\Delta AF_{\mathrm{SLL}}{}^2)}{\Delta|\mathrm{I}|_2^2} \quad (5)$$

$$= \arg\max_{I_n'} \frac{\{AF_{tar}^2(I') - AF_{tar}^2(I)\} - \beta \max\{AF_{SLL}^2(I') - AF_{SLL}^2(I)\}}{|I'|_2^2 - |I|_2^2},$$

where $I' = \Delta I_n + I, \Delta I_n$ is the incremental change in the n^{th} antenna element weight that maximizes the above

ratio and I' is the corresponding new weight vector. Both the half beamwidth ζ and the scalarization parameter β are also varied in order to obtain a solution that gives the best tradeoff between the antenna gain, the beam-width, and the energy gap to the first sidelobe.

Table 1: Optimization algorithm

	Algorithm: Computation of Amplitude Excitation Coefficients
1	Inputs: $N, a_n, \phi_n, \theta_{tar}, \phi_b, F_n(\theta,\phi)$
2	Outputs: I, β_{opt}, ζ_{opt}
3	For $\zeta = \theta_1$ to θ_2 beam-width
4	For $\beta=\beta_1$ to β_2 scalarization parameter
5	Initialization: $I_{N\times 1} = [0,0,\cdots 0]^T$, $AF = 0$;
6	while $\lvert I\rvert_2^2 < 1$ do
7	for $n = 1 \rightarrow N$ do
8	$I_n{}' = I_n + \Delta I$
9	$\Omega(n) = \frac{\Delta AF^2}{\Delta \lvert I\rvert_2^2} = \frac{\Delta AF_{tar}^2 - \beta \max(\Delta AF_{SLL}^2)}{\Delta \lvert I\rvert_2^2}$
10	end for
11	$I^* \leftarrow \arg\max_n \Omega(n)$
12	$I_{n^*}{}' = I_{n^*} + \Delta I$
13	$I_m \leftarrow I_{n^*}{}'$
14	end while
15	end For
16	end For
17	$\arg\max_{I,\zeta,\beta}\left(\frac{AF_{tar}}{AF_{SLL}}\right)$

Table 1 gives the algorithm for the weights selection. It uses a greedy approach, using the locally optimal choice of increasing the power in only one antenna element at a time that maximizes the ratio in (4). The algorithm is optimized in a manner, so that the total transmit power for various bend angles is always normalized to one, i.e., sum$\left(I_n{}^2\right) = 1$.

In Fig. 2, the radiation pattern of the proposed amplitude tapering algorithm (labeled as 'Amplitude tapering') is compared with the optimal phase and amplitude correction algorithm (2) (labeled as 'Optimal') and the uncorrected radiation pattern (labeled as 'Uncorrected'). All three algorithms are simulated for eight-element antenna array for various bend angles of 0 to 45° of a wedge-shaped conformal surface. The value of β is varied from 0 to 8, the half beamwidth is varied between 10° to 45° and the value of γ_{SLL} in (2) is fixed to -10dB.

For bend angles less than 10°, the difference between the gains of corrected and uncorrected radiation patterns is very small. The effect of bend angles on the uncorrected pattern becomes more pronounced at higher angles ($\phi_b \geq 10^\circ$) with the sidelobe levels becoming comparable or even bigger than the main beam in the target direction. The proposed algorithm not only improves the main lobe gain but also reduces the SLL considerably as shown in Fig. 2. The difference in the gains between uncorrected and corrected patterns is highlighted for the bend angles shown. For the simulated bend angles 0 to 45°, the proposed amplitudetapering algorithm gain stays within 6 dB of the optimal scheme, which is within the acceptable limit [5,6,17,18].

The aperture efficiency $\eta_{aperture}$ can be calculated using the expression in [10]:

$$\eta_{aperture} = \frac{\left(\sum_{n=1}^{N} I_n\right)^2}{N\sum_{n=1}^{N}(I_n)^2}. \quad (6)$$

The aperture efficiencies for various bend angles were computed using (6) and are given in Table 2. The results in Table 2 show that conformal surfaces with different bending angles require various amplitude weighting distributions, aperture efficiencies, and hence various deviations of pattern recovery patterns from optimal patterns as illustrated in Fig. 2.

Table 2: Aperture efficiency for various bend angles of the eight-element conformal array

ϕ_b	I_n	$\eta_{aperture}$ (%)
0	[0.23,0.24,0.41,0.43,0.43,0.42,0.24,0.23]	100
5	[0.23,0.34,0.36,0.43,0.43,0.36,0.34,0.23]	97.5
10	[0.14,0.4,0.46,0.32,0.32,0.46,0.4,0.14]	88.4
15	[0,0.29,0.53,0.36,0.36,0.53,0.29,0]	70.7
20	[0, 0,0.46,0.53,0.53,0.46,0, 0]	50
25	[0, 0,0.46,0.53,0.53,0.46, 0,0]	50
30	[0, 0, 0, 0.71,0.71, 0, 0, 0]	25
35	[0.5, 0, 0, 0.5, 0.5, 0, 0, 0.5]	50
40	[0.5, 0, 0, 0.5, 0.5, 0, 0, 0.5]	50
45	[0.46, 0, 0,0.53,0.53, 0, 0, 0.46]	50

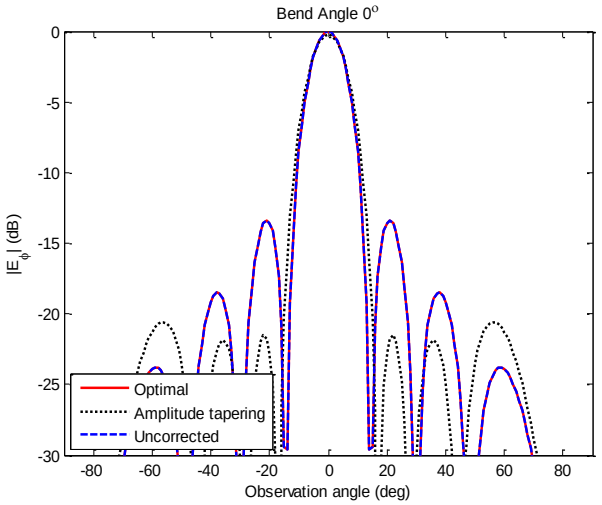

(a)

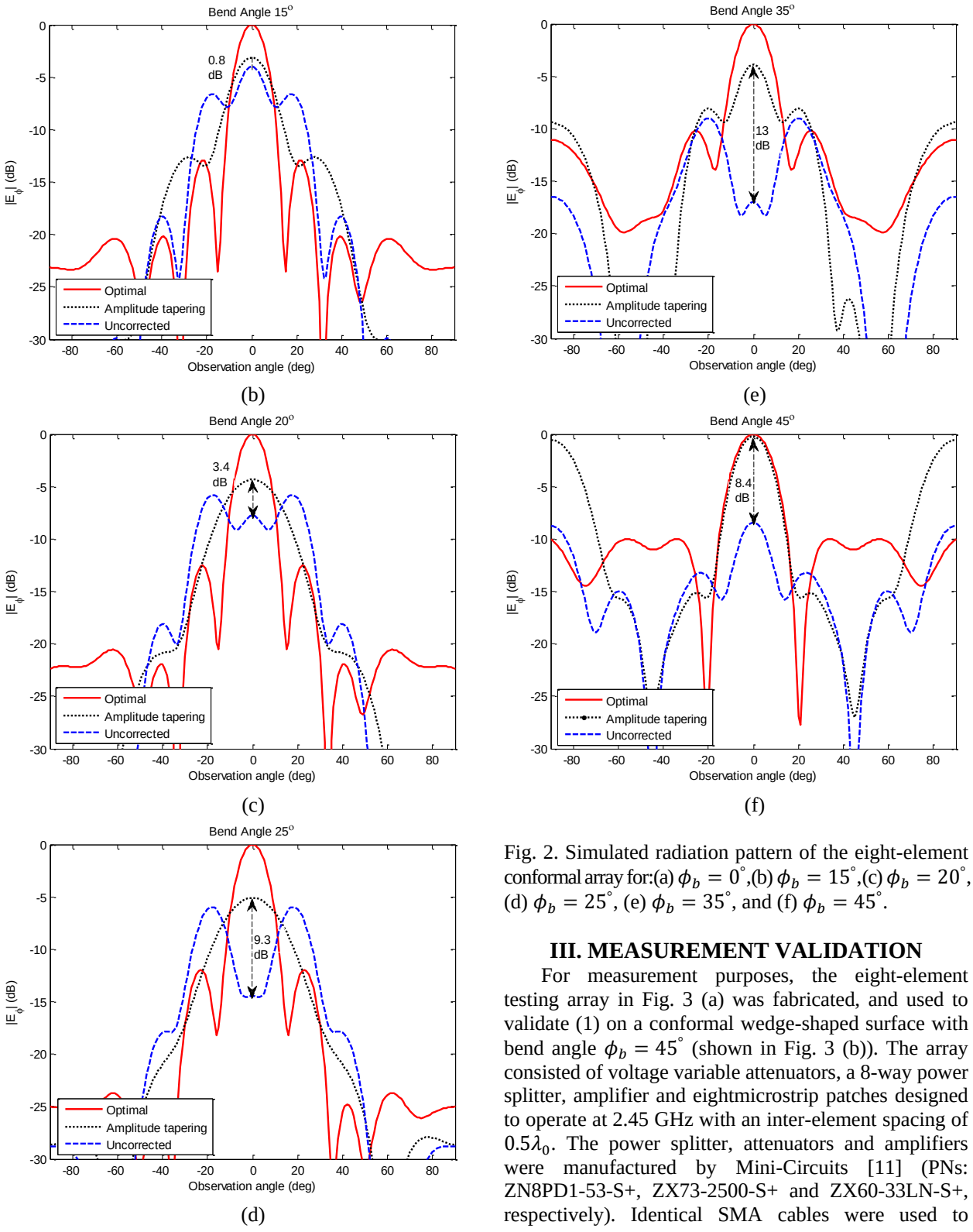

Fig. 2. Simulated radiation pattern of the eight-element conformal array for:(a) $\phi_b = 0^\circ$,(b) $\phi_b = 15^\circ$,(c) $\phi_b = 20^\circ$, (d) $\phi_b = 25^\circ$, (e) $\phi_b = 35^\circ$, and (f) $\phi_b = 45^\circ$.

III. MEASUREMENT VALIDATION

For measurement purposes, the eight-element testing array in Fig. 3 (a) was fabricated, and used to validate (1) on a conformal wedge-shaped surface with bend angle $\phi_b = 45^\circ$ (shown in Fig. 3 (b)). The array consisted of voltage variable attenuators, a 8-way power splitter, amplifier and eightmicrostrip patches designed to operate at 2.45 GHz with an inter-element spacing of $0.5\lambda_0$. The power splitter, attenuators and amplifiers were manufactured by Mini-Circuits [11] (PNs: ZN8PD1-53-S+, ZX73-2500-S+ and ZX60-33LN-S+, respectively). Identical SMA cables were used to

connect each patch to a port on the power splitter through an attenuator.

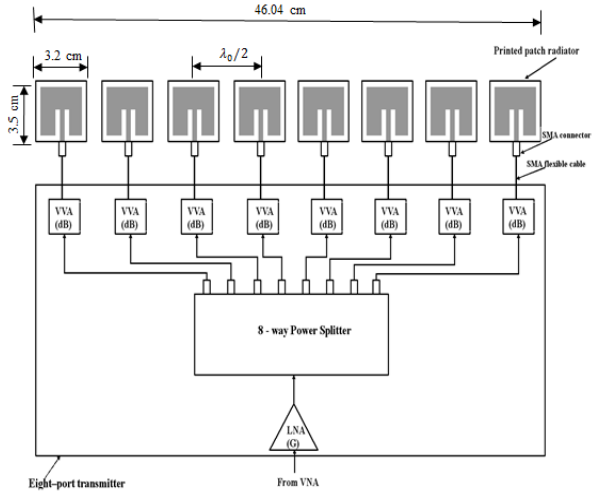

(a)

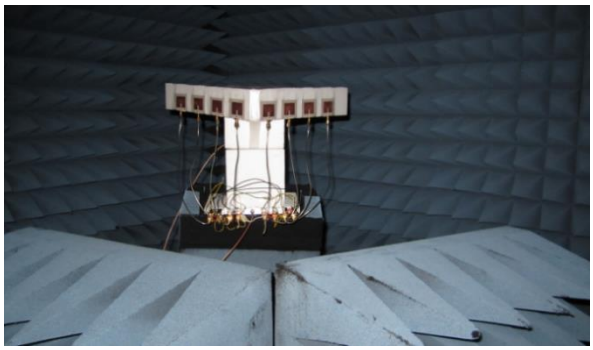

(b)

Fig. 3. (a). Topology of the eight-element array used for attachment to conformal surfaces, and (b) picture of the eight-element array attached to a wedge in the anechoic chamber for bend angle $\phi_b = 45^{\circ}$.

The algorithm in Table 1 was used to calculate the amplitude distribution coefficients to maximize the broadside main beam radiation pattern and -10 dB first sidelobe constraints was defined. The computed amplitude coefficients for $\boldsymbol{\phi_b} = 45^{\circ}$ are given in Table 2. The uniform amplitude tapering coefficients for the uncorrected case are given by $[1,1,1,1,1,1,1,1]/\sqrt{8}$.

Next, the eight-element wedge antenna array of Fig. 3 (b) was driven with uncorrected and corrected amplitude distribution coefficients, and the results for bend angle $\phi_b = 45^{\circ}$ are shown in Fig. 4 (amplitude tapering correction results were normalized with respect to optimal scheme). With amplitude tapering, the broadside main beam direction has been corrected by 8.4dB over the uncorrected pattern.

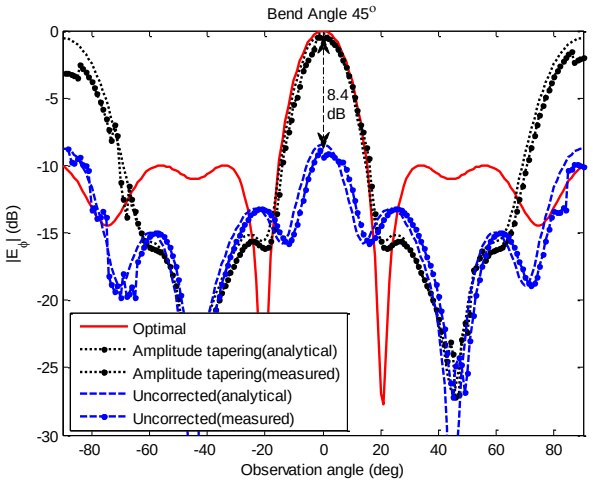

Fig. 4. Measurement and analytical results of the eight-element conformal array for bend angle $\phi_b = 45^{\circ}$.

IV. CONCLUSION

Amplitude tapering algorithm was developed to improve the radiation pattern of eight-element conformal array towards the broadside target direction. The proposed algorithm was compared with the optimal scheme (that utilizes both phase and amplitude correction) for various bend angles of conformal wedge. It was shown that the broadside main beam pattern can be corrected using amplitude excitation coefficients only (instead of both phase and amplitude correction). Therefore a low-cost solution can be utilized to improve the broadside pattern recovery on a conformal surface. A measurement case of 45° conformal wedge showed that 8.4dB correction of main beam direction towards the broadside over uncorrected case can be achieved using the proposed amplitude tapering algorithm.

REFERENCES

[1] R. L. Haupt, *Antenna Arrays: A Computational Approach*. John Wiley and Sons, Ltd., Hoboken, New Jersey, pp. 552, 2010.

[2] R. C. Hansen, *Phased Array Antennas*. John Wiley and Sons, Inc., New York, NY, pp. 547, 2010.

[3] L. Josefsson and P. Persson, *Conformal Array Antenna Theory and Design*. *Wiley-IEEE Press*, pp. 496, 2006.

[4] H. Schippers, J. Verpoorte, P. Jorna, A. Hulzinga, A. Meijerink, C. Roeloffzen, et al., "Broadband conformal phased array with optical beam forming for airborne satellite communication," *IEEE Aerospace Conference*, Big Sky, MT, pp. 1-17, Mar. 2008.

[5] B. D. Braaten, M. A. Aziz, S. Roy, S. Nariyal, Irfanullah, N. F. Chamberlain, M. T. Reich, and

D. E. Anagnostou, "A self-adapting flexible (SELFLEX) antenna array for changing conformal surface applications," *IEEE Transactions on Antennas and Propagation*, vol. 61, no. 2, pp. 655-665, Feb. 2013.

[6] B. D. Braaten, S. Roy, Irfanullah, S. Nariyal, and D. E. Anagnostou, "Phase-compensated conformal antennas for changing spherical surfaces," *IEEE Transactions on Antennas and Propagation*, vol. 62, no. 4, pp. 1880-1887, Apr. 2014.

[7] D. Anagnostou and M. Iskander, "Adaptive flexible antenna array system for deformable wing surfaces," *IEEE Aerospace Conference*, Big Sky, MT, pp. 1-6, Mar. 7-14, 2015.

[8] S. Boyd and L. Vandenberghe. *Convex Optimization*. Cambridge University Press, 2004.

[9] S. Nariyal, Irfanullah, S. A. Naqvi, B. Ijaz, M. M. Masud, B. Booth, K. Asirvatham, and B. D. Braaten, "On the use of amplitude tapering for pattern correction of conformal (curved) antennas," *IEEE International Conference on Wireless for Space and Extreme Environments (WiSEE)*, Baltimore, MD, pp. 1-2, Nov. 7-9, 2013.

[10] G. D. Hopkins, J. Ratner, A. Traille, and V. Tripp, "Aperture efficiency of amplitude weighting distributions for array antennas," *IEEE Aerospace Conference*, Big Sky, MT, pp.1-9, Mar. 3-10, 2007.

[11] Mini-Circuits. [Online]. www.minicircuits.com

[12] C. Loecker, P. Knott, R. Sekora, and S. Algermissen, "Antenna design for a conformal antenna array demonstrator," *6th European Conference on Antennas and Propagation (EUCAP)*, Prague, pp. 151-153, Mar. 2012.

[13] R. L. Haupt, "Adaptive antenna arrays using a genetic algorithm," *IEEE Mountain Workshop on Adaptive and Learning Systems*, Logan, UT, pp. 249-254, July 2006.

[14] R. L. Haupt and J. R. Flemish, "Broadband linear array with photoconductive attenuators," *4th European Conference on Antennas and Propagation (EUCAP)*, Apr. 2010.

[15] R. L. Haupt, J. R. Flemish, and D. W. Aten, "Adaptive nulling using photoconductive attenuators," *IEEE AP-S Trans.*, vol. 59, no. 3, pp. 869-876, Mar. 2011.

[16] R. L. Haupt and S. E. Haupt, *Practical Genetic Algorithms*. 2nd Edition, John Wiley and Sons, Ltd., Hoboken, New Jersey, pp. 272, 2004.

[17] B. D. Braaten, Irfanullah, S. Nariyal, and A. Naqvi, "Scanning characteristics of a self-adapting phased-array antenna on a wedge-shaped conformal surface," *Proceedings of the 2013 IEEE International Symposium on Antennas and Propagation*, Orlando FL, pp. 1220-1221, July 7-13, 2013.

[18] I. Ullah, S. Nariyal, S. Roy, M. M. Masud, B. Ijaz, A. Aftikhar, S. A. Naqvi, and B. D. Braaten, "A note on the fundamental maximum gain limit of the projection method for conformal phased array antennas," *Proceedings of the IEEE International Conference on Wireless Information Technology and Systems*, Maui, Hawaii, Nov. 11-16, 2012.

[19] R. L. Haupt, "Phased array beam steering through serial control of the phase shifters," *ACES Express Journal*, vol. 1, no. 1, Jan. 2016.

[20] P. Rocca and R. L. Haupt, "Biologically inspired optimization of antenna arrays," *ACES Journal*, vol. 29, no. 12, Dec. 2014.

Irfanullah received the Ph.D. degree in Electrical and Computer Eengineering from North Dakota State University, Fargo, ND, USA, in 2013. He is an Assistant Professor in Electrical Engineering Department at COMSATS, Abbottabad, Pakistan. His research interests include the antenna arrays, metamaterials and topics in EMC.

Shahid Khattak received Dr.-Ing. degree from Technische Universität Dresden, Germany in 2008. His research interests include mobile cellular networks, 3G and next generation mobile systems.

Benjamin D. Braaten (S'02-M'09) received the Ph.D. degree in Electrical Engineering from North Dakota State University, Fargo, ND, USA, in 2009.

During the 2009 Fall semester he held a Post-doctoral Research position at the South Dakota School of Mines and Technology in Rapid City, SD. Currently, he is an Associate Professor in the Electrical and Computer Engineering Department at North Dakota State University. His research interests include printed antennas, conformal self-adapting antennas, microwave devices, topics in EMC, and methods in computational electromagnetics.

Electromagnetic Time-Reversal Imaging Using Grouped Sub-Arrays for Resolution Enhancements

Yuan-Qi Li [1], Xiang-Qian Zhang [1], and Ming-Yao Xia [2*]

[1] School of Electronic Engineering
University of Electronic Science and Technology of China, Chengdu, 611731, China
liyuanqiwangheng@163.com, xqzh@uestc.edu.cn

[2] School of Electronics Engineering and Computer Sciences
Peking University, Beijing, 100871, China
myxia@pku.edu.cn

Abstract ─ A new time-reversal (TR) imaging method using grouped sub-arrays for resolution enhancements is presented in this work. The method gives the image of the searching space for each target or scattering center at its own optimum instant, in contrast to the traditional TR imaging method that shows a snapshot of the whole domain at a specified instant. By introducing a grouping scheme that divides the time-reversal mirror (TRM) as many sub-TRMs, resolution enhancements in both cross-range and co-range directions are realized by means of destructive multiplication and incoherent superposition of the normalized sub-TRM imaging signals at non-target positions. The present method permits all targets or scattering centers to be rendered at equal visibility, and has no requirement on the number of transmitters. Several simulation examples are provided to examine the performance of the proposed method.

Index Terms ─ Grouped sub-arrays, imaging, resolution enhancement, signal normalization, time-reversal.

I. INTRODUCTION

Time-reversal (TR) technique was first proposed in acoustics [1,2], and latter extended to electromagnetic wave [3,4]. It lies on the invariance of the wave equations under time reversal operation in reciprocal and lossless media. It contains two stages. First, waves radiated from a source or scattered from a target are received and recorded by each element of an antenna array, called time-reversal mirror (TRM). Then, at each element, the recorded wave is time-reversed, i.e., in a first-in last-out way, and retransmitted into the same media. Space-time focusing of these retransmitted waves from individual elements will happen, i.e., they add coherently or achieve their maximum amplitude values synchronically at the original source or target position, but incoherently or non-synchronically at other positions.

For applications in wireless communications and wireless power transmission or combination, for which actual energy focusing is required, the retransmission and back-propagation must be taken place physically (physical TR) [5-7]. However, for applications in target locating or imaging, for which real energy focusing is not required, the back-propagation can be implemented synthetically or computationally (synthetic TR) [8-20]. This work is concerned with the target imaging by using the synthetic TR fashion.

The traditional TR imaging method is typically manipulated by synthetically back-propagating the time-reversed signals into the imaging domain and showing the image at the appropriate reference time "t=0" [10-12]. However, we may not know the t=0 reference precisely, or the t=0 reference may not be the optimal focusing instant. As revealed in [10], the traditional TR imaging method can locate point-like targets and extended perfectly electrical conducting (PEC) targets at the t=0 reference, but fails to locate the extended dielectric target at the same instant. The reason may be due to the multiple interior scattering, which amounts to a change of the original background medium. Another issue with the traditional TR imaging method is the near-far problem for imaging multiple targets [13], by which the farther or weaker targets are prone to be swamped by the nearer or stronger ones.

There exist other kinds of TR imaging methods based on the analyses of the time-reversal operator (TRO), including the decomposition operator of time-reversal (DORT) and the time-reversal multiple signal classification (TR-MUSIC) [11,14-20]. These methods can produce better imaging results, but their computing burden is heavily increased. Besides, these approaches demand that the number of targets or scattering centers cannot exceed the number of transmitters or receivers, which is somewhat inconvenient in applications.

Previously, we proposed a new TR imaging concept based on synchronism and illustrated with 2D targets

Submitted On: March 5, 2017
Accepted On: April 18, 2017

[21]. The purpose of this work is to present its extension to 3D case for practical applications, because real-world targets are 3D. We will show that the proposed algorithm would have much better imaging results than the traditional TR imaging method at the expense of a slightly increased computing load. Also, the present method should enjoy a significantly reduced computing cost than the DORT and TR-MUSIC methods, and get rid of the demand on the number of transmitters.

II. METHOD OUTLINE

Refer to Fig. 1. Consider a time-reversal imaging scenario in lossless and reciprocal medium. The receiving antennas or the time-reversal mirror (TRM) is deployed over the *xoy* plane, forming a planar array of size N_x by N_y. Their positions are known at $\mathbf{r}_n$ $(1 \le n \le N,\ N = N_x \times N_y)$. A point-like target is located at $\mathbf{r}_s$, which may be taken as an equivalent point current source with strength $\mathbf{J}_s(\mathbf{r},\omega) = \mathbf{P}_s(\omega)\delta(\mathbf{r}-\mathbf{r}_s)$. The radiating or scattering field from the target at the *n*-th antenna position is:

$$\mathbf{E}^s(\mathbf{r}_n,\omega) = \bar{\mathbf{G}}(\mathbf{r}_n,\mathbf{r}_s,\omega)\cdot[-j\omega\mu\mathbf{P}_s(\omega)], \quad (1)$$

where $\bar{\mathbf{G}}(\mathbf{r}_n,\mathbf{r}_s,\omega)$ is the dyadic Green's function from the target point $\mathbf{r}_s$ to the receiver at $\mathbf{r}_n$. If the polarization property of every antenna element is $\hat{q}$, say $\hat{q} = \hat{x}$, the received signal would be $S(\mathbf{r}_n,\omega) = \hat{q}\cdot\mathbf{E}^s(\mathbf{r}_n,\omega)$. After time-reversed, the signal can be taken as an equivalent point source with strength $\mathbf{J}_n(\mathbf{r},\omega) = \hat{q}(j\omega\varepsilon)S^*(\mathbf{r}_n,\omega)\delta(\mathbf{r}-\mathbf{r}_n)$ with $S^*(\mathbf{r}_n,\omega)$ being the complex conjugate of $S(\mathbf{r}_n,\omega)$. The reradiated field by the *n*-th antenna element is:

$$\mathbf{E}_n^{\mathrm{TR}}(\mathbf{r},\omega) = \bar{\mathbf{G}}(\mathbf{r},\mathbf{r}_n,\omega)\cdot[-j\omega\mu\mathbf{P}_n(\omega)], \quad (2)$$

where $\mathbf{P}_n(\omega) = \hat{q}(j\omega\varepsilon)S^*(\mathbf{r}_n,\omega)$. The imaging signal may be chosen to be a component of the retransmitted fields, i.e.,

$$S_{n,p}^{\mathrm{TR}}(\mathbf{r},\omega) = \hat{p}\cdot\mathbf{E}_n^{\mathrm{TR}}(\mathbf{r},\omega),\ 1\le n\le N, \quad (3)$$

where $\hat{p}$ stands for a chosen polarization direction, say $\hat{p} = \hat{x}$. Converted into time domain, the imaging signals are denoted by $s_{n,p}^{\mathrm{TR}}(\mathbf{r},t)$ $(1\le n\le N)$. According to the time reversal focusing principle, these imaging signals will achieve their maximum amplitude values synchronically at the target position $\mathbf{r} = \mathbf{r}_s$, but non-synchronically at any non-target position $\mathbf{r} \ne \mathbf{r}_s$. The traditional TR imaging method shows a snapshot of the summed signal, i.e.,

$$I(\mathbf{r}) = \sum_{n=1}^{N} s_n^{\mathrm{TR}}(\mathbf{r},t_{\mathrm{ref}}), \quad (4)$$

where t_{ref} is a reference time that the snapshot is taken, which is usually set to be 0. This traditional approach has good performance for a single target, except that the resolution cannot beat the diffraction limit. However, if multiple targets are present, the traditional method may suffer: (i) farther or weaker targets are prone to be swamped by nearer or stronger ones; (ii) there may not exist an optimal t_{ref} for all targets or scattering centers to be appropriately rendered in one snapshot or image.

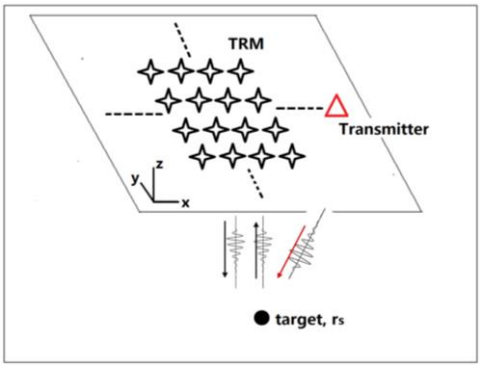

Fig. 1. Time-reversal imaging configuration.

To overcome the two problems mentioned above and improve the resolutions, a new TR imaging algorithm is proposed as follows.

(i) Divide the TRM into many sub-TRMs and construct the sub-TRM signals by:

$$u_m(\mathbf{r},t) = \sum_{l=0}^{L-1} s_{m+l}^{\mathrm{TR}}(\mathbf{r},t),\ 1\le m\le M, \quad (5)$$

where M is the total number of sub-TRMs, and L is the number of antenna elements in each sub-TRM. The *m*-th sub-TRM starts from the *m*-th antenna element, which includes L_x elements in the *x*-direction and L_y elements in the *y*-direction, so that $L = L_x \times L_y$. Specifically, the 1-st sub-TRM is a rectangular array associated with the corner elements (1,1) and (L_x, L_y). The last sub-TRM is associated with the corner elements $(N_x - L_x + 1, N_y - L_y + 1)$ and (N_x, N_y). It is clear that $M = (N_x - L_x + 1)\times(N_y - L_y + 1)$.

(ii) Normalize all the sub-TRM signals by:

$$\bar{u}_m(\mathbf{r},t) = \frac{u_m(\mathbf{r},t)}{u_m(\mathbf{r},t_m(\mathbf{r}))},\ 1\le m\le M, \quad (6)$$

where $t_m(\mathbf{r})$ is the time that makes $u_m(\mathbf{r},t)$ to achieve its maximum amplitude value at the imaging point $\mathbf{r}$. At all target positions $\mathbf{r} = \mathbf{r}_k$ $(1\le k\le K,\ K$ is the number of targets), the $t_m(\mathbf{r}_k)$ is almost independent of the index *m*, that is, all the normalized signals would synchronically achieve their maximum amplitude value 1. At any non-target position $\mathbf{r} \ne \mathbf{r}_k$, $t_m(\mathbf{r})$ is dependent on *m*, so that the normalized signals cannot synchronically achieve their maximum amplitude value 1. The normalization would allow all potential targets or scattering centers to

be shown at equal visibility to avoid swamping of farther or weaker targets by nearer or stronger ones.

(iii) To enhance the synchronism of the normalized signals at each target position and non-synchronism at any non-target position, a multiplicative signal is defined as:

$$U(\mathbf{r},t)=\prod_{m=1}^{M}\bar{u}_m(\mathbf{r},t)\,. \tag{7}$$

This manipulation would substantially improve the cross-range resolution. As a result, locating all the targets is possible by searching the positions for $U(\mathbf{r},t)$ to achieve its maximum amplitude values, which should be 1 in theory at all target positions. However, a threshold value *val* may be specified and a target is recognized if the multiplied signal is greater than the threshold. For instance, if $U(\mathbf{r}_k,t_0(\mathbf{r}_k))\ge val$, a target at $\mathbf{r}=\mathbf{r}_k$ would be recognized and the optimum moment to observe this target is $t_0(\mathbf{r}_k)$.

(iv) To alleviate the negative influence of the normalization and improve the co-range resolution, taking further advantage of the synchronism is possible. Hence, we define the final image by means of the superposition of the images $U(\mathbf{r},t_0(\mathbf{r}_k))$ $(1\le k\le K)$ that are in favor to show all targets as:

$$I(\mathbf{r})=\sum_{k=1}^{K}U(\mathbf{r},t_0(\mathbf{r}_k)). \tag{8}$$

This step would significantly enhance the co-range resolution.

III. SIMULATION VALIDATION

In this section, we provide several examples to examine the performance of the proposed method. They include one point target, two point targets at different distance, two extended targets with different scattering properties, and one point target in multiple clutters.

The simulation scenario is shown in Fig. 1. The TRM is made up of $N=N_x\times N_y=9\times 9=81$ elements, each of which is an *x*-polarized dipole. The array's pitch in both *x*- and *y*-directions is half of the center wavelength $\lambda_c/2$ of the excitation wave, which is taken to be the modulated Gaussian pulse with the center frequency at $f_c=4\,\text{GHz}$ ($\lambda_c=7.5\,\text{cm}$) and the effective bandwidth $\Delta f=4\,\text{GHz}$ ($\lambda_{\min}=5\,\text{cm}$). Only one transmitter is used in the following simulations, which is placed at $(3\lambda_c,0,0)$. The imaging domain is a cube of size $4\lambda_c\times 4\lambda_c\times 4\lambda_c$, from $-2\lambda_c$ to $2\lambda_c$ in both *x*- and *y*-directions, and from $-8\lambda_c$ to $-4\lambda_c$ in *z*-direction. FDTD method is used to perform the calculations for wave radiation, propagation and scattering. The computing domain, including the perfectly matched layers (PML), is a square cylinder with base side size $6\lambda_c$ or 45 cm and height $9\lambda_c$, which is meshed with a spatial cell size $\Delta x=\Delta y=\Delta z=0.375\,\text{cm}$.

A. One point target

For this example, we choose $L_x=L_y=1$, so that a total of $M=9\times 9=81$ sub-TRMs is formed. One point-like target is placed at $(0,0,-6\lambda_c)$. The 3D image is sown in Fig. 2, and its projections onto the *xoy*, *yoz* and *xoz* planes, respectively, are shown in Fig. 3. For comparison, the image obtained by using the traditional TR imaging method is also projected onto the *xoy*, *yoz* and *xoz* planes, respectively, as shown in Fig. 4. To have a close look, a comparison of the relative image values in the *x*- and *z*-directions is shown in Fig. 5. It is obvious that our new method has much higher resolutions in both directions than the traditional approach.

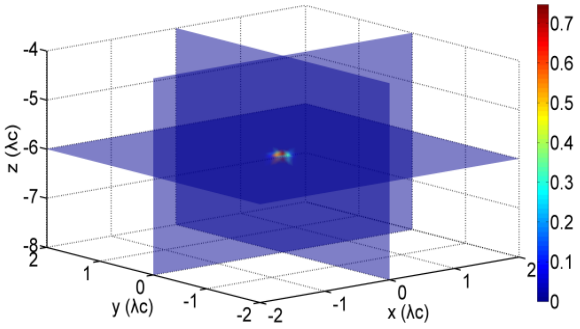

Fig. 2. Time-reversal imaging result for one point-like target by the proposed method.

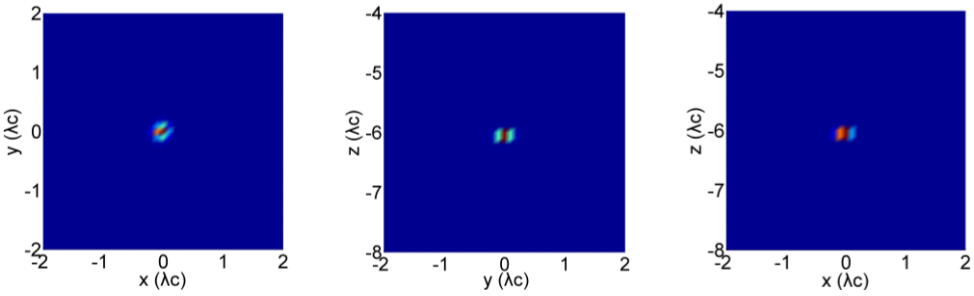

Fig. 3. The projections of Fig. 2 onto the *xoy*, *yoz*, *xoz* planes (from left to right), respectively.

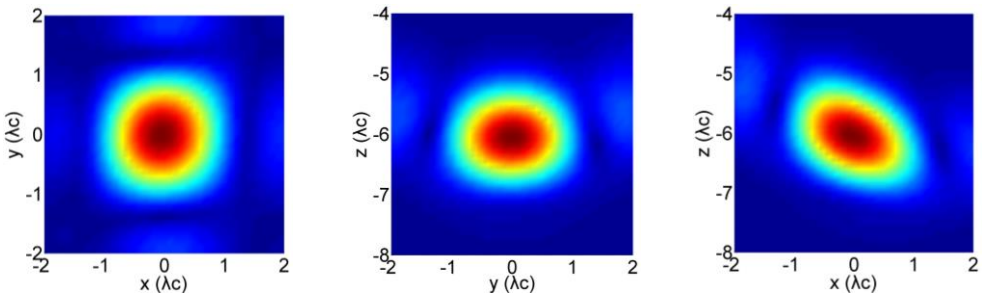

Fig. 4. The imaging results of one point-like target by the traditional method projected onto the *xoy*, *yoz*, *xoz* planes (from left to right), respectively.

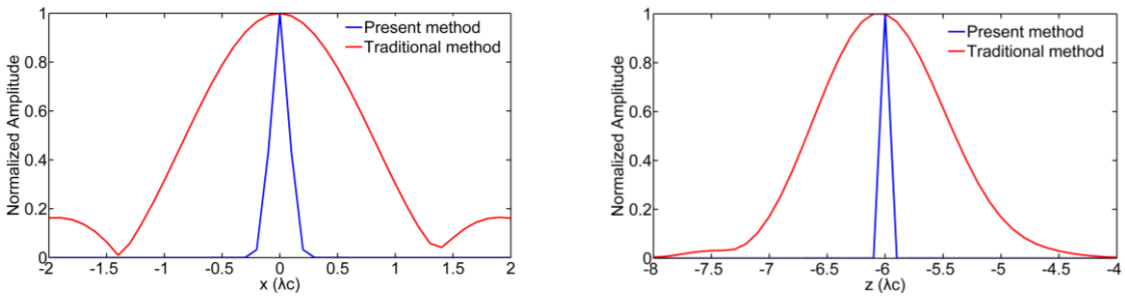

Fig. 5. Comparison of resolutions in terms of normalized amplitude values in the cross-range (left) and co-range (right) directions between the two algorithms: the present method (blue line) and the traditional method (red line).

B. Two targets at different distance

We choose $L_x = L_y = 3$ in this example, so that we get $M = 7 \times 7 = 49$ sub-TRMs. The two point-like targets are placed at $(0,0,-5\lambda_c)$ and $(0,0,-7\lambda_c)$, respectively. The projections of the image onto the *xoy*, *yoz* and *xoz* planes, respectively, are shown in Fig. 6. It is verified that both targets are almost equally well located. However, by using the traditional method, the target at the farther place is seriously degraded as shown in Fig. 7.

C. Two extended targets with different scattering properties

In this example, the simulation configuration is the same as the previous example, except that the two point-like targets are replaced by two extended spherical targets with a radius of $\lambda_c / 4$, centering at $(0,0,-7\lambda_c)$ and $(0,0,-5\lambda_c)$, respectively. The former is made of PEC, and the latter is made of dielectric material $\varepsilon_r = 3$.

The imaging result by the proposed method after being projected onto the *xoy*, *yoz* and *xoz* planes, respectively, is shown in Fig. 8. It is apparent that there are two targets in the imaging space and each target has three prominent scattering centers. However, by using the traditional method, as shown in Fig. 9, it seems hard to judge that there are two targets there. It looks that there are three targets, or there is only one target with three scattering centers.

D. One target in multiple clutters

In this last example, the simulation configuration is shown Fig. 10. But we choose $L_x = L_y = 1$ here, so that the number of sub-TRMs is equal to the number of the whole antenna elements, which is 81. One point-like target as indicated in green is located at $(0,0,-6\lambda_c)$, around which there are eight extended spherical clutters, whose radius is $\lambda_c / 4$, as indicated in yellow. First, the scattered field by the clutters in the absence of the target is calculated. Then the scattered field in the presence of the target is re-calculated. The difference field at each antenna element between the two cases is used for imaging of the target. The 3D imaging result is shown in Fig. 11. It is seen that good agreement between the actual and the constructed target is observed.

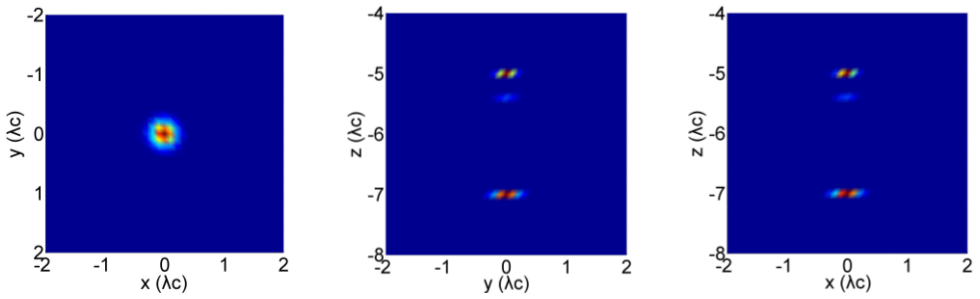

Fig. 6. The imaging results for two point-like targets by the present method projected onto the *xoy*, *yoz*, *xoz* planes (from left to right), respectively.

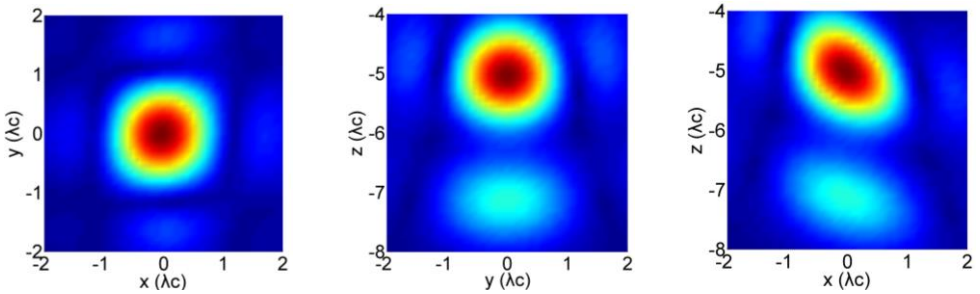

Fig. 7. The imaging results for two point-like targets by the traditional method projected onto the *xoy*, *yoz*, *xoz* planes (from left to right), respectively.

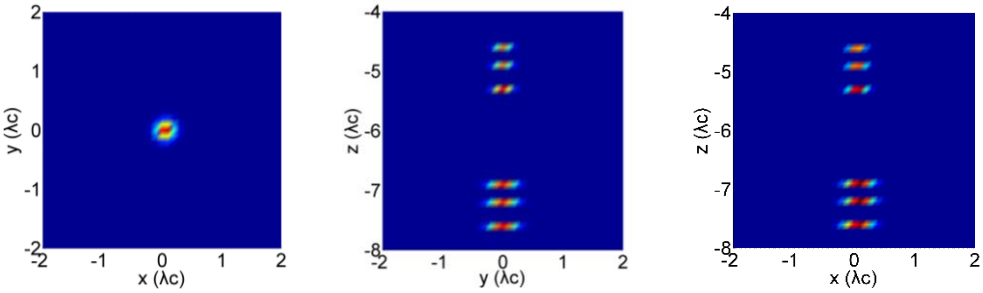

Fig. 8. The imaging results for two extended targets by the present method projected onto the *xoy*, *yoz*, *xoz* planes (from left to right), respectively.

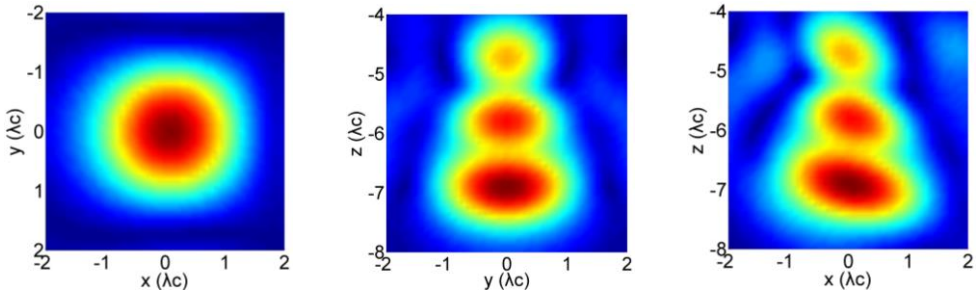

Fig. 9. The imaging results for two extended targets by the traditional method projected onto the *xoy*, *yoz*, *xoz* planes (from left to right), respectively.

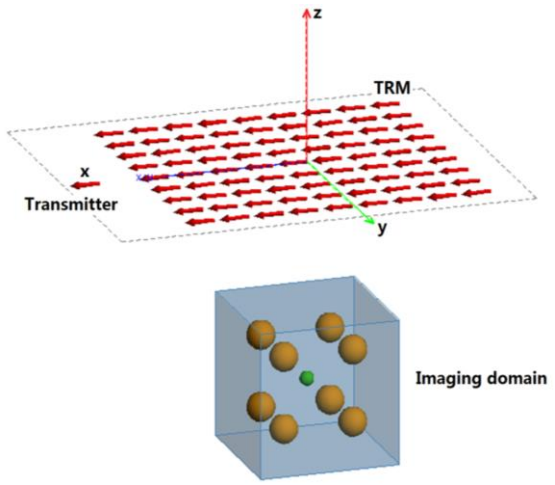

Fig. 10. Simulation configuration for imaging of one point-like target (denoted by a green sphere) in several clutters (denoted by eight yellow spheres).

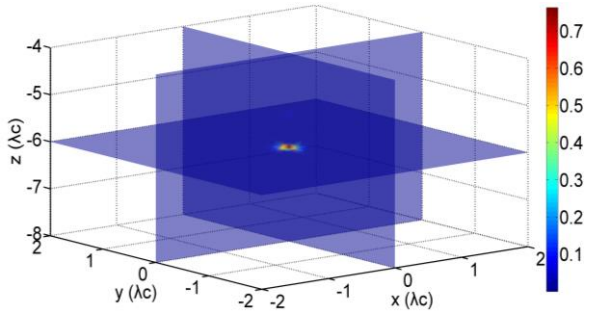

Fig. 11. Time-reversal imaging result for one point-like target situated at $(0,0,-6\lambda_c)$ in the presence of eight extended clutters.

IV. CONCLUDING REMARKS

A new time-reversal imaging method for 3D targets is proposed by making full use of the synchronism that the retransmitted signals from the TRM elements achieve their maximum amplitude values synchronically at target positions but non-synchronically at non-target positions. Implementation of the method is composed of four steps: (i) Grouping of the retransmitted signals, by which the synchronism is maintained for further processing; (ii) Normalization of the sub-TRM signals, by which all targets would be shown at equal visibility to avoid masking; (iii) Multiplication of the normalized signals, by which the cross-range resolution would be greatly enhanced; and (iv) Superposition of the images that are optimum for observation of individual targets, by which all targets would be rendered in one frame with substantially improved co-range resolution. Simulation examples show that the proposed method has satisfying performance in discriminating multiple targets or scattering centers. Further investigation of the method in noisy environment is in progress.

ACKNOWLEDGMENT

This work was supported by the NSFC Projects 61531001 and 61271032.

REFERENCES

[1] M. Fink, "Time reversal of ultrasonic fields-Part I: Basic principles," *IEEE Trans. Ultrason., Ferroelectr., Freq. Control*, vol. 39, pp. 555-566, 1992.

[2] D. Cassereau and M. Fink, "Time-reversal of ultrasonic fields-Part III: Theory of the closed time-reversal cavity," *IEEE Trans. Ultrason., Ferroelectr., Freq. Control*, vol. 39, pp. 579-592, 1992.

[3] G. Lerosey, J. De Rosny, A. Tourin, A. Derode, G. Montaldo, and M. Fink, "Time reversal of electromagnetic waves," *Phys. Rev. Lett.*, vol. 92, pp. 193904, 2004.

[4] G. Lerosey, J. De Rosny, A. Tourin, A. Derode, and M. Fink, "Time reversal of wideband microwaves," *Applied Phys. Lett.*, vol. 88, pp. 154101, 2006.

[5] H. T. Nguyen, J. B. Andersen, G. F. Pedersen, P. Kyritsi, and P. C. F. Eggers, "Time reversal in wireless communications: A measurement- based investigation," *IEEE Trans. Wireless Commun*., vol. 5, no. 8, pp. 2242-2252, Aug. 2006.

[6] H. El-Sallabi, P. Kyritsi, A. Paulraj, and G. Papanicolaou, "Experimental investigation on time reversal precoding for space-time focusing in wireless communications," *IEEE Trans. Instrumentation and Measurement*, vol. 59, no. 6. pp. 1537-1543, 2010.

[7] M. L. Ku, Y. Han, H. Q. Lai, Y. Chen, and K. J. R. Liu, "Power waveforming: Wireless power transfer beyond time reversal," *IEEE Trans. Signal Processing*, vol. 64, no. 22, pp. 5819-5834, 2016.

[8] A. B. Gorji and B. Zakeri, "Time-reversal through-wall microwave imaging in rich scattering environment based on target initial reflection method," *Applied Computational Electromagnetics Society Journal*, vol. 30, no. 6, pp. 626-637, 2015.

[9] B. Li, "Noise suppression detection method based on time reversed signal waveform similarity," *Applied Computational Electromagnetics Society Journal*, vol. 32, no. 2, pp. 141-146, 2017.

[10] D. H. Liu, G. Kang. L. Li, Y. Chen, S. Vasudevan, W. Joines, Q. H. Liu, J. Krolik, and L. Carin, "Electromagnetic time-reversal imaging of a target in a cluttered environment," *IEEE Trans. Antennas Propag*., vol. 53, pp. 3058-3066, Sep. 2005.

[11] M. E. Yavuz and F. L. Teixeira, "Full time-domain DORT for ultrawideband fields in dispersive,

random inhomogeneous media," *IEEE Trans. Antennas Propag.*, vol. 54, pp. 2305-2315, Aug. 2006.

[12] A. E. Fouda and F. L. Teixeira, "Statistical stability of ultrawideband time-reversal imaging in random media," *IEEE Trans. Geosci. Remote Sensing*, vol. 52, no. 2, pp. 870-879, Feb. 2014.

[13] G. Shi and A. Nehorai, "A relationship between time-reversal imaging and maximum likelihood scattering estimation," *IEEE Trans. Signal Process.*, vol. 55, no. 9, pp. 4707-4711, Sep. 2007.

[14] C. Prada, S. Mannevile, D. Spoliansky, and M. Fink, "Decomposition of the time reversal operator: Detection and selective focusing on two scatterers," *J. Acoust. Soc. Am.*, vol. 99, pp. 2067-2076, 1996.

[15] H. Lev-Ari and A. J. Devaney, "The time reversal techniques reinterpreted: Subspace-based signal processing for multistatic target location," *Proc. IEEE Sensor Array Multichanneal Signal Process. Workshop*, pp. 509-513, 2000.

[16] A. J. Devaney, "Super-resolution processing of multi-static data using time reversal and MUSIC," Unpublished paper, available from the author's web site. http://www.ece.neu.edu/fac-ece/devaney/ajd/preprints.htm

[17] M. E. Yavuz and F. L. Teixeira, "Ultra-wideband microwave sensing and imaging using time-reversal techniques: A review," *Remote Sens.*, vol. 1, no. 3, pp. 466-495, 2009.

[18] M. E. Yavuz and F. L. Teixeira, "Space-frequency ultrawideband time-reversal imaging," *IEEE Trans. Geosci. Remote Sens.*, vol. 46, pp. 1115-1124, 2008.

[19] S. Bahrami, A. Cheldavi, and A. Abdolali, "Ultrawideband time-reversal imaging with frequency domain sampling," *IEEE Geosci. Remote Sens. Lett.*, vol. 11, no. 3, pp. 597-601, 2014.

[20] X. M. Zhong, C. Liao, and W. B. Lin, "Space-frequency decomposition and time-reversal imaging," *IEEE Trans. Antennas Propag.*, vol. 63, no. 12, pp. 5619-5628, 2015.

[21] Y. Q. Li and M. Y. Xia, "Target location based on time focusing of time-reversal retransmitting signals," *IEEE Inter. Geosci. Remote Sensing Sym.*, Milan, Italy, pp. 3149-3151, July 2015.

Yuan-Qi Li was born in Sichuan, China, in 1988. He received the M.Sc. degree from the School of Electronic Engineering, University of Electronic Science and Technology of China, Chengdu, China, in 2012, and is currently a Ph.D. student at the same school. His research area is on computational electromagnetics and applications, especially on object detection and imaging.

Xiang-Qian Zhang was born in Shanxi, China, in 1976. He received the M.Sc. degree from the School of Optoelectronic Information, the University of Electronic Science and Technology of China (UESTC), Chengdu, China, in 2005. Currently, he is an Engineer with the School of Electronic Engineering, UESTC. His research interests include microwave antennas, computational electromagnetics and applications, and electromagnetic scattering imaging.

Ming-Yao Xia was born in Jiangxi, China, in 1963. He received the M.Sc. and Ph.D. degrees in Electrical Engineering from the Institute of Electronics, Chinese Academy of Sciences (IECAS), in 1988 and 1999, respectively. From 1988 to 2002, he was with IECAS as an Engineer and a Senior Engineer. He was a Visiting Scholar at the University of Oxford, UK, from October 1995 to October 1996. From June 1999 to August 2000 and from January 2002 to June 2002, he was a Senior Research Assistant and a Research Fellow, respectively, with the City University of Hong Kong. He joined Peking University (PKU) as an Associate Professor in 2002 and was promoted to Full Professor in 2004. He moved to the University of Electronic Science and Technology of China (UESTC) as a Chang-Jiang Professor nominated by the Ministry of Education of China in 2010. He returned to PKU after finishing the appointment in 2013. He was a recipient of the Young Scientist Award of the URSI in 1993. He was awarded the First-Class Prize on Natural Science by the Chinese Academy of Sciences in 2001. He was the recipient of the Foundation for Outstanding Young Investigators presented by the National Science Foundation of China (NSFC) in 2008. He was an Associate Editor of the IEEE Transactions on Antennas and Propagation. His research interests include electromagnetic theory, computational electromagnetics and applications, microwave antennas and components, microwave scattering remote sensing, and electromagnetic detection and imaging.

Ultra-wideband and Polarization-insensitive RCS Reduction of Microstrip Antenna using Polarization Conversion Metasurface

Jianxun Su [1], Chuiyong Kong [1], Zengrui Li [1], Xujin Yuan [2], and Yaoqing (Lamar) Yang [3]

[1] School of Information and Engineering
Communication University of China, Beijing, 100024, China
zrli@cuc.edu.cn

[2] Science and Technology on Electromagnetic Scattering Laboratory
Beijing Institute of Environmental Characteristics, Beijing 100854, China

[3] Department of Electrical and Computer Engineering
University of Nebraska-Lincoln, NE, 68182

Abstract ─ A new type of polarization conversion metasurface (PCM) is presented to reduce radar cross section (RCS) of microstrip antenna. The proposed PCM consists of evolved split ring (ESR) resonators. Through designing of the PCM unit cell with five resonances and symmetrical layout, a high polarization conversion ratio and ultra-wideband passive cancellation are achieved. The proposed antenna (with PCM) and a reference antenna are designed, simulated and measured. The measured results show that our proposed antenna can achieve 10 dB in-band and 5 dB out-of-band RCS reduction in an ultra-wide frequency band from 6 GHz to 26.7 GHz. Moreover, the PCM works efficiently for both x- and y-polarized incident waves. The measured results show a good agreement with the simulations. Compared to previous researches, the proposed PCM features a compact profile and wider operating bandwidth of RCS reduction.

Index Terms ─ Microstrip antenna, polarization conversion metasurface (PCM), radar cross section reduction, ultra-wideband.

I. INTRODUCTION

Metasurface is a kind of artificially periodic structure surface which consists of sub-wavelength unit cells. Due to its unusual performance of manipulating electromagnetic (EM) wave, it has been widely applied to radar stealth. To avoid the radar detection, it is important to reduce the radar cross section of stealth platform. As an electromagnetic radiation and received device of radar systems, antenna always makes great contribution to the overall RCS. Several solutions have been proposed in literature, such as target shaping, radar absorbing materials (RAMs), and passive cancellation. By shaping the radiation patch [1], or exploiting radar absorbing materials which transform the radio frequency energy into heat [2] could greatly reduce RCS of antenna. However, these two methods could lead to negative effects, including narrowing the bandwidth and degrading the gain of antenna, in addition, exploiting RAMs would make device bulky.

The basic principle of passive cancellation is to make a 180° phase difference on the reflect wave, so the backscattering energy could be redirected away from the boresight direction. In 2007, Paquay used artificial magnetic conductors (AMC) and perfect electric conductors (PEC) to constitute of a planar chessboard structure, and realized 20 dB RCS reduction from 15.25 GHz to 15.5 GHz [3]. Due to the bandwidth limitation of AMC, this design worked only in a narrow band. Research in [4] replaced the PEC cell with another AMC structure which worked at other resonance frequency, and achieved a 180° (±30°) phase cancellation in 5.52-6.63 GHz, broadening RCS reduction bandwidth to 20%. Two Jerusalem crosses in different size was used in [5], the RCS reduction bandwidth reached to 40.88%. Similarly, reference [6] exploited a chessboard configuration consists of Jerusalem crosses and square patches, meanwhile achieved 65.2% relative bandwidth. Reference [7,8] proposed a metasurface which composed of two types of electromagnetic band-gap (EBG) lattice, and broaden the relative bandwidth to 80% and 80.2%, respectively. Reference [9] proposed a polarization rotation reflective metasurface which composed of quasi-L-shaped patches, realized 106% relative bandwidth and 2 dB RCS reduction of planer structure. A broadband RCS reduction for microstrip antenna by utilizing polarization conversion metamaterial was realized in [10]. By employing a different design of polarization conversion unit cell, a 3 dB RCS reduction of microstrip antenna from 6 to 18 GHz (100% relative bandwidth) was achieved in [11].

Submitted On: January 15, 2017
Accepted On: April 18, 2017

In this paper, we proposed a new type of polarization conversion metasurface (PCM) to reduce in-band and out-of-band RCS of microstrip antenna. The proposed novel PCM is formed by evolved split ring (ESR) resonator. The RCS reduction bandwidth can be broadened by using the PCM with multiple resonances. Through designing the evolved split ring resonator with five resonances, an ultra-wideband and high efficient polarization conversion is achieved. Then, the radiation patch of the proposed antenna is surrounded by the PCM unit cell in symmetrical layout, thus an ultra-wideband passive cancellation and RCS reduction are realized. The designed PCM is verified through full-wave simulations and experiments. The measured results show that the proposed antenna has a remarkable (5 dB) RCS reduction over 126.5% relative bandwidth from 6 GHz to 26.7 GHz. Compared to other designs, the proposed PCM shows a compact profile and wider operating bandwidth. Moreover, the proposed PCM has excellent RCS reduction performance for both x- and y-polarized incident waves.

II. DESIGN AND SIMULATION

A. Design of the proposed PCM unit cell

Extensive research interest in manipulation of electromagnetic waves by using polarization conversion technology [9-13] has been applied in the microwave, terahertz, and even optical frequency bands. The proposed PCM is based on polarization conversion, and composed of an evolved split ring resonator. Figure 1 shows the geometry of the PCM unit cell, which is separated by a dielectric substrate F4B ($\varepsilon_r=2.65, \tan\delta=0.001$), with its top layer based on evolved split ring, and the bottom layer is metallic ground plane. The structure of ESR has a symmetric axis which along the 45° direction with respect to positive y-axis direction. In particular, the evolved split ring is designed in sunken deformation to increase the length of the entire metallic ring, which can increase the inductance and broaden the bandwidth.

The numerical simulation is carried out to analyze the reflection characteristic of the PCM unit cell with a commercial program, CST2015 (time domain solver). In the simulation, Floquet boundary and genetic algorithm are used to optimize the unit cell to make a better compromise between bandwidth and polarization conversion ratio (PCR). As shown in the Fig. 1, the optimize sizes of PCM unit cell are p=6 mm, R1=2.02 mm, R2=2.27 mm, R3=2.53 mm, R4=2.78 mm, Deg1=55.15°, Deg2=36.60°, Deg3=26.95°, h=3 mm.

To better understand the polarization conversion of electromagnetic waves of PCM, the reflection coefficients of the proposed PCM unit cell for x-polarized waves under normal incidence are depicted in Fig. 2. It is found that the bandwidth of polarization conversion is broaden to an ultrawide range by generating multiple resonances, and more than 80% PCR occurs from 5.8 GHz to 26 GHz. Five resonance frequencies are excited at 6.1 GHz, 8.2 GHz, 14.5 GHz, 22.6 GHz, 25.7 GHz where the PCR are nearly 100%, and which means that nearly all the electric field energy of x-polarized incident waves is converted to the y-polarized direction. Table 1 shows a comparison of PCR between the proposed PCM and other researches. It is noted that the proposed PCM unit cell has an excellent polarization conversion characteristic which can change a linearly polarized incident waves into cross-polarized reflected waves significantly in an ultra-wideband range. In addition, there are 45° angle between the symmetry axis of proposed unit cell and both x-axis and y-axis, so the proposed PCM unit cell can also convert normally incident y-polarized waves into x-polarized reflected waves with the same conversion efficiency.

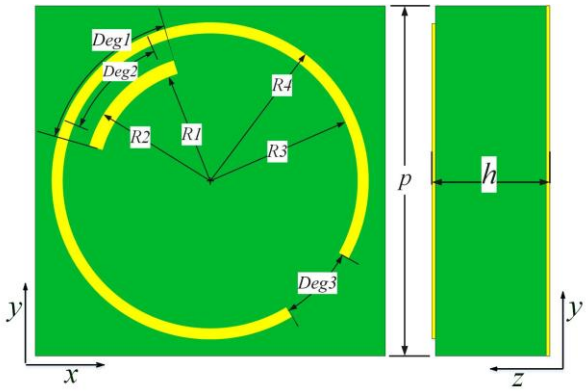

(a) (b)

Fig. 1. Geometry of the PCM unit cell: (a) top view and (b) side view.

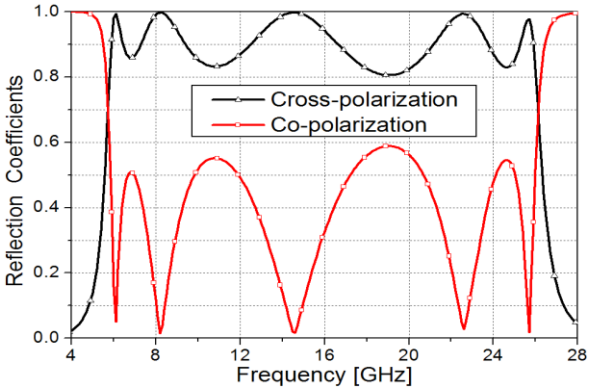

Fig. 2. The reflection coefficients of proposed PCM unit cell for x-polarized waves under normal incidence.

Table 1: Comparison of the PCR and bandwidth

	PCR	Frequency Range [GHz]	Bandwidth
[9]	96.4%	10.74-17.72	49%
[11]	80%	6-18	100%
[12]	90%	12.4-27.96	77.1%
[13]	70%	6-24.2	120.5%
This paper	80%	5.8-26	126.5%

B. Design of the microstrip antenna

The configurations of the reference antenna and proposed antenna are presented in Fig. 3, respectively. The dielectric substrate of antennas is also F4B material, with a dielectric constant ε_r=2.65 and a loss tangent $\tan\delta$=0.001. The reference antenna works at frequency band from 8.75 GHz to 10.1 GHz, and the resonant frequency is designed at 9.3 GHz. The dimensions of antennas are L=10.5 mm, W=8.7 mm, T=72 mm. The thickness of the antennas is 3 mm, so the PCM in the proposed antenna is designed to be coplanar with the antenna, and made up of 4 ESR-blocks. The adjacent ESR-blocks are mirror symmetry with respect to both the x-axis and y-axis. To satisfy period boundary condition used in simulation, every ESR-block is composed of 6×6 unit cells. 16 unit cells in the center of the whole PCM are removed to place the antenna. Furthermore, the structure of overall proposed antenna is mirror symmetry with respect to both the x-axis and y-axis.

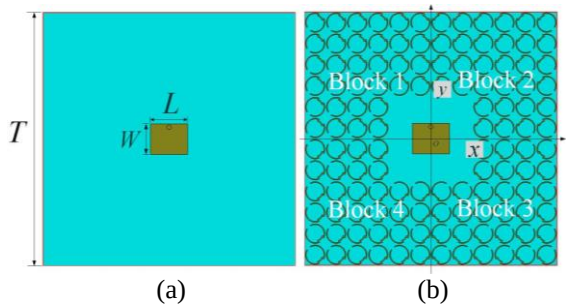

Fig. 3. The configuration of antennas: (a) reference antenna (without PCM), and (b) proposed antenna (with PCM).

Figure 4 shows the reflected electric field of the top layer of proposed antenna at 9.3 GHz for x-polarized waves under normal incidence. Because the adjacent ESR-blocks are mirror symmetry with respect to both the x-axis and y-axis, the y-component of electric field reflected from the adjacent ESR-blocks are mirrored. It is seen that the y-components of the reflected field are reversal (180° phase difference), therefore, a passive cancellation can be obtained. The 3-D scattered patterns of two antennas at 9.3 GHz for x-polarized waves are shown in Fig. 5. Under normal incidence, the proposed antenna converts normally incident x-polarized waves into y-polarized reflected waves, and the passive phase cancellation occurs between the y-polarized reflected waves of adjacent ESR-blocks of proposed antenna, so the backscattering is dramatically reduced along the principal planes (XZ, YZ). Compared with the bistatic RCS of reference antenna, the scattered energy of proposed antenna is redirected away from the boresight direction, and the monostatic RCS is significantly reduced while four sidelobes produce.

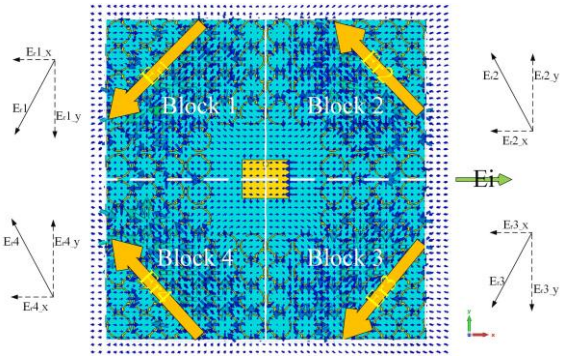

Fig. 4. Reflected electric field of the top layer of proposed antenna at 9.3 GHz for x-polarized waves under normal incidence.

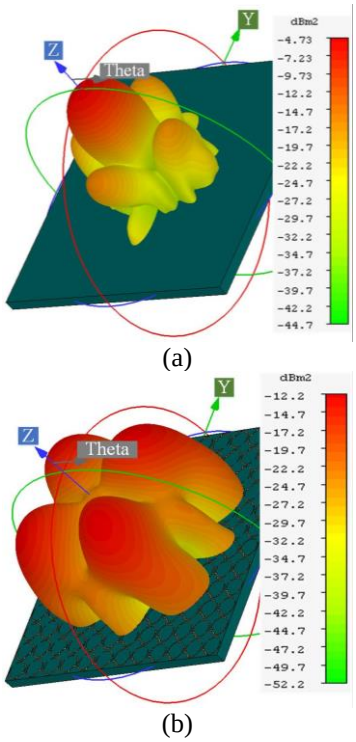

Fig. 5. 3-D scattering patterns of antennas at 9.3 GHz for x-polarized waves under normal incidence: (a) without PCM and (b) with PCM.

C. RCS reduction of the proposed antenna

Figure 6 (a) shows the co-polarized results of simulated monostatic RCS of antennas for x-polarized and y-polarized incident waves under normal incidence. The proposed antenna achieves more than 5 dB RCS reduction from 5.8 GHz to 26 GHz. Especially, the RCS reduction value reaches up to 10 dB on the working band of antenna. In addition, it is noted that the RCS reduction curves are almost coincide for x-polarized and y-polarized incident waves. Due to the proposed antenna are symmetric with respect to both the x-axis and y-axis, RCS reduction is insensitive to the polarization of incident waves. The cross-polarized results of monostatic RCS are presented in Fig. 6 (b). Due to 180° phase difference of cross-polarized reflection between the adjacent ESR-blocks of the proposed PCM, and a passive cancellation is realized in the proposed antenna, leading to an ignorable cross-polarization RCS (<-110 dB). Considering the trade-off of radiation performance and RCS reduction, the proposed metasurface is an excellent design for RCS reduction of low profile antenna.

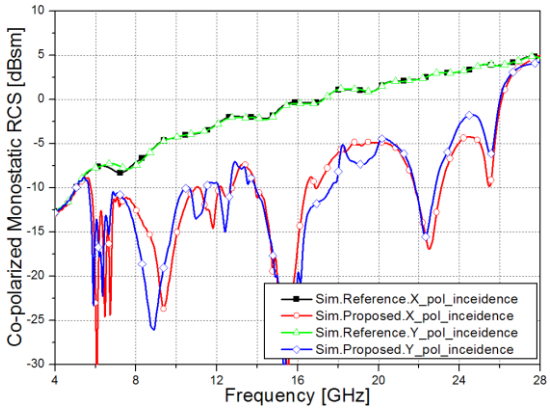

(a)

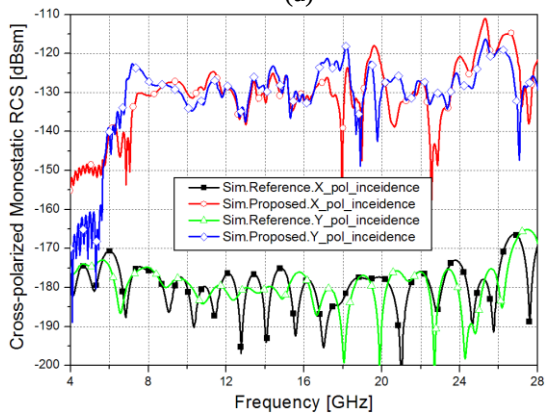

(b)

Fig. 6. Monostatic RCS of antennas for x-polarized and y-polarized incident waves under normal incidence: (a) co-polarized monostatic RCS, and (b) cross-polarized monostatic RCS.

III. MEASUREMENT AND DISCUSSION

In order to verify the novel PCM of RCS reduction, the reference and proposed antennas are fabricated and measured. The fabricated antennas are fed by 50 Ohm SMA coaxial connector whose top view and bottom view are presented in Fig. 7. The overall size of the fabricated antennas is 72 mm × 72 mm, and 128 PCM unit cells are symmetric arrangement in the proposed antenna. Moreover, the periodicity of PCM unit cell is only 0.2λ to the resonant frequency of reference antenna.

All the full wave EM simulations of antennas are conducted in CST (frequency domain solver and PML boundary) and the impedance characteristics of antennas are measured by Agilent E5071C vector network analyzer. Figure 8 shows the measured and simulated results of reflection coefficients. Although the resonant frequency is slightly offset on the measured results, the impedance bandwidth ($|S_{11}|$ < -10 dB) of reference and proposed antennas is in good agreement. Figure 9 indicates the E-plane and H-plane radiation patterns of reference and proposed antennas at the resonant frequency (9.3 GHz). Compared with the reference antenna, the radiation characteristics of proposed antenna are effectively preserved for both E-plane and H-plane.

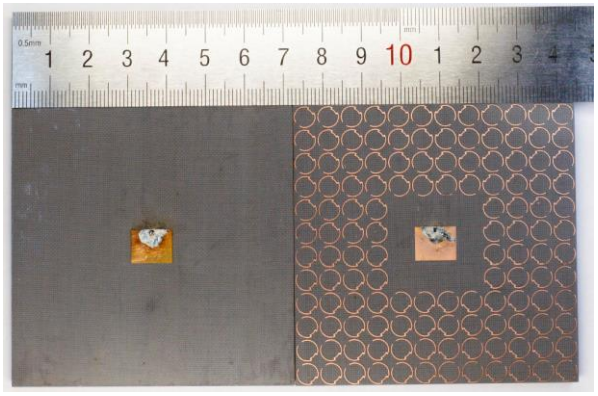

(a)

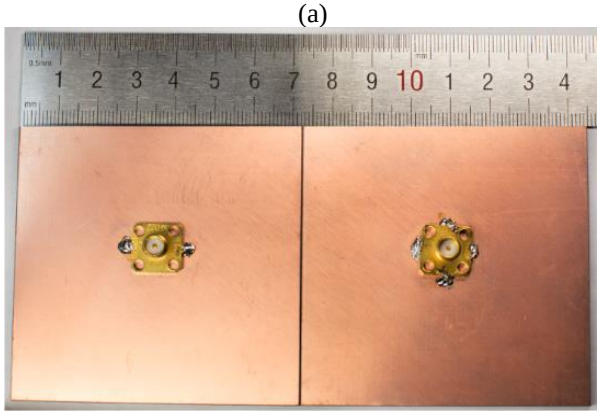

(b)

Fig. 7. Prototype of the fabricated reference and proposed antenna: (a) top view and (b) bottom view.

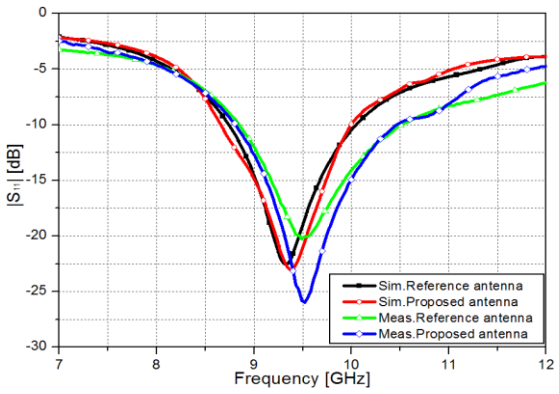

Fig. 8. Comparisons between the simulation and the measured S-parameters of antennas.

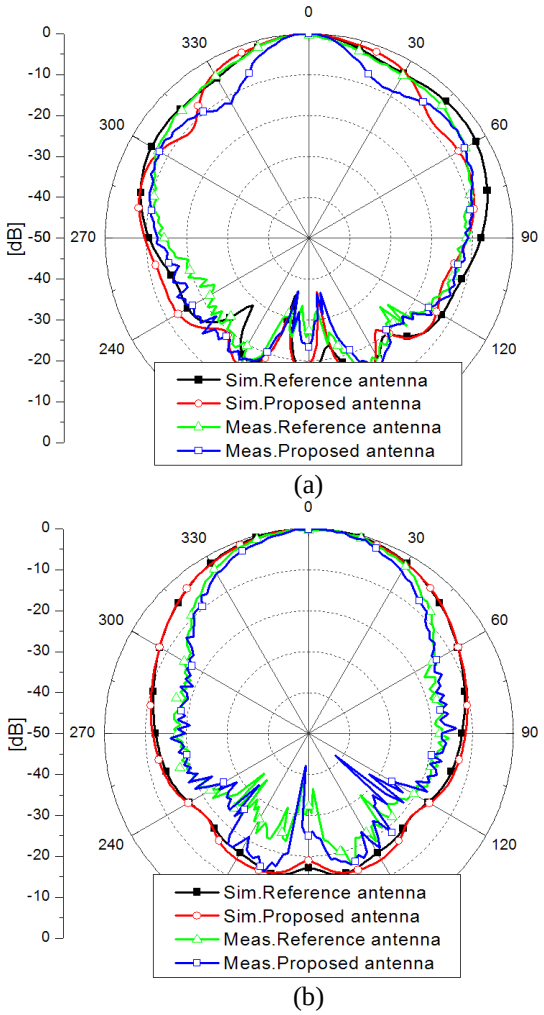

Fig. 9. Comparison between the simulated and measured radiation patterns of antennas at 9.3 GHz: (a) E-plane and (b) H-plane.

In order to confirm the wideband RCS reduction characteristic, the monostatic RCS of reference and proposed antennas are measured in the anechoic chamber of Science and Technology on Electromagnetic Scattering Laboratory in Beijing. Figure 10 shows the schematic setup of RCS measurement. The comparison of simulated and measured results for x-polarized incident waves under normal incidence are shown in Fig. 11. It is clear that the proposed antenna gives a remarkable in-band and out-band RCS reduction from 6 GHz to 26.7 GHz, and the maximum in-band reduction value reaches 20 dB on the resonant frequency of antenna. Experiment results show good agreement with the corresponding simulation. The slight deviation can be attributed to the measurement and fabrication tolerance. Similar to the previous analysis of PCM, an ultra-wideband polarization conversion and passive cancellation are demonstrated in the measurement.

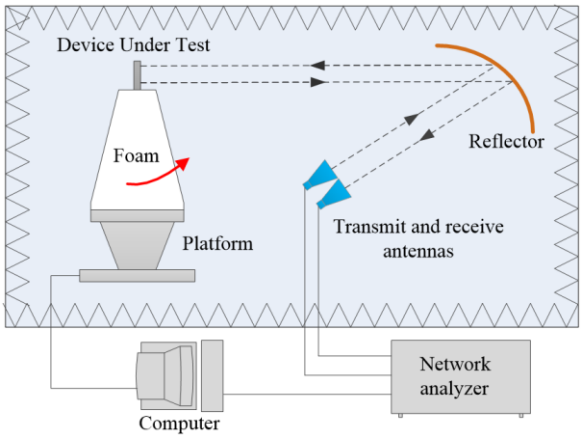

Fig. 10. Schematic setup of the RCS measurement in an anechoic chamber.

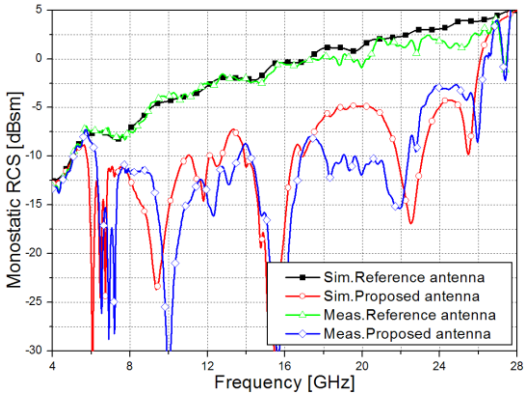

Fig. 11. Comparison of the simulated and measured monostatic RCS of antennas for x-polarized incident waves under normal incidence.

VI. CONCLUSION

In this paper, a novel metasurface of RCS reduction for low profile antenna is presented. By designing the

unit cell of proposed PCM with multiple resonances and symmetrical layout, high polarization conversion ratio and ultra-wideband passive cancellation are achieved. Meanwhile, by loading the proposed PCM, the proposed antenna has a remarkable (5 dB) RCS reduction in ultra-wideband range which the relative bandwidth reach to 126.5%, and the antenna radiation characteristics are also preserved. Meanwhile, because of the symmetry design of both the proposed PCM and antenna, the excellent RCS reduction is insensitive to the polarization of incident waves. The radiation and scattering properties of the proposed antenna is verified by simulations and experiments. The experimental results are in good agreement with the simulated results. Compared to the other kinds of metamaterials, the proposed metasurface is also extremely thin and compact sizes, which makes it convenient for integration with other devices, and can be widely applied to other planar stealth platforms, such as vehicles, ships and aircrafts.

ACKNOWLEDGMENT

Authors thank the supports from the National Natural Science Foundation of China under Grants No. 61671415 and No. 61331002, the Excellent Innovation Team of CUC under Grant No. yxtd201303, and the CUC Scientific Research Project under Grant No. 3132016XNG1604.

REFERENCES

[1] C. M. Dikmen, S. Cimen, and G. Cakir, "Design of double-sided axe-shaped ultra-wideband antenna with reduced radar cross-section," *IET Microwaves, Antennas & Propagation*, vol. 8, pp. 571-579, 2014.

[2] S. Genovesi, F. Costa, and A. Monorchio, "Wideband radar cross section reduction of slot antennas arrays," *IEEE Trans. Antennas and Prop.*, vol. 62, pp. 163-173, 2014.

[3] M. Paquay, J. C. Iriarte, I. Ederra, R. Gonzalo, and P. de Maagt, "Thin AMC structure for radar cross-section reduction," *IEEE Trans. Antennas and Prop.*, vol. 55, pp. 3630-3638, 2007.

[4] Y. Zhao, X. Cao, J. Gao, and W. Li, "Broadband RCS reduction and high gain waveguide slot antenna with orthogonal array of polarisation-dependent AMC," *Electronics Letters*, vol. 49, pp. 1312-1313, 2013.

[5] J. C. Iriarte Galarregui, A. Tellechea Pereda, J. L. Martinez de Falcon, I. Ederra, R. Gonzalo, and P. de Maagt, "Broadband radar cross-section reduction using AMC technology," *IEEE Trans. Antennas and Prop.*, vol. 61, pp. 6136-6143, 2013.

[6] Y. Zheng, J. Gao, X. Cao, Z. Yuan, and H. Yang, "Wideband RCS reduction of a microstrip antenna using artificial magnetic conductor structures," *IEEE Antennas and Wireless Propagation Letters*, vol. 14, pp. 1582-1585, 2015.

[7] J. X. Su, Y. Lu, Z. R. Li, R. R. Zhang, and Y. L. Yang, "A wideband and polarization-independent metasurface based on phase optimization for monostatic and bistatic radar cross section reduction," *International Journal of Antennas and Propagation*, vol. 2016, 2016.

[8] J. X. Su, Y. Lu, Z. Y. Zheng, Z. R. Li, Y. L. Yang, Y. X. Che, and K. N. Qi, "Fast analysis and optimal design of metasurface for wideband monostatic and multistatic radar stealth," *Journal of Applied Physics*, vol. 120, pp. 205107, 2016.

[9] Y. Jia, Y. Liu, Y. J. Guo, K. Li, and S. Gong, "Broadband polarization rotation reflective surfaces and their applications to RCS reduction," *IEEE Trans. Antennas and Prop.*, vol. 64, pp. 179-188, 2016.

[10] Y. Liu, Y. Hao, K. Li, and S. Gong, "Radar cross section reduction of a microstrip antenna based on polarization conversion metamaterial," *IEEE Antennas and Wireless Propagation Letters*, vol. 15, pp. 80-83, 2016.

[11] Y. Liu, K. Li, Y. Jia, Y. Hao, S. Gong, and Y. J. Guo, "Wideband RCS reduction of a slot array antenna using polarization conversion metasurfaces," *IEEE Trans. Antennas and Prop.*, vol. 64, pp. 326-331, 2016.

[12] X. Gao, X. Han, W. P. Cao, H. O. Li, H. F. Ma, and T. J. Cui, "Ultra-wideband and high-efficiency linear polarization converter based on double V shaped metasurface," *IEEE Trans. Antennas and Prop.*, vol. 63, pp. 3522-3530, 2015.

[13] S. Sui, J. Yu, H. Ma, J. Zhang, J. Wang, Z. Xu, and S. Qui, "Ultra-wideband polarization conversion metasurface based on topology optimal design and geometry tailor," *Applied Computational Electromagnetics Society (ACES) Journal*, vol. 31, no. 7, July 2016.

Jianxun Su received the M.S. degree and the Ph.D. degree in Electromagnetic Field and Microwave Technology from the Communication University of China and Beijing Institute of Technology, Beijing, China, in 2008 and 2011, respectively.

From 2011 to 2013, he was with East China Research Institute of Electronic Engineering (ECRIEE), where he engaged in phased-array research. From 2013 to 2015, he worked as Postdoctoral Fellow at Electromagnetic Laboratory, Communication University of China (CUC). Since 2015, he was an Associate Professor in CUC. His research interests include

computational electromagnetics, low scattering metamaterials/metasurface, lens antennas, and multipath propagation.

Chuiyong Kong received the B.S. degree in Communication Engineering from Communication University of China, Beijing, China, in 2015. He is currently pursuing the M.S. degree of Electromagnetic Field and Microwave Technology at Communication University of China, Beijing, China. His research interests include metamaterials, antenna and radar cross section reduction.

Zhengrui Li received the B.S. degree in Communication and Information System from Beijing Jiaotong University, Beijing, China, in 1984, the M.S. degree in Electrical Engineering from Communication University of China, Beijing, China, in 1987, and the Ph.D. degree in Electrical Engineering from Beijing Jiaotong University, Beijing, China, in 2009.

He is currently a Professor with the Communication University of China, Beijing, China. He studied at Yokohama National University, Yokohama, Japan, from 2004 to 2005. And he was a Visiting Scholar at Pennsylvania State University from October 2010 to January 2011. His research interests include the areas of computational electromagnetics, the finite-difference time-domain (FDTD) methods, electromagnetic modeling and simulation of antennas, and communication antennas.

Li is a Senior Member of the Chinese Institute of Electronics.

Yaoqing (Lamar) Yang received his B.S. degree from the Northern Jiaotong University, China, and his M.S. degree from the Beijing Broadcast Institute, China, both in Electrical Engineering. He received his Ph.D. degree in the area of Wireless Communications and Networks from the University of Texas (UT) at Austin. He is now an Associate Professor in the Department of Electrical and Computer Engineering, University of Nebraska-Lincoln (UNL).

His current research interests lie in wireless communications and networks with emphasis on radio channel characterizations, cognitive radio networks, and statistical signal processing. Yang is a Senior Member of IEEE.

Electromagnetic Modelling of Bundle of Single-walled Carbon Nanotubes with Circular Geometry for Antenna Applications

Yaseen N. Jurn [1,2], Mohamedfareq Abdulmalek [3], Hasliza A. Rahim [4], Sawsen A. Mahmood [5], and Wei-Wen Liu [6]

[1] School of Computer and Communication Engineering
University Malaysia Perlis (UniMAP), 02000 Arau, Perlis, Malaysia
yaseen_nasir@yahoo.com

[2] Minister of Science and Technology, Baghdad, Iraq

[3] Faculty of Engineering and Information Sciences
University of Wollongong in Dubai (UOWD), Dubai, United Arab Emirates
mohamedfareqmalek@uowdubai.ac.ae

[4] Bioelectromagnetics Research Group (BioEM), School of Computer and Communication Engineering
University Malaysia Perlis (UniMAP), Pauh Putra, Arau, Perlis 02600, Malaysia
hrahim3@gmail.com

[5] Computer Science Department, College of Education
University of Mustansiriyah, Baghdad, Iraq
mahmood_sawsan@yahoo.com

[6] Institute of Nano Electronic Engineering
University Malaysia Perlis (UniMAP), 01000 Kangar, Perlis, Malaysia
vwenliu@yahoo.com

Abstract ─ This paper aims to present an effective electromagnetic (EM) modelling approach for circular bundle of single-walled carbon nanotubes (CB-SWCNTs), based on the electrical conductivity, relative complex permittivity and linear distribution impedance by applying General Ohm's law for this bundle. The equivalent single conductor material (ESCM) model for personification the CB-SWCNTs is presented in this paper. The main target of this modelling approach is to estimate and investigate the EM properties of CB-SWCNTs using common EM engineering tool solver CST (MWS). For this purpose, the CB-SWCNTs and ESCM dipole antennas will be designed and implemented using CST (MWS). Mathematically, the equivalent conductivity model, relative complex permittivity and other parameters of the CB-SWCNTs will be derived in this paper and considered as equivalent material parameters for the ESCM. This modelling technique is expected to provide new avenues for designing different antenna structures.

Index Terms ─ Bundle of SWCNTs, CB-SWCNTs, CB-SWCNTs dipole antenna, CNTs dipole antenna, nano-dipole antenna.

I. INTRODUCTION

In recent years, the carbon nanotubes composite (CNTs-composite) have been an efficient candidate material for different applications due to their unique electrical and physical properties. However, the CNTs-composite material is still at the forefront of research today. It is also considered as promising material for nano-scale applications.

The essential investigations of the CNTs antenna model have been conducted by many researchers using different comprehensive techniques [1-8]. A lot of research had been presented by Hanson et al. [9-15], in order to investigate and study the fundamental electrical properties as well as the EM behavior of the SWCNT dipole antenna. In the context of these studies, in [6] Hanson provided an equivalent model for SWCNT using a common solid conducting material as nanowire, which will be adopted in this work to present the simple equivalent modelling approach for the SWCNT in the

Submitted On: May 4, 2016
Accepted On: February 6, 2017

CST (MWS).

The bundle of SWCNTs (B-SWCNTs) structure was proposed by many researchers instead of individual SWCNT to mitigate the problems related to the SWCNT-dipole. Therefore, several studies used the circuit modelling technique for modelling the B-SWCNTs, in order to investigate its electrical and EM properties with different cross-sectional area (rectangular and circular cross-section) [17-25]. For this purpose, the B-SWCNTs dipole antenna configuration was utilized by many researchers to investigate the EM properties of B-SWCNTs [26-30]. Previous research was implemented B-SWCNTs dipole antenna using an equivalent circuit modelling approach and numerical mathematical approach. In contrast, it is very difficult to implement these modelling approaches in the available EM engineering tool solver.

The most important issue of the nanotechnology devices was represented by conducting a communication between the devices themselves and the outside world. For this reason, this work presents an attempt to get benefits from the advantages of the CB-SWCNTs properties to mitigate this issue by designing nano-antennas. Therefore, the estimation of the EM behavior of CB-SWCNTs with several cross-sectional areas through available EM engineering software package is a significant matter. Therefore, this paper presents equivalent modelling approach (ESCM) for the bundle of SWCNTs with a circular cross-sectional area (CB-SWCNTs). As well as, the simple modelling approach for the SWCNT is presented for the purpose of design the multi conductors CB-SWCNTs. These modelling approaches will be utilized to exhibit the EM properties of the CB-SWCNTs structure and to validate the equivalent modelling approach of CB-SWCNTs. The equivalent single conductor material model (ESCM) is proposed to personification the CB-SWCNTs, based on applying the electrical conductivity, relative complex permittivity, linear distribution impedance, and General Ohm's law. Also, the nano-solid tube material model (NSTM) is utilized to represent the SWCNT by applying the same rules and conditions. The purpose of ESCM modelling approach is to investigation and prediction the EM properties of this bundle with different numbers of SWCNTs. To validate this modelling approach, the dipole antenna configuration of multi conductors CB-SWCNTs based on NSTM model and the corresponding ESCM model will be designed and implemented in the CST (MWS). The comprehensive performance comparisons between the ESCM modelling approach results and the results of related corresponding works will be performed. Finally, the matching input impedance issue of SWCNT dipole antenna and CB-SWCNTs dipole antenna is discussed.

II. FRAMEWORK

For the purpose of EM modelling of CB-SWCNTs, the progress of this framework is presented as follows: First, explain the general configuration of CB-SWCNTs. Second, the CB-SWCNTs is represented by an equivalent single conductor material (ESCM) model and then implemented in the CST (MWS) with a circular cross-sectional area by inserting the material parameters of CB-SWCNTs into CST (MWS). A mathematical analysis related to an equivalent complex conductivity, complex permittivity and other important parameters of the CB-SWCNTs is presented in this work. Third, the nanoscale solid tube material model (NSTM) which is an equivalent to the SWCNT is presented to design the multi conductors CB-SWCNTsdipole antenna. Finally, the ESCM dipole antenna is utilized to predict the EM properties of CB-SWCNTs structure in different geometrical size and dimensions.

A. Configuration of CB-SWCNTs

The CB-SWCNTs is constructed of several identical numbers (N) of armchair-SWCNTs which has a radius (r), which are arranged in parallel and aligned along the axis of bundle. The number of SWCNTs in this bundle depends on its circular cross-sectional area. Figure 1 shows the sketch of CB-SWCNTs.

This configuration is presented in this work based on neglecting the effects of wrapping and twisting of the SWCNTs in the bundle by assuming that all SWCNTs are parallel aligned along the same axis [31]. In addition, the electron transport along individual SWCNT is slightly affected by the nearest SWCNTs in the bundle because the inter-tube conductance is slightly compared to the conductance along the SWCNT [32].

In this configuration, the cross-section specific area of CB-SWCNTs is calculated as a function of their characteristics (radius of SWCNT r, lattice constant Δ, and number of SWCNTs in the bundle N) and vice versa:

$$R_B = r + (2r + \Delta)(N_x - 1). \tag{1}$$

Due to the hexagonal geometric structure of this bundle, the total number (N) of SWCNTs included in the bundle depending on the number of outer side SWCNTs (Nx) that forms the outer side of the hexagonal structure. Where, the radius of CB-SWCNTs (R_B) represents the radius of the ESCM model:

$$N_x = \left(\frac{R_B - r}{(2r + \Delta)} \right) + 1, \tag{2}$$

$$N = 1 + \sum_{j=2}^{N_x} 6\,(j-1). \tag{3}$$

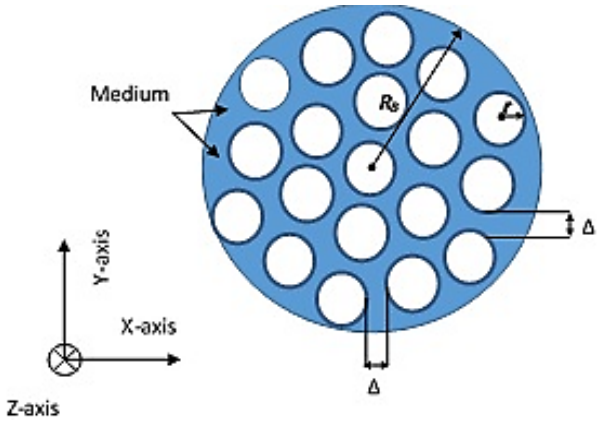

Fig. 1. Cross section of CB-SWCNTs with equivalent radius (R_B) and identical SWCNTs with radius (r).

B. Mathematical analysis of CB-SWCNTs

In this section, the key material parameters of CB-SWCNTs are derived based on the mathematical analysis of this bundle. The effective conductivity model of the CB-SWCNTs is derived mathematically for the purpose of simulation and modelling approach. The equivalent conductivity model of the CB-SWCNTs is represented by a general form bellow:

$$\sigma_{bundle} = \sigma_{scalar}\ I = \begin{bmatrix} \sigma_x \\ \sigma_y \\ \sigma_z \end{bmatrix} \begin{bmatrix} 1\ 0\ 0 \\ 0\ 1\ 0 \\ 0\ 0\ 1 \end{bmatrix} = \begin{bmatrix} \sigma_x & 0 & 0 \\ 0 & \sigma_y & 0 \\ 0 & 0 & \sigma_z \end{bmatrix}. \quad (4)$$

Where (I) is the identity matrix, (σ_{bundle}) is the effective complex conductivity model of CB-SWCNTs and (σ_{scalar}) is the scalar function consist of different components of the conductivity with different directions (x, y, and z-direction). When the bundle is oriented along the z-direction, therefore, the main component of the conductivity is the (σ_z); whereas the other components (σ_x and σ_y) are not taken into account in this work. The embedded medium of this bundle which is assumed has a very small conductivity ($\sigma_{\text{med}} \cong 0$) or ideal dielectric medium. Therefore, at $\sigma_{bundle} >> \sigma_{med}$, $\sigma_{\text{med}} \cong 0$ and $\sigma_x = \sigma_y = 0$, the conductivity of the bundle is deduced as shown below:

$$\sigma_{bundle} = \sum_{j=1}^{k} m_j \sigma_{zj}. \quad (5)$$

Where, k is the number of materials constructed the bundle and m_j is the volume fraction factor of the material. In this work, the number of materials is two (which are SWCNTs and dielectric material of the medium). Therefore, the mentioned Equation (5) is given by the general formula below:

$$\sigma_{bundle} = \sum_{j=1}^{2} m_j \sigma_{zj} = m_1 \sigma_{z1} + m_2\ \sigma_{z2}. \quad (6)$$

Where, (σ_{z1}) is the conductivity of SWCNTs (σ_{SWCNT}), and (σ_{z2}) is the conductivity of the imbedded material (dielectric medium).

$$\sigma_{bundle} = m_1 \sigma_{SWCNT} + m_2\ \sigma_{med}. \quad (7)$$

At $\sigma_{\text{med}} \cong 0$, the conductivity of the CB-SWCNTs is deduced by this formula:

$$\sigma_{bundle} = \sigma_{SWCNT}\ \frac{N\ A_{SWCNT}}{A_B}. \quad (8)$$

Where A_{SWCNT} is a cross-sectional area of the individual SWCNT (circumference of the SWCNT), and A_B is the cross-sectional area of the bundle. The formula mentioned in Equation (8), can be utilized with bundle has (circular or rectangular) cross-sectional area. From the relation between the two areas of SWCNT and CB-SWCNTs (A_{SWCNT} and A_B) the volume fraction V_{FR} for this structure is represented by the form ($V_{FR} = \frac{N\ A_{SWCNT}}{A_B}$). Then, this leads to:

$$\sigma_{bundle} = \sigma_{SWCNT}\ \frac{2r\ N}{R_B^2}. \quad (9)$$

Based on the conductivity of the SWCNT presented in [9], the Equation (9) is given by the form below:

$$\sigma_{bundle} = -\ j\ \frac{4Ne^2 V_f}{\pi^2 R_B^2 h(w - jv)}. \quad (10)$$

Where, e is the electron charge, h is the reduced Plank's constant ($h = 1.05457266 \times 10^{-34}\ J.s$), V_f is the Fermi velocity of CNT ($V_f = 9.71 \times 10^5$ m/s), v is a phenomenological relaxation frequency of SWCNT ($v = 6T/r$), so, $F_v = v/2\pi$, where (T=300) is temperature in kelvin, and w is the angular frequency.

From Equation (10), the complex conductivity of the bundle depends on the number of SWCNTs and the cross-sectional area of the bundle. Hence, this conductivity represents the equivalent conductivity of the ESCM model:

$$\sigma_{bundle} = \sigma_{ESCM}. \quad (11)$$

In addition to the effective conductivity model of the CB-SWCNTs structure, the plasma frequency is considered as a remarkable parameter for the EM modelling and simulation of the CB-SWCNTs structure in different 3D EM simulation software package for

antenna applications. On the bases of the effective conductivity model mentioned in Equation (10) and the bulk conductivity model presented by Hanson [9], the plasma frequency (w_{PB}) of the CB-SWCNTs and ESCM model is deduced as follows:

$$w_{PB} = \frac{2e}{\pi R_B}\sqrt{\frac{N_{eq,B}\ V_f}{\varepsilon^o h}}\ . \tag{12}$$

Where $N_{eq,B} = \left(\frac{4Nm_eV_f}{\pi^2 R_B r^2}\right)$ is the number of electrons per unit volume of the bundle; also, the phenomenological relaxation frequency (v_B) of the CB-SWCNTs is given by this formula below:

$$v_B\ =\ \frac{6T}{R_B}\,. \tag{13}$$

On the other hand, the real part ($\varepsilon_B^{'}$) and imaginary part ($\varepsilon_B^{"}$) of the relative complex permittivity of CB-SWCNTs (ε_B) are concluded based on the plasma frequency

$$\varepsilon_B^{'} = 1 - \frac{w_{PB}^2}{w^2 + v_B^2} \tag{14}$$

$$\varepsilon_B^{"} = \frac{w_{PB}^2 v_B}{w^3 + w v_B^2} \tag{15}$$

In another context, according to the general admitted definition of the complex permittivity demonstrated in the previous research [33], the permittivity and conductivity of CB-SWCNTs are linked by the following relation

$$\varepsilon_B = 1 + \frac{\sigma_{bundle,i}}{w\varepsilon^o}\ -\ j\frac{\sigma_{bundle,r}}{w\varepsilon^o}, \tag{16}$$

$$\varepsilon_B^{'} = 1 + \frac{\sigma_{bundle,i}}{w\varepsilon^o}, \tag{17}$$

$$\varepsilon_B^{"} = \frac{\sigma_{bundle,r}}{w\varepsilon^o}\,. \tag{18}$$

As a result, the relative complex permittivity of CB-SWCNTs is modeled with Equations (14 and 15) or Equations (17 and 18), the both equation sets provide the same results. Therefore, the EM parameters of CB-SWCNTs which are extracted (or estimated) in this work is utilized to represent this composite material in the different 3D EM simulation software packages including CST (MWS) and HFSS and other.

C. Modelling approach of CB-SWCNTs

The material parameters of CB-SWCNTs extracted in the mathematical analysis above are make to possible to represent the CB-SWCNTs by an equivalent single conductor material model (ESCM) through CST (MWS). This modelling approach contributes to investigate the EM behavior of this bundle with different geometrical structures. Therefore, by inserting the material parameters of CB-SWCNTs into the CST (MWS) software package, the ESCM model can be designed and implemented. For the purpose of modelling approach, the schematic of the ESCM model is an equivalent to the CB-SWCNTs Fig. 2. The dipole antenna for both CB-SWCNTs and ESCM was employed to validate this modelling approach depending on the comparison between their results.

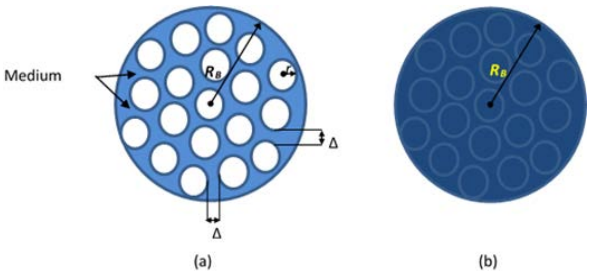

Fig. 2. Schematic configuration of: (a) CB-SWCNT and (b) equivalent ESCM model.

D. Modelling of SWCNT

To overcome the difficulty to dealing with the hollow cylinder of SWCNT, the solid cylinder model was adopted to represent the SWCNT. The transformation factor *TRF* between these structures was presented in previous works [9, 34]. In this work, the nano-solid tube material (NSTM) model is presented to model the SWCNT. The raw material of NSTM is derived from original material of SWCNT. This modelling approach aims to design and predict the EM properties of multi conductors CB-SWCNTs through design the CB-SWCNTs dipole antenna in the CST (MWS) software package. The conductivity of the NSTM model (σ_{NSTM}) is deduced from the surface conductivity of SWCNT (σ_{SWCNT}) presented in [9], as shown in the formula below:

$$\sigma_{NSTM} = \left(\frac{2}{r}\right)\sigma_{SWCNT} = -j\frac{4e^2V_f}{\pi^2 hr^2(w - jv)}\,. \tag{19}$$

The plasma frequency (w_{psw}) of SWCNT can be estimated based on the bulk conductivity model presented in [9]. As well as, the relative complex permittivity of SWCNT (ε) is possible to estimate as shown below

$$w_{psw} = \frac{2e}{\pi r}\sqrt{\frac{V_f}{\varepsilon^o h}}\,, \tag{20}$$

$$\varepsilon^{'} = 1 - \frac{w_{psw}^2}{w^2 + v^2}\,, \tag{21}$$

$$\varepsilon^{"} = \frac{v\ w_{psw}^2}{w^3 + wv^2}\,. \tag{22}$$

Where ($\varepsilon^{'}$) the real part and ($\varepsilon^{"}$) the imaginary part of the SWCNT relative complex permittivity. Hence,

in order to implement the simulation technique of this modelling approach, the material parameters of the SWCNT are inserted in the CST (MWS) as a new normal.

III. APPLICATION OF CB-SWCNTS AND ESCM MODEL

In order to estimate the EM properties of CB-SWCNTs, the dipole antenna of both multi conductors CB-SWCNTs and corresponding ESCM model were applied and solved through CST (MWS). Furthermore, provide a comparison between these structures, in order to validate the ESCM model. The schematics of the CB-SWCNTs and ESCM dipole antennas are shown in Fig. 3.

With regard to both CB-SWCNTs and ESCM dipole antennas, in the CST (MWS) environment, the SWCNT material and CB-SWCNTs material were set up as new, normal materials in Drude method. Their parameters were inserted in the CST (MWS) to represent the equivalent NSTM model for SWCNTs and ESCM model to CB-SWCNTs. These parameters were previously extracted in this work. This process represents the modelling approaches for both SWCNT and CB-SWCNTs in the CST (MWS) software package in order to preface the design of different types of CNT antennas in the simulation mode. That means, a raw material of the equivalent NSTM model and ESCM model is derived from SWCNTs and CB-SWCNTs materials instead of deriving from other material.

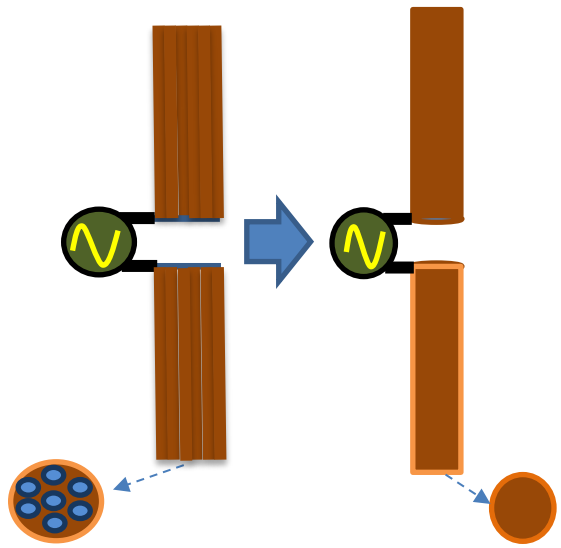

(a) (b)

Fig. 3. Dipole antenna structure for both: (a) CB-SWCNTs and (b) ESCM model.

IV. MATCHING IMPEDANCE OF CB-SWCNT DIPOLE ANTENNA

In order to implement the CB-SWCNTs dipole antenna, the matching input impedance issue is demonstrated in this paper. Mathematically, based on the antenna concepts, the surface impedance is considered as an input impedance for dipole antenna [35]. Hence, according to the equivalent circuit diagram of the SWCNT presented by Burk [1-4], the input impedance of SWCNT antenna, which is equal to the input impedance of the equivalent nanowire model of SWCNT ($Z_{in,equvl}$) which presented in previous work [34], can be estimated. For simplicity, with regards to the SWCNT, the quantum parameters are given below:

$$Z_{in,equvl} = \frac{L}{\pi\sigma_{equvl} r^2} = \frac{L}{2\pi r\sigma_{SWCNT}}, \tag{23}$$

$$Z_{in,equvl} = Rq + jw\zeta. \tag{24}$$

Here, Rq is the quantum resistance, and ζ is the quantum inductance. These quantities are mathematically presented as follows:

$$Z_{in,equvl} = \frac{\pi hvL}{4e^2V_f} + jw\frac{\pi hL}{4e^2V_f}, \tag{25}$$

$$Rq = \frac{\pi hvL}{4e^2V_f} = \frac{3\pi hLT}{2re^2V_f}, \tag{26}$$

$$\zeta = \frac{\pi hL}{4e^2V_f}. \tag{27}$$

On the other hand, with regards to the CB-SWCNTs dipole antenna, the quantum resistance and quantum inductance can be estimated based on the general formula of the effective impedance of the bundle (Z_{bundle}) according to the impedance of SWCNT:

$$Z_{bundle} = \frac{Z_{in,equvl}}{N}. \tag{28}$$

For simplicity, the effective impedance of CB-SWCNTs based on the assumption that all SWCNTs are metallic, identical and arranged in the parallel structure. Thus, the quantum parameters of CB-SWCNTs are computed as given below:

$$R_{qB} = \frac{\pi hvL}{4Ne^2V_f} = \frac{3\pi hLT}{2Nre^2V_f}, \tag{29}$$

$$\zeta_B = \frac{\pi hL}{4Ne^2V_f}. \tag{30}$$

The one of the main problems of CB-SWCNTs dipole antenna is the matching issue between this antenna and the feeding source (discreet port). In this work, the simple matching approach is presented to mitigate this problem in simulation mode. This matching approach depends on adaptation the Normalized Fixed Impedance (NFI) value, which is one parameter of the s11 parameters setting window, in order to balancing the effectiveness of the input impedance of this dipole

antenna with the internal impedance of the feeding source. The NFI option of the s11 parameters in CST (MWS) software package is very important when the initial value of the NFI is selected based on computing the value of R_{qB} from Equation (29). This value represents the impedance value that the system is needed to realize the matching between feeding source and dipole antenna (load). In another context, this value represents a starting value to obtain a well value of matching impedance between source and CB-SWCNTs dipole antenna to obtain the optimum result of s11 parameters. Indeed, the simple matching approach presented in this work is implemented for design CB-SWCNTs dipole antenna. As well as, this matching process is benefits for achieving the matching situation for different nanoelectronic antennas.

V. SIMULATION RESULTS AND DISCUSSION

In this work, the CST (MWS) software package is utilized to implement both equivalent modelling approaches, namely the NSTM for the SWCNT material to design multi conductors CB-SWCNTs, as well as ESCM to design single conductor which is corresponding to CB-SWCNTs, in which the dipole antenna configuration was employed to achieve this purpose. To design CB-SWCNTs dipole antenna, each packed of SWCNTs bundle will be connected to a square contact to make a feeding source touch all SWCNTs. The dimensions of this contact (length × width) are equal to ($W_D \times t$) and thickness is equal to (r). The discreet port was used as a feeding source for all dipole antennas designed in this work. The simulation results of this work could be implemented as follows.

A. Simulation results of CB-SWCNTs and ESCM model

In this section, both structures of CB-SWCNTs and ESCM modelling approach are implemented, in order to investigate the important material parameters of the CB-SWCNTs and to validate the ESCM modelling approach, based on comparison of their results. In addition, estimate the EM properties of CB-SWCNTs in different cross-section area (small and large cross section area) which contains different numbers of SWCNTs.

1. Investigation of CB-SWCNTs material parameters

In order to estimate and study the performance of the conductivity of the CB-SWCNTs (σ_{bundle}), which represent the conductivity of the equivalent ESCM model, the CB-SWCNTs included various numbers of the identical SWCNTs (N = 7, 19, 36, and 61) were implemented for this purpose. Figure 4 represent the behavior of the conductivity versus frequency, based on increases the number of SWCNTs in the bundle. Also, the plasma frequency of the bundle (w_{PB}) is affected by increases the number of SWCNTs (N) in the bundle, as shown in Fig. 5.

As a presented in these figures, the behavior of the conductivity of CB-SWCNTs was illustrated with increases the number of SWCNTs in this bundle (N). This mean, with increases the equivalent radius of the bundle. The plasma frequency of this bundle was decreased due to increases the radius of SWCNT. In contrary, the plasma frequency was increased due to increases the number of SWCNTs included in this bundle.

2. Validation of ESCM model

To validate the ESCM modelling approach, the dipole antenna configuration was designed based on the multi conductors CB-SWCNTs structure and the ESCM model. The CB-SWCNTs with different number of SWCNTs (N = 7, 19, 36 and 61) are mainly used with those corresponding cross-sectional area of ESCM model, in order to investigate the comparison between these structures. In addition, these two structures have the same lengths for designing the dipole antenna. All of the SWCNTs included in the bundle are identical, have the same radius (r = 2.71 nm). Similarly, the lattice distance (Δ) between the two adjacent SWCNTs is equally and equal to (0.34 nm). The length of dipole antenna is (L = 30 μm). The details of CB-SWCNTs and ESCM model are described in Table 1, in order to design the dipole antennas associated with these structures. The two types of dipole antennas centered by a feeding gap ($d = 2R_B$). The results of these antennas are shown in Fig. 6 for CB-SWCNTs and corresponding ESCM dipole antennas.

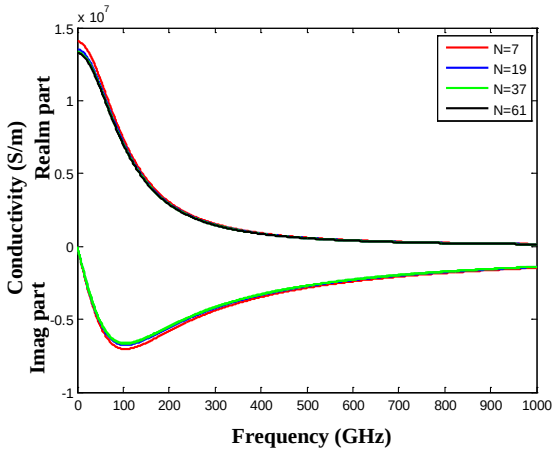

Fig. 4. The conductivity of B-SWCNTs (σ_{bundle}) versus the frequency with various number of SWCNTs (N).

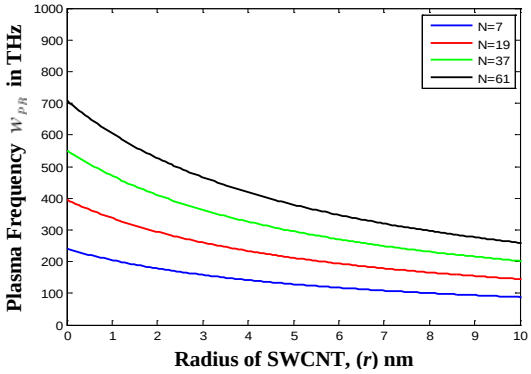

Fig. 5. Plasma frequency of CB-SWCNTs (w_{PB}) versus the radius of SWCNT with various number of SWCNTs (N).

Table 1: Details of B-SWCNTs and corresponding ESCM structures

Number of SWCNTs in the Outer Side of the Bundle Structure N_x	Total Number of SWCNT-s in the Bundle N	Corresponding Radius of CB-SWCNT-s and ESCM R_B (nm)	Cross-Section Area of CB-SWCNTs and ESCM A_B (Micrometer^2)
2	7	8.47	0.2254
3	19	14.23	0.6362
4	37	19.99	1.2554
5	61	25.75	2.0831

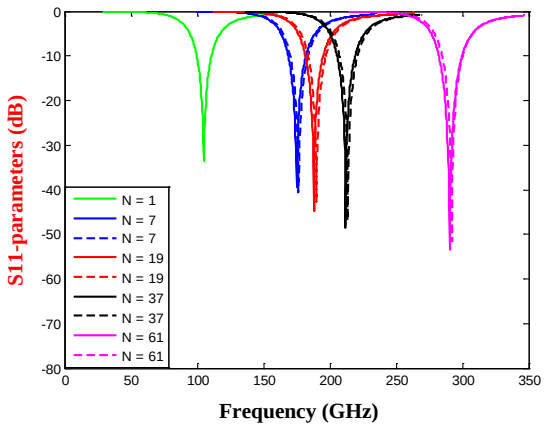

Fig. 6. Simulation results of multi conductor CB-SWCNTs at N = (7, 19, 37 and 61) and an equivalent ESCM dipole antennas. The solid lines are the CB-SWCNT results and the dotted lines are the ESCM results.

The simulation results of CB-SWCNTs and corresponding ESCM dipole antennas exhibited in Fig. 8, indicate the good conformity between the multi conductors CB-SWCNTs structure and ESCM model. As a result, by increasing the number of SWCNTs included in the bundle, the resonant frequency increases and the s11 parameters improved. Meanwhile, by increasing the cross-sectional area of the ESCM model, the same behavior was shown with related to resonant frequency and s11 parameters. In another context, the two structures, multi conductors CB-SWCNTs and ESCM model have the same response to changing the corresponding design parameters. These simulation results represent the EM behavior of CB-SWCNTs with a small cross-sectional area.

3. Verify the accuracy of modelling results

In order to verify the accuracy of the simulation results in this work, the comparisons between the results of CB-SWCNTs and ESCM modelling approach have been presented. The comparison between these structures was carried out based on the behaviour of the resonant frequency versus different number of the SWCNTs included in the bundle. Where, both dipole antennas have same length (L = 30 μm) and same cross-sectional area, which are changed based on the number of SWCNTs in the bundle. The comparison of these simulation results for both dipole antennas was illustrated in Fig. 7. Likewise, the other comparison for both dipole antennas has been implemented based on the efficiency of them, at the same length (L = 30 μm) and same cross-sectional area where (N = 7).

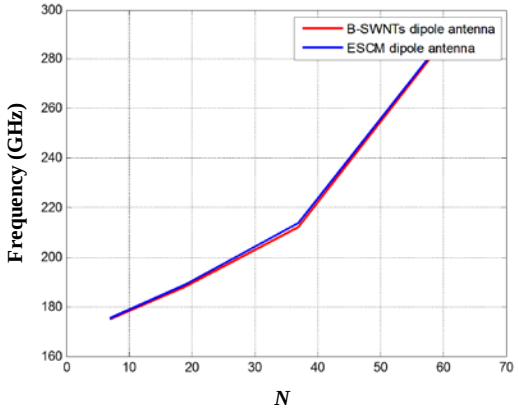

Fig. 7. Comparison results between CB-SWCNT and ESCM dipole antennas, based on the resonant frequency versus the number of SWCNTs included in the bundle at N = (7, 19, 37 and 61).

From the comparisons results presented in Fig. 7 and Fig. 8, a well accuracy results and compatibility can be observed between both CB-SWCNTs and ESCM dipole antennas. That means, the ESCM modelling approach has a good validation to represent the CB-SWCNTs material structure.

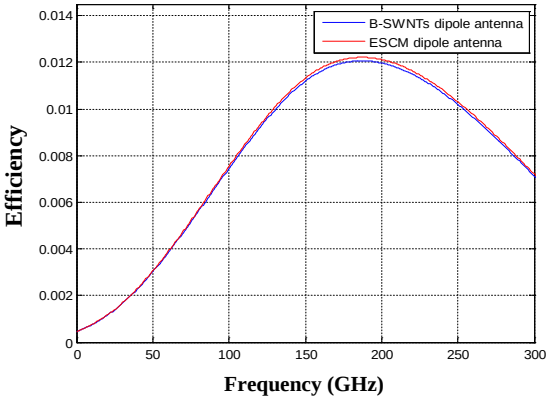

Fig. 8. Comparison results between CB-SWCNT and ESCM dipole antennas, based on the efficiency versus frequency at N = (7).

4. Electromagnetic behaviour of CB-SWCNTs with large cross-section area

The equivalent ESCM model for the CB-SWCNTs area was utilized to predict the electromagnetic properties of CB-SWCNTs with a large cross-section area, based on designing and implementing the ESCM dipole antenna into CST (MWS). The details of different cross-sectional areas of the CB-SWCNTs and corresponding ESCM model are described in Table 2, the cross-sectional areas were selected based on the number of SWCNTs (N) included in the bundle, which is related to the corresponding number of outer SWCNTs of hexagon for the original structure of CB-SWCNTs (N_x = 10, 20 and 30). With regard to these details, the dipole antennas are designed and implemented in CST (MWS), in order to investigate the EM properties of CB-SWCNTs at large scales geometric structures. The results of these antennas were shown in Fig. 9.

Table 2: Simulation details of ESCM that are equivalent to CB-SWCNTs structures

Number of SWCNTs in the Outer Side of the Bundle N_x	Radius of Equivalent ESCM Model to the CB-SWCNTs R_B (*Nanometre*)	Cross-Section Area of ESCM A_B (*Micrometer*^{2})	Corresponding Number of SWCNTs in the CB-SWCNTs N (*Tube*)
10	54.55	9.3484	271
20	112.15	39.5138	1141
30	169.75	90.5252	2611

From this result, the resonant frequency of ESCM dipole antenna was increased by increasing the cross-sectional area of ESCM model. Likewise, the s11 parameters of these dipole antennas improved. This result represents the starting phase to deal with a large geometrical structure of the CB-SWCNTs for the first time.

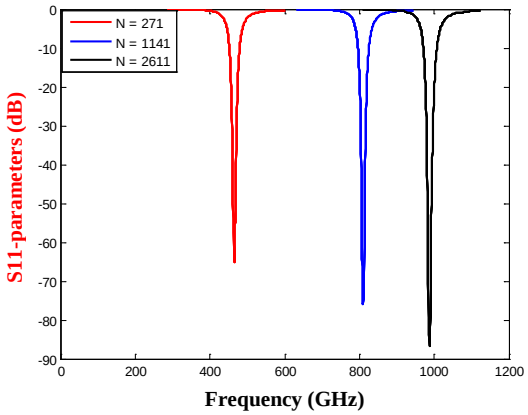

Fig. 9. Simulation results of ESCM dipole antenna with large cross-section areas, which are equivalent to N = (271, 1141, and 2611).

VI. CONCLUSION

In this paper, the two modelling approaches for SWCNT and CB-SWCNTs were presented and carried out into CST (MWS). To validate the ESCM modelling approach, the several numbers of SWCNTs which constructs the bundle with specific cross-section areas were designed and their results are also compared with those of similar cross-section area of the corresponding ESCM model. From these comparisons, a consistency of results was found between ESCM model and CB-SWCNTs.

The simulation results of ESCM and CB-SWCNTs dipole antennas demonstrated using of ESCM model to represent the CB-SWCNTs instead of CB-SWCNTs with hollow or solid cylinder SWCNTs structure. This led to reduce the overall complexity and solving the simulation time problem for estimation of EM properties for CB-SWCNTs with large number of SWCNTs.

The main goal of the ESCM modelling approach is to make a computation analysis less complicated at the simulation mode. The designing of ESCM model with a small and large cross-sectional areas corresponded to CB-SWCNTs with different numbers of SWCNTs make the estimation of the EM properties of CB-SWCNTs with a short time be compared with the traditional method of multi conductors CB-SWCNTs.

Actually, the performance evaluation indicators of CB-SWCNTs dipole antenna are dependent on the diameter and length of CB-SWCNTs, as well as the number of SWCNTs included in this bundle. Further optimization can be done to achieve better radiation performance, based on these performance indicators.

The contribution of this paper is to provide and validate the equivalent single conductor material (ESCM) model approach for the CB-SWCNTs using the CST (MWS) software package. The raw material of ESCM

model is derived from the material properties of CB-SWCNTs.

Moreover, with regards to the antenna applications, the presented modelling approach for CB-SWCNTs is very useful and make possible to design antenna uses in on-chip wireless communication. This leads to make the CNTs is a candidate promising material for this purpose.

REFERENCES

[1] P. J. Burke, "Lüttinger liquid theory as a model of the gigahertz electrical properties of carbon nanotubes," *IEEE Trans. Nanotechnology*, vol. 1, no. 3, pp. 129-144, 2002.

[2] P. J. Burke, "Correction to Lüttinger liquid theory as a model of the gigahertz electrical properties of carbon nanotubes," *IEEE Trans. Nanotechnology*, vol. 3, no. 2, p. 331, 2004.

[3] P. J. Burke, "An RF circuit model for carbon nanotubes," *IEEE Trans. Nanotechnology*, vol. 2, no. 1, pp. 55-58, 2003.

[4] P. J. Burke, "Correction to an RF circuit model for carbon nanotubes," *IEEE Trans. Nanotechnology*, vol. 3, no. 2, pp. 331, 2004.

[5] P. Burke, S. Li, and Z. Yu, "Quantitative theory of nanowire and nanotube antenna performance," *IEEE Transactions on Nanotechnology*, vol. 5, no. 4, pp. 314-334, 2006.

[6] L. Nougaret, G. Dambrine, S. Lepilliet, H. Happy, N. Chimot, V. Derycke, and J.-P. Bourgoin, "Gigahertz characterization of a single carbon nanotube," *Appl. Phys. Lett.*, vol. 96, no. 4, pp. 042109-1-042109-3, 2010.

[7] A. Naeemi and J. D. Meindl, "Physical modeling of temperature coefficient of resistance for single- and multi-wall carbon nanotube interconnects," *IEEE Electron Device Letters*, vol. 28, no. 2, pp. 135-138, 2007.

[8] A. Naeemi, R. Sarvari, and J. D. Meindl, "Performance modeling and optimization for single- and multi-wall carbon nanotube interconnects," *44th ACM/IEEE Design Automation Conference*, pp. 568-573, 2007.

[9] G. W. Hanson, "Fundamental transmitting properties of carbon nanotube antennas," *IEEE Trans. Antennas. and Propag.*, vol. 53, no. 11, pp. 3426-3435, 2005.

[10] G. W. Hanson and Jin Hao, "Infrared and optical properties of carbon nanotube dipole antennas," *IEEE Trans. Nanotechnol*., vol. 5, no. 6, pp. 766-775, 2006.

[11] G. W. Hanson. "Current on an infinitely-long carbon nanotube antenna excited by a gap generator," *IEEE Trans. Antennas. and Propag*., vol. 54, no. 1, pp. 76-81, 2006.

[12] G. W. Hanson and Jay A. Berres, "Multiwall carbon nanotubes at RF-THz frequencies: Scattering, shielding, effective conductivity and power dissipation," *IEEE Trans. Antennas and Propag.*, vol. 59, no. 8, pp. 3098-3103, 2011.

[13] N. Fichtner, X. Zhou, and P. Russer, "Investigation of carbon nanotube antennas using thin wire integral equations," *Advances in Radio Science*, vol. 6, pp. 209-211, 2008.

[14] N. Fichtner, X. Zhou, and P. Russer, "Investigation of copper and carbon nanotube antennas using thin wire integral equations," *IEEE Proceedings of Asia-Pacific Microwave Conference*, pp. 4, 2007.

[15] J. Hao and G. W. Hanson, "Electromagnetic scattering from finite-length metallic carbon nanotubes in the lower IR bands," *Physical Rev. B.*, vol. 74, pp. (035119,1)-(035119,6), 2006.

[16] G. W. Hanson, "A common electromagnetic framework for carbon nanotubes and solid nanowires — Spatially dispersive conductivity, generalized Ohm's law, distributed impedance, and transmission line model," *IEEE Trans. Microwave Theory Tech*., vol. 59, no. 1, pp. 9-20, 2011.

[17] M. S. Sarto, A. Tamburrano, and M. D'Amore, "New electron-waveguide-based modeling for carbon nanotube interconnects," *IEEE Transaction on Nanotechnology*, vol. 8, pp. 214-225, 2009.

[18] M. S. Sarto and A. Tamburrano, "Multiconductor transmission line modeling of SWCNT bundles in common-mode excitation," *IEEE International Symposium on Electromagnetic Compatibility*, vol. 2, pp. 466-471, 2006.

[19] M. Sabrina Sarto and A. Tamburrano, "Electromagnetic analysis of radio-frequency signal propagation along SWCN bundles," *6th IEEE Conference on Nanotechnology*, pp. 201-204, 2006.

[20] M. D'Amore, M. S. Sarto, and A. Tamburrano, "Signal integrity of carbon nanotube bundles," *IEEE International Symposium on Electromagnetic Compatibility*, pp. 1-6, 2007.

[21] M. D'Amore, M. Ricci, and A. Tamburrano, "Equivalent single conductor modeling of carbon nanotube bundles for transient analysis of high-speed interconnects," *8th IEEE Conference on Nanotechnology*, Arlington, Texas, pp. 307-310, 2008.

[22] M. D'Amore, M. S. Sarto, and A. G. D'Aloia, "Equivalent single conductor for modeling near field radiated emission of carbon nanotube bundles," *9th IEEE Conference on Nanotechnology*, Genoa, pp. 75-78, 2009.

[23] M. D'Amore, A. G. D'Aloia, M. S. Sarto, and A. Tamburrano, "Near field radiated from carbon nanotube bundles," *IEEE Transactions on Electromagnetic Compatibility*, vol. 54, pp. 998-1005, 2012.

[24] Q. Libo, Z. Zhangming, D. Ruixue, and Y. Yintang, "Circuit modeling and performance analysis of SWCNT bundle 3D interconnects,"

Journal of Semiconductors, vol. 34, pp. (095014-1)–(095014-7), 2013.

[25] M. D'Amore, F. Maradei, S. Cruciani, and M. Feliziani, "High frequency performance of carbon nanotube-based spiral inductors," *Conference of International Symposium on Electromagnetic Compatibility (EMC Europe)*, Brugge, Belgium, pp. 765-770, 2013.

[26] Y. Huang and W.-Y. Yin, "Performance predication of carbon nanotube bundle dipole antenna," *Proceedings of Asia-Pacific Microwave Conference*, pp. 1-4, 2007.

[27] Y. Huang, W.-Y. Yin, and Q. H. Liu, "Performance prediction of carbon nanotube bundle dipole antennas," *IEEE Transactions on Nanotechnology*, vol. 7, pp. 331-337, 2008.

[28] Y. Wang, Y. M. Wu, L. L. Zhuang, S. Q. Zhang, L. W. Li, and Q. Wu, "Electromagnetic performance of single walled carbon nanotube bundles," *Microwave Conference, Asia Pacific*, pp. 190-193, 2009.

[29] A. M Attiya, "Lower frequency limit of carbon nanotube antenna," *PIER 94*, pp. 419-433, 2009.

[30] S. Choi and K. Sarabandi, "Performance assessment of bundled carbon nanotube for antenna applications at terahertz frequencies and higher," *IEEE Transactions on Antennas and Propagation*, vol. 59, pp. 802-809, 2011.

[31] M. S. Sarto and A. Tamburrano, "Multiconductor transmission line modeling of SWCNT bundles in common-mode excitation," *IEEE International Symposium on Electromagnetic Compatibility*, vol. 2, pp. 466-471, 2006.

[32] H. Stahl, J. Appenzeller, R. Martel, P. Avouris, and B. Lengeler, "Intertube coupling in ropes of single-wall carbon nanotubes," *Phys. Rev. Lett.*, vol. 85, no. 24, pp. 5186-5189, 2000.

[33] S. J. Orfanidis, *Maxwell's Equations*. Chapter 1, Electromagnetic Waves and Antennas, 2010.

[34] G. W. Hanson, "A common electromagnetic framework for carbon nanotubes and solid nanowires-spatially distributed impedance, and transmission line model," *IEEE Transaction on Microwave Theory and Techniques*, vol. 59, pp. 9-20, 2011.

[35] C. A. Balanis, *Antenna Theory Analysis and Design*. 3rd edition, John Wiley and Sons, USA, 2005.

Yaseen Naser Jurn was born in Baghdad, Iraq. He received the B.Sc. degree in Communication Engineering from the University of Technology, Baghdad, Iraq, in 1995, the M.Sc. degree in Communication Engineering (Direction of Arrival) from the Universiti Technology, Baghdad in 2002 and the Ph.D. degree in Communication Engineering (Nano Antenna Design) from the University Malaysia Perlis (UniMap), Perlis, Malaysia, in 2017. Currently he is a Senior Engineer in Minister of Science and Technology, Baghdad, Iraq, where he has been an Engineer since 1995 in Ministry of Science and Technology. His main personal research interests are modelling, simulation, and antenna design, antennas and propagations, electromagnetics, modern nanomaterial structure design, nano antenna design, modelling and simulation of nano antenna.

Mohamedfareq Abdulmalek obtained his B.Eng. (Hons.) - Electronic and Communication Engineering from the University of Birmingham, U. K. in 1997. He received his M.Sc. (Eng.) in Microelectronic Systems and Telecommunications at The University of Liverpool, U. K. in 2004 and Ph.D. Electrical Engineering (Radio Frequency and Microwave) in 2008 from The University of Liverpool, U. K. Recently, he is an Associate Professor in Faculty of Engineering and Information Sciences, University of Wollongong in Dubai. His main research interests are antenna design, embedded computing, microwave absorbers from agricultural waste and effects of RF on human's health.

Hasliza Binti A. Rahim received the Bachelor degree in Electrical Engineering from University of Southern California (USC), Los Angeles, USA in 2003. Later, she received the Master in Electronics Design System from the University Sains Malaysia, Transkrian, Pulau Pinang, Malaysia in 2006 and Ph.D in Communication Engineering from the University Malaysia Perlis, Perlis, Malaysia in 2015. She joined the School of Computer and Communication Engineering, UniMAP in 16th August 2006 as Lecturer and now as Senior Lecturer. She is the Head and Principle Researcher of Bioelectromagnetic Excellence Research Group (BioEM). Her extensive research area covers a range of applied engineering including advanced technologies for 4G/5G, antennas, wireless body area networks (WBAN), effects of RF on health, electromagnetics, and bioelectromagnetics. Several research funds were granted nationally such as Fundamental Research Grant Scheme, National ScienceFund, and Malaysian Communications and Multimedia Commission. She has authored and co-authored more than 50 peer reviewed scientific publications, including 2 articles in Nature Publishing Group journal (Scientific Reports), 3 patents, and 2 book chapters. She has been awarded with the Excellence

Woman Inventor by the University Malaysia Perlis in 2010.

Sawsen Abdulahadi Mahmood was born in Baghdad, Iraq. She obtained her B.Sc. in Mathematics from the University of Baghdad, Baghdad, Iraq, in 1992, the M.Sc. degree in Computer Science from the University of Technology, Baghdad, Iraq, in 2002. She received her Ph.D. in Computer Science at the Faculty of Computer Science in 2015 at University of Technology, Baghdad, Iraq. Recently, she is an Associate Professor in Faculty of Computer Science, University of Mustansiriyah, in Baghdad, Iraq. Her main personal research interests are Pattern Recognition and Machine Learning, 3D image analysis recognition, 3D video analysis, Surveillance System based on Internet of things environment, and Voice Recognition.

Liu Wei Wen obtained the B.Sc. with Education (B.Sc. Hons.) in Physics, 2002, from Physics Department, Faculty of Science, University Putra Malaysia (UPM), Serdang, Selangor. The M.Sc. in Materials Science, 2005 Physics Department, Faculty of Science, University Putra Malaysia (UPM), Serdang, Selangor. He received the Ph.D. in Nano Materials, 2012, from School of Materials and Mineral Resources Engineering, Universiti Sains Malaysia (USM), Nibong Tebal, Penang. His main personal research interest is in synthesis of carbon nanotubes and graphene and their application in biosensor.

K-band Planar and Low-profile Fabry-Perot Cavity Antenna with a Coupled Strip-Slitline Feed Structure

Huy Hung Tran [1,2] and Truong Khang Nguyen [1,2,*]

[1] Division of Computational Physics, Institute for Computational Science
Ton Duc Thang University, Ho Chi Minh City, Vietnam

[2] Faculty of Electrical & Electronics Engineering, Ton Duc Thang University, Ho Chi Minh City, Vietnam
tranhuyhung@tdt.edu.vn, *nguyentruongkhang@tdt.edu.vn

Abstract ─ In this paper, a design of a planar, low-profile, and high gain Fabry-Perot cavity antenna for *K*-band applications is presented. The antenna is consisted of a frequency selective surface (FSS) made of a circular hole array and a feeding structure made of a coupled strip-slitline. The FSS and the slitline both are lithographically patterned on a high permittivity substrate while the stripline is printed on top of a thin and low permittivity substrate. These two substrates are then closely appressed each other to form a planar structure. The measured results show that the proposed antenna has an impedance bandwidth of about 4% (|S11|≤-10 dB), a maximum gain of about 10.4 dBi, and a 3-dB gain bandwidth of approximately 2.9% at the resonance frequency of around 20.8 GHz. The antenna's compact, planar, and lightweight profile, i.e., approximately $4\lambda_o \times 4\lambda_o \times 0.24\lambda_o$ of a free-space wavelength at 21.0 GHz makes it promising for a small and efficient source in *K*-band applications.

Index Terms ─ Antennas, Fabry-Perot cavity, leaky-wave.

I. INTRODUCTION

In the last years, the idea of using a planar and low-profile Fabry-Perot (FP) cavity antenna for applications demanding easy and cost-effective fabrication have received significantly attention because of its number of attractive properties, such as low profile, high directivity, mechanical robustness, and capability of conformal deployment [1-7]. This kind of technique with the fully dielectric integration poses two main design challenges, particularly for high permittivity substrate in order for miniaturization, that are low radiation efficiency causing reduced antenna gain and narrow 3-dB gain/power bandwidth limiting the uses of antenna to wireless communication systems [8-10]. In addition, there have few papers considered on the common (available) bandwidth in a Fabry-Perot resonator antenna. The common bandwidth specification is the overlapping frequency range between the 10-dB return loss bandwidth and the 3-dB gain bandwidth [11].

In this paper, a Fabry-Perot resonator cavity antenna satisfying planar, low profile, high gain, and moderate common bandwidth requirements is designed. The antenna is consisted of a frequency selective surface (FSS) made of a circular hole array and a coupled strip-slitline feed. The resonator is formed by the FSS and the slitline ground plane. In particular, the cavity resonance is efficiently excited by a coupling mechanism of a microstrip-substrate integrated waveguide transition and thus the high gain characteristic is obtained.

II. ANTENNA DESIGN AND MODELLING THE STRUCTURE

The geometry of the proposed antenna is depicted in Fig. 1 with front and top views. The cavity was made of a Taconic substrate whose dielectric constant and loss tangent are ε_{r1} = 10.2 and tanδ = 0.0035, respectively. A leaky-wave open-ended narrow slitline of width W_{slit} and a very thin metallic FSS were lithographically patterned both on the top side and bottom side of the substrate. Therefore, the cavity is formed by the FSS sheet and the ground plane of the slitline and its resonance length is determined by the substrate thickness of *H*. The FSS is a bi-periodic 9×9 array of circular holes whose hole diameter and periodicity are *D* and *P*, respectively. In order to excite the cavity resonance, a slit-coupled feeding technique with a simple stripline is used. The stripline is printed on a thin and very low dielectric constant RT/Duroid 5880 substrate whose thickness is denoted by *T* and dielectric constant is ε_{r2} = 2.2. The length and width of the stripline are designated by L_{strip} and W_{strip}, respectively. The overall dimension of the proposed antenna is $A \times A \times (H+T)$ mm^3. The optimized parameters of the antenna were as follows: *A* = 56 mm, *H* = 3.175 mm, *T* = 0.254 mm, *D* = 3.8 mm, *P* = 5.2 mm, L_{strip} = 31.1 mm, W_{strip} = 0.9 mm, and W_{slit} = 0.3 mm.

Submitted On: March 2, 2016
Accepted On: November 27, 2016

All electromagnetic simulation is performed using CST Microwave Studio which is based on based on the finite-integration time-domain (FIT) technique [12]. A unit cell model was first employed to evaluate the reflection characteristics of the cavity which is formed by FSS and the ground plane of the open-ended slitline. In this model, a two-Floquet-ports model with magnetic and electric boundary conditions enforced along $\pm x$ and $\pm y$. This allows to simulate a normal mode propagation for the waveguide configuration. Frequency-domain solver with tetrahedral meshes is used in this simulation step. Figure 2 shows that the FP cavity mode is excited when S11 presents an 180^0 reflection phase. The predicted resonance frequency of the FP cavity is approximately 21.3 GHz. At this resonance frequency, the hole is efficiently excited, and the field leaked through the hole, which contributes to the antenna directivity, is maximized.

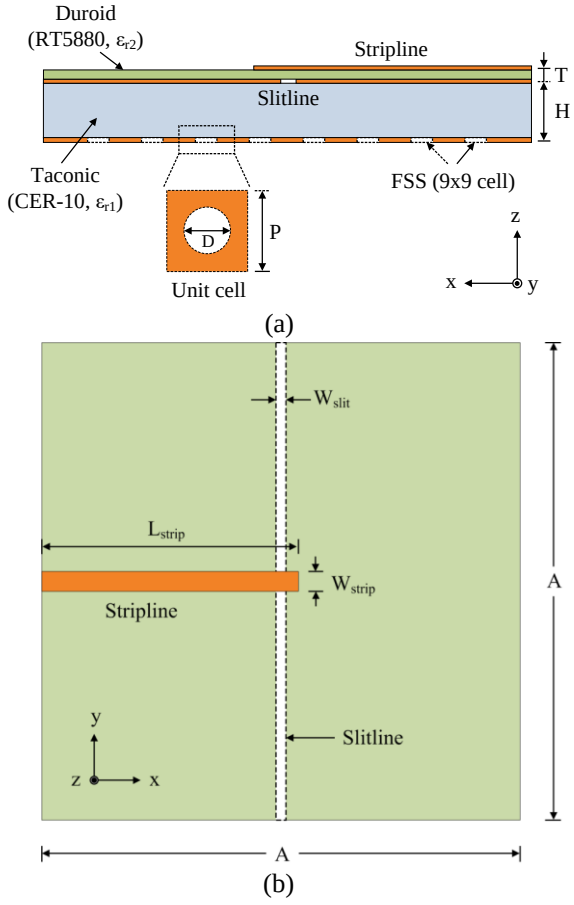

Fig. 1. (a) Side and (b) top views of the proposed FPC antenna.

II. ANTENNA CHARACTERISTICS

The antenna characteristic is investigated and optimized by using a full three-dimensional structure finite size and real shape. In this model, principally open with some added space boundaries are used in order to accurately calculate the antenna radiation patterns. In this simulation, transient time-domain solver and a hexahedral mesh scheme is used. This approach saves the computation time and resources while allows to monitor the radiation performance of the antenna in a broad frequency range within one simulation run.

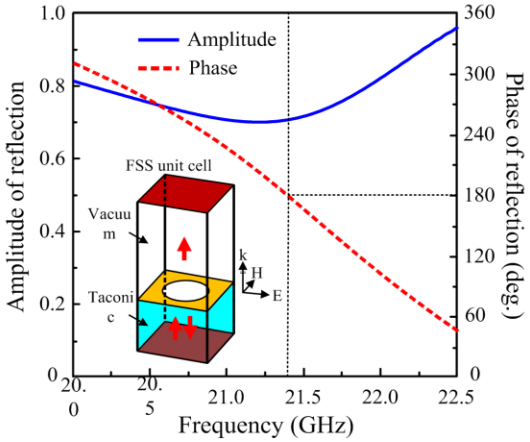

Fig. 2. Reflection characteristic of the FP cavity in the unit cell model (inset).

Figures 3 (a)-(c) shows the boresight gain characteristic with respect to the design parameters such as substrate cavity dimensions and number of hole in the FSS array, respectively. In general, the increases in the thickness and the lateral size of the substrate lead to a linear shift in the frequency. Besides, the boresight gain profile of the antenna in the variation of the substrate lateral size was altered along with the frequency shift, which behaved differently compared with the cases having substrate thickness variation. This behavior is attributed to the truncation effect resulting from the finite lateral dimension of the substrate [13]. The number of holes also affected the effective permittivity of the cavity. As seen in Fig. 3 (c), when the number of holes in the array changed from 1 × 1 to 2 × 2 to 3 × 3 to 4 × 4, that is, while fixing the lateral size *A*, the gain profile changed, particularly in the lower frequency region, and the frequency occurring maximum gain slightly decreased. In general, more number of holes in the array resulted in a larger effective aperture and thus enhancing the antenna gain. From these results, it can be seen that the Taconic substrate dimensions contributed to the effective permittivity of the cavity, and consequently determined the resonance condition to obtain maximum boresight gain of the antenna. Therefore, such changes on these parameters caused an out-of-resonance condition in both the cavity and the FSS, thereby reducing the beam collimation or the antenna boresight gain.

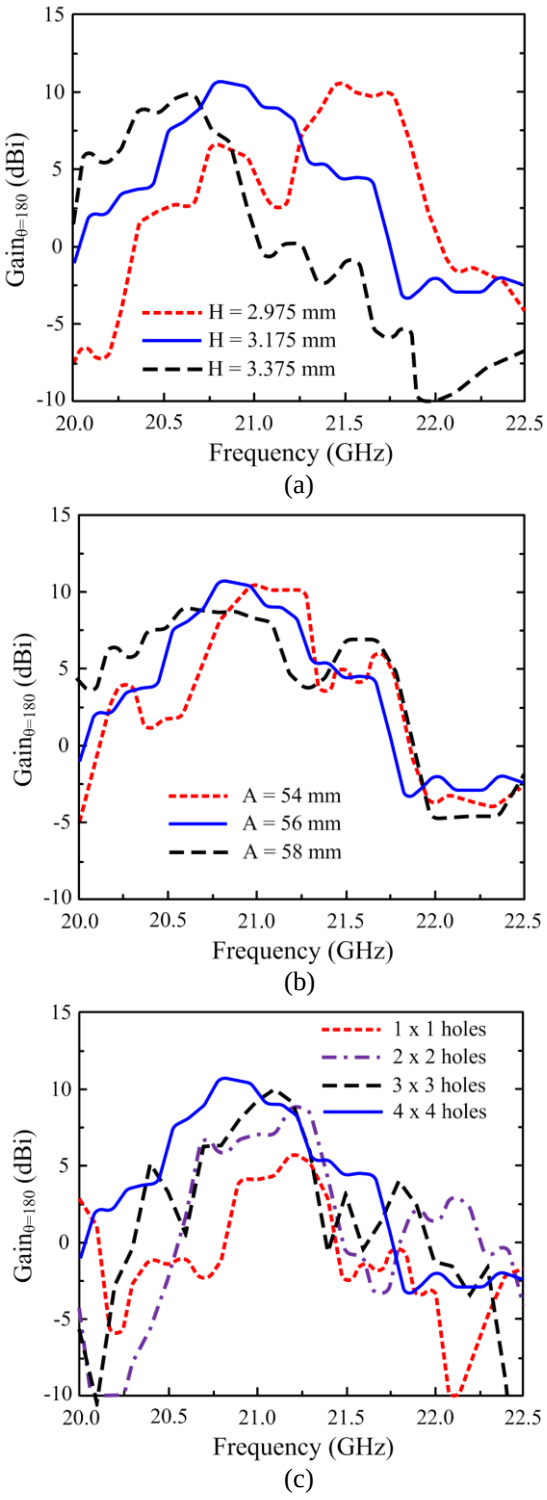

Fig. 3. Antenna gain characteristics with respect to: (a) Taconic substrate thickness *H*, (b) lateral size *A* for both substrates, and (c) number of circular holes in the array.

The electric field distributions along the stripline (*xz*-plane) and along the leaky-wave slitline (*yz*-plane) have been calculated and described in Fig. 4. The results show that, at the resonance frequency of 20.8 GHz, radiation is minimized at the edges of the substrate and in the back side of the antenna. This observation, thereby, verifies the directional beam pattern of the proposed antenna. In other words, this demonstrates that the Fabry-Perot cavity made of Taconic substrate the FSS hole array and was effectively excited by the slit-coupled feeding structure while avoiding unwanted back-side-radiation across a broad frequency range.

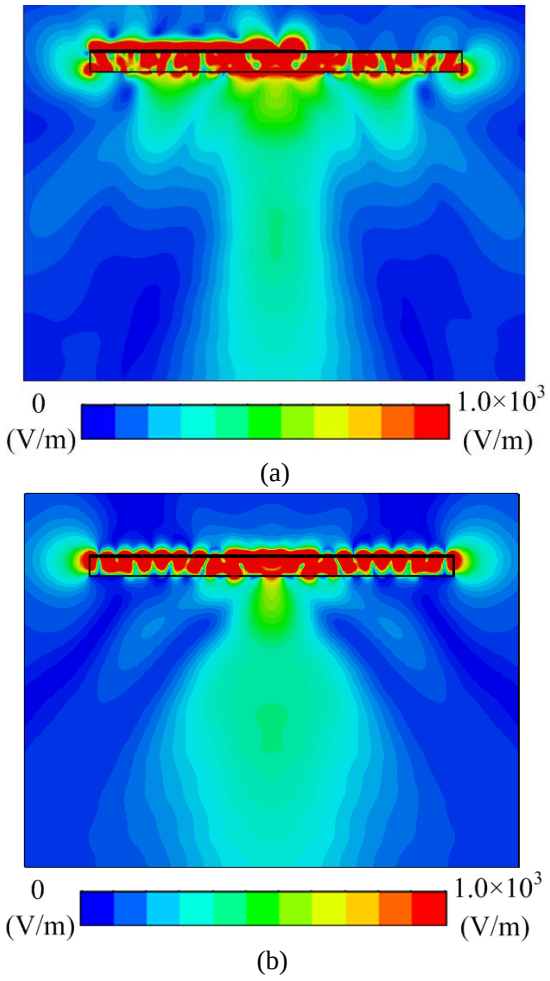

Fig. 4. E-field distributions at 20.8 GHz in: (a) *xz*-plane and (b) *yz*-plane of the optimized antenna.

III. MEASUREMENT RESULTS

The photograph of the fabricated antenna is shown in Fig. 5 with top, bottom, and side views. Figure 6 shows the results of $|S_{11}|$ and boresight gain as a

function of frequency in a comparison between the simulation and measurement. The E8362C Agilent PNA Microwave Network Analyzer was used to measure the |S11| of the fabricated antenna. Generally, the measured $|S_{11}|$ and boresight gain were close to the simulated ones. The approximate 0.1 GHz downward shifts of the measured |S11| and boresight gain in comparison to the simulated ones were observed which were mainly due to the tolerance of the dielectric constant of the Taconic substrate, i.e., specified as 10.2 ± 0.5, and the tiny gap between the two closely appressed substrates, i.e., Duroid and Taconic substrates. The measured impedance bandwidth for $|S_{11}| \leq$ -10 dB was about 0.9 GHz (20.6–21.5 GHz), which is approximately 4% fractional bandwidth at the 21.0 GHz center frequency. The antenna produced a measured maximum gain of about 10.4 dBi at 20.8 GHz. The achieved 3-dB gain bandwidth of the measured antenna was about 0.6 GHz, i.e., from 20.5 GHz to 21.1 GHz, corresponding to approximately 2.9% at the center frequency of 20.8 GHz. From these results, the proposed antenna obtained an approximate of 2.4% (20.6–21.1 GHz) common (available) bandwidth which is improved compared to the previously reported [10].

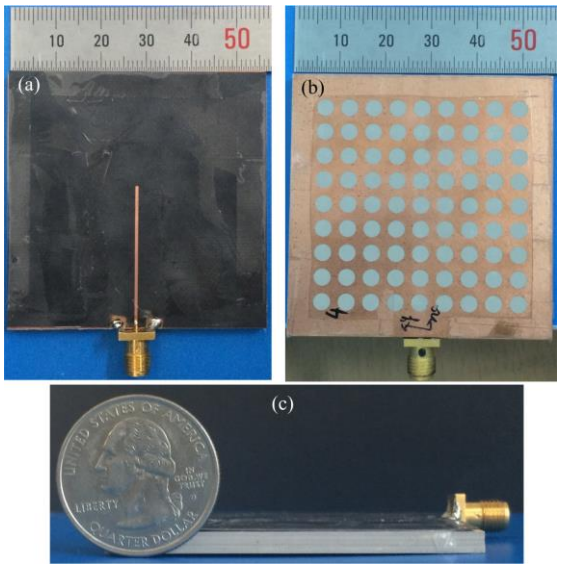

Fig. 5. Photographs of the fabricated antenna with: (a) top, (b) bottom, and (c) side views.

Figure 7 plots the measured radiation patterns in two principle planes at three selected frequencies within the 3-dB gain bandwidth of the antenna. The *yz*-plane presented symmetry radiation patterns whereas the *xz*-plane presented asymmetry radiation pattern which is due to the feeding configuration. The main beams in the *xz*-plane became narrower remarkably as increasing the frequency, whereas those in the *yz*-plane were almost the *yz*-plane indicates the traveling-wave effect of the open-ended slitline. Generally, it is obvious that the unchanged. Such stability of the main beam pattern in proposed antenna produced good radiation characteristics that are good beam collimation, clean main beam, and low side lobes levels.

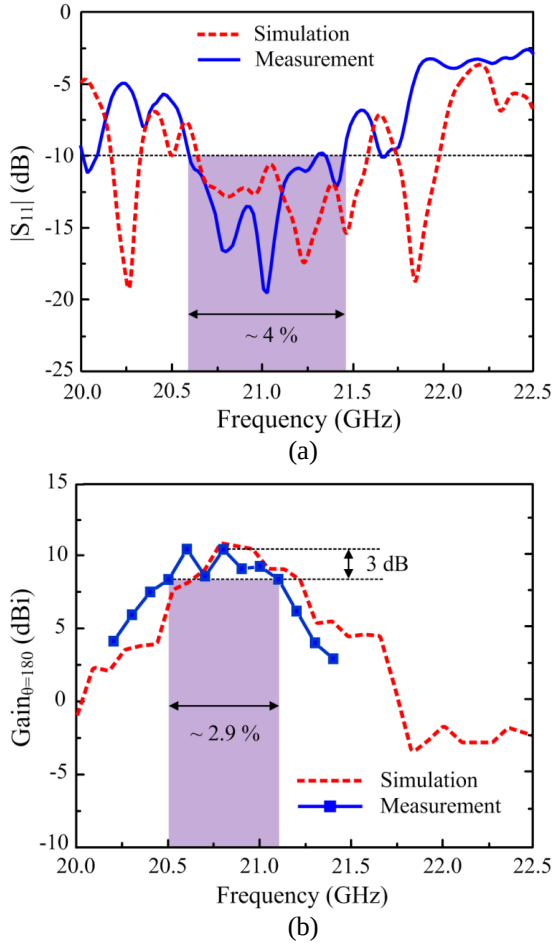

Fig. 6. (a) Reflection coefficient $|S_{11}|$, and (b) boresight gain of the proposed antenna.

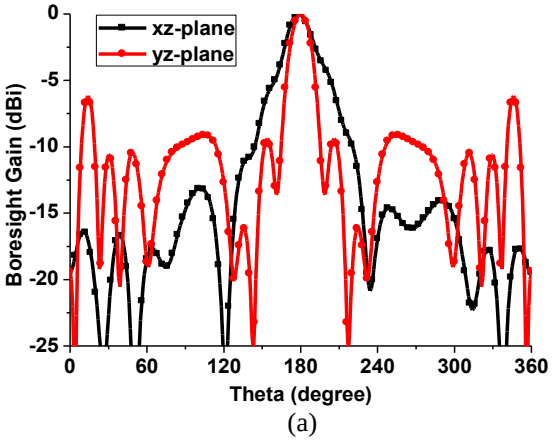

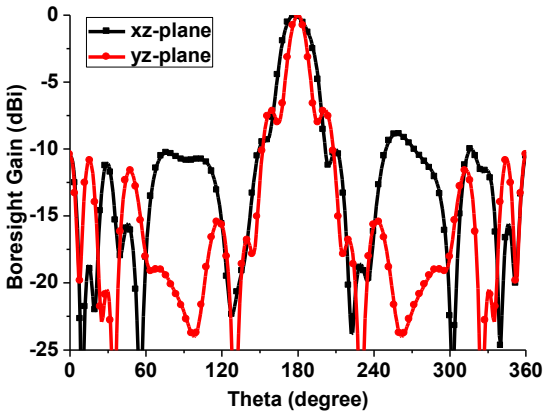

(b)

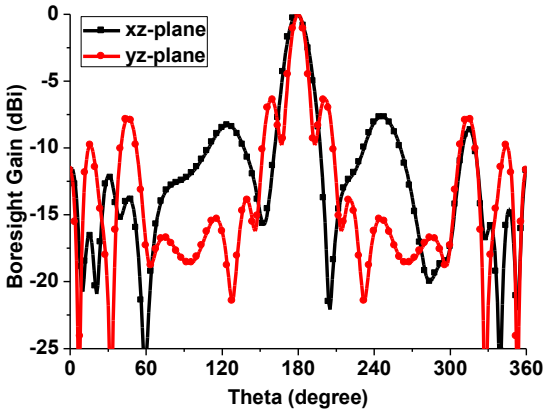

(c)

Fig. 7. Measured radiation patterns of the proposed antenna at different frequencies: (a) 20.6 GHz, (b) 20.8 GHz, and (c) 21.0 GHz.

VI. CONCLUSION

In this paper, we present a Fabry-Perot cavity antenna for *K*-band applications. The antenna presents its planar, low-profile, high gain, and improved common bandwidth characteristics. The results indicate that the strip-coupled-slitline feeding structure effectively excited the resonance of the substrate cavity. The antenna obtained good radiation patterns over the entire the 3-dB gain frequency bandwidth. In particular, the common (available) bandwidth is improved. The study shows that the performance of such planar Fabry-Perot resonator antenna can be improved by properly designing the feeding structure besides carefully modifying and optimizing of the FSS geometry [14].

ACKNOWLEDGMENT

This research is funded by Vietnam National Foundation for Science and Technology Development (NAFOSTED) under grant number 103.05-2016.37.

REFERENCES

[1] G. V. Trentini, "Partially reflecting sheet array," *IRE Trans. Antenn. Propagat.*, vol. 4, pp. 666-671, 1956.

[2] R. E. Collin and F. J. Zucker, *Antenna Theory*. New York, Wiley, 1969.

[3] D. R. Jackson and N. Alexopoulos, "Gain enhancement methods for printed circuits antennas," *IEEE Trans. Antenn. Propagat.*, vol. 33 pp. 976-987, 1985.

[4] A. P. Feresidis and J. C. Vardaxoglou, "High-gain planar antenna using optimized partially reflective surfaces," *IEE Proc. Microw. Antenn. Propagat.*, vol. 148, pp. 345-350, 2001.

[5] H. Boutayeb, K. Mahdjoubi, A.-C. Tarot, and T. A. Denidni, "Directivity of an antenna embedded inside a Fabry-Perot cavity: Analysis and design," *Microw. Opt. Technol. Lett.*, vol. 48, pp. 12-17, 2006.

[6] Y. Zhang, W. Yu, and W. Li, "Study on Fabry-Pérot antennas using dipole exciters," *Applied Computational Electromag. Soc. J.*, vol. 29 no. 12, pp. 1112-1116, 2014.

[7] G. Di Massa, S. Costanzo, and H. O. Moreno, "Planar Fabry-Perot directive antenna: A simplified analysis by equivalent circuit approach," *J. Electromagn. Waves Appl.*, vol. 29, no. 2, pp. 261-274, 2015.

[8] Y. Sun, Z. N. Chen, Y. Zhang, H. Chen, and T. S. P. See, "Subwave-length substrate-integrated Fabry-Pérot cavity antennas using artificial magnetic conductor," *IEEE Trans. Antenn. Propagat.*, vol. 60, pp. 30-35, 2012.

[9] J. Ju, D. Kim, and J. Choi, "Fabry-Perot cavity antenna with lateral metallic walls for WiBro base station applications," *Electron. Lett.*, vol. 45, pp. 141-142, 2009.

[10] T. K. Nguyen and I. Park, "Design of a substrate-integrated Fabry-Perot cavity antenna for *K*-band applications," *Int. J. Antenn. Propagat.*, 373801, pp. 1-12, 2015.

[11] T. K. Nguyen and I. Park, "Design of a low-profile, high-gain Fabry-Perot cavity antenna for Ku-band applications," *J. Electromagn. Eng. Sci.*, vol. 14 pp. 306-313, 2014.

[12] CST Microwave Studio, CST GmbH, 2016. http://www.cst.com

[13] T. K. Nguyen, B. Q. Ta, and I. Park, "Design of a planar, high-gain, substrate-integrated Fabry-Perot cavity antenna at terahertz frequency," *Current Applied Phys.*, vol. 15, no. 9, pp. 1047-1053, 2015.

[14] L. Zhou, X. Chen, and X. Duan, "High gain

Fabry-Perot cavity antenna with phase shifting surface," *IEEE/ACES Int. Conf. on Wireless Infor. Tech. and Sys. (ICWITS) and Applied Comput. Electromag. (ACES)*, Hawaii, USA, 2016.

Huy Hung Tran received the B.S. degree in Electronics and Telecommunications from Hanoi University of Science and Technology, Hanoi, Vietnam in 2013, and the M.S. degree in the Department of Electrical and Computer Engineering, Ajou University, Suwon, Korea in 2015. His research is focused on wideband circularly polarized, and metamaterial for next generation wireless communication systems.

Truong Khang Nguyen received the B.S. degree in Computational Physics from the University of Science, Vietnam National University, Ho Chi Minh City, and the M.S. and Ph.D. degrees in Electrical and Computer Engineering from Ajou University in Suwon, Korea. He is currently Head of Division of Computational Physics, Institute for Computational Science & Faculty of Electrical-Electronics Engineering, Ton Duc Thang University in Ho Chi Minh City, Vietnam. He has authored and co-authored over 60 peer-reviewed international journal and conference papers. He has written one book chapter in the area of terahertz antenna and filed one patent on THz stripline antenna. His current research interests include the design and analysis of microwave, millimeter-wave, terahertz wave, and nano-structured antennas.

Design and Analysis of a Koch Snowflake Fractal Monopole Antenna for Wideband Communication

Ankan Bhattacharya [1*], Bappadittya Roy [1], Santosh K. Chowdhury [2], and Anup K. Bhattacharjee [1]

[1] Department of Electronics and Communication Engineering
National Institute of Technology, Durgapur-713209, India
*bhattacharya.ankan1987@gmail.com

[2] Department of Electronics and Telecommunication Engineering
Jadavpur University, Kolkata-700032, India

Abstract — In this article a compact wideband monopole antenna with constant high gain has been designed and fabricated for wideband microwave communication. Koch fractal geometry has been applied for design of this antenna structure. A wide bandwidth of 3.3 GHz (3.0 GHz to 6.3 GHz) has been obtained, which covers the IEEE 802.11 WLAN bands (5.2 GHz and 5.8 GHz) and WiMAX bands (3.5 GHz and 5.5 GHz). The proposed antenna is characterized by its high gain which remains constant throughout the entire operation bandwidth. An average gain of 5.07 dBi has been realized at all the frequencies of interest. The realized antenna gains are 5.01 dBi, 5.07 dBi, 5.09 dBi and 5.11 dBi at frequencies of 3.5 GHz, 5.2 GHz, 5.5 GHz and 5.8 GHz respectively. Good agreement between simulated and measured results justifies the applicability of the proposed antenna for wideband communication purpose, particularly for the WLAN and WiMAX microwave frequency bands of interest.

Index Terms — Constant gain, fractal geometry, wideband antenna, wireless communication.

I. INTRODUCTION

Wideband antennas are gaining huge popularity now-a-days in the field of wireless communication and technology. The conventional patch antenna used in communication technologies suffer from narrow bandwidth and return loss issues. To overcome this disadvantage fractal shapes have been introduced in design of patches in order to improve the impedance-bandwidth and incorporate wideband characteristics. Monopole antennas with various fractal shaped patch structures have shown good return loss characteristics with wide bandwidth, which have fulfilled the need for wideband communication, particularly for the IEEE 802.11 WLAN and WiMAX bands, as available in existing literatures. A fractal hexagonal monopole has been presented in [1] by Fallahi and Atlasbaf, but the maximum available gain is around 3.25 dBi and the average gain is less than 2.5 dBi at the WLAN and WiMAX bands. An H-shaped fractal antenna has been presented in [2] by Weng and Hung, optimized using PSO method for WLAN, but the average gain is much less than 5.0 dBi. A dual band antenna with fractal ground for WLAN has been presented in [3] by Gemio et al. Variable gain less than 5.0 dBi has been obtained as mentioned in the work. Sierpinski carpet fractal antenna with CPW feed has been presented in [4] by Ghatak et al., the average gain obtained is around 4.5 dBi. A wideband fractal loop monopole has been presented in [5] by Chaimool et al., where the realized gain is around 2.0 dBi. Various other slotted and fractal geometries for wideband antennas have been observed in articles [6]-[10], but the realized gain of operation is not constant and falls below the 5.0 dBi margin at some or all the frequencies of interest. In this work we have proposed a fractal shaped monopole antenna with constant high gain ~ 5.0 dBi. It may be noted that the thickness of the proposed structure is kept only 2.00 mm. Koch snowflake fractal geometry has been applied in design of the patch structure along with a slotted ground plane. A wide bandwidth of 3.3 GHz has been observed, which effectively covers the IEEE 802.11 WLAN bands (5.2 GHz and 5.8 GHz) and WiMAX bands (3.5 GHz and 5.5 GHz). The antenna has an average gain of 5.07 dBi at the IEEE 802.11 WLAN and WiMAX bands (5.01 dBi, 5.07 dBi, 5.09 dBi and 5.11 dBi at frequencies of 3.5 GHz, 5.2 GHz, 5.5 GHz and 5.8 GHz respectively). Parametric study of the proposed structure has been elaborated for better understanding of the frequency response characteristics of the proposed structure.

Submitted On: June 23, 2016
Accepted On: March 10, 2017

II. ANTENNA DESIGN PROCEDURE

Koch snowflake fractal geometry has been incorporated in the patch of the proposed radiating structure. Koch first introduced this geometry in 1904. This geometry is generated by an iterative function system (IFS). It is obtained by a set of overlapping equilateral triangles. In Fig. 1, the iterative Koch structure has been displayed. After an iterative transform *n*, there is an increase in the overall geometrical area.

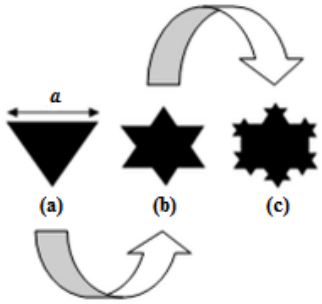

Fig. 1. Koch fractal geometry in successive iterations: (a) basic geometry, (b) 1st iteration, and (c) 2nd iteration.

If S_n be the area at each iteration n, then the overall area of the successive iteration can be obtained as:

$$S_{n+1} = S_n + (\sqrt{3}/12) .(4/9)^{n-1} .a^2, \quad (1)$$

where a is the length of the side of an equilateral triangle, whose area is equal to:

$$S_o = (\sqrt{3}/4) .a^2. \quad (2)$$

Figure 2 shows the comparison plot of basic geometry, 1st iteration and 2nd iteration stages of Koch fractal geometry. Best result has been achieved in the final or 2nd iterative stage. As observed from Fig. 2, a wide impedance-bandwidth of 3.3 GHz (3.0 – 6.3 GHz) has been obtained in the 2nd iterative stage. Our objective is to design a compact high gain wideband antenna. The task has been achieved in the 2nd iterative stage. All other standards for wideband communication have been successfully achieved. Therefore the 2nd iterative stage has been chosen as the final stage of the design. Figure 3 shows the complete structure of the proposed antenna along with side view. The proposed antenna is a unique combination of fractal and slotted structures, incorporated in a monopole configuration, in order to achieve wideband characteristics along with constant high gain at the frequency bands of interest. The patch and the ground plane are composed of copper (annealed). The patch is designed using Koch snowflake fractal geometry, fed by a feed line of width 1.5 mm in order to match the characteristic impedance, which has been explained in the next section

Fractal structures help in implementing large electrical length within a small surface area. The nearly spaced resonant frequencies come closer with the increase in the number of iterations of the fractal structures. The ground plane is etched from the top and a rectangular slot is cut midway. The low-cost substrate (Arlon AR 600) having a dielectric constant ε_r of 6.0 is sandwiched between the fractal patch and the slotted ground plane. The substrate thickness is kept equal to 1.0 mm. The reason is, thicker substrates increases the impedance-bandwidth but generates surface waves, which have a negative effect on antenna radiation. The overall thickness of the structure is 2.0 mm including the thickness of the patch (0.5 mm) and the ground plane (0.5 mm). For the proposed design parameter a is taken as 6.0 mm. The design has been kept compact, for the antenna to be easily incorporated in wireless devices. The detailed dimensions of the structure are provided in Table 1.

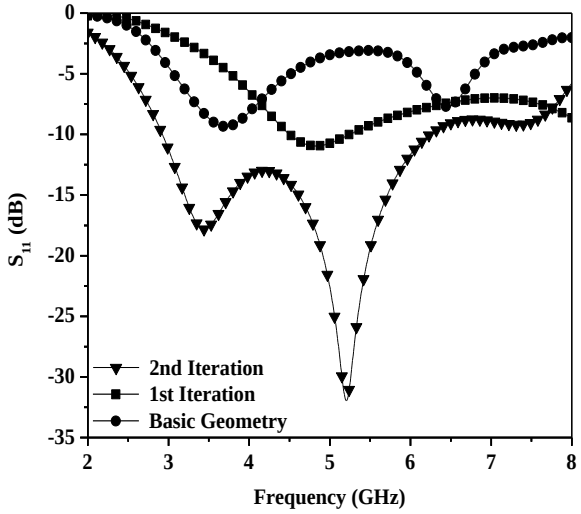

Fig. 2. Comparison plot of various iterative stages.

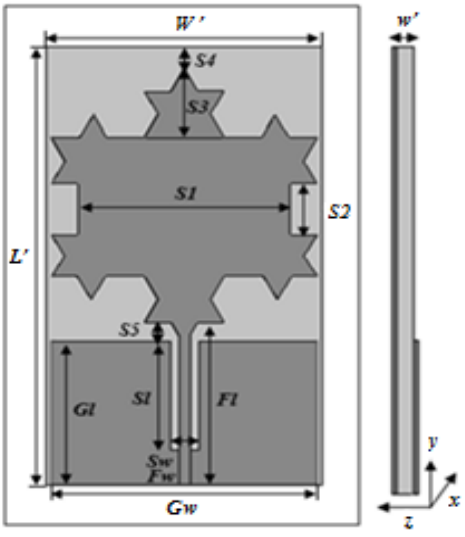

Fig. 3. Proposed fractal monopole antenna along with side view.

Table 1: Parameter dimensions (in mm)

Parameters	Dimensions	Parameter	Dimensions
W'	26.50	*Fw*	01.50
L'	47.00	*Fl*	16.50
S1	20.50	*Gw*	25.50
S2	06.00	*Gl*	16.00
S3	06.25	*Sw*	02.50
S4	02.50	*Sl*	12.00
S5	02.00	*w'*	02.50

III. PARAMETRIC STUDIES AND DISCUSSION

In this section, keeping the substrate parameter same, i.e., Arlon AR 600, the effect of other design parameters of the antenna such as the feed length (*Fl*), slot width (*Sw*) and slot length (*Sl*) of the rectangular slot in the ground plane, the ground width (*Gw*) and ground length (*Gl*) of the ground plane are observed and the results are discussed sequentially.

The feed line width (*Fw*) should be carefully selected. It is an important parameter which affects the impedance matching between the current source and the radiating element, i.e., the antenna. There should be an impedance match between the source element and the load resistance for maximum power to be transferred. The feed line is designed to match the 50 Ω characteristic impedance using Equations (3) and (4). For the proposed design, substrate dielectric constant, ε_r = 6.0 (Arlon 600), substrate height, h = 1.0 mm and width of feed line, Fw = 1.5 mm.

$$\varepsilon_{eff} = \frac{\varepsilon r+1}{2} + \frac{\varepsilon r-1}{2}\left[\sqrt{1 + 12\,(h/Fw)}\right]^{-1}, \quad (3)$$

$$Z_o = \frac{120\pi}{\sqrt{\varepsilon eff}\left[\frac{Fw}{h} + 1.393 + 0.667\,ln\left(\frac{Fw}{h} + 1.444\right)\right]}, \quad (4)$$

for $Fw/h \geq 1$. Zo is the aracteristic impedance and ε_{eff} is the effective dielectric constant of substrate [9].

An optimum feed line width *Fw* of 1.5 mm has been selected to approximately match the 50 Ω input impedance and to obtain desired bandwidth and return loss level. Our next aim is to obtain an optimum dimension for the length of the feed line. Therefore, keeping the other parameters fixed the feed length *Fl* has been varied. The optimized feed length obtained is 27.75 mm (Fig. 4). The overall feed line dimension is therefore given as *Fw* x *Fl* = 1.5 x 27.75 mm.

The dimensions of the ground plane has an effect on the impedance-bandwidth as well as on the available resonant modes of the designed structure. A portion of the ground plane has been etched. Etching a portion of the ground plane yields improved S_{11} characteristics. Keeping the other design parameters constant, the width of the ground plane *Gw* is varied. The optimized dimension obtained for *Gw* is 25.50 mm (Fig. 5). Next, the ground length *Gl* is varied keeping the other parameters unchanged. As is observed from Fig. 6, there is an increment in bandwidth when the length of the ground plane *Gl* increases from 21.5 mm to 23.5 mm. But on further increment of the length of the ground plane, *Gl* beyond 24.00 mm, it has been observed that though there is an increment of impedance-bandwidth, there is a decrement in $|S_{11}|$, which provides a negative effect on antenna response. The effect of ground plane length *Gl* on frequency response of the structure is well illustrated in Fig. 6. The optimized dimension for ground length *Gl* is therefore kept equal to 24.00 mm. The ground plane dimension is given as, *Gw* x *Gl* = 25.50 x 24.00 mm. The effect of slot in the ground plane is discussed in the next section.

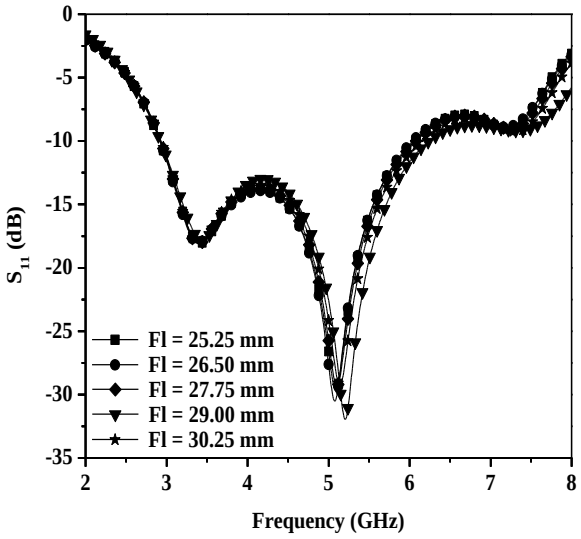

Fig. 4. Feed length effect on antenna response.

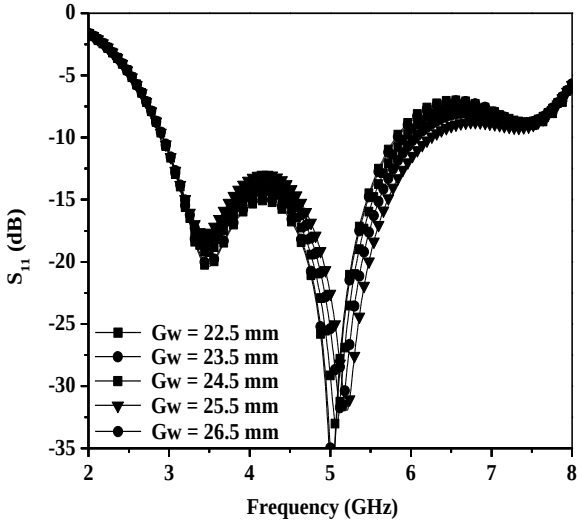

Fig. 5. Ground width effect on antenna response.

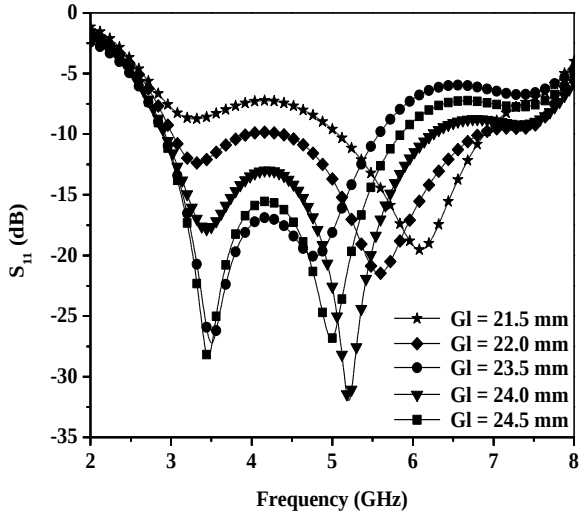

Fig. 6. Ground length effect on antenna response.

The current density is mainly concentrated near the ground slots and sparsely distributed elsewhere, which has an effect on the impedance bandwidth of the antenna. Slots in the ground plane reduces the ground effect by the suppression of currents in the ground plane at the operating frequency in the lower end. It also plays a significant role in impedance matching. Such ground plane structures are regarded as defected ground structures (DGS) in antenna engineering. A rectangular slot has been incorporated in the ground plane of the proposed structure. Figure 7 shows the variation of slot width *Sw* with frequency of the proposed structure, when the other design parameters have been kept constant. Increase in slot width increases the $|S_{11}|$. Optimized response has been obtained when the slot width is kept as 2.5 mm. Figure 7 and Fig. 8 justify the optimized set of dimensions for the ground plane slot.

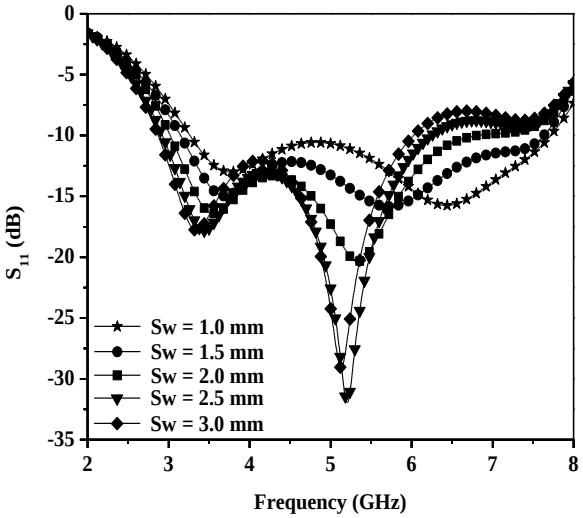

Fig. 7. Effect of slot width on antenna response.

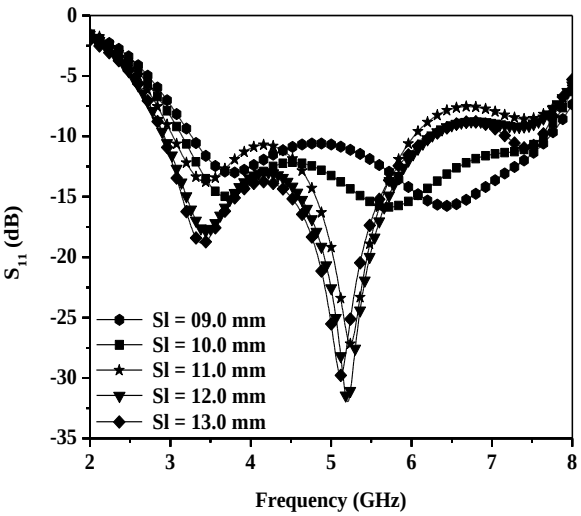

Fig. 8. Effect of slot length on antenna response.

As seen from Fig. 7, the slot width has a direct effect on the variation of $|S_{11}|$, which is minimum when *Sw* is kept equal to 1 mm. Similarly, as observed from Fig. 8, the slot length *Sl* is directly proportional to variation of $|S_{11}|$, when *Sl* is sequentially changed keeping the other design parameters fixed. $|S_{11}|$ increases on increase in slot length, which is kept equal to *Sl* = 12.00 mm (Fig. 8). The dimensions of the rectangular slot in the ground plane is therefore chosen as, *Sw* x *Sl* = 02.5 x 12.00 mm for achieving an optimized frequency response for wideband operation.

IV. FABRICATION AND MEASUREMENT

Prototype of the proposed antenna (as displayed in Fig. 3) has been fabricated (Fig. 9) and tested. The return loss characteristic is measured using 'Vector-Network-Analyzer' or VNA; spec. Agilent Technology N5-230A.

Figure 10 shows the comparison plot of the measured and simulated return losses of the fabricated antenna. The deviation between the VNA measured and CST simulated results is very negligible and it occurs due to the effect of the soldering and fabrication tolerance. The antenna shows an average realized gain of 5.07 dBi at all the proposed IEEE 802.11 WLAN and WiMAX bands, which is depicted in Fig. 11. The measured gain is also in good agreement with the simulated gain. Some discrepancies between simulated and measured results may also occur due to the soldering effect of the SMA connector.

The current distribution pattern of antenna surface is shown in Fig. 12. Analysis of surface current distribution pattern is extremely important in order to get an idea of the antenna characteristics. As observed from Fig. 12, the current originates from the feed and gradually distributes itself towards the edges of the patch, creating nearly spaced resonant frequencies, which results in

enhancement of the impedance bandwidth, gain and low variation in the gain parameter at the resonant frequency points. This phenomenon happens due to the self-similarity property of fractals. The maximum surface current is 36.8 A/m and the minimum surface current is 2.30 A/m. The realized antenna gains are 5.01 dBi, 5.07 dBi, 5.09 dBi and 5.11 dBi at frequencies of 3.5 GHz, 5.2 GHz, 5.5 GHz and 5.8 GHz respectively. The average realized gain is 5.07 dBi at the frequency bands of interest (Fig. 11). As observed from Fig. 11, the antenna gain is almost constant around the 5.0 dBi margin. Simulated and measured results are in good agreement.

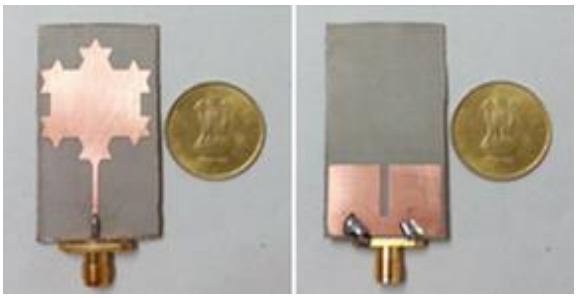

Fig. 9. Fabricated prototype - front and rear view.

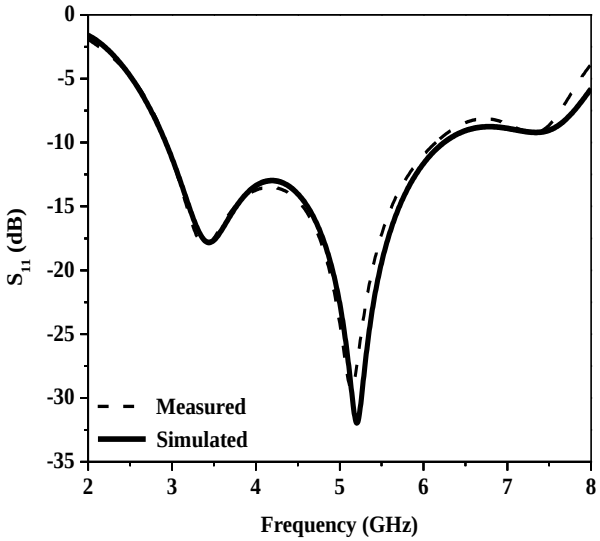

Fig. 10. Response of simulated and fabricated prototype.

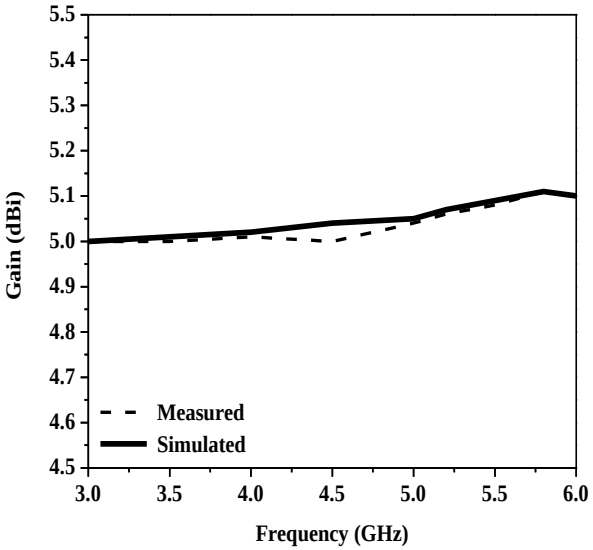

Fig. 11. Measured and simulated antenna gain.

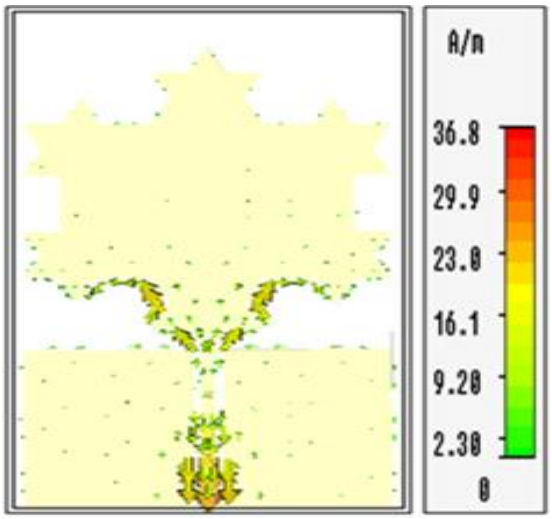

Fig. 12. Current distribution pattern of antenna surface.

Effect of co- and cross-polar components at the frequencies of interest have also been considered. Desired co-polar and cross-polar isolation are obtained, which is depicted in Fig. 13 for a beamwidth consideration higher than 90°.

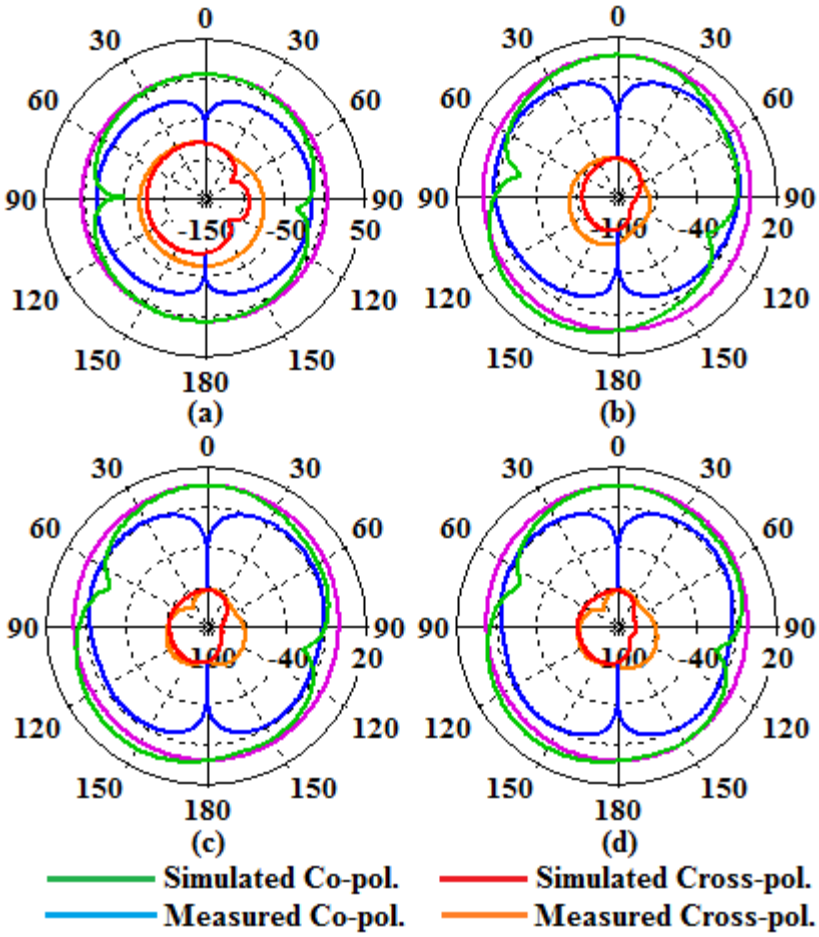

Fig. 13. Radiation pattern of proposed antenna: (a) 3.5 GHz, (b) 5.2 GHz, (c) 5.5 GHz, and (d) 5.8 GHz.

V. CONCLUSION

This article presents a novel approach in monopole antenna design in combination with fractal shaped patch element and slotted ground plane in a monopole configuration. The most significant feature of the antenna is its almost constant high gain which is maintained at all the frequencies of interest. The structure is easy to fabricate and due to its compactness it can be easily incorporated in portable devices suited for wireless communication purposes. The presented structure shows a wide bandwidth of 3.3 GHz (3.0 GHz to 6.3 GHz), which covers the IEEE 802.11 WLAN bands (5.2 GHz and 5.8 GHz) and WiMAX bands (3.5 GHz and 5.5 GHz). The antenna has gain of 5.01 dBi, 5.07 dBi, 5.09 dBi and 5.11 dBi at frequencies of 3.5 GHz, 5.2 GHz, 5.5 GHz and 5.8 GHz respectively. An average gain of 5.07 dBi realized at the proposed WLAN and WiMAX bands is an added advantage in this regard.

REFERENCES

[1] H. Fallahi and Z. Atlasbaf, "Study of a class of UWB CPW-fed monopole antenna with fractal elements," *IEEE Antennas and Wireless Propagation Letters*, vol. 12, pp. 1484-1487, 2013.

[2] W. C. Weng and C. L. Hung, "An H-fractal antenna for multiband applications," *IEEE Antennas and Wireless Propagation Letters*, vol. 13, pp. 1705-1708, 2014.

[3] J. Gemio, J. Parron Granados, and J. Soler Castany, "Dual-band antenna with fractal-based ground plane for WLAN applications," *IEEE Antennas and Wireless Propagation Letters*, vol. 8, pp. 748-751, 2009.

[4] R. Ghatak, R. K. Mishra, and D. R. Poddar, "Perturbed Sierpinski carpet antenna with CPW feed for IEEE 802.11 a/b WLAN application," *IEEE Antennas and Wireless Propagation Letters*, vol. 7, pp. 742-744, 2008.

[5] S. Chaimool, C. Chokchai, and P. Akkaraekthalin, "Multiband loaded fractal loop monopole antenna for USB dongle applications," *Electronics Letters*, vol. 48, no. 23, pp. 1446-1447, Nov. 8, 2012.

[6] W. L. Chen, G. M. Wang, and C. X. Zhang, "Bandwidth enhancement of a microstrip-line-fed

printed wide-slot antenna with a fractal-shaped slot," *IEEE Transactions on Antennas and Propagation*, vol. 57, no. 7, pp. 2176-2179, July 2009.

[7] A. Kundu, U. Chakraborty, and A. K. Bhattacharjee, "Design of a compact wide band microstrip antenna with very low VSWR for WiMAX applications," *International Journal of Microwave and Wireless Technologies*, vol. 9, iss. 3, pp. 685-690, Apr. 2017.

[8] K. El. Mahgoub, "Slotted triangular monopole antenna for UHF RFID readers," *Applied Computational Electromagnetics Society (ACES) Express Journal*, vol. 1, no. 1, pp. 24-27, Jan. 2016.

[9] M. Naghshvarian-Jahromi, "Novel wideband planar fractal monopole antenna," *IEEE Transactions on Antennas and Propagation*, vol. 56, no. 12 pp. 3844-3849, Dec. 2008.

[10] A. Bhattacharya, B. Roy, S. K. Chowdhury, and A. K. Bhattacharjee, "A compact fractal monopole antenna with defected ground structure for wideband communication," *Applied Computational Electromagnetics Society (ACES) Express Journal*, vol. 1, no. 8, pp. 228-231, Oct. 2016.

Ankan Bhattacharya obtained B.Tech and M.Tech degrees in Electronics and Communication Engineering from West Bengal University of Technology in 2010 and 2012 respectively. He is a Ph.D. Research Scholar in the Department of Electronics and Communication Engineering at National Institute of Technology, Durgapur, West Bengal, India. He is a Life-Member of FOSET (Forum of Scientists, Engineers and Technologists), Member of IEEE (Institute of Electrical and Electronics Engineers) and Member of Applied Computational Electromagnetics Society (ACES). His area of research is design and development of Compact Slotted Antennas for wireless applications. His research articles have been published in many national and international journals and conferences.

Bappadittya Roy obtained B.Tech and M.Tech degrees in Electronics and Communication Engineering from West Bengal University of Technology, West Bengal, India in 2008 and 2011 respectively. He is a TQIP-Sponsored Ph.D. Research Scholar in the Department of Electronics and Communication Engineering at National Institute of Technology, Durgapur, West Bengal, India. He is a member of IEEE (Institute of Electrical and Electronics Engineers). His research areas are Microstrip Antennas, Fractal Antennas and Mobile Communication. He has received many national and international travel grants and has travelled abroad for seminars, conferences and workshops. He has published several articles in reputed journals and conferences.

Santosh Kumar Chowdhury received his B.E. degree in Electronics and Telecommunication Engineering from Jadavpur University, Kolkata in 1964. He received M.E. and Ph.D. degrees from Jadavpur University, Kolkata in 1968 and 1973 respectively. He was a Professor of the Department of Electronics and Telecommunication Engineering, Jadavpur University, Kolkata from 1973 to 2003. He is also associated with NITMAS, Kolkata, West Bengal, India. He is a Member of the International Advisory Board of Journal of OR Society, UK and IFORS. He is also a Member of Institute of Operational Research and Management Science, USA since 1992. His research areas are Microstrip Antennas, Large Scale Optimization Models and Mathematical Models in Insurance and Finance. He has supervised over 18 Ph.D. students and has published more than 150 national and international journal and conference articles.

Anup Kumar Bhattacharjee received his B.E. degree in Electronics and Telecommunication Engineering from B.E. College Shibpur, Howrah, India in 1983. He received M.E. and Ph.D. degrees from Jadavpur University, Kolkata, India in 1985 and 1989 respectively. Presently he is associated with National Institute of Technology, Durgapur, West Bengal, India as a Senior Professor of Electronics and Communication Engineering Department. His research areas are Electronic Devices and Circuits, Microwave Devices, Microstrip Antennas, Embedded Systems, VLSI Systems, Mobile Communications, Satellite Communications etc. He has successfully supervised over 13 Ph.D. students and has published over 120 articles in national and international journals, magazines and conferences.